University of Southampton, 2016

FACULTY OF ENGINEERING AND THE ENVIRONMENT

INSTITUTE OF SOUND AND VIBRATION RESEARCH

ON THE PREDICTION OF THE EFFECT OF INTERSTAGE LINERS IN TURBOFAN ENGINES

by Ana Luisa Pereira Maldonado

Thesis submitted in partial fulfilment of the
requirements for the degree of PhD by research course

..

Declaration of Authorship

I, Ana Luisa Pereira Maldonado, declare that the thesis entitled ON THE PREDICTION OF THE EFFECT OF INTERSTAGE LINERS IN TURBOFAN ENGINES and the work presented in the thesis are both my own, and have been generated by me as the result of my own original research. I confirm that:

- this work was done wholly or mainly while in candidature for a research degree at this University;
- where any part of this thesis has previously been submitted for a research degree or any other qualification at this University or any other institution, this has been clearly stated;
- where I have consulted the published work of others, this is always clearly attributed;
- where I have quoted from the work of others, the source is always given. With the exception of such quotations, this thesis is entirely my own work;
- I have acknowledged all main sources of help;
- where the thesis is based on work done by myself jointly with others, I have made clear exactly what was done by others and what I have contributed myself;
- parts of this work have been published as:

  A. L. P. Maldonado, R. J. Astley, G. Gabard, *The Impact of Mean swirling Flows on the Sound Propagation in the Absence of Liners: A Parametric Study*, International Conference of Sound and Vibration, Athens, July 2016

  A. L. P. Maldonado, R. J. Astley, G. Gabard, *On the Prediction of the Effect of Interstage Liners in Turbofan Engines* United Kingdom X-Noise Network in Aeroacoustics, Lyon, France 2nd June 2016

  A. L. P. Maldonado, R. J. Astley, J. Coupland, G. Gabard, D. Sutliff, *Sound Propagation in Lined Annular Ducts with Mean Swirling Flow*, 21st AIAA/CEAS Aeroacoustics Conference, Dallas, TX, AIAA 2015-2522, 22nd June 2015

  A. L. P. Maldonado, R. J. Astley, G. Gabard, *On the Prediction of the Effect of Interstage Liners in Turbofan Engines* United Kingdom X-Noise Network in Aeroacoustics, Manchester, UK, 20th April 2015

  A. L. P. Maldonado, R. J. Astley, G. Gabard, *Sound Propagation in Lined Annular Ducts with Mean Swirling Flow* United Kingdom X-Noise Network in Aeroacoustics, Greenwich, UK, 2nd April 2014

Signed:.....

Date:.....

Acknowledgements

This thesis is dedicated to my mother, Leni C. P. Maldonado, for her deepest love and inspiration. She passed away during the course of this thesis and is the determination in every page. I will be forever grateful to my father Jesus that has always stressed the importance of education and I know that this respect for education has, in some unconscious way, shaped my values and made me the person that I am today. Many thanks also to my sister Larissa for always being there for me in the best and worst moments.

I would like to express my deepest gratitude to my partner, Marcio, who has been a constant source of support and encouragement and at times believed in me more that I believed in myself. He is the one that had to deal with my bad mood during the hardest times.

I would like to express my gratitude to my supervisors Jeremy Astley and Gwenael Gabard for the useful comments, remarks and engagement through the learning process of this thesis. I will be forever grateful to Brian Tester for his helpful advice and valuable mentorship. I really appreciate it. Many thanks to Paul Murray for his advice and for sharing his expertise related to liners. I would like to express my special appreciation to Daniel Sutliff for the experimental results and for always being available for science discussions since a long time ago.

My sincere gratitude to the Engineering and Physical Science Research Council (EPSRC) that together with Rolls-Royce plc supported this research under the under the Dorothy Hodgkin Post-graduate Award. My appreciation also for the Royal Aeronautical Society for the support under the Aeroespace Speakers travel grant.

Finally, for all of my many friends that supported me during this PhD journey.

Abstract

The current trends for next generation turbofan engines are towards shorter nacelles and increased distances between the fan and the outlet guide vanes. This leads to an overall reduction in lined surface areas as well as an increase in the relative importance of the interstage liner, which is the liner placed between the rotor blades and the stator vanes. The interstage is different in that the liner is subject to a mean flow with a strong swirl component and shear. This project will contribute to understanding and predicting the effect of the swirl on liner attenuation and consists of 4 steps: To model an eigenvalue problem that includes sheared and swirling mean flows and acoustic absorption, to develop a code based on this eigenvalue problem and to validate it, to compare results from this code with experimental results and to carry out a parametric study to evaluate how the swirling flow afects liner attenuation and optimum impedance. Two models were developed. The first one considers a ducted sheared mean flow and is based on the Pridmore-Brown equation and the second one takes into consideration a mean flow with swirl and shear and is based on the Linearized Euler Equations. For both cases an eigenvalue problem was obtained by applying the normal mode analysis to the governing equations together with the impedance boundary condition. Both models were discretized using a Finite Difference Method. The codes were exhaustively validated against predicted values obtained by other methods for uniform, sheared and swirling mean flows and hard-walled and lined ducts. The swirling mean flow, when present, is a combination of rigid body and vortex swirl. A cross-validation between the Finite difference code based on the Linearized Euler Equation and the JM66 code from Rolls-Royce was carried out for a more realistic case. Axial wavenumbers and pressure and velocity eigenvectors obtained with the JM66 code were compared with the current predictions. A comparison has been conducted of predictions from the current Finite Difference code with measured data at a single frequency for a range of spinning mode numbers. Qualitative agreement is obtained for the measured Power Transmission loss (TL) but the low Mach numbers and modest TL levels meant that the effect of swirl was small nad it was difficult to validate the accuracy at the Finite Difference code specifically for the swirl case. Finally, a parametric study was undertaken for hard-walled and lined ducts for realistic interstage conditions to evaluate the effect sound propagation in swirling flows. This confirmed that the effect of swirl is higher for radial modes near cut-off and tends to vanish for higher radial mode orders. The swirl strongly changes the modal content. When swirl is included, the modal distribution for positive and negative azimuthal mode orders is no longer symmetrical. The higher the swirling flow magnitude, the more the modal content is shifted to negative circumferential mode orders. Co-rotating modes become more cut-on and contra-rotating modes become more cut-off. When acoustic absorptive liners are considered, the swirl changes the liner optimum resistance and reactance and affects the optimum insertion loss. The optimum resistance becomes considerably higher and the change in optimal liner reactance is not as pronounced. The swirling flow also reduces attenuation; the insertion loss is lower when swirl is considered. As a conclusion, swirling flow should be considered when designing liners.

Contents

List of Figures

Chapter 1

Introduction

1.1 Background

With the advent of the turbojet and turbofan engines in the 1960s, federal, state and local regulations were designed to protect the environment [5] . The US Federal Aviation Administration (FAA), the International Civil Aviation Organisation (ICAO) and the Environmental Protection Agency (EPA) have been working aggressively to regulate the environmental impact of aircraft operations, such as aircraft noise, discharges of chemicals into water bodies, air pollution and airports expansion impact.

On the other hand, as the regulations have become more strict, the demand for domestic flights has grown. A forecast by the Federal Aviation Administration (FAA) dated 2010 shows that commercial airports are under increasing pressure to expand their operations to increase by 3.6 percent annually through 2011. This trend remains, since in a separate report the Boeing market outlook $2013 - 2030$ shows that in-service commercial aircraft must expand an average 3.6 percent per year to double in size from $20,310$ aeroplanes today to $41,240$, corroborating the previous report [6]. This growing demand concerns environmental groups, communities around airports, aircraft companies, engine manufacturers and others to which the airport operations may be pertinent.

To address the environmental impact of this growing demand, the U.S. Government Accountability Office (GAO) surveyed officials from the fifty busiest airports in the United States to understand which were the key challenges and concerns regarding the current operations and future growths in airports [7]. GAO also visited 11 of those airports and interviewed a wide range of interested parties, such as federal, state and local officials. Some of the results are presented in Figure 1.2. It is evident that aircraft noise is the most significant environmental concern and the most challenging issue now and in the future.

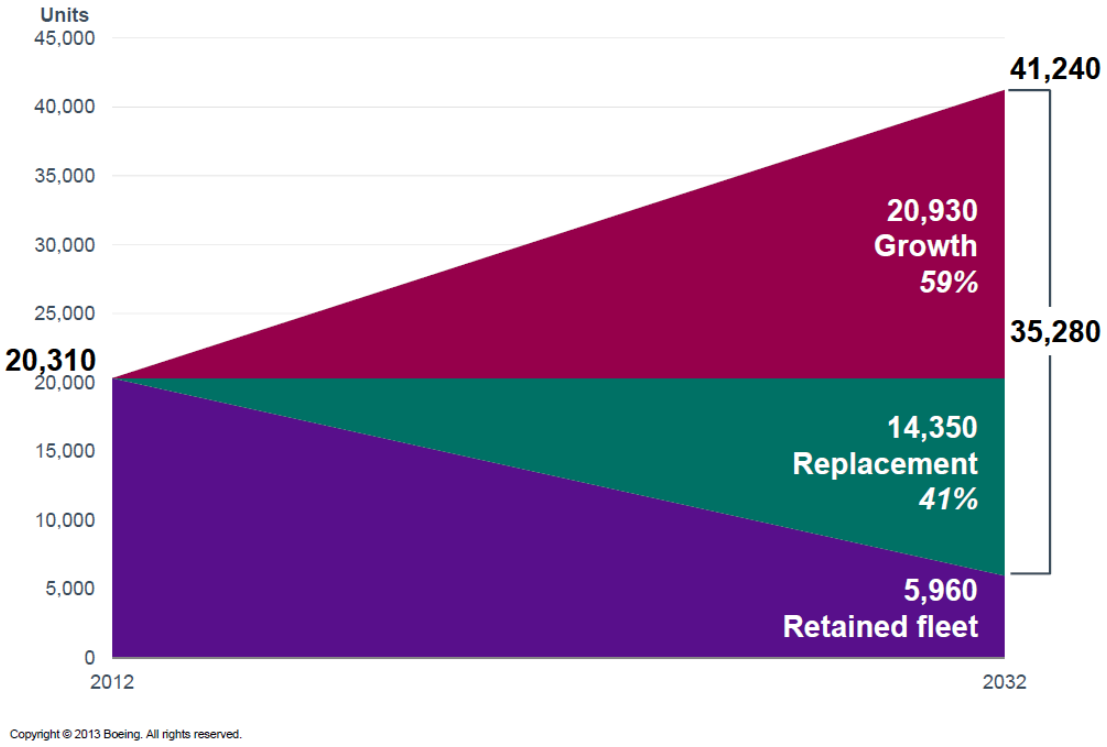

Fig. 1.1 – According to the Boeing market outlook 2013 – 2030, the in-service commercial aeroplanes must expand an average 3.6 percent per year to double in size. New generation aeroplanes will replace the less efficient ones. [6]

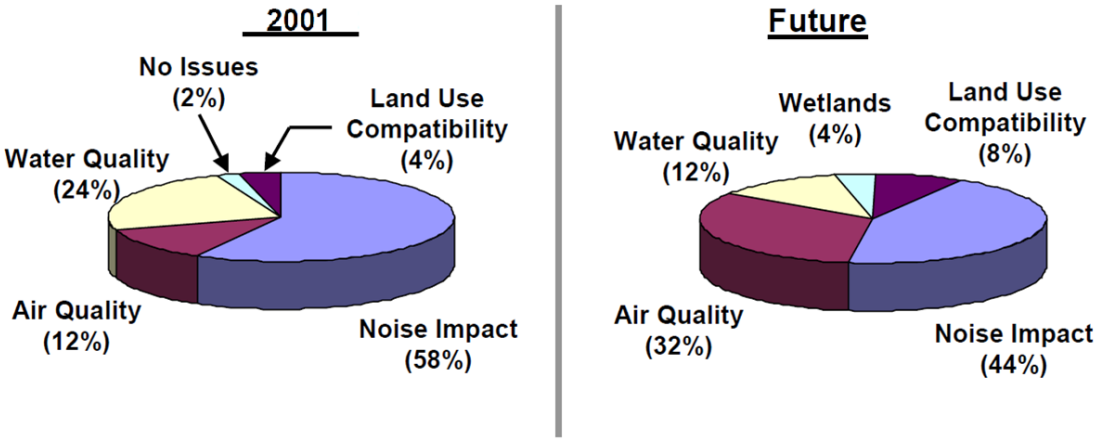

Fig. 1.2 – Noise is the most important concern of 29 airports and 22 airports answered that it will remain a problem in the future. FAA and EPA officials concurred with this result [7].

1.2 Turbofan Noise sources

One of the major sources of noise in aircraft is the turbomachinery noise. Figure 1.3 shows the turbomachinery noise sources and propagation paths in a turbofan engine. A significant noise source both at take-off and approach is fan noise, which propagates through the intake duct to the inlet and through the bypass duct to the rear, as presented in the figure 1.3 and in references [8], [9] and [10]. This noise source is even more important in high bypass ratio engines and is the object of study of this work.

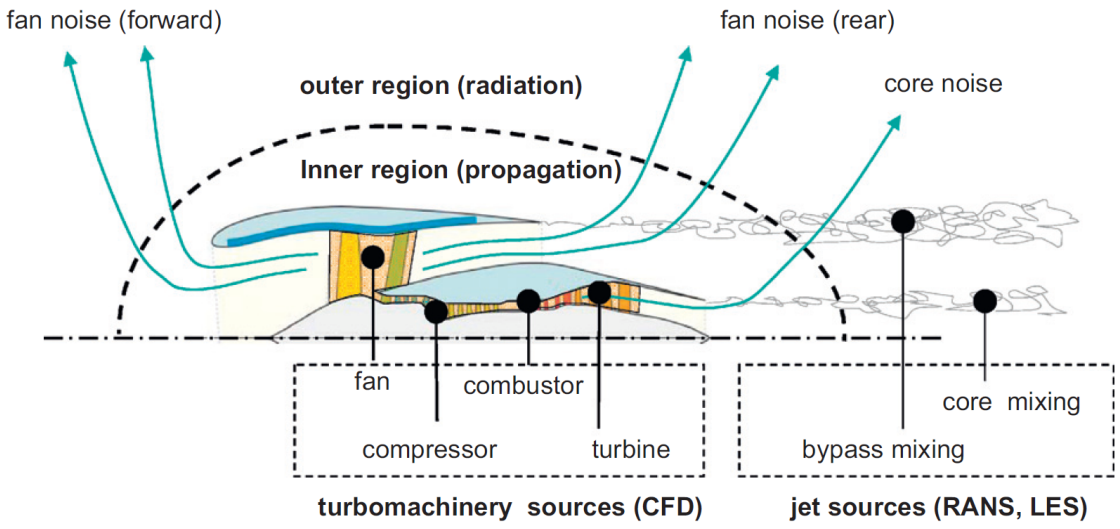

Fig. 1.3 – Turbofan noise sources [8]

The noise sources are divided into two subcategories: Tonal and broadband noise sources. Discrete tones are generated when there is an interaction between airflow perturbations in the path of a rotating blade row or stage and are associated with the blade passing frequency (BPF) and its harmonics and, at supersonic speeds, with buzz-saw noise. Examples of tonal noise sources are the rotor-alone and the rotor-stator interaction noise sources [11]. Broadband noise is a consequence of pressure fluctuations associated with turbulent flow interacting with the blade surfaces . The main noise sources of a turbofan are described in the following subsections. For more information see references [5], [11], [12] and [13].

1.2.1 Tonal Noise Sources

Rotor alone noise

Rotor-alone noise is an important source of turbomachinery noise, specially during the take-off phase of aircraft operation at high power. The rotor-alone noise is generated by a pressure field that radiates with the shaft velocity of the fan. At subsonic tip speeds, the sound does not propagate. However, when rotor tips rotate with supersonic speed, which is the case for many turbofan engines

during the take-off phase of aircraft operation at high power, the sound can propagate to the farfield. Three situations are possible:

- The rotor is in an uniform flow and the blades are identical and equally spaced: The forces on each blade are steady in the rotating coordinate system of reference. For a fixed observer, the rotor pressure field changes B times in circumferential direction, generating modes with azimuthal orders $m = hB$ (where h is an integer), and unknown radial order n. Considering that the rotor shaft rotates with a frequency Ω Hz and the rotor has B blades, spaced $2\pi/B$ radians apart, the blade passing frequency (BPF) will be given by:

$$f = B\Omega \tag{1.1}$$

  The rotor generates radial duct modes with azimuthal orders that are multiples of the blade passing frequency.

- Buzz-Saw Noise or multiple pure tone noise: At supersonic blade tip speeds, stand-off shocks start to develop ahead the fan blades. [5],[13] If the shocks for each blade is exactly the same, they propagate at the blade-passing frequency and its higher harmonics. However, small variations between blades lead can lead to different shock strengths and directions. In this case, multiple tones propagate at harmonics of the shaft frequency. Figure 1.4 shows an example of buzz-saw noise on an airbus A319 with CF56-5A engine. Blade Passing Frequency (BPF) around 2650Hz and rotor shaft frequency of 74Hz. The first and second BPF are highlighted with the red lines. Major tick interval corresponds to 10dB.

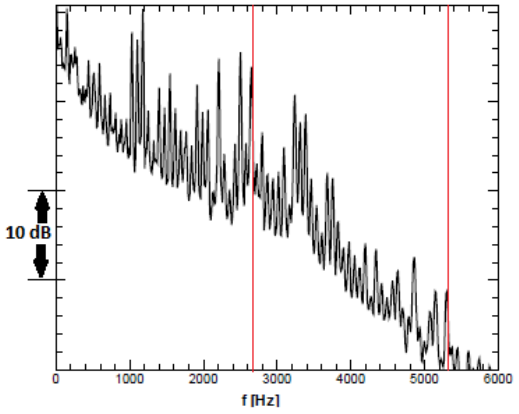

Fig. 1.4 – Example of buzz-saw noise on an airbus A319 with CF56-5A engine for an emission angle of 45 degrees in the forward arc. BPF around 2650Hz and rotor shaft frequency of 74Hz. Major tick interval corresponds to 10dB. [13]

Rotor-Stator Interaction

The rotor-stator interaction noise is mainly caused by two physical mechanisms: the impingement of rotating wakes and tip vortex on downstream stators; and the interruption of the rotating periodic pressure field of the rotor by the proximity of reflecting objects apart from wake effects such as struts. According to Peake [5], the rotor wake is composed mainly by three elements:

- an azimuthally uniform mean swirling component: Not noisy by itself, but exerts a high influence on noise propagation downstream and is a key factor in understanding the noise generation and propagation in the interstage region, which is the region between the rotor and the stator. The understanding of this swirl is objective of this work,
- the mean component of the blade wakes: wakes from each blade that are steady and identical in the rotating frame of reference and lead in the stationary frame to a rotating field with azimuthal orders that are multiples of B,
- unsteady components corresponding to the fluctuating parts of the turbulent blade wakes: The fan wakes interact with the outlet guide vanes (OGVs) downstream, and noise is produced principally by the effect of the unsteady wake momentum being blocked by the rigid OGVs. This is tonal noise, again at multiples of the BPF, but now at a very wide range of azimuthal orders corresponding to the interference between the rotating-wake harmonics and the OGVs. These are the Tyler & Sofrin [14] mode orders, $m = nB \pm kV$.

One way to study the complicated behavior of the tonal component of the rotor-stator interaction is to decompose this complex pressure field into simpler rotating pressure patterns called spinning modes, which represent the simplest ways in which the pressure can be distributed.

Steady Flow Distortion

It happens when the incoming flow is nonuniform and the nonuniformity is stationary in the fixed frame of reference. One example of is the flow distortion produced by a temperature sensor installed in the inlet of turbofan engines. Another example is the droop-fan interaction [5]. Sometimes the engine is not exactly aligned with the fan axis to avoid downward deflection of the oncoming flow by the wing or the engine cross section is not perfectly circular to meet ground clearance requirements. This leads to a nonuniform flow that hits the fan and generate tones.

1.2.2 Broadband Noise Sources

Broadband noise is a consequence of pressure fluctuations associated with turbulent flow interacting with the blade surfaces and the resulting pressure fluctuations.

Important sources of turbulence in the turbofan are:

- Rotor Self-Noise: The rotor itself produces noise. Turbulence in the rotor blades boundary layer scattering from the trailing edge is a source of broadband noise [5].

- Rotor-Stator interaction: Turbulence in wakes shed by rotor-blades generate noise when they hit the stator vanes
- Rotor blade-tips interact with the turbulent eddies in boundary layer at the casing wall
- Ingested turbulence in the mean flow interacts with the fan. This is particularly important in static rig engine tests where a turbulent control screen is used to reduce this effect.

The rotor is in a nonuniform flow and the nonuniformity is unsteady: The forces on each blade still change during the rotation of the rotor, but broadband noise is generated in addition. This is the case of the interaction of the turbulent boundary layer on the outer wall of the flow duct with the rotor. This case will be discussed in section 1.2.2

1.3 Noise Reduction Technology: Interstage Liners

The interstage region, which is the region between the rotor and the stator is of high significance when it comes to turbomachinery noise since much of the aircraft noise is generated in this region. The current trends for next generation turbofan engines are towards even higher bypass ratio engines, with shorter nacelles and increased distances between the fan and the outlet guide vanes. In high-bypass ratio turbofans, the swirl generated by the stator in the interstage region is very relevant and should be considered when designing the new engines.

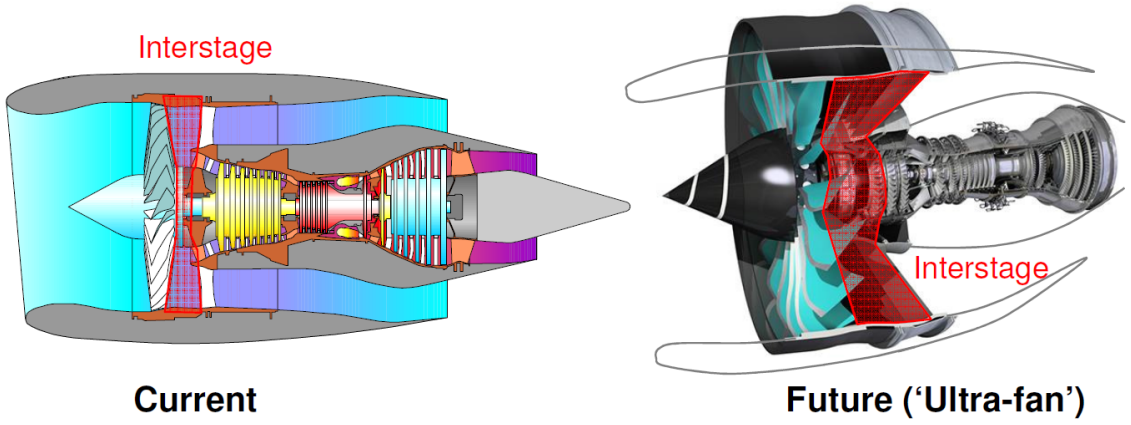

Fig. 1.5 – New engines will have shorter nacelles and less lined area in intake and bypass, increasing the importance of interstage liners. [15] [16]

Meanwhile, acoustic liners in the intake and bypass ducts have proven to be effective in reducing turbofan sound emission. Liners are mainly single or double layer honeycomb structures covered by a perforate or mesh facing sheet. Commonly, the liner depth varies from 10 to 50 millimiters and the open area in the facing sheet from 1 to 10 percent. This technology is durable, self-draining and relatively easy to manufacture. Liners are able to reduce both tonal and broadband noise. In practice, a liner is able to reduce broadband noise by up to 10 to 20 dB at certain frequencies.

When designing liners, one should consider two main important constraints: weight and cell depth. They should also be thin to fit in the space available. In addition, as the aircraft weight limits

are strict and this parameter is closely related to fuel consumption, liner design and optimization is an important issue [17]. Single and double layered liners are shown in Figure 1.6, as well as the positions in an engine where they are commonly placed. For more information about liners design see Motsinger and Kraft [17].

New noise reduction concepts must be developed to meet current noise targets for aircraft. Acoustic liners are widely used in current turbofans. However, so far most of the effort has been directed at liners for intakes and bypass ducts (in the physical insight, prediction methods and experimental data). Until the present moment, little has been done about liners placed in the interstage region. Making effective use of any potential to reduce noise by lining the interstage region will become more important as the lineable area decreases in new ultra-high bypass ratio engines . As previously explained, the interstage liners differ from the liners placed in the intake and bypass, in the sense that they are subject to a mean flow with a strong swirl component. The work reported in this thesis will contribute to the understanding and prediction of the effect of the swirl on liner attenuation.

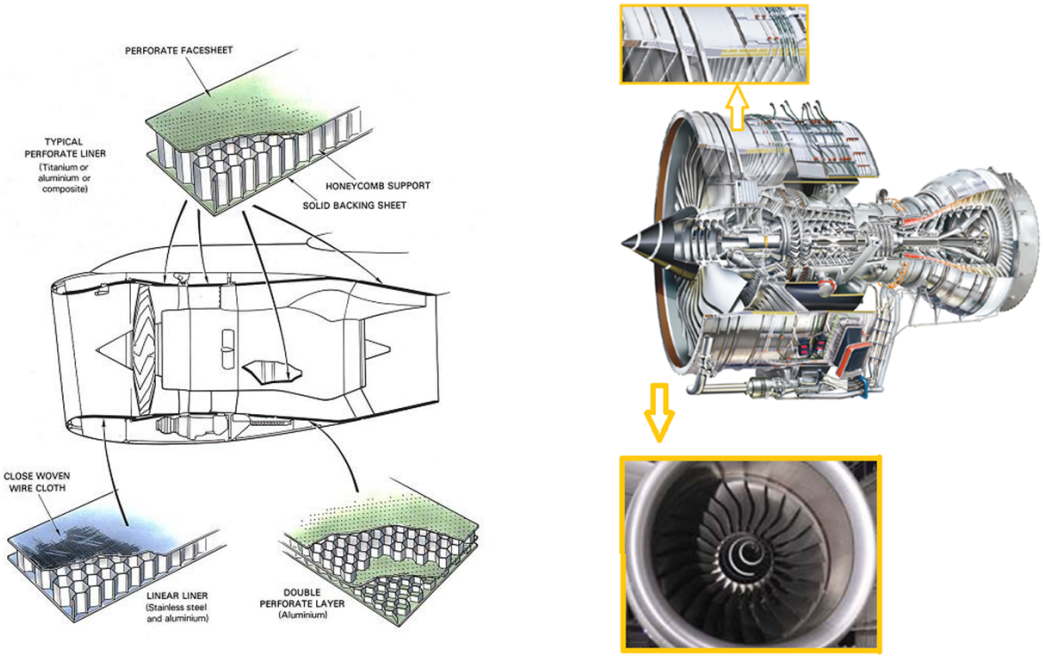

Fig. 1.6 – Turbofan Liner. [16] (a) Typical Liners (b) Inlet and interstage liners positions. Adapted from [15]

The interstage region, which is the region between the rotor and the stator, is of high significance when it comes to turbomachinery noise. New concepts must be developed to suppress the noise generated in this region enable to design quieter engines and meet the noise regulations requirements.

1.4 Research Objectives and Original Contributions

The purpose of this study is to asses the acoustic effect on noise propagation of interstage liners in turbofan engines. The objectives of this project were :

- Analytical Modeling: To model the effect on noise propagation of the swirl behind the rotor and in front of the stator in the presence of acoustic liners.
- Engineering models: To develop a tool to predict noise attenuation that is able to deal with mean axial flow and mean swirling flow and liners.
- Parametric Study: To undertake a parametric study to understand the effect of swirling flows on broadband noise propagation at the interstage region in the presence of liners

The prediction of sound propagation in the interstage in the presence of acoustic liner is challenging mainly because of the complexity of modelling the sound propagation in mean swirling flow a lined duct. The challenge is to create a trustable engineering tool, to validate this tool against numerical results and to apply it to the prediction of the noise propagation for realistic parameters. The key achievements and original contributions of this thesis are:

- Development of an engineering model that is able to deal with the effect of the swirl behind the rotor and in front of the stator and that considers the effect of liners on the inner and outer walls. In the current study the duct is considered approximately uniform. The tool is based on an axisymetric Finite Difference formulation for modes in swirling flow and is implemented in Matlab.
- A validation of the engineering model is presented against predictions from different methodologies including the shooting method methodology, an alternative modal model from Poisson & Peake [2] and results from a Rolls-Royce in-house code.
- Comparison with real data from the Advanced Noise Control Fan at NASA Glenn Research Center. It was possible to take part in all stages of this comparison. From the tests design to, through the data acquisition and finally in the comparison between measurements and predictions
- Parametric Study: A parametric study has been carried out with the objective of understanding the effect of swirling flows on broadband noise propagation in the interstage region in the presence of liners.

1.5 Scope

The outline of this report is as follows. In chapter 2, the bibliographic review is presented for the non-uniform propagation in axisymmetric parallel sheared flows and for swirling flows.

In chapter 3 the theoretical models for sound propagation are presented. This chapted is divided in two subsections: the first one describes the model for sound propagation in ducts without swirl and the second one presents the model for sound propagation in ducts when the swirl is considered. Modal solutions are formulated for the propagation in ducts without swirl and the eigenvalue problem is obtained in the matrix form for the case where swirl is included.

In the chapter 4, the numerical formulation to obtain solutions for mode propagation is presented. The first section shows the numerical formulation for mode propagation in parallel sheared flows, while the second section shows the numerical formulation to obtain solutions for mode propagation in swirling flows is presented.

The results are presented in chapters 5, 6 and 7. In chapter 5 the validation of the Pridmore-Brown code and of the swirling flow code are presented. In chapter 6 results from the current swirling flow code are compared with experimental data from the Advanced Noise Control Fan from Nasa Glenn Research Center . In chapter 7 a parametric analysis with the purpose of understanding the effect of swirling flows in liners is presented.

In the last chapter the conclusions are highlighted.

Chapter 2

Bibliographic Review

In the interstage region of turbofan engines, the flow is characterized by a non-uniform compressible sheared flow and a strong swirl. In Section 2.1 previous work on acoustic propagation in non-uniform compressible sheared flow is reviewed and in section 2.2 previous work on acoustic propagation in which the swirling effect is included is reviewed.

2.1 Propagation in Axisymmetric Parallel Sheared Flows

As a first step towards understanding ducted swirling flows, the propagation of modes in a axisymmetric parallel sheared flow is considered. The fluid properties in such a flow are constant in the stream-wise direction but change in the transverse direction with distance from the duct axis. This problem is governed by the Pridmore-Brown Equation [18], a third-order scalar equation in pressure that must generally be solved by means of numerical methods.

Pridmore-Brown derived the governing equation for the sound propagation in a mean non-viscous sheared flow for a two dimensional hard-walled rectangular duct, assuming the flow to be isentropic and the density to change only with the transverse coordinate y. Pridmore-Brown used the method of separation of variables and studied two particular velocity profiles [18], a linear profile and a turbulent $1/7^{th}$ profile, and obtained solutions for the lowest modes. In a first stage, the hard-wall boundary condition was applied and asymptotically approximate solutions valid for large frequencies were obtained. In a second stage, a very small absorption of acoustic energy at the walls is considered to observe the impact of sheared flows in sound absorption at the walls. Pridmore-Brown demonstrated that the refractive effects of the mean velocity gradients were large and that this effect has even more significance at higher frequencies. The author was criticized because his solution breaks down near the wall (where $M = 0$) for the turbulent $1/7^{th}$ profile, as reported by Savkar [19]. It happens because this profile has a singularity in the velocity gradient at the wall that leads to infinite shear , which is unrealistic. It should be noted, however, that the problem lies in the profile which was chosen and not in the method of analysis. In terms of numerical methods, one possible way to obtain solutions is to remove the singularity by using a linear sublayer at the wall.

After Pridmore-Brown, several authors investigated the modal propagation in non-uniform parallel sheared flow. Most of the work of sound propagation in parallel sheared flows took place

between the 1950s and 1980s and a good review up to 1975 is the paper published by Nayfeh, Kaiser and Telionis [20].

Tack and Lambert [21] addressed the problem proposed by Pridmore-Brown for low frequencies for the same power-law profile. However, Tack and Lambert used a power series expansion valid for a limited interval in which the Mach number is the independent variable. Although the solution failed to properly account for refraction effects observed experimentally by the same authors, specially regarding the upstream propagation, this is the first study using a power-law profile and impedance boundary condition. Some authors such as Mungur and Gladwell [22], Mungur and Plumbee [23] and Eversman [24] used a boundary layer profile generated by linear segments or portions of a sine wave. The representation of Power law boundary layers is studied by Eversman [25].

In early stages, authors were concerned to: (1) understand the physical phenomena (2) choose a convenient mathematical tool to model the problem (3) model the conditions at the boundary and (4) obtain solutions for the problem.

Two approaches have been used to find solutions for the Pridmore-Brown equation together with the impedance boundary condition: Initial value analysis based on Fourier and Laplace transforms and normal mode analysis. For uniform flow and no-flow analysis, green's functions were also used. The initial value analysis based on Fourier and Laplace transforms was applied by Shankar [26] and Mohring [27]. Sound propagation in uniform mean flow and in the absence of flow using Green's functions was studied by Tester [28] [29] .The most common method is the normal mode analysis approach used by Pridmore-Brown [18], Kaiser, Nayfeh and Telionis [30], and most of the recent papers. At that time it was not clear whether the normal mode analysis should be used since theorems of completeness and orthogonality were not proven.

Uniform flow studies had always provided a good insight about sound propagation in lined ducts and the effect of sheared flow was evaluated by comparing sheared flow results with results for uniform flow. Ko [31] carried out a theoretical study for lined rectangular ducts with uniform flow and the comparison with experimental results fails to predict upstream propagation, although proves to be in good agreement for downstream propagation. Previous studies show that the shear causes the sound attenuation to be higher in the exhaust and lower in the inlet (see references [18], [21], [22], [23], [32], [26], [33], [24], [34]). Ko published another study [35] in the following year in which he tries to develop a theoretical method to predict the sound attenuation in an acoustically lined circular duct with flow. Ko concludes that the understanding of modal distribution in a real duct is necessary to make more realistic comparisons between theoretical and numerical results and points out that a shear model should be used for inlet conditions in order to obtain a good noise prediction. Savkar [19] also demonstrated that the classical calculations using uniform profile are not sufficient at the high frequencies and high Mach numbers encountered in practice. He proposes a method in which the eigenfunctions appear in an explicit functional form which is easier to manipulate than the one proposed by Mungur and Plumbee [23]. In this thesis the nonuniform effect of the flow will be included and the uniform solution will be used as a first stage to validate the results obtained. In uniform flows, acoustics and hydrodynamic modes can be studied separately,

providing a very helpful theoretical insight.

In 1969, Mungur and Gladwell [22] investigated the same eigenvalue problem of Pridmore-Brown. The authors carry out their study in two stages: (1) The first stage consists of an analytical study. Contrary to Pridmore Brown and Tack and Lambert [21], the flow is considered viscous. The two-dimensional linear wave equation with a sheared viscous mean flow is derived. (2) The second stage consists of a numerical simulation based on a fourth-order Runge Kutta algorithm. The inviscid case (which is the Pridmore-Brown Equation) is analysed from a numerical point of view to validate the code. The computational results obtained are in good agreement with the analytical theory for the constant gradient shear flow case, and do not fail at the wall in the turbulent flow profile case as in Pridmore-Brown studies [18]. Only the lowest even modes are considered. Mungur and Plumbee [23] extended the study of Mungur and Gladwell [22] for the case of a lined annular duct. Higher order modes are considered. The calculated eigenfunctions are available in tabular or graphical form. The studies of Mungur and Gladwell [22] and Mungur and Plumbee [23] were very significant, as they are the first ones in which numerical methods were used to find the solution for this problem.

Dokumaci [36] presented a simplified (quasi 1D) plane wave formulation for steady sheared flow. The governing equations are derived in more generally for non-uniform ducts, non-isentropic compressible non-uniform flows with an arbitrary profile. For uniform ducts with incompressible flow, an analytic solution is presented in which the wave field is said to be the superposition of forward and backward acoustic waves and a hydrodynamic wave.

The issue of how to impose the liner boundary condition at the wall was solved by Tester [29]. This author looked for solutions within the boundary layer region using an expansion of the acoustic pressure in an asymptotic series for small values of boundary layer thickness and observed that when the boundary layer thickness tends to zero, the continuity of particle displacement at the wall is verified. He concluded that the derivation of a correct boundary condition should be based on the confirmed of particle displacement instead of in the continuity of particle velocity. This formulation will be used in this thesis.

As mentioned previously, another issue in the last decades was whether a normal mode analysis could be used to study the sound propagation of sheared flows. Shankar published two studies in which he analyses this problem [37] [26]. In reference [37] Shankar formulated an initial-value problem and obtained a solution for the pressure field using a perturbation technique based on weak shear. In this way Shankar could find solutions for the pressure field without assuming the form of the solution a priori, since at the time theorems of completeness and orthogonality were not proven. Shankar concluded that the pressure solution is indeed separable but was still not sure if the Pridmore-Brown eigenfunctions form an orthogonal and complete set. Shankar studies were based on the weak shear assumption and were not valid when refractive effects became large. Also, because of the linear dependence of Mach number and quadratic dependence on frequency, his calculations were limited to low Mach numbers and frequency.

In 1972, Shankar [26] published a paper studying the sound propagation in a hard-wall cylindrical duct with shear layers to try to overcome the difficulties of the previous study in which concerns the weak shear limitation. Although this study was carried out for the hard-wall case, the author points out that that it could also be applied to the soft wall case. Based on results from the previous paper Shankar concluded that Pridmore-Brown was right to consider that the methods of separation of variables should be applied to find the eigenvalue solution. He states that although the resulting eigenfunctions cannot be proven to be complete or orthogonal, they can be combined by a least total squared method to give a good representation of the initial pressure profile. Unlike Pridmore-Brown and Mungur and Gladwell [22], Shankar considered all the modes and not only the lowest ones. In this PhD thesis, the method of separation of variables was used to obtain the modal pressure solutions, as will be presented in the following chapter.

Having defined the mathematical model, the next step is the discretization phase. Along the years, mathematical models have been discretized in different ways. To obtain solutions with a certain generality, it is vital to use numerical methods. To the author's knowledge, the most common methods are the shooting method, the method of weighted residuals in the form of a Galerkin Method, finite element and the finite difference method, to be briefly described in the following paragraphs.

The numerical integration of governing equation, which is also addressed as shooting method or mode tracking technique was used by Mungur and Gladwell [22] for the 2D case using a forward numerical integration, by Eversman [24] which used a Runge Kutta numerical integration for circular ducts and by Mungur & Plumbee which studied the annular duct case. Recently, this method was applied by Vileski and Rienstra [38] and by McAlpine [39].

In this method, a transfer matrix relates the values of the pressure and the pressure gradient in the inner wall with the values of the pressure and the pressure gradient in the outer wall. The pressure gradients in each wall is proportional to the pressure value in the same wall. The coefficients from the transfer function are obtained by integrating the Pridmore-Brown equation using a numerical scheme and are dependant of the axial wavenumber. McAlpine et al [39], for example, used a fourth-order Runge-Kutta numerical scheme. The author used a variable step size to account for the boundary layer. The boundary conditions are of the form:

$$\begin{aligned} (dP/dr)_{in} &= \varepsilon_1 P_{in} \\ (dP/dr)_{out} &= \varepsilon_2 P_{out} \end{aligned} \tag{2.1}$$

where P_{in} and P_{out} are the pressure values at the inner and outer wall respectively and where $(dP/dr)_{in}$ and $(dP/dr)_{out}$ are the pressure derivative values at the inner and outer wall. The constants ε_1 and ε_2 relate the pressure and the pressure derivative values in each of the boundaries. Then, a transfer matrix is calculated, which relates pressure and pressure gradient at the inner wall

the with pressure and pressure gradient at the outer wall as

$$\left| \begin{array}{c} P \\ dP/dr \end{array} \right|_{in} = \left| \begin{array}{cc} T_{11} & T_{12} \\ T_{21} & T_{22} \end{array} \right| \left| \begin{array}{c} P \\ dP/dr \end{array} \right|_{out}. \tag{2.2}$$

The coefficients T_{ij} from the transfer function are obtained by integrating the Pridmore-Brown equation using a numerical scheme and are dependant of the axial wavenumber. McAlpine et al [39], for example, used a fourth-order Runge-Kutta numerical scheme.

By substituting the boundary conditions given by equation 2.1, a non-trivial solution of equation 2.2 will be

$$F(k_x/\eta) = 0 \tag{2.3}$$

Leading to an an equation of the form:

$$F(k_x/\eta) = T_{21} + \varepsilon_1 T_{22} - \varepsilon_2 T_{11} + \varepsilon_1 T_{12} = 0 \tag{2.4}$$

The problem consists on finding values of k_x/η which satisfy equation 2.4. The most common solution is to obtain those values using a Newton-Raphson scheme. Mariano [34] formulates his shooting method in a slightly different way. The author considers two regions: the central region with uniform flow and the boundary layer region with sheared flow and a certain thickness.The uniform region is solved analytically and the boundary layer region in solved with a central finite difference method. Two additional finite difference equations are used to match the interface. McAlpine et al [39] does it in a similar way. Having the analytical uniform solution as a starting point, the author slowly decreases the slip at the wall and the change in the axial wavenumber is tracked at the wall. The downside of the shooting method is that one mode is calculated at a time.

The Method of weighted residuals in the form of a Galerkin Method, which is another way to discretize the governing equations and boundary conditions. This method was used by Hersh & Catton [33], Savkar [19], J. Unruh & W. Eversman [40]. In this method the solution is approximated by a solution of the form:

$$p(y)_{approx} = \sum_{i=1}^{N} q_i \phi_i(y), \tag{2.5}$$

where N is the number of basis functions ϕ_i necessary to obtain convergence,q_i are unknown coefficients that minimize the residual error R. The residual is forced to be orthogonal to the set of functions $\phi_i(y)$. As a consequence, the expression

$$\int_0^1 \phi_i(y) R dy = 0, j = 1...N \tag{2.6}$$

leads to N homogeneous equations and the eigenvalue problem can be written as:

$$Aq = \lambda q, \tag{2.7}$$

where A is a matrix of coefficients, q is the vector containing the variables and λ is the eigenvalue related to k_x/η.

The Finite Difference Method (FDM), one of the most well-stablished methods of discretization based on the properties of Taylor expansions. The application of FDM to solve the sound propagation in mean sheared flows was first proposed by G. A. Wynne and H. E. Plumbee [41] and applied by Kousen [42]. It is only applied to structured grids. This method solves the problem for all the modes with one single calculation.

Firstly used for structural mechanics, the Finite Element Method has also been used for CAA applications. In this method, the space domain is discretized in a set of cells with arbitrary shapes called elements which makes it very convenient for non-structured grids. After that, parametric representation of the unknown variables based on shape functions is associated to each element. Finally, an integral formulation of the equations is defined and solved in each element [43]. This method was applied by R. Astley & W. Eversman [44] [45] and G. Gabard & R.J. Astley [46].

Recent studies focus on solving the Pridmore-Brown equation by means of numerical methods. Some important studies are the ones of Vilenski and Rienstra (2005 and 2007), Brooks & McAlpine (2007), Guan and Wang (2007 and 2008) and Oppeneer (2013)

Vilenski and Rienstra [38] [47] publish two studies in which they studied the eigenvalue problem proposed by Pridmore-Brown with Myer's locally reacting impedance boundary condition [75]. The mean flow density is considered constant and the flow isentropic.

In the first study Vilenski and Rienstra [38] studied the induct propagation of small amplitude modes in an inviscid sheared flow. They propose a numerical method similar to Tam & Ariault [48] to solve the modal equation. Their interested lies in solving this problem for high helmholtz and wavenumbers, which are of great interest for applications. Their solution is checked against uniform flow results and their method is validated for helmholtz numbers up to 100, circunferential wavenumber as high as 50 and Mach numbers up to 0.65. The authors show that for sheared flow with non-zero wall velocity and in the absence of lining the number of hydrodynamic modes is finite and they are localized near the duct walls.

In the other study [47], their intent is to have some insight about the effects of shear and wall lining in the spectrum of the Pridmore-Brown equation by comparing the results a previous study in which the flow is considered uniform [49]. He derives a high-frequency, short-wavelength asymptotic solution for the acoustic part of the problem based on the WKB method. The authors also search for some insight about the hydrodynamic part of the spectrum for both the short-wavelength limit and the case of the narrow duct. To reach this, only the hard-wall case is considered. The governing equations are derived for cases: In the first case, both swirl and shear are considered and in the second case only the shear is taken into account. After that, this paper goes deeper in the sheared-only flow. In which concerns the acoustic part of the spectrum, although qualitative

differences in the modal wavenumbers are found, the effect of the shear in this part of the spectrum is not significative. This result is in agreement with Vilenski and Rienstra [50]. The lining has a strong impact on the acoustic spectrum. The hydrodynamic part of the spectrum is caused by the mean flow nonuniformity.

Guan and Wang [51] [52] use spectral colocation technique based on chebyshev gauss lobato points to find the axial wavenumbers and mode shape functions and present results for axial and swirling flows and For the case of axial uniform mean flow, they show the axial wavenumber spectrum and compare their results with McAlpine et al. for hard-walls, inner wall lined only, outer wall lined only and both walls lined. They perform a normal-mode analysis to obtain the eigenvalues and a collocation technique to discretize the equations. In this PhD thesis, the uniform and sheared flow results will be validated against results provided from Dr. McAlpine, whose code is a shooting method code described in [53]

The work of Brooks & McAlpine [53] has two main objectives: First, to calculate the acoustic modes in a lined annular duct with mean sheared flow. Secondly, to use a mode-matching method to calculate sound transmission in a lined annular duct with sheared mean flow to deal with impedance discontinuities. Their study uses realistic values for duct dimensions, mass flow rate, sound frequency and acoustic liner impedance. Mode $m = 0$ is analysed, as higher azimuthal orders are better absorbed by acoustic lining and several velocity profiles with and without boundary layers are studied. The authors wanted to understand how different mean flow profiles affect the eigenmode spectrum. First, the uniform flow solution is obtained using a shooting method, slowly varying the admittance. For an annular duct, this procedure is repeated twice as the admittance of one wall remains constant while the admittance of the other wall changes slowly. Secondly, for the sheared flow case, two options are available to track the modes using the shooting method proposed by the authors: (1) Given a flow profile, vary the wall admittance from zero to the desired value and then, keeping the admittance fixed, slowly change the flow profile from uniform to sheared flow profile as the axial wavenumber is tracked. (2) Assume a hard-wall duct and vary the flow profile and after that, keeping the flow profile fixed, change the impedance at the wall. In which concerns the mode-matching method, they implement the mode-matching method proposed by Astley et al in which the weighted residuals of continuity and momentum equations are used to match the modes on the interface instead of using continuity of pressure or velocity. For validation purposes, the shear flow solver based on a shooting method is compared to the results of a Galerkin method of weighted residuals code and the shear-flow mode-matching technique is compared to the ACTRAN finite element code for the uniform case only. The first ten propagating modes are plotted for the uniform case for both the shooting method and the method of weighted residuals for different impedances at the wall and it is observed that the two sets of axial wavenumbers agree very well for the hard-wall case and for the case in which only the outer wall is lined. Although the results are still good for the case in which the inner wall is lined, it was found out by the authors that the method of weighted residuals is less accurate. They think this is due to the fact that the basis functions used in this study do not suit well the case in which the inner wall is lined. This same trend repeats for different flow profiles.

Oppeneer et al [54] study the sound propagation through the APU exhaust duct, which carries a non uniform flow with strong temperature gradients. They develop a mode-matching method in their study. In mode-matching methods, the acoustic field is expressed in each segment as a series of modes. The properties are assumed to be constant in each segment and then the modal amplitudes are obtained by matching certain continuity conditions at the interface. Those continuity conditions might be pressure or velocity functions in the case of uniform flows or pressure and temperature in the non-uniform case for example. The modal shape functions are more complicated and the increasingly oscillatory behavior of higher order modes leads to numerical errors in higher order integrals used in the mode-matching method. The authors develop a different mode-matching method to avoid this. The method is verified against uniform flow analytical solution.

In this thesis the normal modal analysis will be applied to study sound propagation in a lined annular duct with non-uniform flow. The equations will be discretized using a finite difference approach. For uniform flows, all modes obtained by solving the wave equation are acoustic. When shear is included in the equation, there are two possible solutions: Acoustic and hydrodynamic. Acoustic modes propagate with the phase speed of the mode, while hydrodynamic modes remain stationary with respect to the fluid and are convected with the mean flow. The code will be validated for the uniform flow case by comparing the results obtained with the analytical solution. For the sheared flow case, the results will be validated against a shooting method proposed by Dr. McAlpine [53] [39] and a Finite difference code proposed by Gabard [55].

2.2 Swirling Flows

The swirling mean flow between the rotor and the stator is a key aspect when modelling turbomachinery noise in the interstage region where the swirl is of the order of 15 to 45 percent of the mean axial velocity [56], [51]. Swirl can prevent unsteady disturbances from reaching the walls and make expensive wall treatments ineffective [5]. The swirl changes the phase speed relative to the mean flow [5]. If on the one hand the relative phase speed decreases in modes that rotate in the same direction as the swirl and those modes become more cut-off, on the other hand,the relative phase speed increases in modes that rotate in the opposite direction as the swirl and they become more cut-on as the swirl increases [57],[58]. The downside is that modelling of ducted swirling flows is more challenging than parallel flows, since compressible and rotational phenomena are coupled [58]. Instead of using a single second order equations, one has to solve the 3D linearized Euler equations [51] or a sophisticated single sixth order operator equation in pressure [5],[59] .

In the last 30 years, several researchers have studied the behaviour of swirling flows with different properties and classified the modes into families with similar characteristics. [57],[60],[5],[59] For uniform flows, unsteady disturbances are classified as vortical and entropical waves, that are purely convected by the flow, and acoustic waves. In hard-walled ducts, acoustic waves propagate unattenuated or decay exponentially [42]. Modes propagating in swirling flows are classified into acoustic modes, nearly convected modes and continuous spectrum. The location of the axial wavenumbers of the acoustic modes, hydrodynamic modes and a continuum of modes are ilustrated in the complex plane in figure 2.1 [5].

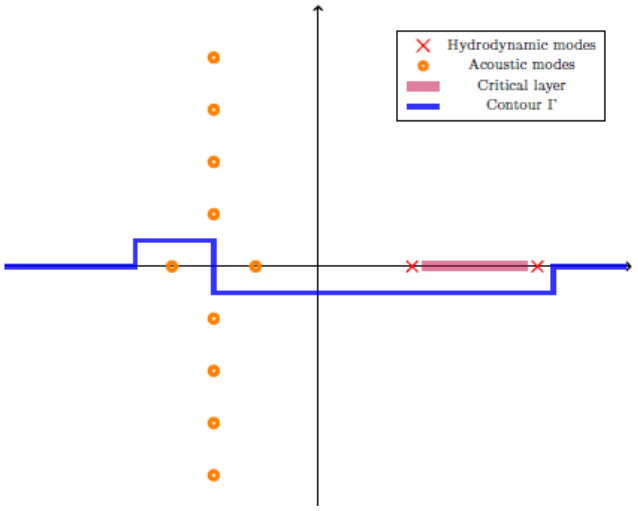

Fig. 2.1 – Axial wavenumbers of the hydrodynamic modes , acoustic modes and a continuum of modes plotted in the complex plane in a hard-walled duct [61]

The well-known acoustic modes are directly related to the compressibility of the fluid. Pressure-dominated, they carry most of the usteady pressure of the flow and are composed of propagating (or cut-on) modes and modes that are attenuated along the duct (or cut-off modes) [14]. The nearly convected modes[62], are related to the swirl of the mean flow. They are discrete hydrodynamic modes that carry a small pressure component and convect at a speed similar although not exactly

the same as the mean flow speed. The continuous spectrum is a set of the purely convected modes whose existence was reported by Kerrebrock [62], [63] . The derivative of these modes is such that the convective derivative D/Dt is zero.

Studies of the propagation of small disturbances in a duct with mean swirling flow dates back to 1977. By using normal mode analysis, Kerrebrock [62] showed that vorticity, entropy and pressure modes were coupled in the presence of swirl. He pointed out that the shear disturbances are not purely convected by the mean flow, but rather they also carry a slight pressure component with them and are termed nearly-convected modes. In this study the flow was considered isentropic and the mean flow was a superposition of a solid body and a free vortex swirl of small amplitude

Golubev & Atassi [56],[64] seek clarification of the nearly-convected modes and the continuous spectrum. By using Goldstein's decomposition of the perturbation velocity field into potential and vortical components, the authors show that vortical disturbances are independent of the acoustic field, while acoustic disturbances are generated by vortical ones. The potential mean flow is a combination of vortex swirl and rigid body rotation. Applying those simplifications in the Linearized Euler Equations, a system of two equations is obtained. One of them shows that vortical disturbances create an unsteady pressure field. The other equation shows that if the mean flow is irrotational, an incident acoustic field will not create vorticity.

Mean swirling flows such as solid body rotation, free vortex swirl, constant swirl profiles or a superposition of them have been analysed over the years. Important work in the field was performed by Kerrebrock [63], [62], Kousen [60],[65],[42], Golubev & Atassi [56],[64] ,Tam & Ariault[48] ,Nijboer[1] ,Guan et al[51],[52] ,Cooper & Peake[58],[57] ,Cooper[66], Posson & Peake[59] and Heaton & Peake[67]

The most common methods used to obtain solutions for the Linearized Euler Equations are initial value analysis and normal mode analysis. Since in swirling compressible ducted flows the question of completeness cannot be easily ascertained, Tam & Ariault [48] proposed an initial value analysis to make the complete rigorous analysis of the wave modes and seek clarification to the families of modes generated by hard-wall inviscid swirling compressible ducted flows. Kousen [60],[65],[42] ,Golubev & Atassi[56], [64] Guan et al[51],[52] performed a normal mode analysis instead. Based on the method of separation of variables, the normal mode analysis is the method used in this paper. The only difference is that Golubev & Atassi decomposed the disturbance velocity into a vortical and a potential part.

Isentropic mean flow was investigated by Kousen [60],[65],[42] Guan & Wang[52] and Golubev & Atassi [68], [56], [64], while non-isentropic mean flow with constant mean density was analysed by Tam & Ariault [48] and Guan & Wang[51]. Tam & Ariault [48] consider constant density mean flow, while this assumption is not made by Guan & Wang[51].Nijboer [1] analysed the testcases proposed by Tam & Ariault [48] and Kousen [65] pointing out that the authors are comparing slightly different mean flows and that this leads to different results in some cases. Differences between results from those cases are negligible if the mean swirl Mach number is small ($M_{\phi_0} \sim 0.1$). By comparing results for isentropic flow and results for constant density flow the author concludes that although the eigenvalues show the same patterns, the mean density variation affects the stability

of the modes of the swirling flow. Heaton & Peake [67], highlighted that the uniform density causes the appearance of an unstable mode found by Tam & Ariault [48] and that in reality it is expected that the density increases with radius in a compressible swirling flow because of increase in pressure to balance the centrifugal forces.

The effect of non-uniform mean entropy on eigenmodes was analysed by Guan & Wang [52] for a hard-walled straight annular duct with swirling flow and by Cooper [66] for a slowly varying duct with mean swirling flow. It is shown that modes become more cut-on in the presence of positive entropy gradients and less propagating in the presence of negative entropy gradients when compared to uniform entropy regimes. The higher the swirl, the higher the entropy is.

Published results for sound propagation in lined swirling flows are limited. Guan et al [52] used a Chebyshev polynomial spectral method to to calculate the eigenvalues of the three-dimensional Linearized Euler Equations and used two different mode-matching schemes to calculate the sound transmission in ducts. They compared the two mode-matching methods between themselves and with a finite element method and compared the results between themselves. A spectral collocation technique was used in which the solution is assumed to be composed of a linear combination of basic functions. The function is discretized in the physical space at some chosen points, called collocation points and the solution is forced to satisfy the partial differential equations only at the collocation points. A normal mode analysis is performed and the modified mode matching scheme proposed by the authors is used to evaluate the effect of the swirling flow on the sound power transmission loss and to conduct liner optimization in the impedance plane.

A different methodology to analyse the sound propagation in ducts with mean swirling flows was recently developed by Posson & Peake [59].The authors develop a acoustic analogy to account for sound generation in a swirling sheared mean flow in an annular duct, including the presence of moving solid surfaces by rearranging the Navier-Stokes equation in the form of a sixth-order differential operator equation.

Posson & Peake [2] develop a semi-analytical approach that is an extension of previous studies and combines the Ffowcs-Williams & Hawkings acoustic analogy in a medium at rest with moving surfaces, the Goldstein acoustic analogy in a Hard-Walled duct with uniform mean flow and the Rienstra and Tester's green's function in an annular lined duct with uniform mean flow to expand it to the case of a swirling mean flow in an lined annular duct. They perform an extensive and most valuable parametric study to evaluate the effect of swirling flows and liners on the axial wavenumber and on a Green's function in an annular duct. The study includes different combinations of mean flows including uniform and sheared axial flows and swirling flows that are a combination of rigid body and vortex swirl and six values of impedances. When acoustic absorption is considered, the duct is lined on both walls. The magnitude of the rigid body swirling flow profile ranges from 0 to 0.28 and the magnitude of the vortex swirl swirling flow profile ranges from 0 to 0.2. The hub-to-tip is 0.5 and the non-dimensional frequency is 30. Calculations are done for a single mode, $m = 16$. Some of those results will be used to validate the current methodology. Their study shows that co-rotating modes become more cut-off, while contra-rotating modes become more cut-on.

Another question that is addressed in this thesis is how the swirling flow affects the sound

absorption. For isentropic irrotational flow the acoustic energy is conserved and an energy conservation equation can be derived from the Euler equations. However, mean flow non-uniformity modifies the expression for sound power calculation. The acoustic intensity expression was derived by Myers [69], [70], who showed that the time-averaged intensity flux in a non-uniform mean flow is not conserved. Since in this case modes are not orthogonal any more, interference between radial modes should be accounted for. Atassi [71] derived an expression to calculate the sound power in an annular duct with swirling flow in the high frequency limit using normal mode solutions and showed that since the coupling between vorticity and acoustic waves is weak in the high frequency limit, the acoustic energy can be considered to be conserved in an approximate sense.

In this thesis the effect of swirl on liner attenuation is evaluated. The governing equations are derived for an isentropic swirling mean flow and a homentropic unsteady field. The eigenvalue problem is obtained by applying the normal mode analysis to the linearized Euler Equations together with the Ingard-Myers Boundary Condition [72]. Properties are assumed to vary at most with radius. A fourth order finite difference code is compared to published results of specific flows such as solid body and free vortex swirl. The method is then applied to more realistic interstage flow profiles and liners.

Chapter 3

Duct Mode Propagation Theoretical Models

3.1 Introduction

The fan stage of a turbofan engine can be represented by a simple schematic, as shown in Figure 3.1. This model consists of a rotor, a stator, a nacelle and a hub. Other engine sources such as compressor, turbine and combustor are neglected. The most significant noise sources are the rotor and the stator, as described in chapter 1. Noise propagation occurs inside a duct, that is approximately cylindrical in the inlet and annular in the outlet and in the interstage region, which is the region between the rotor and the stator. The flow is often considered uniform in the inlet, as the boundary layer in this region is negligible. In the bypass duct the swirl is small. In the interstage region, however, the flow is sheared and swirling. In this region, the hydrodynamic, entropic and aeroacoustic fields coexist and can be coupled.

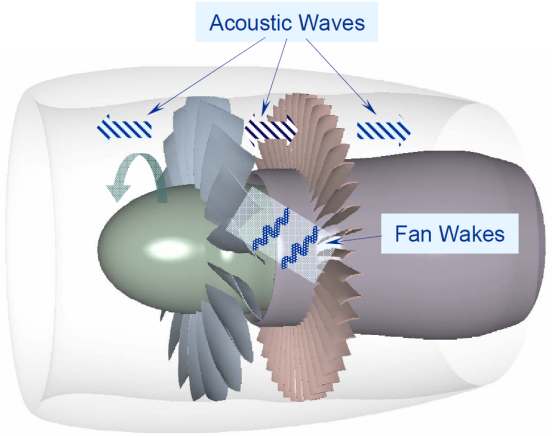

Fig. 3.1 – Simple model of a turbofan, including a rotor, a stator, a nacelle and a hub. Other engine sources such as compressor, turbine and combustor are neglected. [73]

Many models have been used to understand noise propagation in a turbofan engine duct. Ducts with different cross sections shapes (rectangular, cylindrical, annular and variable shape) and under different flow conditions (zero flow, uniform mean flow or plug flow, sheared flow and swirling flow) have been investigated, as reviewed in the previous chapters. Neglecting the mean flow is appropriate at very low Mach numbers, and a uniform axial mean flow is often assumed for higher

subsonic Mach numbers. The duct walls are generally modeled as being rigid and impervious or lined with a prescribed impedance. Although there are many ways to model the impedance condition [74], in all that follows the impedance is regarded as locally reacting. This is generally a reasonable assumption for liners formed by cell close dimensions are small whn compared to the acoustic wavelength

This chapter deals with ways of modelling the propagation of sound in ducts with axial and swirling flows. In the two next sections, the governing equations for inviscid compressible flows are presented in full and in the linearised forms. Section 3.4 introduces the formulation for sound propagation in ducts without swirl by means of the Pridmore-Brown Equation, while section 3.5 presents the formulation for sound propagation in ducts with and without swirl using the Linearized Euler Equations.

3.2 Governing Equations for Inviscid Compressible Flows

The governing equations are now presented. The first equation is the conservation of mass, the inviscid second equation is the conservation of momentum and the third one is the energy equation for an inviscid isentropic perfect gas. These are given by

$$\frac{\partial \rho}{\partial t} + \nabla \cdot (\rho \mathbf{u}) = 0 (Mass) \tag{3.1}$$

$$\rho \frac{D\mathbf{u}}{Dt} + \nabla p = 0 (Momentum) \tag{3.2}$$

$$\frac{Ds}{Dt} = 0 (Energy) \tag{3.3}$$

In these of equations, ρ is the density, $\mathbf{u}$ is the velocity vector, s in the entropy and p is the pressure. D/Dt is the material derivative operator, given by:

$$\frac{D}{Dt} = \frac{\partial}{\partial t} + \mathbf{u} \cdot \nabla. \tag{3.4}$$

There are still more unknowns than equations so far. To close the problem, a constitutive equation such as the equation of state $p = p(\rho, s)$ is needed. This equation is written in the differential form as:

$$\frac{Dp}{Dt} = c_0^2 \frac{D\rho}{Dt} + \left(\frac{\partial p}{\partial s}\right)_\rho \frac{Ds}{Dt}, \tag{3.5}$$

where c_0^2 is the isentropic speed of sound given by

$$c_0^2 = \left(\frac{\partial p}{\partial \rho}\right)_s. \tag{3.6}$$

In the energy equation 3.3 and in the momentum equation 3.2, viscous and heat effects are neglected.

Although Eq. 3.3 is written in terms of entropy, it can also be written in terms of pressure as follows.

Substituting Eq. 3.3 in Eq. 3.5 gives

$$\frac{Dp}{Dt} = c_0^2 \frac{D\rho}{Dt}. \tag{3.7}$$

The continuity equation 3.1 is written in the non-conservative form as

$$\frac{D\rho}{Dt} = -\rho(\nabla \cdot \mathbf{u}). \tag{3.8}$$

Substituting Eq. 3.8 , together with the isentropic relation for a perfect gas $c_0^2 = \gamma p/\rho$ [76] Eq. 3.7 gives

$$\frac{Dp}{Dt} + \gamma p(\nabla \cdot \mathbf{u}) = 0. \tag{3.9}$$

Equation 3.9 is the energy equation for an isentropic gas written in terms of pressure. The energy equation will be used in this form from now on. Equations 3.1, 3.2 and 3.9 now define the full compressible problem.

3.3 Linearization of Governing Equations:

The flow variables p ρ and $\mathbf{u}$ are assumed to consist of a steady mean flow component and a small fluctuation component. They are written in the form:

$$\begin{aligned} \rho &= \rho_0 + \rho', \\ p &= p_0 + p', \\ \mathbf{u} &= \mathbf{u}_0 + \mathbf{u}', \end{aligned} \tag{3.10}$$

where the mean steady value of each variable is represented by the subscript zero and the small unsteady perturbation value is represented by the superscript dash. The perturbation quantities are assumed to be much smaller than those of the mean flow. If the variables in the form given by 3.10 are substituted in equations 3.1, 3.2 and 3.9, those equations can be rewritten as:

$$\frac{\partial \rho_0}{\partial t} + \frac{\partial \rho'}{\partial t} + \nabla \cdot \left(\rho_0 \mathbf{u_0} + \rho_0 \mathbf{u}' + \rho' \mathbf{u_0} + \rho' \mathbf{u}' \right) = 0 \tag{3.11}$$

$$\begin{aligned} \rho_0 \left[\frac{\partial \mathbf{u}_0}{\partial t} + \frac{\partial \mathbf{u}'}{\partial t} + \mathbf{u}_0 \cdot \nabla \mathbf{u}_0 + \mathbf{u}_0 \cdot \nabla \mathbf{u}' + \mathbf{u}' \cdot \nabla \mathbf{u}_0 + \mathbf{u}' \cdot \nabla \mathbf{u}' \right] + \\ + \rho' \left[\frac{\partial \mathbf{u}_0}{\partial t} + \frac{\partial \mathbf{u}'}{\partial t} + \mathbf{u}_0 \cdot \nabla \mathbf{u}_0 + \mathbf{u}_0 \cdot \nabla \mathbf{u}' + \mathbf{u}' \cdot \nabla \mathbf{u}_0 + \mathbf{u}' \cdot \nabla \mathbf{u}' \right] + \\ + \nabla p_0 + \nabla p' = 0 \end{aligned} \tag{3.12}$$

$$\frac{\partial p_0}{\partial t}+\frac{\partial p^{'}}{\partial t}+\mathbf{u}_0\cdot\nabla p_0+\mathbf{u}_0\cdot\nabla p^{'}+\mathbf{u}^{'}\cdot\nabla p_0+\mathbf{u}^{'}\cdot\nabla p^{'}+\gamma p_0\nabla\cdot\mathbf{u}_0+\gamma p_0\nabla\cdot\mathbf{u}^{'}+$$
$$+\gamma p^{'}\nabla\cdot\mathbf{u}_0+\gamma p^{'}\nabla\cdot\mathbf{u}^{'}=0 \quad (3.13)$$

Equations 3.11 to 3.13 are the Linearized Euler Equations for an isentropic flow. When perturbations are neglected, the steady set of equations are given by ([52]):

$$\nabla\cdot(\rho_0\mathbf{u_0})=0 \quad (3.14)$$

$$\rho_0\mathbf{u}_0\cdot\nabla\mathbf{u}_0+\nabla p_0=0 \quad (3.15)$$

$$\mathbf{u}_0\cdot\nabla p_0+\gamma p_0\nabla\cdot\mathbf{u}_0=0 \quad (3.16)$$

If the mean flow equations are satisfied and the product of two fluctuation quantities is neglected because it is small compared to first order terms, the linearized Euler Equations for the perturbation field are given by

$$\frac{\partial\rho^{'}}{\partial t}+\nabla\cdot\left(\rho_0\mathbf{u}^{'}+\rho^{'}\mathbf{u_0}\right)=0 \quad (3.17)$$

$$\rho_0\left[\frac{\partial\mathbf{u}^{'}}{\partial t}+\mathbf{u}_0\cdot\nabla\mathbf{u}^{'}+\mathbf{u}^{'}\cdot\nabla\mathbf{u}_0\right]+\rho^{'}\left[\mathbf{u}_0\cdot\nabla\mathbf{u}_0\right]+\nabla p^{'}=0 \quad (3.18)$$

$$\frac{\partial p^{'}}{\partial t}+\mathbf{u}_0\cdot\nabla p^{'}+\mathbf{u}^{'}\cdot\nabla p_0+\gamma p_0\nabla\cdot\mathbf{u}^{'}+\gamma p^{'}\nabla\cdot\mathbf{u}_0=0 \quad (3.19)$$

3.4 Propagation in ducts without swirl

3.4.1 Parallel sheared Flow

An axial sheared flow is now considered. In this case, the mean velocity components v_0 and w_0 are null and the mean flow velocity is given by $\mathbf{u}_0=(u_0,0,0)$. In addition, the mean velocity is a function of transverse coordinates y and z, that is, $u_0=u_0(y,z)$. Mean flow pressure p_0 and density ρ_0 are constant. Figure 3.2 shows the shear flow in a duct with annular cross-section, indicating the flow direction and the axial axis.

For parallel sheared flow, the mean flow equations 3.14 to 3.16 reduce to:

$$\nabla\cdot(\rho_0\mathbf{u_0})=0 \quad (3.20)$$

$$\nabla p_0=0 \quad (3.21)$$

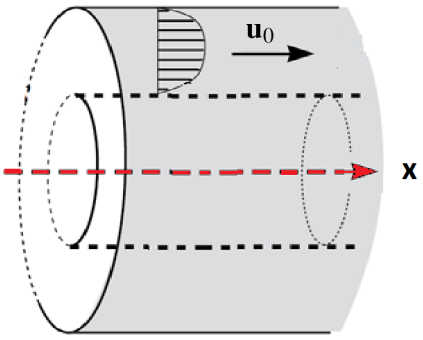

Fig. 3.2 – Shear flow in a duct with annular cross-section, indicating the flow direction and the axial axis.

$$\mathbf{u}_0 \cdot \nabla p_0 + \gamma p_0 \nabla \cdot \mathbf{u}_0 = 0 \tag{3.22}$$

Equation 3.21 shows that p_0 is constant. Substituting this result in equation 3.22, the equations for the mean flow become:

$$\nabla \cdot (\rho_0 \mathbf{u_0}) = 0 \tag{3.23}$$

$$\nabla p_0 = 0 \tag{3.24}$$

$$\nabla \cdot \mathbf{u}_0 = 0 \tag{3.25}$$

Substituting equations 3.24 and 3.25 in the equations for the perturbation field and noting that $\mathbf{u}_0 \cdot \nabla \mathbf{u}_0 = 0$:

$$\frac{\partial \rho^{'}}{\partial t} + \nabla \cdot \left(\rho_0 \mathbf{u}^{'} + \rho^{'} \mathbf{u_0} \right) = 0 \tag{3.26}$$

$$\rho_0 \left[\frac{\partial \mathbf{u}^{'}}{\partial t} + \mathbf{u}_0 \cdot \nabla \mathbf{u}^{'} + \mathbf{u}^{'} \cdot \nabla \mathbf{u}_0 \right] + \nabla p^{'} = 0 \tag{3.27}$$

$$\frac{\partial p^{'}}{\partial t} + \mathbf{u}_0 \cdot \nabla p^{'} + \gamma p_0 \nabla \cdot \mathbf{u}^{'} = 0 \tag{3.28}$$

Defining the operator

$$\frac{D_0}{Dt} = \frac{\partial}{\partial t} + \mathbf{u}_0 \cdot \nabla = \frac{\partial}{\partial t} + u_0 \frac{\partial}{\partial x} \tag{3.29}$$

and using it to rewrite equations 3.26 to 3.28 gives

$$\frac{D_0 \rho^{'}}{Dt} + \nabla \cdot \left(\rho_0 \mathbf{u}^{'} \right) = 0, \tag{3.30}$$

$$\rho_0 \frac{D_0 \mathbf{u}^{'}}{Dt} + \rho_0 (\mathbf{u}^{'} \cdot \nabla) \mathbf{u}_0 + \nabla p^{'} = 0, \tag{3.31}$$

and

$$\frac{D_0 p^{'}}{Dt} + \gamma p_0 \nabla \cdot \mathbf{u}^{'} = 0. \tag{3.32}$$

The linearized equations for the perturbation field are written in the cartesian cordinates as

$$\frac{D_0 \rho^{'}}{Dt} + \rho_0 \left(\frac{\partial u^{'}}{\partial x} + \frac{\partial v^{'}}{\partial y} + \frac{\partial w^{'}}{\partial z} \right) = 0 \tag{3.33}$$

$$\rho_0 \frac{D_0 u^{'}}{Dt} + \left(\rho_0 v^{'} \frac{\partial u_0}{\partial y} \right) + \left(\rho_0 w^{'} \frac{\partial u_0}{\partial z} \right) + \frac{\partial p^{'}}{\partial x} = 0 \tag{3.34}$$

$$\rho_0 \frac{D_0 v^{'}}{Dt} + \frac{\partial p^{'}}{\partial y} = 0 \tag{3.35}$$

$$\rho_0 \frac{D_0 w^{'}}{Dt} + \frac{\partial p^{'}}{\partial z} = 0 \tag{3.36}$$

$$\frac{D_0 p^{'}}{Dt} + \gamma p_0 \left(\frac{\partial u^{'}}{\partial x} + \frac{\partial v^{'}}{\partial y} + \frac{\partial w^{'}}{\partial z} \right) = 0 \tag{3.37}$$

Assuming that $p^{'} = c_0^2 \rho^{'}$, Eq. 3.33 reduces to Eq. 3.37. Equations 3.34 to 3.37 will be used to derive the Pridmore-Brown equation in the following section.

3.4.2 Derivation of Pridmore-Brown Equation

The Pridmore-Brown equation is derived in this section in its more general form and then simplified for some specific cases. This equation is obtained by summing the x-derivative of the momentum equation in the axial direction with the y-derivative of the momentum equation in the y-direction, and the z-derivative of the momentum equation in the z-direction and by using the material derivative of the energy equation. Details of the derivation of the Pridmore-Brown equation are presented now.

The $x-$derivative of the momentum equation in the axial direction is gives

$$\rho_0 \frac{D_0}{Dt} \left(\frac{\partial u^{'}}{\partial x} \right) + \rho_0 \left(\frac{\partial v^{'}}{\partial x} \frac{\partial u_0}{\partial y} \right) + \rho_0 \left(\frac{\partial w^{'}}{\partial x} \frac{\partial u_0}{\partial z} \right) + \frac{\partial^2 p^{'}}{\partial x^2} = 0 \tag{3.38}$$

The y-derivative of the momentum equation in the y-direction gives after some manipulation

$$\rho_0 \frac{D_0}{Dt} \frac{\partial v^{'}}{\partial y} + \rho_0 \frac{\partial u_0}{\partial y} \frac{\partial v^{'}}{\partial x} + \left[\frac{D_0 v^{'}}{Dt} \frac{\partial \rho_0}{\partial y} \right] + \frac{\partial^2 p^{'}}{\partial y^2} = 0 \tag{3.39}$$

Similarly, the z-derivative of the momentum equation in the z-direction gives:

$$\rho_0 \frac{D_0}{Dt} \frac{\partial w^{'}}{\partial z} + \rho_0 \frac{\partial u_0}{\partial z} \left(\frac{\partial w^{'}}{\partial x} \right) + \frac{D_0 w^{'}}{Dt} \frac{\partial \rho_0}{\partial z} + \frac{\partial^2 p^{'}}{\partial z^2} = 0 \tag{3.40}$$

The material derivative of of the linearised energy equation (3.37) is

$$\frac{D_0^2 p^{'}}{Dt^2} + \gamma p_0 \left(\frac{D_0}{Dt}\frac{\partial u^{'}}{\partial x} + \frac{D_0}{Dt}\frac{\partial v^{'}}{\partial y} + \frac{D_0}{Dt}\frac{\partial w^{'}}{\partial z} \right) = 0 \tag{3.41}$$

Dividing Eq.(3.41) by c_0^2 and subtracting the derivatives given by Eq.(3.38), Eq.(3.40), and Eq.(3.39) gives

$$\frac{1}{c_0^2}\frac{D_0^2 p^{'}}{Dt^2} - \left(\frac{\partial^2 p^{'}}{\partial x^2} + \frac{\partial^2 p^{'}}{\partial y^2} + \frac{\partial^2 p^{'}}{\partial z^2} \right) - 2\rho_0 \left(\frac{\partial v^{'}}{\partial x}\frac{\partial u_0}{\partial y} \right) - \frac{\partial \rho_0}{\partial y}\left(\frac{D_0 v^{'}}{Dt} \right) - \\ - 2\rho_0 \left(\frac{\partial w^{'}}{\partial x}\frac{\partial u_0}{\partial z} \right) - \frac{\partial \rho_0}{\partial z}\left(\frac{D_0 w^{'}}{Dt} \right) = 0 \tag{3.42}$$

Taking the material derivative of Eq. (3.42), gives after some rearrangement of terms

$$\frac{D_0}{Dt}\left[\frac{1}{c_0^2}\frac{D_0^2 p^{'}}{Dt^2} - \left(\frac{\partial^2 p^{'}}{\partial x^2} + \frac{\partial^2 p^{'}}{\partial y^2} + \frac{\partial^2 p^{'}}{\partial z^2} \right) - \frac{\partial \rho_0}{\partial y}\left(\frac{D_0 v^{'}}{Dt} \right) - \frac{\partial \rho_0}{\partial z}\left(\frac{D_0 w^{'}}{Dt} \right) \right] - \\ - 2\rho_0 \frac{\partial u_0}{\partial y}\frac{\partial}{\partial x}\frac{D_0 v^{'}}{Dt} - 2\rho_0 \frac{\partial u_0}{\partial z}\frac{\partial}{\partial x}\frac{D_0 w^{'}}{Dt} = 0. \tag{3.43}$$

From Eq.(3.35)and (3.36) it is known that:

$$\rho_0 \frac{D_0 v^{'}}{Dt} = -\frac{\partial p^{'}}{\partial y} \tag{3.44}$$

$$\rho_0 \frac{D_0 w^{'}}{Dt} = -\frac{\partial p^{'}}{\partial z} \tag{3.45}$$

By using those equations above to rewrite the velocity fluctuation terms of Eq.(3.43) in terms of acoustic pressure, to give

$$\frac{D_0}{Dt}\left[\frac{1}{c_0^2}\frac{D_0^2 p^{'}}{Dt^2} - \left(\frac{\partial^2 p^{'}}{\partial x^2} + \frac{\partial^2 p^{'}}{\partial y^2} + \frac{\partial^2 p^{'}}{\partial z^2} \right) + \frac{\partial \rho_0}{\partial y}\left(\frac{1}{\rho_0}\frac{\partial p^{'}}{\partial y} \right) + \frac{\partial \rho_0}{\partial z}\left(\frac{1}{\rho_0}\frac{\partial p^{'}}{\partial z} \right) \right] + \\ + 2\rho_0 \frac{\partial u_0}{\partial y}\frac{\partial}{\partial x}\left(\frac{1}{\rho_0}\frac{\partial p^{'}}{\partial y} \right) + 2\rho_0 \frac{\partial u_0}{\partial z}\frac{\partial}{\partial x}\left(\frac{1}{\rho_0}\frac{\partial p^{'}}{\partial z} \right) = 0 \tag{3.46}$$

Rewriting in terms of the vector operator $\nabla_\perp = \mathbf{j}\frac{\partial}{\partial y} + \mathbf{k}\frac{\partial}{\partial z}$ gives

$$\frac{D_0}{Dt}\left[\frac{1}{c_0^2}\frac{D_0^2 p^{'}}{Dt^2} - \nabla^2 p^{'} + \frac{1}{\rho_0}\nabla_\perp \rho_o \cdot \nabla_\perp p^{'} \right] + 2\frac{\partial}{\partial x}\left(\nabla_\perp u_0 \cdot \nabla_\perp p^{'} \right) = 0, \tag{3.47}$$

In cylindrical coordinates (x, r, ϕ), equation 3.47 can be written as :

$$\frac{D_0}{Dt}\left[\frac{1}{c_0^2}\frac{D_0^2 p'}{Dt^2}-\left(\frac{\partial^2 p'}{\partial x^2}+\frac{1}{r}\frac{\partial}{\partial r}\left(r\frac{\partial p'}{\partial r}\right)+\frac{1}{r^2}\frac{\partial^2 p'}{\partial \phi^2}\right)+\frac{\partial \rho_0}{\partial r}\left(\frac{1}{\rho_0}\frac{\partial p'}{\partial r}\right)+\frac{1}{r}\frac{\partial \rho_0}{\partial \phi}\left(\frac{1}{\rho_0 r}\frac{\partial p'}{\partial \phi}\right)\right]+ \\ +2\frac{\partial u_0}{\partial r}\frac{\partial}{\partial x}\left(\frac{\partial p'}{\partial r}\right)+2\left(\frac{1}{r}\frac{\partial u_0}{\partial \phi}\right)\frac{\partial}{\partial x}\left(\frac{1}{r}\frac{\partial p'}{\partial \phi}\right)=0 \quad (3.48)$$

Equations 3.46 and 3.48 are the modified Pridmore-Brown equations in Cartesian and cylindrical coordinates for the case in which the density is assumed to change in the transverse direction. If the density is assumed to vary only with the transverse coordinate y, a more common form of the Pridmore-Brown equation is obtained which was first presented by Pridmore-Brown in 1958 [18]. In this case, equation (3.46) reduces to:

$$\frac{D_0}{Dt}\left[\frac{1}{c_0^2}\frac{D_0^2 p'}{Dt^2}-\left(\frac{\partial^2 p'}{\partial x^2}+\frac{\partial^2 p'}{\partial y^2}+\frac{\partial^2 p'}{\partial z^2}\right)+\frac{1}{\rho_0}\frac{\partial \rho_0}{\partial y}\left(\frac{\partial p'}{\partial y}\right)\right]+2\frac{\partial u_0}{\partial y}\frac{\partial}{\partial x}\left(\frac{\partial p'}{\partial y}\right)=0 \quad (3.49)$$

If the flow is assumed to be homentropic so that the mean density ρ_0 is constant with y, equation (3.49) becomes

$$\frac{D_0}{Dt}\left[\frac{1}{c_0^2}\frac{D_0^2 p'}{Dt^2}-\left(\frac{\partial^2 p'}{\partial x^2}+\frac{\partial^2 p'}{\partial y^2}+\frac{\partial^2 p'}{\partial z^2}\right)\right]+2\frac{\partial u_0}{\partial y}\frac{\partial}{\partial x}\left(\frac{\partial p'}{\partial y}\right)=0, \quad (3.50)$$

as presented by Savkar in 1971 [19]. Or, in the case of a two-dimensional acoustic field:

$$\frac{D_0}{Dt}\left[\frac{1}{c_0^2}\frac{D_0^2 p'}{Dt^2}-\left(\frac{\partial^2 p'}{\partial x^2}+\frac{\partial^2 p'}{\partial y^2}\right)\right]+2\frac{\partial u_0}{\partial y}\frac{\partial}{\partial x}\left(\frac{\partial p'}{\partial y}\right)=0 \quad (3.51)$$

as presented by Shankar [26] in 1972. If it is also considered that u_0 does not change in the y direction, this equation becomes:

$$\frac{D_0}{Dt}\left[\frac{1}{c_0^2}\frac{D_0^2}{Dt^2}-\left(\frac{\partial^2}{\partial x^2}+\frac{\partial^2}{\partial y^2}+\frac{\partial^2}{\partial z^2}\right)\right]p'=0. \quad (3.52)$$

This is the equation for sound propagation in uniform flow. This equation can also be written as:

$$\left[\frac{1}{c_0^2}\frac{D_0^2}{Dt^2}-\left(\frac{\partial^2}{\partial x^2}+\frac{\partial^2}{\partial y^2}+\frac{\partial^2}{\partial z^2}\right)\right]\frac{D_0}{Dt}p'=0. \quad (3.53)$$

This equation is satisfied by solutions of

$$\frac{D_0}{Dt}p'=0. \quad (3.54)$$

or

$$\left[\frac{1}{c_0^2}\frac{D_0^2}{Dt^2}-\left(\frac{\partial^2}{\partial x^2}+\frac{\partial^2}{\partial y^2}+\frac{\partial^2}{\partial z^2}\right)\right]p'=0. \quad (3.55)$$

It is often convenient to simplify the study of propagation of small disturbances in ducted flows by

assuming that the mean flow is uniform. This assumption is widely used to study the sound propagation through the inlet duct, for example. In order to analyse this problem, the use of normal mode analysis is convenient and provides theoretical insight about the complex propagation phenomena. This modal analysis will be presented in the following sections. Equation 3.55can also be written as

$$\frac{1}{c_0^2}\left(\frac{\partial}{\partial t}+u_0\frac{\partial}{\partial x}\right)^2 p^{'} = \nabla^2 p^{'} \tag{3.56}$$

or, in in cylindrical coordinates:

$$\frac{1}{c_0^2}\left(\frac{\partial}{\partial t}+u_0\frac{\partial}{\partial x}\right)^2 p^{'} = \left(\frac{\partial^2}{\partial x^2}+\frac{\partial^2}{\partial r^2}+\frac{1}{r}\frac{\partial}{\partial r}+\frac{1}{r^2}\frac{\partial^2}{\partial \theta^2}\right) p^{'}, \tag{3.57}$$

where r and θ are the radial and azimuthal coordinates. If no flow is considered, Equation 3.57 becomes:

$$\frac{1}{c_0^2}\frac{\partial^2 p^{'}}{\partial t^2} = \left(\frac{\partial^2}{\partial x^2}+\frac{\partial^2}{\partial r^2}+\frac{1}{r}\frac{\partial}{\partial r}+\frac{1}{r^2}\frac{\partial^2}{\partial \theta^2}\right) p^{'}, \tag{3.58}$$

3.4.3 Modal Solutions of the Pridmore-Brown Equation: The general form of the Solution

The pressure field solution is assumed to be harmonic of the form:

$$p^{'}(x,r,\phi,t) = Re\left\{p(r,\phi,x)e^{i\omega t}\right\} \tag{3.59}$$

where $p(r,\phi,x)$ is the complex amplitude of $p^{'}$.

Assuming solutions that vary axially with $e^{-ik_x x}$, where k_x is the axial wavenumber, written also as $k\lambda$, $k=\omega/c_0$ and λ is a non-dimensional wavenumber, the pressure solutions can be written as

$$p^{'}(x,r,\phi,t) = Re\left\{p(r,\phi)e^{-ik\lambda x+i\omega t}\right\} \tag{3.60}$$

In the next two sections we will look at modal solutions in circular and annular ducts with axisymmetric liners using the Pridmore - Brown equation. Section 3.4.4 presents the modal formulation for the Pridmore-Brown equation, while section 3.4.5 presents the Ingard boundary condition [72] in the frequency domain.

3.4.4 Modal Solutions for circular and Annular ducts with axisymmetric liners

The modified Pridmore-Brown equation with a transverse density gradient is given by Eq. (3.47). If the pressure solution is be assumed to be of the form presented in equation 3.60, The frequency

domain of the Pridmore-Brown Equation can be written in cylindrical coordinates as

$$i\omega(1-\lambda M_0)\left[-k^2(1-\lambda M_0)^2 p(r,\phi)+k^2\lambda^2 p(r,\phi))-\nabla_\perp^2 p(r,\phi)+\frac{1}{\rho_0}\nabla_\perp\rho_o\cdot\nabla_\perp p(r,\phi)\right]+ \\ -2i\lambda k(\nabla_\perp u_0\cdot\nabla_\perp p(r,\phi))=0, \quad (3.61)$$

where $M_0 = u_0/c_0$. If $p(r,\theta) = p(r)e^{-im\theta}$, the transverse Laplacian becomes:

$$\nabla_\perp^2 p(r,\theta) = \frac{1}{r}\frac{\partial r}{\partial r}\frac{\partial p(r)}{\partial r}+\frac{r}{r}\frac{\partial^2 p(r)}{\partial r^2}-\frac{m^2}{r^2}p(r)=\frac{1}{r}\frac{\partial p(r)}{\partial r}+\frac{\partial^2 p(r)}{\partial r^2}-\frac{m^2}{r^2}p(r) \quad (3.62)$$

and Eq.(3.61) is written as

$$i\omega(1-\lambda M_0)\left[(-k^2(1-\lambda M_0)^2+k^2\lambda^2)p(r)-\left[\frac{1}{r}\frac{\partial}{\partial r}\left(r\frac{\partial}{\partial r}\right)-\frac{m^2}{r^2}\right]p(r)\right]+ \\ +i\omega(1-\lambda M_0)\left[\frac{1}{\rho_0}\frac{\partial\rho_0}{\partial r}\frac{\partial p(r)}{\partial r}\right]-2i\lambda k\frac{\partial u_0}{\partial r}\frac{\partial p(r)}{\partial r}=0 \quad (3.63)$$

This is the most general form of the modal Pridmore-Brown Equation in cylindrical coordinates in the frequency domain. In the case when the transverse pressure gradient is zero, this equation reduces to

$$i\omega(1-\lambda M_0)\left[(-k^2(1-\lambda M_0)^2+k^2\lambda^2)p(r)-\left[\frac{1}{r}\frac{\partial}{\partial r}\left(r\frac{\partial}{\partial r}\right)-\frac{m^2}{r^2}\right]p(r)\right]- \\ -2i\lambda k\frac{\partial u_0}{\partial r}\frac{\partial p(r)}{\partial r}=0 \quad (3.64)$$

Equation 3.64 can be rewritten in terms of the powers of λ. This gives

$$[(M_0^3k^2-M_0k^2)p(r)]\lambda^3+[(-3k^2M_0^2+k^2)p(r)]\lambda^2+ \\ \left[\left(3M_0k^2-M_0\frac{m^2}{r^2}\right)p(r)-\frac{2k}{\omega}\frac{\partial u_0}{\partial r}\frac{\partial p(r)}{\partial r}+\frac{M_0}{r}\frac{\partial p(r)}{\partial r}+M_0\frac{\partial^2 p(r)}{\partial r^2}\right]\lambda+ \\ \left[\left(-k^2+\frac{m^2}{r^2}\right)p(r)-\frac{1}{r}\frac{\partial p(r)}{\partial r}-\frac{\partial^2 p(r)}{\partial r^2}\right]=0 \quad (3.65)$$

Equation 3.65 when combined with the boundary conditions derived in the following section forms an eigenvalue problem in λ.

3.4.5 Boundary conditions at the duct wall

To promote the noise reduction inside ducts, the walls are frequently lined with acoustically absorbing material. In the absence of liners , walls are considered to be rigid or impervious. In this section the concept of impedance is introduced and the impedance boundary condition is derived that and

will be used to derive the pressure solution in the following sections. The hard-wall boundary condition is included as a special case.

Acoustic Impedance

The acoustic impedance indicates the amount by which the motion induced by a pressure applied to a surface is impeded. It can be defined on the time-domain as the instantaneous ratio of pressure and velocity on a notional or physical surface.

More frequently it is defined in the frequency domain as the ratio of complex pressure and complex velocity amplitudes at a particular frequency and is written in its complex form [75]

$$Z(x,\omega) = \frac{p}{v} = R + iX, \tag{3.66}$$

where p is the pressure amplitude, v is the velocity amplitude normal to the surface, the real part R is the resistance and the imaginary part X is the reactance.

Boundary condition for locally-reacting acoustic lining in a duct with moving medium

Consider a duct in which the outer or inner wall is lined with an acoustically absorptive layer. Assume that the liner is locally reacting in the sense that the pressure at a point on the surface is related only to the normal velocity at the acoustic field at that point. As this work deals with circular axisymetric ducts, the radial direction will be considered and will be identified by the index r. At the wall, the particle displacement is assumed to be of the form:

$$\varepsilon_r^{wall} = \varepsilon e^{i\omega t}, \tag{3.67}$$

where ε denotes the particle radial displacement amplitude and ε_r^{wall} is the displacement at the wall. Since there is no flow at the wall, the particle velocity in the radial direction at the wall is given by:

$$v_r^{wall} = \frac{\partial \varepsilon_r^{wall}}{\partial t} = i\omega\varepsilon_r^{wall} \tag{3.68}$$

The amplitude of the particle displacement at the wall as a function of the impedance is obtained by substituting Eq. (3.68) in Eq (3.66):

$$Z(x,\omega) = \frac{p}{i\omega\varepsilon_r^{wall}} \longrightarrow \varepsilon_r^{wall} = \frac{p}{i\omega Z} \tag{3.69}$$

Outside the boundary layer, the velocity at a fluid particle is governed by the acoustic momentum equation [72]

$$\left(i\omega + u_0\frac{\partial}{\partial x}\right) v_r^{flow} = -\frac{1}{\rho_0}\frac{\partial p}{\partial r}, \tag{3.70}$$

where v_r^{flow} is the radial velocity at a fluid particle outside the boundary layer. The particle velocity and the complex displacement of a fluid particle above the boundary layer are related by:

$$v_r^{flow} = \frac{D_0 \varepsilon_r^{flow}}{Dt} \tag{3.71}$$

where ε_r^{flow} is the complex displacement of a fluid particle above the boundary layer. Substituting Eq.(3.71) in Eq.(3.70) :

$$\left(i\omega + u_0 \frac{\partial}{\partial x}\right)^2 \varepsilon_r^{flow} = -\frac{1}{\rho_0}\frac{\partial p}{\partial r} \tag{3.72}$$

If continuity of the particle displacement is assumed through the boundary layer, $\varepsilon_r^{wall} = \varepsilon_r^{flow}$, then

$$\left(i\omega + u_0 \frac{\partial}{\partial x}\right)^2 \frac{p}{i\omega Z} = -\frac{1,}{\rho_0}\frac{\partial p}{\partial r} \tag{3.73}$$

or

$$\frac{\partial p}{\partial r} + \frac{1}{i\omega z c_0}\left(i\omega + u_0 \frac{\partial}{\partial x}\right)^2 p = 0, \tag{3.74}$$

where z is the non-dimensional acoustic impedance defined as:

$$z = \frac{Z}{\rho_0 c_0}. \tag{3.75}$$

When no flow is present, the convection effect vanishes and the boundary condition becomes:

$$\frac{\partial p}{\partial r} = -\frac{i\omega}{z c_0} p, \text{ or } \frac{\partial p}{\partial r} = -\frac{ik}{z} p. \tag{3.76}$$

Equation 3.76 can also be written in terms of the non-dimensional admittance a, defined as the reciprocal of the impedance ($a = \frac{1}{z}$):

$$\frac{\partial p}{\partial r} = -ikap, \tag{3.77}$$

For a hard-wall case, the impedance tends to infinity and the admittance tends to zero. In this case, the boundary condition is given by:

$$\frac{\partial p}{\partial r} = 0 \tag{3.78}$$

When the walls are lined, the Ingard boundary condition [72] is applied at the duct inner (R_1) and outter (R_2) walls. This gives

$$\left[\frac{\partial p}{\partial r}\right]_{R1,R2} = \pm \frac{1}{i\omega z c_0}\left(i\omega + u_0 \frac{\partial}{\partial x}\right)^2 p \tag{3.79}$$

where $k = \omega / c_0$, the $+$ sign relates to the outer surface and the $-$ sign relates to the inner surface. This boundary condition can also be written in terms of the Mach number as

$$\left[\frac{\partial p}{\partial r}\right]_{R1,R2} = \pm \frac{i\omega}{z c_0}(1 - \lambda M_0)^2 p = \pm ikA(1 - \lambda M_0)^2 p \tag{3.80}$$

An eigenvalue problem is specified in λ by the solution of equation 3.64 or 3.65 that satisfy the boundary condition given by equation 3.80. This eigenvalue problem is studied in the following sections.

3.4.6 Analytic Modal Solutions for hard-wall circular and annular ducts with uniform flow

For uniform flow, equation 3.64 reduces to the Bessel equation:

$$\frac{d^2p(r)}{dr^2}+\frac{1}{r}\frac{dp(r)}{dr}+\left[k_r^2-\frac{m^2}{r^2}\right]p(r)=0 \tag{3.81}$$

where

$$k_r^2=(k-k\lambda M_0)^2-k^2\lambda^2. \tag{3.82}$$

In this equation, k_r is the wavenumber in the radial direction, k_x is the axial wavenumber (defined also as $k\lambda$). The general solution of the equation 3.81 is given by

$$p(r)=AJ_m(k_r r)+BN_m(k_r r), \tag{3.83}$$

where J_m and N_m are the Bessel and Neuman functions of order m, A and B are constants, k_r is the radial wavenumber, $M_0=\frac{u_0}{c_0}$ is the flow Mach number. For the case of acylindrical circular duct, Eq. 3.83 reduces to

$$p(r)=AJ_m(k_r r). \tag{3.84}$$

The axial wavenumber $k_x=k\lambda$ shown in Eq.(3.82) can be rewritten in terms of k_r as:

$$k_x=\frac{k}{1-M_0^2}\left(M_0\pm\sqrt{1-(1-M_0^2)\frac{k_r^2}{k^2}}\right) \tag{3.85}$$

Notice that when flow is included, axial wave numbers are larger for upstream propagation than the ones for the downstream propagation. If the axial wavenumber k_x is real, the mode propagates without attenuation and is termed cut-on mode. If k_x is imaginary, the mode decays and is termed cut-off. If the term inside the square root is negative, k_x is complex and the mode decays. Otherwise, if this term is positive, k_x is real and the mode propagates. The limiting case between cut-on and cut-off occurs when the expression inside the square root is zero. In this case, a cut-off ratio β can be defined as:

$$\beta=\frac{1}{\sqrt{1-M_0^2}}\frac{k}{k_r} \tag{3.86}$$

If $\beta>1$, k_x is real and the mode is cut-on. If $\beta<1$, k_x is complex and the mode is cut-off. In the absence of flow, $M_0=0$ and

$$k_x=\pm k\left(\sqrt{1-\frac{k_r^2}{k^2}}\right) \tag{3.87}$$

Without flow, acoustic waves propagate upstream and downstream with the same speed.

Hard-Wall Boundary Condition

The radial wavenumber k_r, the nondimensional wavenumber λ and the axial wavenumber k_x are determined by applying the boundary conditions at the inner and outer walls of the duct. For hard walls, equation 3.78 applies:

$$\frac{\partial p}{\partial r} = 0. \tag{3.88}$$

The pressure solution is given by:

$$p(x,r,\theta,t) = \left(A_r J_m(k_r r) + B_r Y_m(k_r r)\right) e^{-i(k_x x + m\theta - \omega t)} \tag{3.89}$$

where k_r is a root of equation 3.93 As a consequence:

$$A\frac{\partial \left(J_m(k_r r)\right)}{\partial r} + B\frac{\partial \left(N_m(k_r r)\right)}{\partial r} = 0 \quad \text{at the boundary} \tag{3.90}$$

In the case of an annular duct with hard-walls at $r = R_1$ and $r = R_2$, the equation above gives

$$AJ_m^{'}(k_r R_1) + BN_m^{'}(k_r R_1) = 0 \tag{3.91}$$

$$A_r J_m^{'}(k_r R_2) + B_r N_m^{'}(k_r R_2) = 0 \tag{3.92}$$

This equations are satisfied if

$$N_m^{'}(k_r R_1) J_m^{'}(k_r R_2) = N_m^{'}(k_r R_2) J_m^{'}(k_r R_1) \tag{3.93}$$

Equation (3.93) does not have an analytical solution. Numerical methods must be used in order to obtain the discrete values of k_r for which the solution is possible.

For the case of cylindrical circular ducts,the solution has the form:

$$p(x,r,\theta,t) = A_r J_m(k_r r) e^{-i(k_x x + m\theta - \omega t)}, \tag{3.94}$$

where k_r should satisfy

$$J_m^{'}(k_r R_2) = J_m^{'}(k_r R_1) = 0. \tag{3.95}$$

3.5 Propagation in ducts with swirl

When swirl is present, there is no simple second order equation to solve the problem. The methodology to predict sound propagation in mean swirling flows is now described.

3.5.1 Mean Swirling Flow

The steady Euler equations for the mean field for an isentropic perfect gas are derived in section 3.2 and are given by equations 3.14 to 3.16.

Consider the mean flow in a duct with constant inner and outer radius in which the mean flow

is steady, axisymmetric and has zero radial velocity and in addition to that the axial and azimuthal velocities are dependent only upon the radius, [5]

$$\mathbf{u_0} = u_\phi(r)\mathbf{e}_\phi + u_{0x}(r)\mathbf{e}_x. \tag{3.96}$$

This is an idealized model for the mean flow in the interstage regions of turbofan engines. The fan generates a strong swirling flow and the azimuthal velocity cannot be neglected [51]. When swirl is included, mean flow variables such as pressure, density and speed of sound can vary radially. Substituting 3.96 in Eq. 3.15, the pressure gradient is obtained for the radial, azimuthal and axial directions.

$$\frac{\partial p_0}{\partial r} = \rho_0\left(\frac{u_{0\phi}^2}{r}\right), \quad \frac{\partial p_0}{\partial \phi} = 0, \quad \frac{\partial p_0}{\partial x} = 0 \quad . \tag{3.97}$$

Notice that although the mean pressure is constant in the azimuthal and axial direction, it varies in the radial direction as a function of the azimuthal velocity. For an axial flow the pressure gradient is zero in all directions.

Density ρ_0 and speed of sound c_0 are also related to pressure p_0 in a perfect gas. If the pressure gradient is changed when the azimuthal velocity component $u_{0\phi}$ is present, density and speed of sound will also change. For a perfect gas, the speed of sound, mean pressure and mean density are related by:

$$c_0^2 = \frac{\gamma p_0}{\rho_0} \tag{3.98}$$

It is possible to write the speed of sound in terms of azimuthal velocity and pressure and density in terms of the speed of sound to give a full set of equations that define the mean swirling flow properties as follows. Differentiating equation (3.98) in relation to the radius, gives

$$\frac{\partial c_0^2}{\partial r} = \frac{\gamma p_0}{\rho_0^2}\frac{\partial \rho_0}{\partial r} + \frac{\gamma}{\rho_0}\frac{\partial p_0}{\partial r} \tag{3.99}$$

The terms on the right-hand side of Eq. 3.99 depend upon the pressure and density gradients in the radial direction. The pressure gradient is given by 3.97. To obtain the density gradient it is assumed from now on that the entropy is constant in the whole domain and not only along a streamline, ie homentropic flow. Since a homentropic is necessarily isentropic, the whole formulation developed so far still holds. In this case,

$$p_0\rho_0^{-\gamma} = Q, \tag{3.100}$$

where Q is a constant. The density gradient is obtained is obtained by differentiating Eq.3.100 and is given by:

$$\frac{\partial \rho_0}{\partial r} = \frac{\rho_0}{\gamma p_0}\frac{\partial p_0}{\partial r} \tag{3.101}$$

For a homeontropic flow both the mean pressure and the mean density for a given swirl distribution can be determined, while for a non-homentropic flow only the pressure gradient is determined. This

fact was emphasised by Nijboer [1] who showed that an unfavourable density distribution may yield an unstable flow. Substituting (3.97) and(3.101) in 3.99 and integrating between a position along the radius and a reference point, which in this case is the outer radius gives

$$c_0^2(r) = c_0^2(r_{out}) - (\gamma - 1)\int_r^{r_{out}} \frac{u_{0\phi}^2}{r} dr \tag{3.102}$$

The speed of sound is now written in terms of the azimuthal velocity component. Notice that for an axial flow the speed of sound would be constant. The mean variables are non-dimensionalized by the respective values at a reference position (which in this case is the outer radius) as follows:

$$c_0^* = c_0/c_{0ref} \tag{3.103}$$

$$\rho_0^* = \rho_0/\rho_{0ref} \tag{3.104}$$

$$p_0^* = \frac{p_0}{c_{0ref}^2 \rho_{0ref}}, \tag{3.105}$$

where ρ_{0ref} and c_{0ref} are the reference values of mean density and the mean sound speed at the outer radius. If the isentropic relations are applied between two radial locations, say, a point inside the duct and the outer wall, the following relations are obtained:

$$p_0^* = (\rho_0^*)^\gamma \tag{3.106}$$

$$(c_0^*)^2 = \frac{p_0^*}{\rho_0^*} \tag{3.107}$$

and mean flow variables as a function of radius for an isentropic flow are given in the non-dimensional form by:

$$c_0^{*2}(r^*) = 1 - (\gamma - 1)\int_{r^*}^1 \frac{u_{0\phi}^{*2}}{r^*} dr^*, \tag{3.108}$$

$$\rho_0^*(r^*) = (c_0^{*2})^{\frac{1}{\gamma-1}}, \tag{3.109}$$

and

$$p_0^*(r^*) = (c_0^{*2})^{\frac{\gamma}{\gamma-1}}, \tag{3.110}$$

where the radius is non-dimensionalized by the outer radius ($r^* = r/r_{out}$).

Equations 3.108 to 3.110 fully define the mean swirling flow. Given an azimuthal velocity distribution, pressure and density distributions are defined by those equatons. In the next subsection, representative types of swirling flows will be presented.

3.5.2 Representative Mean Swirling Flows

In this section two types of mean swirling flow will be discussed, rigid body and vortex swirl. A combination of both types is also presented. The first special case of swirling flow that we will be looking at is the free vortex swirl, that has the advantage of being a potential flow. The azimuthal

velocity of a vortex swirl type of flow is given by:

$$u_{0\phi} = \frac{\Gamma}{r}, \tag{3.111}$$

where Γ is the vortex strength, or in a non-dimensional form,

$$u^*_{0\phi} = \frac{\Gamma^*}{r^*}, \tag{3.112}$$

where $\Gamma^* = \Gamma / r_{out} c_{0ref}$. For a free vortex swirl with azimuthal velocity defined by Eq. 3.112, the mean sound speed, mean density and mean pressure profiles are given by

$$c^{*2}_0(r^*) = 1 - \left(\frac{\gamma-1}{2}\right)(\Gamma^*)^2 \left(\frac{1}{(r^*)^2} - 1\right), \tag{3.113}$$

$$\rho^*_0(r^*) = \left[1 - \left(\frac{\gamma-1}{2}\right)(\Gamma^*)^2 \left(\frac{1}{(r^*)^2} - 1\right)\right]^{\frac{1}{\gamma-1}}, \tag{3.114}$$

and

$$p^*_0(r^*) = \left[1 - \left(\frac{\gamma-1}{2}\right)(\Gamma^*)^2 \left(\frac{1}{(r^*)^2} - 1\right)\right]^{\frac{2}{\gamma-1}}. \tag{3.115}$$

The second representative type of flow is the solid-body rotation type. Consider that a fluid enclosed in a duct rotates about an axis (say, the turbofan shaft) without any translation and assume that the fluid is rotating steadily at a constant speed. The azimuthal velocity of this fluid is then given by:

$$u_{0\phi} = \Omega r \tag{3.116}$$

or, in a non-dimensional form,

$$u^*_{0\phi} = \Omega^* r^*. \tag{3.117}$$

where $\Omega^* = \frac{\Omega r_{out}}{c_0(r_{out})}$. For a rigid body swirl, the mean sound speed, mean density and mean pressure profiles are given by

$$u^*_{0\phi} = \Omega^* r^*, \tag{3.118}$$

$$c^{*2}_0(r^*) = 1 - \left(\frac{\gamma-1}{2}\right)(\Omega^*)^2 \left(1 - (r^*)^2\right), \tag{3.119}$$

$$\rho^*_0(r^*) = \left[1 - \left(\frac{\gamma-1}{2}\right)(\Omega^*)^2 \left(1 - (r^*)^2\right)\right]^{\frac{1}{\gamma-1}}, \tag{3.120}$$

and

$$p^*_0(r^*) = \left[1 - \left(\frac{\gamma-1}{2}\right)(\Omega^*)^2 \left(1 - (r^*)^2\right)\right]^{\frac{\gamma}{\gamma-1}}, \tag{3.121}$$

A combination of free vortex swirl and solid body rotation is also considered. For this type of flow, the azimuthal velocity, the mean sound speed, mean density and mean pressure profiles are given by

$$u^*_{0\phi} = \frac{\Gamma^*}{r^*} + \Omega^* r^*, \tag{3.122}$$

$$c_0^{*2}(r^*) = 1 - \left(\frac{\gamma-1}{2}\right)\left[(\Omega^*)^2(1-r^*) + (\Gamma^*)^2\left(\frac{1}{(r^*)^2}-1\right)\right] + 2(\gamma-1)\Gamma^*\Omega^*\log r^*, \quad (3.123)$$

$$\rho_0^*(r^*) = \left\{\left[(\Omega^*)^2(1-r^*) + (\Gamma^*)^2\left(\frac{1}{(r^*)^2}-1\right)\right] + 2(\gamma-1)\Gamma^*\Omega^*\log r^*\right\}^{\frac{1}{\gamma-1}}, \quad (3.124)$$

and

$$p_0^*(r^*) = \left\{\left[(\Omega^*)^2(1-r^*) + (\Gamma^*)^2\left(\frac{1}{(r^*)^2}-1\right)\right] + 2(\gamma-1)\Gamma^*\Omega^*\log r^*\right\}^{\frac{2}{\gamma-1}}. \quad (3.125)$$

where $\Gamma^* = \Gamma/r_{out}c_{0_{out}}$. Figure 3.3 shows a representation model of a turbofan cointaining a rotor, a stator and a hub. Assume that those are enclosed by a nacelle. According to Kerrebrock [62], the swirling flow can be modelled as a combination of vortex swirl and rigid body between the rotor and the stator (region 1) while the small swirl that can still remain after the stator (region 2) can be modelled as a rigid body.

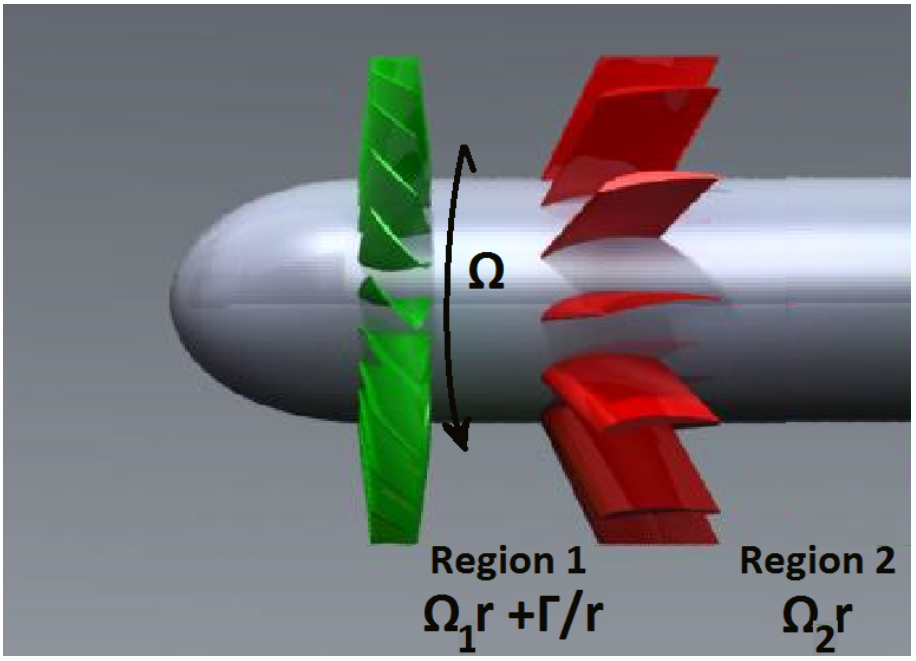

Fig. 3.3 – Turbofan engine simplifyed model showing representative types of mean swirling flows

In terms of the axial flow profile, uniform axial flow is the most commonly used. However, a different axial profile profile was proposed by Posson & Peake [2]. This profile is termed radium equilibrium and is consistent with the mean flow momentum balance. A short derivation is presented as follows.

The steady momentum equation 3.15 can be rewritten as:

$$\nabla\left(\frac{\mathbf{u}_0^2}{2}\right) - \mathbf{u}_0 \times \xi = -\frac{1}{\rho_0}\nabla p_0 \quad (3.126)$$

where $\xi = (\nabla \times \mathbf{u}_0)$ is the vorticity. By applying the first law of thermodynamics, the last term of

equation 3.126 can be rewritten as

$$\frac{\nabla p_0}{\rho_0} = \nabla h_0 - T ds_0, \tag{3.127}$$

where s_0 is the specific enthalpy and h_0 is the specific entropy. The first term of equation 3.126 can be rewritten by defining the gradient of enthalpy as

$$\nabla \left(\frac{\mathbf{u}_0^2}{2} \right) = \nabla H - \nabla h_0, \tag{3.128}$$

where H is the stagnation enthalpy. For an adiabatic process the stagnation enthalpy remains constant ($\nabla H = 0$) and for a homentropic flow the entropy remains the same (∇h_0). Eq. 3.126 is then given by:

$$\mathbf{u}_0 \times \xi = 0 \tag{3.129}$$

The radial component of Eq.3.129 then gives

$$\frac{u_{0\phi}}{r} \frac{\partial (u_{0\phi} r)}{\partial r} + u_{0x} \frac{\partial u_{0x}}{\partial r} = 0. \tag{3.130}$$

By integrating Eq. 3.130 between a point along the radius and a reference a point in the outer radius and assuming that the azimuthal velocity is a combination of rigid body rotation and vortex swirl profile we obtain

$${u_{x0}}^2(r) = {u_{x0}}^2(r_{ref}) + 2[(\Omega)^2 \left(r_{ref} - (r)^2 \right) - 2\Omega\Gamma \ln \left(\frac{r_{ref}}{r} \right)] \tag{3.131}$$

or, in a non-dimensional form,

$$u_{x0}^{*2}(r^*) = 1 + 2[(\Omega^*)^2 \left(1 - (r^*)^2 \right) - 2\Omega^*\Gamma^* \ln(r^*)] \tag{3.132}$$

3.5.3 Unsteady Swirling Flow

The linearised Euler equations for an isentropic perturbation field are given by equations 3.17 to 3.19. By writing those equations in cylindrical coordinates and assuming the velocity fluctuations to be of the form

$$\mathbf{u}' = u_r' \mathbf{e}_r + u_\phi' \mathbf{e}_\phi + u_x' \mathbf{e}_x, \tag{3.133}$$

the continuity equation reduces to the energy equation and the governing equations for the perturbation field are written as

$$\frac{\partial p'}{\partial t} + \frac{u_{0\phi}(r)}{r} \frac{\partial p'}{\partial \phi} + u_{0x} \frac{\partial p'}{\partial x} + u_r' \frac{\rho_0 u_{0\phi}}{r} + \gamma p_0 \left[\frac{\partial u_r'}{\partial r} + \frac{1}{r} \frac{\partial u_\phi'}{\partial \phi} + \frac{\partial u_x'}{\partial x} + \frac{u_r'}{r} \right] = 0 \tag{3.134}$$

$$\frac{\partial u_r^{'}}{\partial t}+\frac{u_{0\phi}(r)}{r}\frac{\partial u_r^{'}}{\partial \phi}+u_{0x}(r)\frac{\partial u_r^{'}}{\partial x}-2\frac{u_{0\phi}u^{'}{}_{\phi}}{r}+\frac{p^{'}}{\rho_0 c_0^2}\left(-\frac{u_{0\phi}^2}{r}\right)+\frac{1}{\rho_0}\frac{\partial p^{'}}{\partial r}=0 \tag{3.135}$$

$$\frac{\partial u_x^{'}}{\partial t}+\frac{u_{0\phi}(r)}{r}\frac{\partial u_x^{'}}{\partial \phi}+u_{0x}(r)\frac{\partial u_x^{'}}{\partial x}+\left(u_r^{'}\frac{\partial u_{0x}(r)}{\partial r}\right)+\frac{1}{\rho_0}\frac{\partial p^{'}}{\partial x}=0 \tag{3.136}$$

$$\frac{\partial u_\phi^{'}}{\partial t}+\frac{u_{0\phi}(r)}{r}\frac{\partial u^{'}\phi}{\partial \phi}+u_{0x}(r)\frac{\partial u^{'}\phi}{\partial x}+\frac{u_{0\phi}u^{'}{}_r}{r}+u_r^{'}\frac{\partial u_{0\phi}(r)}{\partial r}+\frac{1}{\rho_0 r}\frac{\partial p^{'}}{\partial \phi}=0 \tag{3.137}$$

3.5.4 Normal Mode Analysis

Perturbation variables $\rho^{'}$, $p^{'}$, $u_r^{'}$, $u_\phi^{'}$ and $u_x^{'}$ are assumed to have the exponential dependence:

$$f^{'}(r,\phi,x,t)=\mathrm{Re}\left\{f(r)e^{i(-k\lambda x+\omega t-m\phi)}\right\}, \tag{3.138}$$

where $f^{'}$ is the perturbation variable, $k\lambda=k_x=\omega/c_p$ is the axial acoustic wavenumber, c_p is the axial mode phase speed, m is the circunferential mode order and ω is the frequency. Substituting equation (3.144) in equations (3.134) to (3.137), considering that the mean density does not change with the axial and azimuthal direction, placing the axial wavenumbers on the right hand side of the equation and writing the mean flow velocities in terms of Mach numbers, the governing equations for the perturbation field are written as

$$\left(i\omega-c_0\frac{M_{0\phi}im}{r}\right)p+c_0^2\left(\frac{\rho_0 M_{0\phi}^2}{r}+\gamma p_o\left(\frac{\partial}{\partial r}+\frac{1}{r}\right)\right)u_r-\left(\gamma\frac{p_0 mi}{r}\right)u_\phi=-ik\lambda\left(-c_0M_{0x}p-\gamma p_0 u_x\right), \tag{3.139}$$

$$\left(\frac{1}{\rho_0}\frac{\partial}{\partial r}-\frac{1}{\rho_0}\frac{M_{0\phi}^2}{r}\right)p+\left(i\omega-c_0\frac{M_{0\phi}im}{r}\right)u_r+\left(-2c_0\frac{M_{0\phi}}{r}\right)u_\phi=-ik\lambda(-c_0M_{0x}u_r). \tag{3.140}$$

$$\left(c_0\frac{\partial M_{0x}}{\partial r}\right)u_r+\left(i\omega-c_0\frac{imM_{0\phi}}{r}\right)u_x=-ik\lambda\left(-\frac{p}{\rho_0}-c_0M_{0x}u_x\right), \tag{3.141}$$

and

$$-\left(\frac{im}{\rho_0 r}\right)p+\left(c_0\frac{M_{0\phi}}{r}+c_0\frac{\partial M_{0\phi}}{\partial r}\right)u_r+\left(i\omega-c_0\frac{imM_{0\phi}}{r}\right)u_\phi=-ik\lambda\left(-c_0M_{0x}u_\phi\right), \tag{3.142}$$

where $M_{0\phi}$ and M_{0x} are the local Mach numbers in the circunferential and axial directions defined by $M_{0\phi} = u_{0\phi}/c_0$ and $M_{0\phi} = u_{0x}/c_0$

3.5.5 Boundary Condition

For lined ducts the the velocity radial component at the walls is given by the Ingard-Myers Boundary Condition [72]:

$$u_r = n\left(i\omega + \frac{u_{0\phi}}{r}\frac{\partial}{\partial\phi} + u_{0x}\frac{\partial}{\partial x}\right)\frac{p}{i\omega Z}, \tag{3.143}$$

where $n = +1$ at the outer radius and $n = -1$ at the hub. For hard-walled ducts, the impedance goes to infinity and equation (3.143) reduces to

$$u_r = 0. \tag{3.144}$$

If it is assumed that the perturbation variables have the exponential dependence given by , the boundary condition is written in the modal form as:

$$u_r = n\left(i\omega - im\frac{u_{0\phi}}{r} - ik\lambda u_{0x}\right)\frac{p}{i\omega z}, \tag{3.145}$$

where $n = +1$ at the outer radius and $n = -1$ at the hub. For hard-walled ducts, the boundary condition is reduced to:

$$u_r = 0. \tag{3.146}$$

3.5.6 Acoustic Power

An objective of this work is to assess the performance of acoustic liners. In order to do that, it is essential to calculate the power and the insertion loss. The expression for acoustic power will be introduced in this subsection and for insertion loss in the next subsection.

For isentropic irrotational flow the acoustic energy is conserved and an energy conservation equation can be derived from the Euler equations. However, mean flow non-uniformity modifies the expression for sound power calculation. The acoustic intensity expression was derived by Myers [69], [70], who showed that the time-averaged intensity flux in a non-uniform mean flow is not conserved. Since in this case modes are not orthogonal any more [70], interference between radial modes should be accounted for. Atassi [71] derived an expression to calculate the sound power in an annular duct with swirling flow in the high frequency limit using normal mode solutions and showed that since the coupling between vorticity and acoustic waves is weak in the high frequency limit, the acoustic energy can be considered to be conserved in an approximate. Although this formulation has its limitations [76], it was also used by other authors for the sound propagation in swirling flows [2] [71] and in irrotational homentropic swirling flow [77]

Acoustic intensity is defined as the flux of acoustic energy per unit area across a surface. For swirling flows, the acoustic intensity in the axial direction it is defined as [71]:

$$\mathrm{I}_x = p^{'}u_x^{'} + \frac{u_{0x}}{\rho_0}p^{'}\rho^{'} + u_{x0}\rho_0 u_x^{'}u_x^{'} + u_{x0}^2 u_x^{'}\rho^{'} + u_{\phi 0}\rho_0 u_\phi^{'}u_x^{'} + u_{\phi 0}u_{0x}u_\phi^{'}\rho^{'} \tag{3.147}$$

Consider a solution of the form

$$\{u_x^{'}, u_\phi^{'}, p^{'}\}(r,\phi,x,t) = \mathrm{Re}\left\{A\{u_x, u_\phi, p\}(r)e^{i(-k\lambda x - m\phi)}e^{i(\omega t)}\right\}. \tag{3.148}$$

which corresponds to the modal solutions previously used. In this equation, A is the modal amplitude and $\{u_x, u_\phi, p\}(r)$ are mode shape functions. When any two quantities of the form described in Eq. 3.148 are multiplied, say $u_x^{'} \times u_\phi^{'}$ for example, and the product of those two quantities is time averaged over a period of harmonic motion,

$$\begin{aligned}\overline{u_x^{'} \times u_\phi^{'}} = &\frac{1}{4}\left\{Au_x(r)e^{i(-k\lambda x - m\phi)}e^{i(\omega t)}\right\}\left\{Au_\phi(r)e^{i(-k\lambda x - m\phi)}e^{i(\omega t)}\right\}^* \\ &+\frac{1}{4}\left\{Au_x(r)e^{i(-k\lambda x - m\phi)}e^{i(\omega t)}\right\}^*\left\{Au_\phi(r)e^{i(-k\lambda x - m\phi)}e^{i(\omega t)}\right\},\end{aligned} \tag{3.149}$$

where m and ω are real numbers and λ is an immaginary quantity. The asterisk represents the complex conjugate. After some manipulation, Eq. 3.149 can be rewritten as

$$\overline{u_x^{'} \times u_\phi^{'}} = \frac{A^2}{2}\mathrm{Re}\left\{u_x(r)u_\phi(r)^* e^{-2\lambda_i k x}\right\} \tag{3.150}$$

where λ_i is the imaginary part of λ. This result will be used to calculate the acoustic intensity as follows.

The axial acoustic intensity is averaged over time as

$$\bar{\mathrm{I}}_x = \frac{1}{T}\int_{-T/2}^{+T/2}\mathrm{I}_x dt. \tag{3.151}$$

Substituting Eq. 3.147 in 3.151 and applying the process used to obtain expression 3.150 applies to other product of perturbed variables, an expression for the time averaged acoustic intensity for a single mode is obtained

$$\begin{aligned}\bar{\mathrm{I}}_x = A^2\frac{1}{2}\mathrm{Re}\left\{pu_x^*\left[1+\frac{u_{0x}^2}{c_0^2}\right] + pp^*\left[\frac{u_{0x}}{\rho_0 c_0^2}\right] + pu_\phi^*\left[\frac{u_{0x}u_{0\phi}}{c_0^2}\right]\right\}e^{-i(2k\lambda_i x)} + \\ A^2\frac{1}{2}\mathrm{Re}\left\{u_x u_x^*\left[u_{0x}\rho_0\right] + u_\phi u_x^*\left[u_{0\phi}\rho_0\right]\right\}e^{-i(2k\lambda_i x)}\end{aligned} \tag{3.152}$$

The acoustic power for a single mode is given by the integration of the above expression over the duct area

$$W = \int_{r_{in}}^{r_{out}}\int_0^{2\pi}\bar{\mathrm{I}}_x r d\phi dr, \tag{3.153}$$

Substituting the acoustic intensity expression given by 3.160, the acoustic power is rewritten as

$$W = A^2 \alpha \pi e^{-i(2k\lambda_i x)}, \tag{3.154}$$

where α is a normalization constant given by

$$\alpha = \mathrm{Re}\left[\int_{r_{in}}^{r_o ut} r\left[pu_x^*\left[1+\frac{u_{0x}^2}{c_0^2}\right]+pp^*\left[\frac{u_{0x}}{\rho_0 c_0^2}\right]+pu_\phi^*\left[\frac{u_{0x}u_{0\phi}}{c_0^2}\right]+u_x u_x^*\left[u_{0x}\rho_0\right]+u_\phi u_x^*\left[u_{0\phi}\rho_0\right]\right]dr\right]. \tag{3.155}$$

In this thesis it is assumed that in the broadband source modes are uncorrelated and carry equal power so that 3.154 is rewritten as

$$W = W_0 e^{-i(2k\lambda_i x)} \tag{3.156}$$

where $W_0 = A^2\alpha\pi$ is the constant power of a single mode at the inlet.

The total sound power is calculated by summing up the power of all individual modes of azimuthal order m and radial order n:

$$W = \sum_{m,n} W_0 e^{-i(2k\lambda_i x)} \tag{3.157}$$

3.5.7 Insertion Loss

The insertion loss is then calculated by the difference between power levels of sound propagation in hard-walled and lined ducts.

$$IL = 10\log\left(\frac{W_{HW}}{W_{LW}}\right), \tag{3.158}$$

where W_{LW} is the power for a lined duct and W_{HW} is the power for a hard-walled duct measured in the end of the duct. In a hard-walled duct, the sound propagates unattenuated and the power in the duct end is the same as in the beginning of the duct,

$$W_{HW,exhaust} = W_{HW,inlet} = \sum_{m,n} W_0. \tag{3.159}$$

In a lined duct, for instance, the sound is attenuated,

$$W_{LW,exhaust} = \sum_{m,n} W_0 \times e^{-2\mathrm{Im}(k\lambda)L} \tag{3.160}$$

Substituting equation 3.168 and 3.167 in 3.158, the expression to calculate the insertion loss in the duct exhaust is written as

$$IL = 10\log_{10}\left(\frac{m_{HW}\times n_{HW}}{\sum_{m=0}^{m_{HW}} e^{-2\mathrm{Im}(k\lambda)\mathrm{L}}}\right), \tag{3.161}$$

in which L is the liner length and m_{HW} and n_{HW} is the number of azimuthal and radial cut-on modes

for the radial mode case. The modes to be considered in the lined case will be evaluated based on the mode triangles for the hard wall case from previous section. In other words, the number of radial modes to be accounted for in the lined case will be the number of cut-on radial modes in the hard-walled case. This equation will be used for the insertion loss calculations in chapter 7

$$IL = 10\log_{10}(m_{HW} \times n_{HW}) - 10\log_{10} \sum_{m=0}^{m_{HW}} e^{-2\mathrm{Im}(k\lambda)\mathrm{L}} \tag{3.162}$$

For a given frequency and azimuthal mode order, the axial wavenumbers correspondent to each radial mode n are calculated and stored in order of attenuation (from lower to higher). The transmission loss is then calculated using the first n_{HW} radial modes.

Chapter 4

Numerical Method

In the previous chapter two eigenvalue problems were formulated. The first is based on the Pridmore-Brown equation while the second is based on the full set of Linearized Euler equations. In both eigenvalue problems, the Ingard impedance boundary condition is used. For a parallel sheared flow the solutions can be obtained by using either formulation. When swirl is included, one has to use the second eigenvalue problem that is based on the full set of Linearized Euler Equations.

In this chapter the next step is discussed, which is the discretization phase. Section 4.1 presents the discretisation for the eigenvalue problem based on the Pridmore-Brown Equation, while section 4.2 presents the discretisation for the eigenvalue problem based on the Linearized Euler Equations.

For both cases the continuous domain is discretized radially by a structured regular cartesian grid. The radial derivatives are discretized in space by using a Finite Difference approximation.

4.1 Finite Difference formulation for mode propagation on Parallel Sheared Flows based on the Pridmore-Brown Equation

The eigenvalue problem to be solved numerically is defined by the Pridmore-Brown governing equation and the Ingard boundary condition, given by Eq. 3.66 and 3.82 and rewritten here as equations 4.1 and 4.2. The Pridmore-Brown equation is a second-order, linear, variable-coefficient ordinary differential equation that describes the radial distribution of pressure. Because this equation has variable coefficients, it does not have an analytic solution but can be solved by numerical methods in which the problem is discretized in the radial direction.

$$\begin{aligned}&[(M_0(r)^3k^2 - M_0(r)k^2)p(r)]\,\lambda^3 + [(-3k^2M_0(r)^2 + k^2)p(r)]\,\lambda^2 + \\ &\left[\left(3M_0(r)k^2 - M_0(r)\frac{m^2}{r^2}\right)p(r) - 2\frac{\partial M_0(r)}{\partial r}\frac{\partial p(r)}{\partial r} + \frac{M_0(r)}{r}\frac{\partial p(r)}{\partial r} + M_0(r)\frac{\partial^2 p(r)}{\partial r^2}\right]\lambda^1 + \\ &\left[\left(-k^2 + \frac{m^2}{r^2}\right)p(r) - \frac{1}{r}\frac{\partial p(r)}{\partial r} - \frac{\partial^2 p(r)}{\partial r^2}\right]\lambda^0 = 0 \quad (4.1)\end{aligned}$$

$$\left[\frac{\partial p}{\partial r}\right]_{R1,R2} = \pm\frac{i\omega}{zc_0}(1-\lambda M_0)^2 p \tag{4.2}$$

The Pridmore-Brown equation is a good starting point for studying more complex mean flows with swirl. It is simpler to code when comparing than the full set of Linearized Euler Equations and can be used to validade subsequent solutions based on the Linearized Euler Equations to be described in the next section.

4.1.1 The Computational Grid

The one-dimensional domain is discretized from the inner radius R_1 to the outer radius R_2. Consider p_i the value of the function $p(r)$ at the point r_i, that is, $p_i = p(r_i)$. The spacing between two consecutive points is constant Δr so that $r_i = R_{in} + (i-1)\Delta r$, where i varies from one to N, being N the total number of nodes in the grid. The regular axissymmetric grid is shown in figure 4.1.

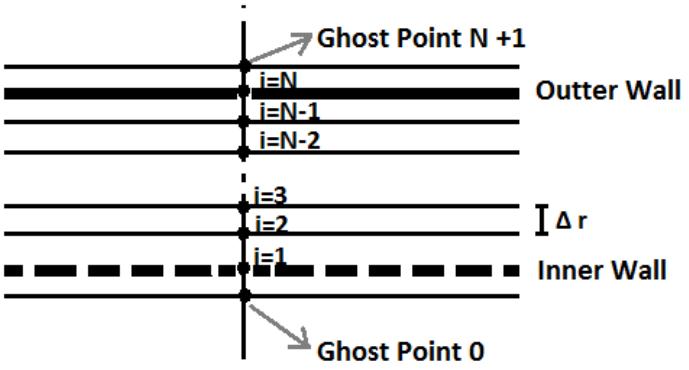

Fig. 4.1 – One-dimensional regular cartesian mesh

Ghost points are used before the inner wall ($N = 0$) and after the outer wall ($N = N + 1$). These were used to impose the boundary conditions as will be presented in section 4.1.4. No grid refinement is used in the boundaries, but a high resolution is used everywhere.

4.1.2 Discretization of the Governing Equation

A second-order central Finite Difference Method is applied to discretize the radial derivatives. The first and second radial derivatives of pressure are given by:

$$\frac{\partial p}{\partial r} = \frac{p_{i+1} - p_{i-1}}{2\Delta r} + O(\Delta r^2) \tag{4.3}$$

$$\frac{\partial^2 p}{\partial r^2} = \frac{p_{i+1} - 2p_i + p_{i-1}}{\Delta r^2} + O(\Delta r^2) \tag{4.4}$$

Substituting $p(r)$ by p_i, r by r_i and equations 4.3 and 4.4, equation 4.1 is written as:

$$\begin{aligned} &p_i\lambda^3\left[M_{0_i}^3k^2 - M_{0_i}k^2\right] + p_i\lambda^2\left[-3k^2M_{0_i}^2 + k^2\right] + p_{i-1}\lambda^1\left[-\frac{M_{0i}}{r_i}\frac{1}{2\Delta r} + \frac{M_{0i}}{\Delta r^2} + \frac{\partial M_{0i}}{\partial r}\frac{1}{\Delta r}\right] + \\ &p_i\lambda^1\left[3M_{0_i}k^2 - M_{0_i}\frac{m^2}{r_i^2} - \frac{2M_{0i}}{\Delta r^2}\right] + p_{i+1}\lambda^1\left[\frac{M_{0i}}{r_i}\frac{1}{2\Delta r} + \frac{M_{0i}}{\Delta r^2} - \frac{1}{\Delta r}\frac{\partial M_{0i}}{\partial r}\right] + \\ &p_{i-1}\lambda^0\left[\frac{1}{2r_i}\frac{1}{\Delta r} - \frac{1}{\Delta r^2}\right] + p_i\lambda^0\left[-k^2 + \frac{m^2}{r_i^2} + \frac{2}{\Delta r^2}\right] + p_{i+1}\lambda^0\left[-\frac{1}{2r_i}\frac{1}{\Delta r} - \frac{1}{\Delta r^2}\right] = 0, \end{aligned} \tag{4.5}$$

Here the radial derivative of the mean flow Mach number is calculated by using a second-order forward a difference scheme at the inner boundary, a second order backward difference scheme in the outer boundary and central difference scheme at the remaining grid points.

4.1.3 Discretization of the Boundary Condition

The boundary condition given by equation 4.2 is rewritten in terms of the powers of λ for the inner (R_1) and outer (R_2) walls as

$$\left[\frac{\partial p}{\partial r}\right]_{R1} = \left[\frac{i\omega M_{0_i}^2}{zc_0}\right]\lambda^2 p(R_1) + \left[-\frac{2i\omega M_{0_i}}{zc_0}\right]\lambda p(R_1) + \left[\frac{i\omega}{zc_0}\right]p(R_1) \tag{4.6}$$

and

$$\left[\frac{\partial p}{\partial r}\right]_{R2} = \left[-\frac{i\omega M_{0_i}^2}{zc_0}\right]\lambda^2 p(R_2) + \left[\frac{2i\omega M_{0_i}}{zc_0}\right]\lambda p(R_2) + \left[-\frac{i\omega}{zc_0}\right]p(R_2). \tag{4.7}$$

Applying the Finite Difference method in Equations 4.6 and 4.7, $p(r)$ is written as p_1 or p_N and the first derivative of pressure for a second-order central difference scheme is written as equation 4.3 for $i = 1$ and $i = N$. As a consequence, equations 4.6 and 4.7 are writen in the discrete form as

$$\left[\frac{p_2 - p_0}{2\Delta r}\right]_{R1} = \left[\frac{i\omega M_{0_1}^2}{zc_0}\right]\lambda^2 p_1 + \left[-\frac{2i\omega M_{01}}{zc_0}\right]\lambda p_1 + \left[\frac{i\omega}{zc_0}\right]p_1 \tag{4.8}$$

and

$$\left[\frac{p_{N+1} - p_{N-1}}{2\Delta r}\right]_{R2} = \left[-\frac{i\omega M_{0_N}^2}{zc_0}\right]\lambda^2 p_N + \left[\frac{2i\omega M_{0N}}{zc_0}\right]\lambda p_i + \left[-\frac{i\omega}{zc_0}\right]p_N, \tag{4.9}$$

or, after some manipulation,

$$[p_0]_{R1} = \left[-2\Delta r\frac{i\omega M_{0_1}^2}{zc_0}\right]\lambda^2 p_1 + \left[\frac{4\Delta r i\omega M_{01}}{zc_0}\right]\lambda p_1 - 2\Delta r\left[\frac{i\omega}{zc_0}\right]p_1 + p_2 \tag{4.10}$$

$$[p_{N+1}]_{R2} = p_{N-1} + \left[-2\Delta r\frac{i\omega M_{0_N}^2}{zc_0}\right]\lambda^2 p_N + \left[\frac{4\Delta r i\omega M_{0N}}{zc_0}\right]\lambda p_N + \left[-2\Delta r\frac{i\omega}{zc_0}\right]p_N \tag{4.11}$$

Equations 4.10 and 4.11 are used to eliminate the dependence of pressure values at the ghost points when calculating the pressure values at the boundaries, as presented in the next subsection.

4.1.4 Incorporating the boundary conditions at $R = R_1$ and $R = R_2$

The discrete version of the field equation in the inner boundary is obtained by substituting $i = 1$ in the discretized governing equation given by Eq. 4.5

$$p_1\lambda^3\left[M_{01}^3k^2 - M_{01}k^2\right] + p_1\lambda^2\left[-3k^2M_{01}^2 + k^2\right] + p_0\lambda^1\left[-\frac{M_{01}}{r_0}\frac{1}{2\Delta r} + \frac{M_{01}}{\Delta r^2} + \frac{\partial M_{01}}{\partial r}\frac{1}{\Delta r}\right] + p_1\lambda^1\left[3M_{01}k^2 - M_{01}\frac{m^2}{r_0^2} - \frac{2M_{01}}{\Delta r^2}\right] + p_2\lambda^1\left[\frac{M_{01}}{r_0}\frac{1}{2\Delta r} + \frac{M_{01}}{\Delta r^2} - \frac{1}{\Delta r}\frac{\partial M_{01}}{\partial r}\right] + p_0\lambda^0\left[\frac{1}{2r_0}\frac{1}{\Delta r} - \frac{1}{\Delta r^2}\right] + p_0\lambda^0\left[-k^2 + \frac{m^2}{r_0^2} + \frac{2}{\Delta r^2}\right] + p_{+1}\lambda^0\left[-\frac{1}{2r_0}\frac{1}{\Delta r} - \frac{1}{\Delta r^2}\right] = 0 \quad (4.12)$$

When Equation 4.10 is substituted in Equation 4.12 to eliminate the variable p_0 at the ghost points, the following equation is obtained

$$\left\{M_{01}^3k^2 - M_{01}k^2 + \frac{i\omega M_{01}^3}{zc_0r_1} - 2\frac{i\omega M_{01}^3}{zc_0\Delta r} - 2\frac{iM_{01}^2k}{z}\frac{\partial M_{01}}{\partial r}\right\}\lambda^3p_1 + \left\{-3M_{01}^2k^2 + k^2 - 2\frac{M_{01}^2}{r_1}\frac{i\omega}{zc_0} + \frac{4M_{01}^2i\omega}{\Delta rzc_0} + \frac{4kiM_{01}^2}{z}\frac{\partial M_{01}}{\partial r} - \frac{1}{r_1}\frac{i\omega M_{01}^2}{zc_0} + 2\frac{1}{\Delta r}\frac{i\omega M_{01}^2}{zc_0}\right\}\lambda^2p_1 + \left\{\frac{i\omega M_{01}}{zc_0r_1} - 2\frac{i\omega M_{01}}{zc_0\Delta r} - 2\frac{ik}{z}\frac{\partial M_{01}}{\partial r} + 3M_{01}k^2 - M_{01}\frac{m^2}{r_1^2} - \frac{2M_{01}}{\Delta r^2} + \frac{2i\omega M_{01}}{r_1zc_0} - \frac{1}{\Delta r}\frac{4i\omega M_{01}}{zc_0}\right\}\lambda p_1 + \left\{-k^2 + \frac{m^2}{r_1^2} + \frac{2}{\Delta r^2} - \frac{i\omega}{r_1zc_0} + 2\frac{i\omega}{zc_0\Delta r}\right\}p_1 + \left\{\frac{2M_{01}}{\Delta r^2}\right\}\lambda p_2 - \left\{\frac{2}{\Delta r^2}\right\}p_2 = 0, \quad (4.13)$$

where the mean flow Mach number radial derivative is given by the forward scheme:

$$\frac{\partial M_{01}}{\partial r} = \left(\frac{-3M_1 + 4M_2 - M_3}{2\Delta r}\right). \quad (4.14)$$

In a similar way, the discretized equation to be solved in the outer boundary is obtained by substituting $i = N$ in the discretized governing equation given by Eq.4.5 together with the boundary condition in given by Eq. 4.11,which gives:

$$\left\{\left[M_{0_N}^3k^2-M_{0N}k^2-\frac{i\omega M_{0_N}^3}{zc_0r_N}-\frac{2i\omega M_{0_N}^3}{zc_0\Delta r}+\frac{2ikM_{0_N}^2}{z}\frac{\partial M_{0N}}{\partial r}\right]\right\}\lambda^3p_N+$$
$$+\left\{\left[-3M_{0_N}^2k^2+k^2+\frac{i\omega M_{0_N}^2}{zc_0r_N}+\frac{2i\omega M_{0_N}^2}{zc_0\Delta r}+\frac{2i\omega M_{0_N}^2}{zc_0r_N}+\frac{4i\omega M_{0_N}^2}{zc_0\Delta r}-\frac{4ikM_{0N}}{z}\frac{\partial M_{0N}}{\partial r}\right]\right\}\lambda^2p_N+$$
$$+\left\{p_N\left[-\frac{2i\omega M_{0N}}{zc_0r_N}-\frac{4i\omega M_{0N}}{zc_0\Delta r}+3M_{0N}k^2-M_{0N}\frac{m^2}{r_N^2}-\frac{2M_{0N}}{\Delta r^2}-\frac{i\omega M_{0N}}{zc_0r_N}-\frac{2i\omega M_{0N}}{zc_0\Delta r}+\frac{2ik}{z}\frac{\partial M_{0N}}{\partial r}\right]\right\}\lambda+$$
$$+\left\{p_{N-1}\left[\frac{2M_{0N}}{\Delta r^2}\right]\right\}\lambda$$
$$-\frac{2}{\Delta r^2}p_{N-1}+\left[-k^2+\frac{m^2}{r_N^2}+\frac{2}{\Delta r^2}+\frac{i\omega}{zc_0r_N}+\frac{2i\omega}{zc_0\Delta r}\right]p_N=0, \quad (4.15)$$

where the mean flow Mach number radial derivative is given by the backward scheme:

$$\frac{\partial M_{0N}}{\partial r}=\left(\frac{3M_N-4M_{N-1}+M_{N-2}}{2\Delta r}\right) \quad (4.16)$$

Equations 4.13 and 4.15 now replace Eq. 4.5 for $i=1$ and $i=N$

4.1.5 Solving the eigenvalue problem

The discrete eigenvalue problem is written as

$$\begin{bmatrix}D_{ij} & C_{ij} & B_{ij}\\ 0 & I & 0\\ 0 & 0 & I\end{bmatrix}\begin{bmatrix}q\\ \lambda q\\ \lambda^2 q\end{bmatrix}=\lambda\begin{bmatrix}0 & 0 & -A_{ij}\\ I & 0 & 0\\ 0 & I & 0\end{bmatrix}\begin{bmatrix}q\\ \lambda q\\ \lambda^2 q\end{bmatrix}, \quad (4.17)$$

where I is the identity matrix, q is the vector

$$q=\begin{bmatrix}p_1\\ .\\ .\\ .\\ p_N\end{bmatrix}, \quad (4.18)$$

the diagonal matrices A_{ij} and B_{ij} are written as

$$A_{ij}=\begin{bmatrix}a_{1,1} & . & . & . & . & . & . & . & .\\ . & a_{i,i} & . & . & . & . & . & . & .\\ . & . & . & . & . & & & & \\ & & . & a_{i,i} & . & . & & & \\ & & . & . & . & . & . & & \\ & & & . & . & . & a_{i,i} & . & \\ & & & . & . & . & . & a_{N,N} & \end{bmatrix}, \quad (4.19)$$

$$B_{ij} = \begin{bmatrix} b_{1,1} & . & . & . & . & . & . & . & . \\ & . & b_{i,i} & & . & . & . & . & . \\ & . & . & . & . & . & & & \\ & & & . & b_{i,i} & . & . & & \\ & & & . & . & . & . & . & \\ & & & & . & . & . & b_{i,i} & . \\ & & & & . & . & . & . & b_{N,N} \end{bmatrix}, \tag{4.20}$$

and the tridiagonal matrices C_{ij}, and D_{ij} are written as

$$C_{ij} = \begin{bmatrix} c_{1,1} & c_{1,2} & . & . & . & . & . & . & . \\ & c_{i,i-1} & c_{i,i} & c_{i,i+1} & . & . & . & . & . \\ & . & . & . & . & . & & & \\ & & & c_{i,i-1} & c_{i,i} & c_{i,i+1} & . & & \\ & & & . & . & . & . & . & \\ & & & & . & . & c_{i,i-1} & c_{i,i} & c_{i,i+1} \\ & & & & . & . & . & c_{N-1,N} & c_{N,N} \end{bmatrix}, \tag{4.21}$$

$$D_{ij} = \begin{bmatrix} d_{1,1} & d_{1,2} & . & . & . & . & . & . & . \\ & d_{i,i-1} & d_{i,i} & d_{i,i+1} & . & . & . & . & . \\ & . & . & . & . & . & & & \\ & & & d_{i,i-1} & d_{i,i} & d_{i,i+1} & . & & \\ & & & . & . & . & . & . & \\ & & & & . & . & d_{i,i-1} & d_{i,i} & d_{i,i+1} \\ & & & & . & . & . & d_{N-1,N} & d_{N,N} \end{bmatrix}. \tag{4.22}$$

and the elements of matrices A, B, C and D are given by

$$\begin{aligned} a_{1,1} &= M_{01}^3 k^2 - M_{01} k^2 + \frac{i\omega M_{01}^3}{z c_0 r_1} - 2\frac{i\omega M_{01}^3}{z c_0 \Delta r} - 2\frac{i M_{01}^2 k}{z}\frac{\partial M_{01}}{\partial r} \\ a_{i,i} &= M_{0i}^3 k^2 - M_{0i} k^2 \\ a_{N,N} &= M_{0N}^3 k^2 - M_{0N} k^2 - \frac{i\omega M_{0N}^3}{z c_0 r_N} - \frac{2i\omega M_{0N}^3}{z c_0 \Delta r} + \frac{2ikM_{0N}^2}{z}\frac{\partial M_{0N}}{\partial r}, \end{aligned} \tag{4.23}$$

$$\begin{aligned} b_{1,1} &= -3M_{01}^2 k^2 + k^2 - 2\frac{M_{01}^2}{r_1}\frac{i\omega}{z c_0} + \frac{4M_{01}^2 i\omega}{\Delta r z c_0} + \frac{4kiM_{01}^2}{z}\frac{\partial M_{01}}{\partial r} - \frac{1}{r_1}\frac{i\omega M_{01}^2}{z c_0} + 2\frac{1}{\Delta r}\frac{i\omega M_{01}^2}{z c_0} \\ b_{i,i} &= -3k^2 M_{0i}^2 + k^2 \\ b_{N,N} &= -3M_{0N}^2 k^2 + k^2 + \frac{i\omega M_{0N}^2}{z c_0 r_N} + \frac{2i\omega M_{0N}^2}{z c_0 \Delta r} + \frac{2i\omega M_{0N}^2}{z c_0 r_N} + \frac{4i\omega M_{0N}^2}{z c_0 \Delta r} - \frac{4ikM_{0N}}{z}\frac{\partial M_{0N}}{\partial r}, \end{aligned} \tag{4.24}$$

$$c_{1,1} = \frac{i\omega M_{01}}{zc_0 r_i} - 2\frac{i\omega M_{01}}{zc_0\Delta r} - 2\frac{ik}{z}\frac{\partial M_{01}}{\partial r} + 3M_{01}k^2 - M_{01}\frac{m^2}{r_i^2} - \frac{2M_{01}}{\Delta r^2} + \frac{2i\omega M_{01}}{r_i zc_0} - \frac{1}{\Delta r}\frac{4i\omega M_{01}}{zc_0} \tag{4.25}$$

$$c_{1,2} = \frac{2M_{01}}{\Delta r^2}$$

$$c_{i-1,i} = -\frac{M_{0i}}{r_i}\frac{1}{2\Delta r} + \frac{M_{0i}}{\Delta r^2} + \frac{\partial M_{0i}}{\partial r}\frac{1}{\Delta r}$$

$$c_{i,i} = 3M_{0i}k^2 - M_{0i}\frac{m^2}{r_i^2} - \frac{2M_{0i}}{\Delta r^2}$$

$$c_{i,i+1} = \frac{M_{0i}}{r_i}\frac{1}{2\Delta r} + \frac{M_{0i}}{\Delta r^2} - \frac{1}{\Delta r}\frac{\partial M_{0i}}{\partial r} \tag{4.26}$$

$$c_{N,N-1} = \frac{2M_{0N}}{\Delta r^2}$$

$$c_{N,N} = -\frac{2i\omega M_{0N}}{zc_0 r_N} - \frac{4i\omega M_{0N}}{zc_0\Delta r} + 3M_{0N}k^2 - M_{0N}\frac{m^2}{r_N^2} - \frac{2M_{0N}}{\Delta r^2} - \frac{i\omega M_{0N}}{zc_0 r_N} - \frac{2i\omega M_{0N}}{zc_0\Delta r} + \frac{2ik}{z}\frac{\partial M_{0N}}{\partial r},$$

and

$$d_{1,1} = -k^2 + \frac{m^2}{r_i^2} + \frac{2}{\Delta r^2} - \frac{i\omega}{r_i zc_0} + 2\frac{i\omega}{zc_0\Delta r} \tag{4.27}$$

$$d_{1,2} = \frac{2}{\Delta r^2}$$

$$d_{i-1,i} = \frac{1}{2r_i}\frac{1}{\Delta r} - \frac{1}{\Delta r^2}$$

$$d_{i,i} = -k^2 + \frac{m^2}{r_i^2} + \frac{2}{\Delta r^2}$$

$$d_{i,i+1} = -\frac{1}{2r_i}\frac{1}{\Delta r} - \frac{1}{\Delta r^2}$$

$$d_{N,N-1} = -\frac{2}{\Delta r^2}$$

$$d_{N,N} = -k^2 + \frac{m^2}{r_N^2} + \frac{2}{\Delta r^2} + \frac{i\omega}{zc_0 r_N} + \frac{2i\omega}{zc_0\Delta r}.$$

The discrete eigenvalue problem given by 4.18 is solved using the matlab function eig, which is based on a standard linear algebra library LAPACK, that uses the QZ algorithm [78]. There are two outputs. These are the wavenumber $\lambda = k_x/k$ (eigenvalue) and eigenvector q defined at the grid points .

The eigenvalues are firstly separated by direction of propagation. Eigenvalues with a positive imaginary part and negative real part correspond to modes propagating upstream. Eigenvalues with negative imaginary part and positive purely real eigenvalues refer to modes that propagate downstream. Eigenvalues corresponding to hydrodynamic modes, that is, with real part higher than $k/(M_0+1)$, in which M_0 is the averaged mean flow Mach number, are discarded.

4.2 Finite Difference formulation for mode propagation in Swirling Flows

When swirl is included the problem cannot be reduced to a single second-order equation as in the case described in section 4.1 and the full set of Linearized Euler Equations described have to be solved numerically. This numerical method is presented in this section. This methodology is unique in the sense that any mean flow profile can be used (as it is not restricted to the combination of rigid body and vortex swirl), there are no damping artefacts and the boundary condition is imposed in the velocity field, as detailed in sections 4.2.2, 4.2.3 and 5.3.

4.2.1 Governing Equations in the Matrix Form

Equations (3.139) to (3.142) are written as

$$[\mathbf{M}]\mathbf{x} = -ik\lambda\,[\mathbf{N}]\mathbf{x}, \tag{4.28}$$

where the vector x and the matrix operators M and N are given by

$$\mathbf{x} = \begin{bmatrix} p \\ u_r \\ u_\phi \\ u_x \end{bmatrix}, \tag{4.29}$$

$$\mathbf{M} = \begin{bmatrix} i\omega - c_0\frac{M_{0\phi}im}{r} & c_0^2\left(\frac{\rho_0 M_{0\phi}^2}{r} + \gamma p_o\left(\frac{\partial}{\partial r}+\frac{1}{r}\right)\right) & -\gamma\frac{p_0 mi}{r} & 0 \\ \frac{1}{\rho_0}\frac{\partial}{\partial r} - \frac{1}{\rho_0}\frac{M_{0\phi}^2}{r} & i\omega - c_0\frac{M_{0\phi}im}{r} & -2c_0\frac{M_{0\phi}}{r} & 0 \\ -\frac{im}{\rho_0 r} & c_0\frac{M_{0\phi}}{r} + c_0\frac{\partial M_{0\phi}}{\partial r} & i\omega - c_0\frac{imM_{0\phi}}{r} & 0 \\ 0 & c_0\frac{\partial M_{0x}}{\partial r} & 0 & i\omega - c_0\frac{imM_{0\phi}}{r} \end{bmatrix}, \tag{4.30}$$

and

$$\mathbf{N} = \begin{bmatrix} -c_0 M_{0x} & 0 & 0 & -\gamma p_0 \\ 0 & -c_0 M_{0x} & 0 & 0 \\ 0 & 0 & -c_0 M_{0x} & 0 \\ -\frac{1}{\rho_0} & 0 & 0 & -c_0 M_{0x} \end{bmatrix}. \tag{4.31}$$

4.2.2 Applying the Boundary Condition

In the inner and outer walls, the momentum equation in the radial direction is replaced by the Ingard-Myers boundary condition given by equation (3.145). This is implemented by replacing the second line of matrix operators M and N corresponding to the radial momentum equation by the

boundary condition given by Eq.(3.145), which gives

$$\mathbf{M_{inner}} = \begin{bmatrix} i\omega - c_0\frac{M_{0\phi}im}{r} & c_0^2\left(\frac{\rho_0 M_{0\phi}^2}{r} + \gamma p_o\left(\frac{\partial}{\partial r}+\frac{1}{r}\right)\right) & -\gamma\frac{p_0 mi}{r} & 0 \\ -i\omega + c_0\frac{M_{0\phi}im}{r} & -i\omega z & 0 & 0 \\ -\frac{im}{\rho_0 r} & c_0\frac{M_{0\phi}}{r} + c_0\frac{\partial M_{0\phi}}{\partial r} & i\omega - c_0\frac{imM_{0\phi}}{r} & 0 \\ 0 & c_0\frac{\partial M_{0x}}{\partial r} & 0 & i\omega - c_0\frac{imM_{0\phi}}{r} \end{bmatrix}, \quad (4.32)$$

and

$$\mathbf{N_{inner}} = \begin{bmatrix} -c_0 M_{0x} & 0 & 0 & -\gamma p_0 \\ -c_0 M_{0x} & 0 & 0 & 0 \\ 0 & 0 & -c_0 M_{0x} & 0 \\ -\frac{1}{\rho_0} & 0 & 0 & -c_0 M_{0x} \end{bmatrix} \quad (4.33)$$

for the inner boundary. The same procedure for the outer boundary gives

$$\mathbf{M_{outer}} = \begin{bmatrix} i\omega - c_0\frac{M_{0\phi}im}{r} & c_0^2\left(\frac{\rho_0 M_{0\phi}^2}{r} + \gamma p_o\left(\frac{\partial}{\partial r}+\frac{1}{r}\right)\right) & -\gamma\frac{p_0 mi}{r} & 0 \\ -i\omega + c_0\frac{M_{0\phi}im}{r} & i\omega z & 0 & 0 \\ -\frac{im}{\rho_0 r} & c_0\frac{M_{0\phi}}{r} + c_0\frac{\partial M_{0\phi}}{\partial r} & i\omega - c_0\frac{imM_{0\phi}}{r} & 0 \\ 0 & c_0\frac{\partial M_{0x}}{\partial r} & 0 & i\omega - c_0\frac{imM_{0\phi}}{r} \end{bmatrix}, \quad (4.34)$$

and

$$\mathbf{N_{outer}} = \begin{bmatrix} -c_0 M_{0x} & 0 & 0 & -\gamma p_0 \\ c_0 M_{0x} & 0 & 0 & 0 \\ 0 & 0 & -c_0 M_{0x} & 0 \\ -\frac{1}{\rho_0} & 0 & 0 & -c_0 M_{0x} \end{bmatrix}. \quad (4.35)$$

4.2.3 The Particular Case of the Hard-Walled Boundary Condition

As presented in the previous section, the Ingard-Myers boundary condition is imposed by replacing the momentum equation in the radial direction in the inner and outer walls by equation (3.145). The hard-walled boundary condition is a particular case of the Ingard-Myers boundary condition in which the impedance of the wall tends to infinity.

So far, it was observed in the bibliographic review that the hard-walled boundary condition has been implemented by other authors in the velocity field in two different ways. The first option is to implemented the boundary condition by replacing the second line of matrix operators M_{inner}, N_{inner}, M_{outer} and N_{outer} by the equation $u_r = 0$ and to make all elements of the columns of matrix operators M and N that correspond to u_r in the inner and outer wall equal to zero. This gives

$$\mathbf{M_{inner}} = \begin{bmatrix} i\omega - c_0\frac{M_{0\phi}im}{r} & 0 & -\gamma\frac{p_0 mi}{r} & 0 \\ 0 & 1 & 0 & 0 \\ -\frac{im}{\rho_0 r} & 0 & i\omega - c_0\frac{imM_{0\phi}}{r} & 0 \\ 0 & 0 & 0 & i\omega - c_0\frac{imM_{0\phi}}{r} \end{bmatrix}, \quad (4.36)$$

and

$$\mathbf{N_{inner}} = \begin{bmatrix} -c_0 M_{0_x} & 0 & 0 & -\gamma p_0 \\ 0 & 0 & 0 & 0 \\ 0 & 0 & -c_0 M_{0_x} & 0 \\ -\frac{1}{\rho_0} & 0 & 0 & -c_0 M_{0_x} \end{bmatrix}, \tag{4.37}$$

for the inner boundary and

$$\mathbf{M_{outer}} = \begin{bmatrix} i\omega - c_0 \frac{M_{0\phi} im}{r} & 0 & -\gamma \frac{p_0 mi}{r} & 0 \\ 0 & 1 & 0 & 0 \\ -\frac{im}{\rho_0 r} & 0 & i\omega - c_0 \frac{imM_{0\phi}}{r} & 0 \\ 0 & 0 & 0 & i\omega - c_0 \frac{imM_{0\phi}}{r} \end{bmatrix}, \tag{4.38}$$

and

$$\mathbf{N_{outer}} = \begin{bmatrix} -c_0 M_{0_x} & 0 & 0 & -\gamma p_0 \\ 0 & 0 & 0 & 0 \\ 0 & 0 & -c_0 M_{0_x} & 0 \\ -\frac{1}{\rho_0} & 0 & 0 & -c_0 M_{0_x} \end{bmatrix}, \tag{4.39}$$

for the outer boundary.

The second option would be to remove the second line and second column of M_{inner} and N_{inner} and the second line and second column of M_{outer} and N_{outer} completely. The second line of both matrices correspond to the impedance boundary condition and the second column of matrices correspond to the variable u_r.

The downside of implementing the boundary condition in the velocity field is the fact that no restriction is imposed in the pressure field. The radial pressure derivative is zero for axial flows, but this is not true when swirl is considered. The imposition of the boundary condition in the pressure field does not considers this physics. Although this implementation was tested in the current code (because its use is so common in the literature), it was verifyed that this implementation can lead to unstable codes or even to spurious results.

In the current code a different way to impose the boundary condition is proposed. The boundary-condition is implemented in the pressure instead of in the velocity by making $u_r = 0$ in Equation 3.152 for in the inner and outer wall and implementing the remaining terms of this equation in the second line of matrices M_{inner}, N_{inner},M_{outer} and N_{outer}. This gives

$$\mathbf{M_{inner}} = \begin{bmatrix} i\omega - c_0 \frac{M_{0\phi} im}{r} & c_0^2 \gamma p_o \frac{\partial}{\partial r} & -\gamma \frac{p_0 mi}{r} & 0 \\ -i\omega + c_0 \frac{M_{0\phi} im}{r} & 0 & 0 & 0 \\ -\frac{im}{\rho_0 r} & 0 & i\omega - c_0 \frac{imM_{0\phi}}{r} & 0 \\ 0 & 0 & 0 & i\omega - c_0 \frac{imM_{0\phi}}{r} \end{bmatrix}, \tag{4.40}$$

and

$$\mathbf{N_{inner}} = \begin{bmatrix} -c_0 M_{0x} & 0 & 0 & -\gamma p_0 \\ -c_0 M_{0x} & 0 & 0 & 0 \\ 0 & 0 & -c_0 M_{0x} & 0 \\ -\frac{1}{\rho_0} & 0 & 0 & -c_0 M_{0x} \end{bmatrix}, \tag{4.41}$$

for the inner boundary and

$$\mathbf{M_{outer}} = \begin{bmatrix} i\omega - c_0 \frac{M_{0\phi} im}{r} & c_0^2 \gamma p_o \frac{\partial}{\partial r} & -\gamma \frac{p_0 mi}{r} & 0 \\ -i\omega + c_0 \frac{M_{0\phi} im}{r} & 0 & 0 & 0 \\ -\frac{im}{\rho_0 r} & 0 & i\omega - c_0 \frac{imM_{0\phi}}{r} & 0 \\ 0 & 0 & 0 & i\omega - c_0 \frac{imM_{0\phi}}{r} \end{bmatrix}, \tag{4.42}$$

and

$$\mathbf{N_{outer}} = \begin{bmatrix} -c_0 M_{0x} & 0 & 0 & -\gamma p_0 \\ c_0 M_{0x} & 0 & 0 & 0 \\ 0 & 0 & -c_0 M_{0x} & 0 \\ -\frac{1}{\rho_0} & 0 & 0 & -c_0 M_{0x} \end{bmatrix}, \tag{4.43}$$

for the outer boundary.

If the boundary condition is implemented in this way, the expression for the pressure derivative at the wall is kept. This is something important because when swirl is included the pressure derivative at the wall is no longer zero. The implementation of the boundary condition in the pressure field is one of the novelties of this work.For now the radial derivatives remain in the continuous form. The discretization process is presented in the next subsection.

4.2.4 Discretization Process and Numerical Solution

Because this eigenvalue problem is more complex than the previous one, the eigenvelue problem is discretized using a central fourth-order Finite Difference scheme instead of a second-order one. To approximate radial derivatives, the derivative matrix proposed by Kousen [42] and given by 4.44 is used. This uses a central difference template at the inner part and a forward and backward templates at points in the inner and outter boundaries. For an arbitrary discretized function $f_j = f(r_j)$, the

derivative matrix is described as [42]

$$\frac{\partial f_j}{\partial r} = \left[\frac{1}{12\Delta r}\right] \begin{bmatrix} \text{-25} & \text{+48} & \text{-36} & \text{+16} & \text{-3} & . & . & . & . \\ \text{-3} & \text{-10} & \text{+18} & \text{-6} & \text{+1} & . & . & . & . \\ \text{+1} & \text{-8} & 0 & \text{+8} & \text{-1} & . & . & . & . \\ & . & . & . & . & . & & & \\ & & \text{+1} & \text{-8} & 0 & \text{+8} & \text{-1} & & \\ & & & . & . & . & . & . & \\ & & & & \text{+1} & \text{-8} & 0 & \text{+8} & \text{-1} \\ & & & & \text{-1} & \text{+6} & \text{-18} & \text{+10} & \text{+3} \\ & & & & \text{+3} & \text{-16} & \text{+36} & \text{-48} & \text{+25} \end{bmatrix} f(r_j). \tag{4.44}$$

The arbitrary discretized function $f_j = f(r_j)$ may represent pressure or any velocity component.

The computational grid is very similar to the one used in the previous case for the code based on the Pridmore-Brown equation presented in Figure 4.1. It is a one-dimensional axysimetric uniform cartesian grid discretized from the inner radius to the outer radius. The only difference is that no ghost points are used in this case. There is no grid refinement in the boundaries and a high resolution is used. For the results shown in this report, 100 elements were used between the inner and outer radius.

To solve the problem numerically, equation (4.28) is written as

$$(-i[\mathbf{N}])\,\mathbf{x} = c_p \left(\frac{1}{\omega}[\mathbf{M}]\right)\mathbf{x}, \tag{4.45}$$

where c_p is the mode phase speed. The eigenvectors and eigenvalues are calculated using the linear algebra library LAPACK, that uses the QZ algorithm [42]. The axial wavenumbers $k_x = k\lambda$ are calculated by:

$$k_x = \frac{\omega}{c_p} \tag{4.46}$$

4.2.5 Filtering Process

A subset of the modes obtained is not well resolved and should be filtered. Those modes are purelly numerical and dominated by point-to point oscillations. A selective filter developed by Tam [79] retains only shorter wavelength components and uses a 15-point stencil DRP scheme to separate physical modes from numerical ones. The filtered solution is calculated as

$$\widetilde{p}(r_n) = \sum_{i=-7}^{+7} a_i p(r_{n+i}) \tag{4.47}$$

where a_i are the filter coefficients given by

$$\begin{aligned} a_{-7} &= -9.0091603462069583e-05 \\ a_{-6} &= 1.1117554451990776e-03 \\ a_{-5} &= -6.5519987489327603e-03 \\ a_{-4} &= 2.4341225689340974e-02 \\ a_{-3} &= -6.3456279827554890e-02 \\ a_{-2} &= 0.1224349282118140 \\ a_{-1} &= -0.1799016298200503 \\ a_0 &= 0.2042241813072920 \\ a_{+2} &= 0.1224349282118140 \\ a_{+1} &= -0.1799016298200503 \\ a_{+3} &= -6.3456279827554890e-02 \\ a_{+4} &= 2.4341225689340974e-02 \\ a_{+5} &= -6.5519987489327603e-03 \\ a_{+6} &= 1.1117554451990776e-03 \\ a_{+7} &= -9.0091603462069583e-05 \end{aligned} \tag{4.48}$$

and p is the pressure eigenvector. If the mode is well resolved, the filtered eigenvector $\widetilde{p}$ is much smaller than p. Otherwise, if the mode is dominated by point-to-point oscillations $\widetilde{p}$ will be of the similar order of $p(r)$. The filtered results are compared with the original results as:

$$\alpha = \frac{\| \widetilde{p}(r) \|}{\| p(r) \|}, \tag{4.49}$$

where the norms above are given by

$$\| f \|^2 = \frac{1}{2} \sum_{n=1}^{N-1} (r_{n+1} - r_n)[r_n f(r_n)^2 + r_{n+1} f(r_n + 1)^2]. \tag{4.50}$$

Since the filter uses a 15-point stencil, the seven first values of $\widetilde{p}(r_n)$ are set to zero. Filtered modes are organized as α increases and only a subset of those modes are considered. In the current work, axial modes correspondent to values of α smaller that 10^{-6} are kept. This value of α was based on experience. By running several simulations, 10^{-6} proved to be a good number.

Because convective modes are highly oscillating, this filtering process also removes these modes. Nearly convective modes are kept because its pressure eigenvector is well behaved.

Chapter 5

Validation of the Numerical Schemes

This chapter presents the validation of the two codes introduced in the previous chapter. Section 5.1 presents the validation of the first code, which is based on the Pridmore-Brown Equation. This code was an intermediate step of the research and in a later stage results from this code were used to validate the second code. Results from the Pridmore-Brown code were compared to numerical results from another finite difference code and a shooting method code. Results from the current code were also compared with analytical results when possible.

Section 5.2 presents the validation of the second code, which is based on the Linearized Euler Equations. This code named SwirlProp is more complex than the first one and involves the solutions of a set of four equations instead of a single equation as it was the case of the Pridmore-Brown code. Firstly, the code was validated against analytical results for the uniform flow without swirl. Secondly, results were compared to results from the Pridmore-Brown code for the case of uniform flow with lined walls and for the case of shear flow with hard-walls, both withou swirl. Finally, results from the second code were compared with numerical results from different methods.

For the validation cases that follow, notice that the reduced frequency and the Helmholtz number will always have the same value, since the Helmholtz number is calculated based on the outer radius as $He = k \times R_{out}$, where k is the reduced frequency and the outer radius is equal to 1m in all cases.

An original feature of the SwirlProp code is the way of the boundary condition is imposed. The implementation is presented in the previous chapter and details of the tests of different boundary conditions are presented in section 5.3

5.1 Validation of the Pridmore-Brown Code

The Finite Difference Pridmore-Brown code developed in this work was validated by comparison with results obtained by another Finite Difference code and a shooting method code. For the uniform flow case, results are also compared with the analytic solution. As a strategy to validate the code calculations for no-flow, uniform flow and sheared flow were carried out in this sequence. The geometry considered is an annular duct with outer radius 1 and inner radius 0.3. For all of them, calculations with and without liners were carried out. The parameters used are Helmholtz number 10 and mode orders $m = 0$ and $m = +5$. For uniform flows, the Mach numbers are 0 and 0.5. For the

lined wall case the impedance is $z = 0.4 + 0.2i$. For each case, the axial wavenumbers are plotted in the complex plane.

Figure 5.1 shows the natural logarithm of the error against the natural logarithm of the number of the radial points for the case of uniform axial flow ($M = 0.5$) and mode order $m = 5$.The error is calculated based on the difference between the calculated axial wavenumber and the analytical solution. The first axial wavenumber is used. Based on this convergence study, it is considered that 100 elements are sufficient to give accurate results.

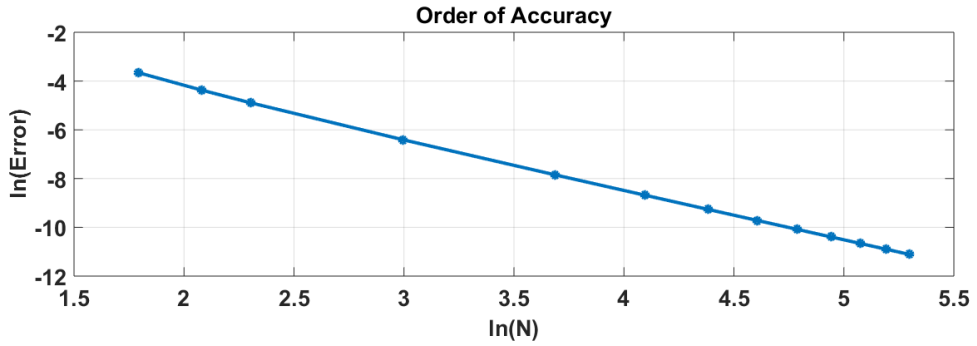

Fig. 5.1 – Order of accuracy for M=0.5 and mode m=5.

5.1.1 Code Verification: Uniform Axial Flow

First, results will be presented for sound propagation in the absence of flow for modes m=0 and m=5. Figure 5.2 shows the comparison between the the axial wavenumber spectrum calculated using the analytic solution [76] and the current finite difference code for mode m=0 for the no flow case. The first 20 axial wavenumbers are presented. Real axial wavenumbers correspond to propagating acoustic modes, while purely imaginary modes wavenumbers correspond to cut-off modes. If the imaginary part of the axial wavenumber is positive, the mode decays in the negative direction and propagates in the left direction. If the immaginary part of the axial wavenumber is negative, the mode decays in the positive direction and propagates to the right. There is an excellent agreement between the two sets of results.

Figure 5.3 show the comparison between predictions from the current FD code and the analytic solution for for mode $m = +5$ for the first 20 wavenumbers, also for the no flow case. Axial wavenumbers -7.6715 and $+7.6715$ correspond to propagating acoustic modes. The remaining purely imaginary wavenumbers correspond to cut-off modes. Results are in agreement.

In the next stage, simulations for uniform flow were carried out for Mach=0.5 and modes m=0 and m=+5. The axial wavenumber spectrum for each case is shown in figures 5.4 to 5.11. Only acoustic wavenumbers are presented in the figures. However, when a uniform flow is considered, a hydrodynamic axial wavenumber defined as ω/c_0M_0 appears in the spectrum. In this study this wavenumber is equal to 20. The axial wavenumbers of the sound propagation in a hard-walled annular duct with uniform flow for mode $m = 0$ are shown in figure 5.4, in which the comparison between predictions of the Finite Difference code and the analytic solution is presented. The cut-offline is shifted because of the convective effect of the flow. The six real axial wavenumbers refer

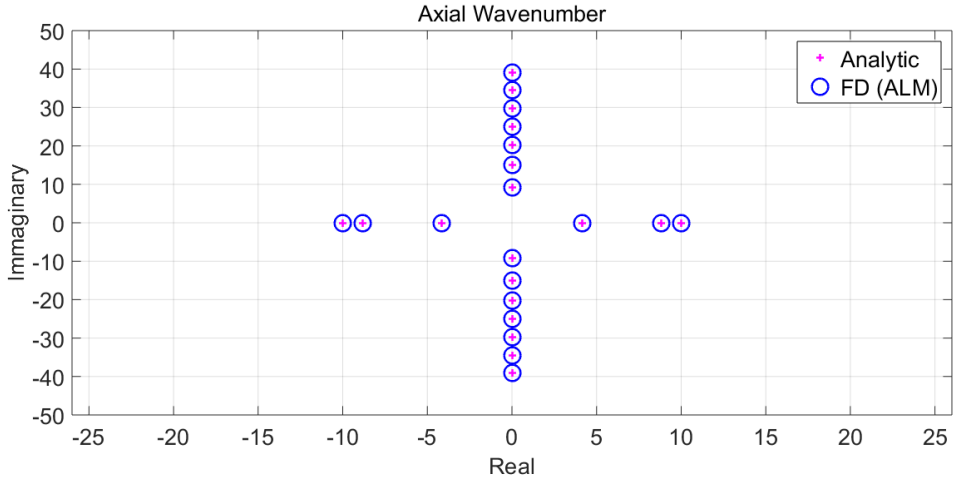

Fig. 5.2 – Axial wavenumber spectrum for the no-flow case. Comparison with the analytic solution. Blue circles refer to results obtained with the code developed in this work and purple crosses refer to the analytic solution. Mach=0, m=0, He=10

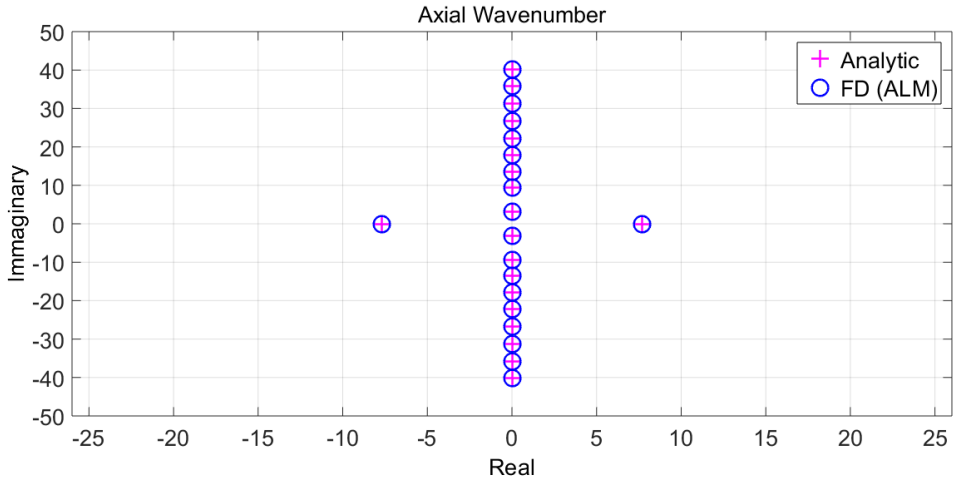

Fig. 5.3 – Axial wavenumber spectrum for the no-flow case. Comparison with the analytic solution. Blue circles refer to results obtained with the code developed in this work and purple crosses refer to the analytic solution. Mach=0, m=+5, He=10

to propagating modes and are symmetric in relation to the imaginary axis.

Similarly, the comparison between axial wavenumbers from predictions and the analytic solution for the sound propagation in a hard-walled annular duct with uniform flow for mode $m = +5$ is shown in figure 5.5. When the mean flow is included there are four propagating modes instead of two as it was the case when there was no flow. The propagating modes are symmetric in relation to the imaginary axis. Following the same pattern, the cut-off line is also shifted.

Results for uniform flow and lined walls are presented in figures 5.6 to 5.11. Figures 5.6 to 5.8 show results for mode $m = 0$ for each of the three following cases, respectively: (i) when the inner wall is hard and the outer wall is lined, (ii) when the inner wall is lined and the outer wall is hard and (iii) when both walls are lined. All modes are now attenuated. The higher the imaginary part of the axial wavenumber, the more attenuated the mode is. If the imaginary part of the axial wavenumber is positive, the mode decays and propagates in the negative x-direction. If the imaginary part of

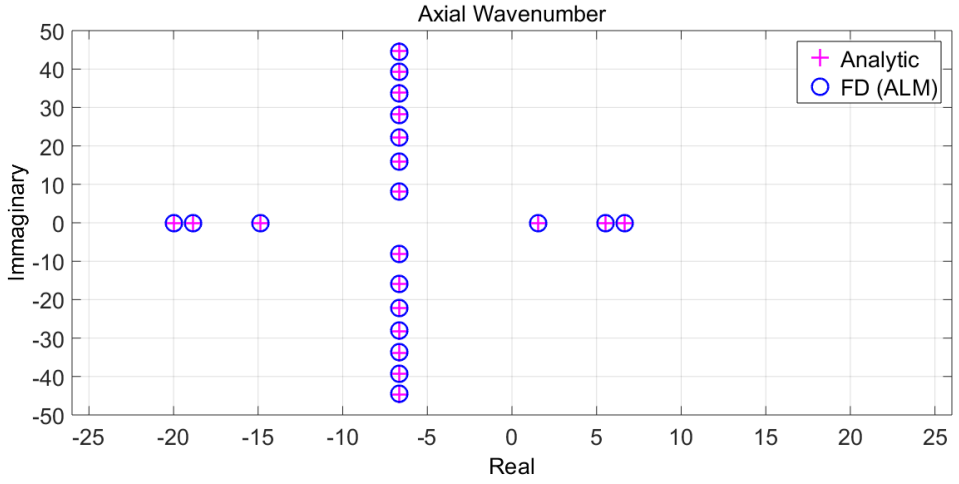

Fig. 5.4 – Axial wavenumber for the uniform flow case. Comparison with the analytic solution. Blue circles refer to results obtained with the code developed in this work and purple crosses refer to the analytic solution. Mach=0.5, m=0, He=10

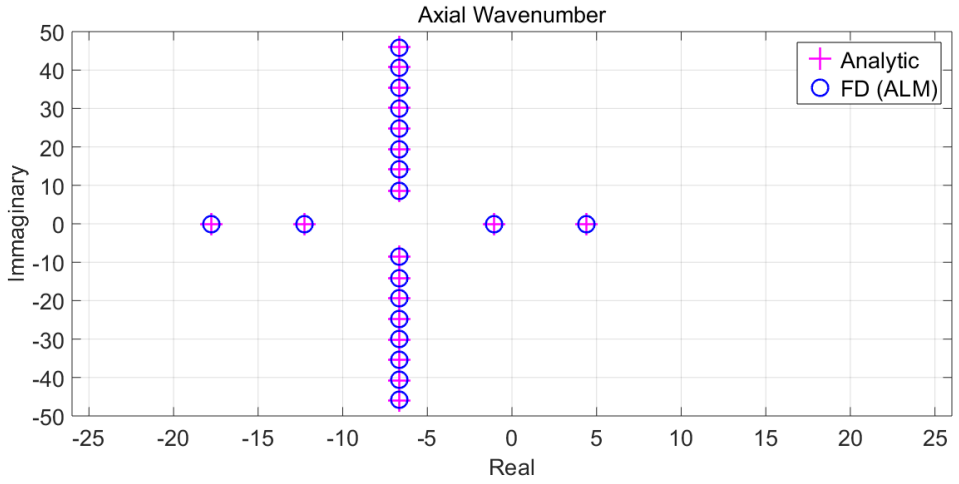

Fig. 5.5 – Axial wavenumber for the uniform flow case. Comparison with the analytic solution. Blue circles refer to results obtained with the code developed in this work and purple crosses refer to the analytic solution. Mach=0.5, m=+5, He=10

the axial wavenumber is negative, the mode decays and propagates in the positive x-direction. The modes are more attenuated for $m = +5$ than for $m = 0$.

When liners are included, analytic solutions are no longer readily available and comparisons are made between the current Finite Difference code and two other methodologies, i.e. a different Finite difference code and a shooting method code [39]. For each case, a plot showing the comparison is presented as well as the correspondent tabulated results. The three sets of results are in very good agreement for the cases where only the outer wall is lined or both walls are lined. The result of both Finite Difference codes is not in such a good agreement with the shooting method code for modes propagating against the flow in the case where only the inner wall is lined.

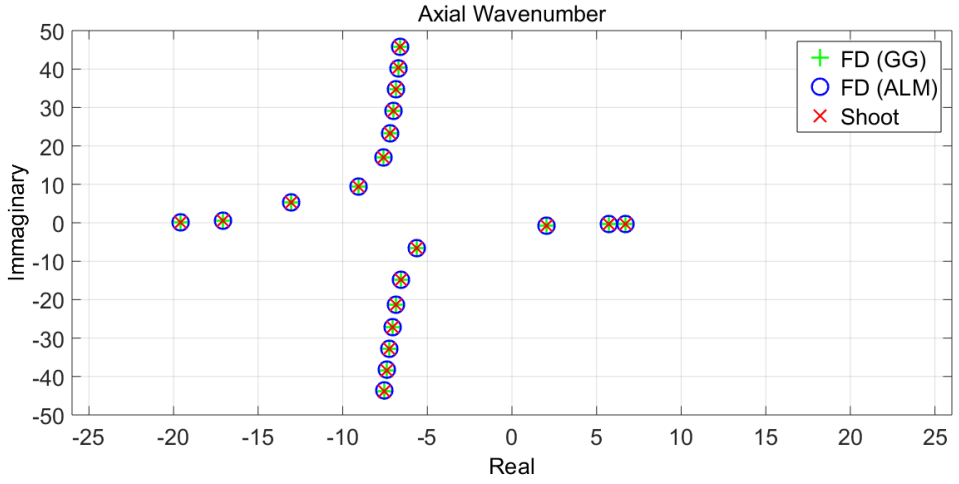

Fig. 5.6 – Axial wavenumber spectrum for the uniform flow case with lined outer wall. Comparison between results of two different Finite Difference codes and a shooting method code. Blue circles refer to results obtained with the code developed in this work - FD (ALM)-, green crosses refer to results provided by Dr. Gabbard- FD (GG) and red crosses refer to results from the shooting method code. Mach=0.5, m=0, He=10

Comparison between axial wavenumbers for Mach=0.5, m=0 and lined outer wall.		
GG	ALM	Shoot
6.6951e+00 - 2.6288e-01i	6.6951e+00 - 2.6288e-01i	6.6951e+00 - 2.6288e-01i
5.7067e+00 - 3.0304e-01i	5.7068e+00 - 3.0302e-01i	5.7067e+00 - 3.0304e-01i
2.0176e+00 - 6.7441e-01i	2.0199e+00 - 6.7405e-01i	2.0176e+00 - 6.7442e-01i
-5.6245e+00 - 6.5890e+00i	-5.6218e+00 - 6.5761e+00i	-5.6245e+00 - 6.5891e+00i
-6.5782e+00 - 1.4819e+01i	-6.5772e+00 - 1.4800e+01i	-6.5782e+00 - 1.4819e+01i
-6.8688e+00 - 2.1267e+01i	-6.8671e+00 - 2.1235e+01i	-6.8687e+00 - 2.1267e+01i
-7.0653e+00 - 2.7179e+01i	-7.0625e+00 - 2.7125e+01i	-7.0650e+00 - 2.7178e+01i
-7.2310e+00 - 3.2838e+01i	-7.2267e+00 - 3.2755e+01i	-7.2307e+00 - 3.2836e+01i
-7.3855e+00 - 3.8352e+01i	-7.3785e+00 - 3.8231e+01i	-7.3846e+00 - 3.8350e+01i
-7.5352e+00 - 4.3773e+01i	-7.5257e+00 - 4.3599e+01i	-7.5348e+00 - 4.3767e+01i
-1.9583e+01 + 5.6599e-02i	-1.9583e+01 + 5.6587e-02i	-1.9583e+01 + 5.6599e-02i
-1.7056e+01 + 5.8304e-01i	-1.7057e+01 + 5.8234e-01i	-1.7056e+01 + 5.8306e-01i
-1.3041e+01 + 5.2578e+00i	-1.3034e+01 + 5.2562e+00i	-1.3041e+01 + 5.2579e+00i
-9.0811e+00 + 9.3579e+00i	-9.0861e+00 + 9.3493e+00i	-9.0810e+00 + 9.3580e+00i
-7.6052e+00 + 1.6952e+01i	-7.6061e+00 + 1.6934e+01i	-7.6051e+00 + 1.6952e+01i
-7.2052e+00 + 2.3277e+01i	-7.2056e+00 + 2.3244e+01i	-7.2049e+00 + 2.3277e+01i
-6.9858e+00 + 2.9160e+01i	-6.9865e+00 + 2.9106e+01i	-6.9857e+00 + 2.9159e+01i
-6.8345e+00 + 3.4832e+01i	-6.8354e+00 + 3.4747e+01i	-6.8342e+00 + 3.4830e+01i
-6.7174e+00 + 4.0384e+01i	-6.7192e+00 + 4.0258e+01i	-6.7171e+00 + 4.0380e+01i
-6.6214e+00 + 4.5861e+01i	-6.6244e+00 + 4.5684e+01i	-6.6213e+00 + 4.5855e+01i

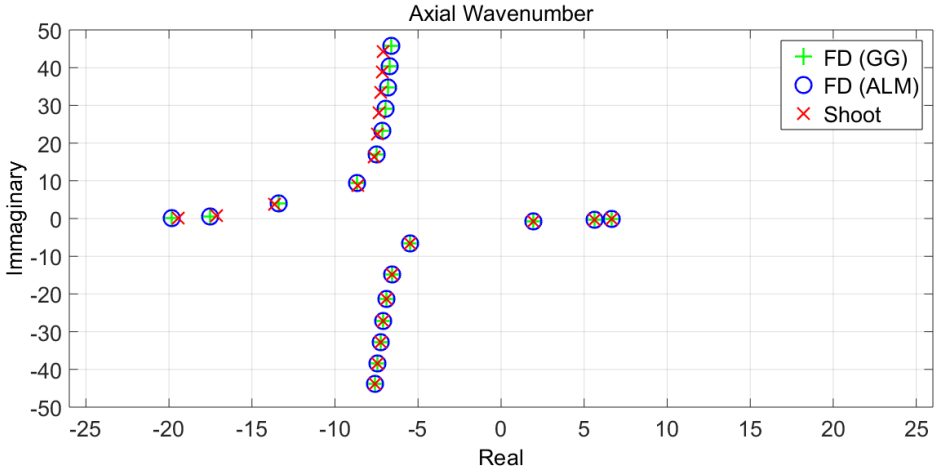

Fig. 5.7 – Axial wavenumber for the uniform flow case with lined inner wall. Comparison between results of two different Finite Difference codes and a shooting method code. Blue circles refer to results obtained with the code developed in this work - FD (ALM)-, green crosses refer to results provided by Dr. Gabbard - FD (GG)- and red crosses refer to results from the shooting method code. Mach=0.5, m=0, He=10

Comparison between axial wavenumbers for Mach=0.5, m=0, He=10 and lined inner wall		
GG	ALM	Shoot
6.6728e+00 - 7.4441e-02i	6.6728e+00 - 7.4439e-02i	6.6728e+00 - 7.4441e-02i
5.6337e+00 - 3.1153e-01i	5.6337e+00 - 3.1152e-01i	5.6337e+00 - 3.1153e-01i
1.9654e+00 - 7.1867e-01i	1.9660e+00 - 7.1855e-01i	1.9654e+00 - 7.1868e-01i
-5.4726e+00 - 6.5677e+00i	-5.4719e+00 - 6.5647e+00i	-5.4726e+00 - 6.5678e+00i
-6.5644e+00 - 1.4759e+01i	-6.5641e+00 - 1.4754e+01i	-6.5643e+00 - 1.4759e+01i
-6.8851e+00 - 2.1223e+01i	-6.8846e+00 - 2.1215e+01i	-6.8850e+00 - 2.1223e+01i
-7.0944e+00 - 2.7147e+01i	-7.0935e+00 - 2.7133e+01i	-7.0942e+00 - 2.7146e+01i
-7.2682e+00 - 3.2814e+01i	-7.2668e+00 - 3.2793e+01i	-7.2680e+00 - 3.2813e+01i
-7.4294e+00 - 3.8335e+01i	-7.4268e+00 - 3.8303e+01i	-7.4286e+00 - 3.8332e+01i
-7.5862e+00 - 4.3760e+01i	-7.5830e+00 - 4.3713e+01i	-7.5856e+00 - 4.3754e+01i
-1.9836e+01 + 3.8684e-02i	-1.9836e+01 + 3.8687e-02i	-1.9460e+01 + 8.4248e-02i
-1.7515e+01 + 5.7360e-01i	-1.7515e+01 + 5.7352e-01i	-1.7148e+01 + 6.6441e-01i
-1.3417e+01 + 4.0190e+00i	-1.3416e+01 + 4.0192e+00i	-1.3621e+01 + 3.8046e+00i
-8.6822e+00 + 9.3604e+00i	-8.6832e+00 + 9.3580e+00i	-8.6195e+00 + 8.8578e+00i
-7.5108e+00 + 1.6912e+01i	-7.5110e+00 + 1.6907e+01i	-7.6543e+00 + 1.6270e+01i
-7.1624e+00 + 2.3234e+01i	-7.1626e+00 + 2.3225e+01i	-7.4418e+00 + 2.2375e+01i
-6.9648e+00 + 2.9119e+01i	-6.9649e+00 + 2.9105e+01i	-7.3330e+00 + 2.8050e+01i
-6.8251e+00 + 3.4793e+01i	-6.8251e+00 + 3.4771e+01i	-7.2456e+00 + 3.3542e+01i
-6.7152e+00 + 4.0347e+01i	-6.7155e+00 + 4.0314e+01i	-7.1649e+00 + 3.8955e+01i
-6.6242e+00 + 4.5827e+01i	-6.6248e+00 + 4.5778e+01i	-7.0917e+00 + 4.4330e+01i

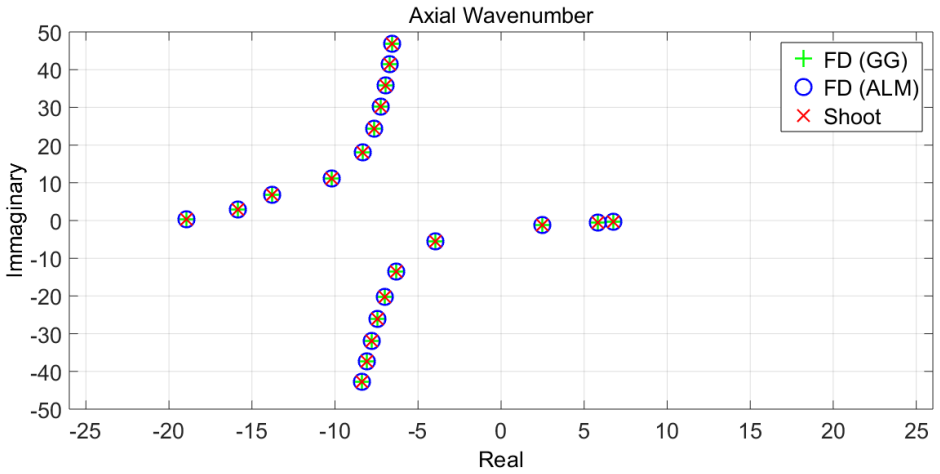

Fig. 5.8 – Axial wavenumber for the uniform flow case with both walls lined . Comparison between results of two different Finite Difference codes and a shooting method code. Blue circles refer to results obtained with the code developed in this work - FD (ALM)-, green crosses refer to results provided by Dr. Gabbard - FD (GG)- and red crosses refer to results from the shooting method code. Mach=0.5, m=0, He=10

Comparison between axial wavenumbers for Mach=0.5, m=0 and both walls lined.		
GG	ALM	Shoot
6.7511e+00 - 3.0064e-01i	6.7511e+00 - 3.0063e-01i	6.7511e+00 - 3.0064e-01i
5.8131e+00 - 6.0184e-01i	5.8131e+00 - 6.0182e-01i	5.8131e+00 - 6.0184e-01i
2.4679e+00 - 1.2387e+00i	2.4684e+00 - 1.2386e+00i	2.4679e+00 - 1.2387e+00i
-3.9659e+00 - 5.5848e+00i	-3.9646e+00 - 5.5823e+00i	-3.9659e+00 - 5.5849e+00i
-6.3182e+00 - 1.3587e+01i	-6.3176e+00 - 1.3583e+01i	-6.3181e+00 - 1.3588e+01i
-7.0035e+00 - 2.0167e+01i	-7.0026e+00 - 2.0159e+01i	-7.0034e+00 - 2.0167e+01i
-7.4293e+00 - 2.6143e+01i	-7.4277e+00 - 2.6129e+01i	-7.4290e+00 - 2.6142e+01i
-7.7741e+00 - 3.1830e+01i	-7.7717e+00 - 3.1809e+01i	-7.7739e+00 - 3.1829e+01i
-8.0875e+00 - 3.7349e+01i	-8.0837e+00 - 3.7317e+01i	-8.0870e+00 - 3.7347e+01i
-8.3895e+00 - 4.2755e+01i	-8.3831e+00 - 4.2708e+01i	-8.3880e+00 - 4.2750e+01i
-1.8927e+01 + 4.1412e-01i	-1.8927e+01 + 4.1411e-01i	-1.8927e+01 + 4.1413e-01i
-1.5859e+01 + 2.8858e+00i	-1.5858e+01 + 2.8856e+00i	-1.5858e+01 + 2.8859e+00i
-1.3810e+01 + 6.7430e+00i	-1.3810e+01 + 6.7433e+00i	-1.3810e+01 + 6.7430e+00i
-1.0222e+01 + 1.1178e+01i	-1.0223e+01 + 1.1176e+01i	-1.0222e+01 + 1.1178e+01i
-8.3191e+00 + 1.8019e+01i	-8.3194e+00 + 1.8014e+01i	-8.3189e+00 + 1.8019e+01i
-7.6305e+00 + 2.4273e+01i	-7.6306e+00 + 2.4265e+01i	-7.6303e+00 + 2.4273e+01i
-7.2321e+00 + 3.0163e+01i	-7.2324e+00 + 3.0148e+01i	-7.2320e+00 + 3.0162e+01i
-6.9493e+00 + 3.5863e+01i	-6.9496e+00 + 3.5839e+01i	-6.9490e+00 + 3.5860e+01i
-6.7269e+00 + 4.1450e+01i	-6.7277e+00 + 4.1416e+01i	-6.7267e+00 + 4.1446e+01i
-6.5425e+00 + 4.6969e+01i	-6.5441e+00 + 4.6920e+01i	-6.5425e+00 + 4.6963e+01i

Similar results for mode $m = +5$ are shown in Figures 5.9 to 5.11 for the same three cases as for m=0. The comparison between results from the two Finite Diference codes and the Shooting Method code [39] are generally in good agreement. Results from the shooting method code were not

presented in Figure 5.10 because they were not available at the time. However, the cases presented in Figures 5.9 and 5.11 are sufficient for validation purposes.

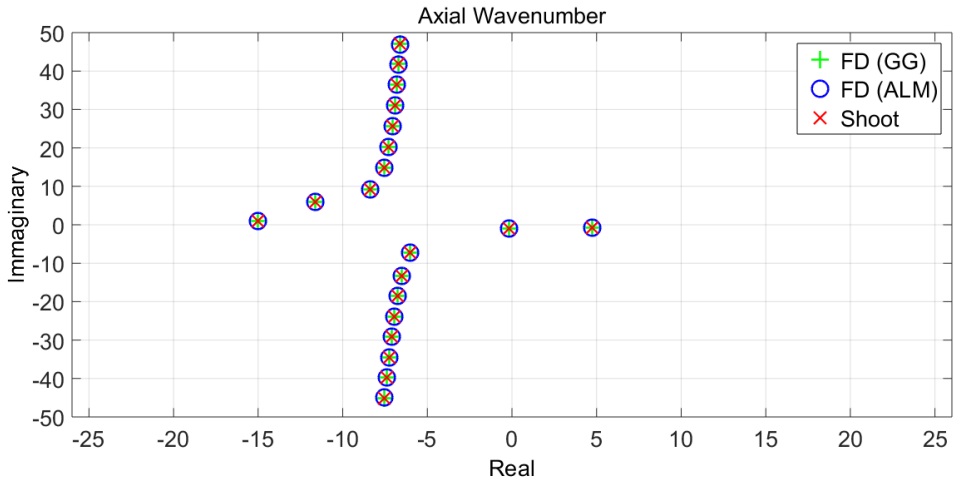

Fig. 5.9 – Axial wavenumber for the uniform flow case with lined outer wall. Comparison between results of two different Finite Difference codes. Blue circles refer to results obtained with the code developed in this work - FD (ALM) and green crosses refer to results provided by Dr. Gabbard. Mach=0.5, m=5, He=10

Comparison between axial wavenumbers for Mach=0.5, m=5 and outer wall lined.		
GG	ALM	Shoot
-1.5000e+01 + 9.0679e-01i	-1.5001e+01 + 9.0610e-01i	-15.000397 0.906801
-1.1636e+01 + 5.8449e+00i	-1.1630e+01 + 5.8466e+00i	-11.635553 5.844955
-8.3902e+00 + 9.2875e+00i	-8.3922e+00 + 9.2876e+00i	-8.390088 9.287643
-7.5674e+00 + 1.4893e+01i	-7.5677e+00 + 1.4888e+01i	-7.567302 14.892673
-7.2764e+00 + 2.0307e+01i	-7.2764e+00 + 2.0293e+01i	-7.276234 20.307056
-7.0707e+00 + 2.5724e+01i	-7.0709e+00 + 2.5695e+01i	-7.070563 25.723634
-6.9157e+00 + 3.1107e+01i	-6.9162e+00 + 3.1057e+01i	-6.915558 31.106603
-6.7927e+00 + 3.6458e+01i	-6.7935e+00 + 3.6378e+01i	-6.792423 36.456269
-6.6906e+00 + 4.1784e+01i	-6.6923e+00 + 4.1664e+01i	-6.690332 41.780802
-6.6034e+00 + 4.7093e+01i	-6.6063e+00 + 4.6921e+01i	-6.603270 47.087290
4.7641e+00 - 8.2931e-01i	4.7642e+00 - 8.2938e-01i	4.764080 -0.829316
-1.9326e-01 - 1.0018e+00i	-1.9204e-01 - 1.0018e+00i	-0.193284 -1.001822i
-6.0405e+00 - 7.3429e+00i	-6.0399e+00 - 7.3396e+00i	-6.040543-7.343042i
-6.5267e+00 - 1.3210e+01i	-6.5264e+00 - 1.3204e+01i	-6.526668-13.209814i
-6.7462e+00 - 1.8521e+01i	-6.7455e+00 - 1.8506e+01i	-6.746100-18.520573i
-6.9345e+00 - 2.3879e+01i	-6.9331e+00 - 2.3851e+01i	-6.934405-23.878895i
-7.1006e+00 - 2.9220e+01i	-7.0980e+00 - 2.9170e+01i	-7.100358-29.218916i
-7.2541e+00 - 3.4522e+01i	-7.2499e+00 - 3.4444e+01i	-7.253798-34.521111i
-7.4028e+00 - 3.9790e+01i	-7.3958e+00 - 3.9673e+01i	-7.401863-39.787669i
-7.5494e+00 - 4.5028e+01i	-7.5400e+00 - 4.4859e+01i	-7.549009-45.022560i

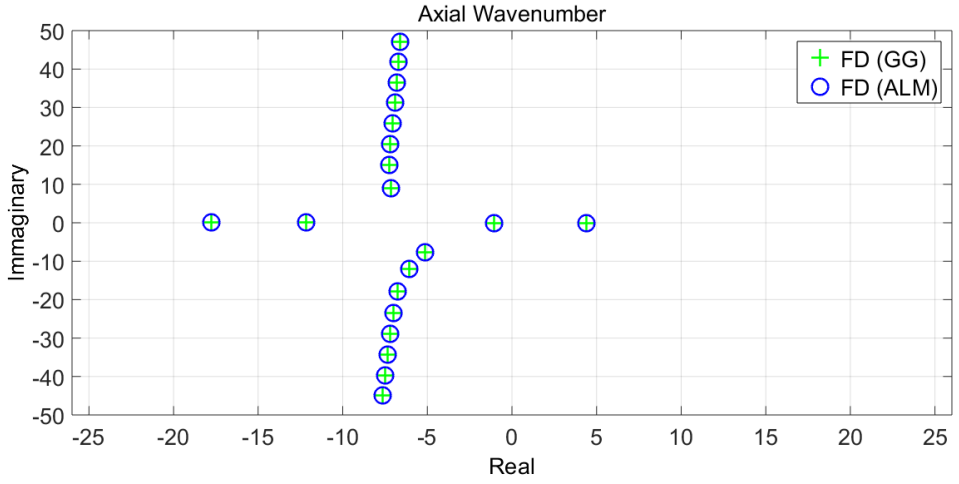

Fig. 5.10 – Axial wavenumber for the uniform flow case with lined inner wall. Comparison between results of two different Finite Difference codes. Blue circles refer to results obtained with the code developed in this work - FD (ALM)- and green crosses refer to results provided by Dr. Gabbard - FD (GG). Mach=0.5, m=5, He=10

Comparison between axial wavenumbers for Mach=0.5, m=5 and inner wall lined.	
GG	ALM
4.4201e+00 - 2.6388e-04i	4.4201e+00 - 2.6374e-04i
-1.0501e+00 - 9.6420e-02i	-1.0499e+00 - 9.6328e-02i
-5.1214e+00 - 7.7497e+00i	-5.1229e+00 - 7.7497e+00i
-6.0587e+00 - 1.2041e+01i	-6.0586e+00 - 1.2040e+01i
-6.7627e+00 - 1.7896e+01i	-6.7624e+00 - 1.7892e+01i
-7.0196e+00 - 2.3521e+01i	-7.0190e+00 - 2.3514e+01i
-7.1993e+00 - 2.8979e+01i	-7.1982e+00 - 2.8967e+01i
-7.3561e+00 - 3.4342e+01i	-7.3544e+00 - 3.4322e+01i
-7.5060e+00 - 3.9644e+01i	-7.5031e+00 - 3.9613e+01i
-7.6545e+00 - 4.4900e+01i	-7.6507e+00 - 4.4855e+01i
-1.7753e+01 + 1.1455e-03i	-1.7753e+01 + 1.1457e-03i
-1.2181e+01 + 1.7183e-01i	-1.2182e+01 + 1.7176e-01i
-7.1482e+00 + 9.0434e+00i	-7.1479e+00 + 9.0424e+00i
-7.2661e+00 + 1.5075e+01i	-7.2658e+00 + 1.5073e+01i
-7.1866e+00 + 2.0482e+01i	-7.1863e+00 + 2.0478e+01i
-7.0369e+00 + 2.5834e+01i	-7.0367e+00 + 2.5826e+01i
-6.8999e+00 + 3.1176e+01i	-6.8998e+00 + 3.1162e+01i
-6.7854e+00 + 3.6502e+01i	-6.7854e+00 + 3.6480e+01i
-6.6889e+00 + 4.1813e+01i	-6.6892e+00 + 4.1780e+01i
-6.6061e+00 + 4.7112e+01i	-6.6066e+00 + 4.7064e+01i

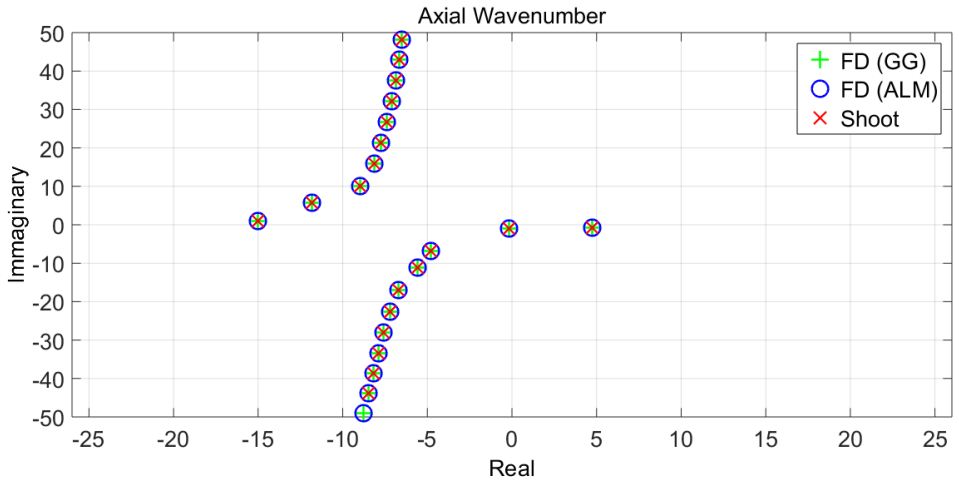

Fig. 5.11 – Axial wavenumber for the uniform flow case with both walls lined. Comparison between results of two different Finite Difference codes. Blue circles refer to results obtained with the code developed in this work - FD (ALM) and green crosses refer to results provided by Dr. Gabbard. Mach=0.5, m=5, He=10

Comparison between axial wavenumbers for Mach=0.5, m=5 and both walls lined.		
GG	ALM	Shoot
-1.5013e+01 + 9.4625e-01i	-1.4976e+01 + 9.1522e-01i	-1.5013e+01 + 9.4627e-01i
-1.1829e+01 + 5.8406e+00i	-1.1649e+01 + 5.9856e+00i	-1.1829e+01 + 5.8406e+00i
-8.9605e+00 + 9.9737e+00i	-7.5137e+00 + 9.9703e+00i	-8.9605e+00 + 9.9737e+00i
-8.1429e+00 + 1.5934e+01i	-5.2441e+00 + 1.4498e+01i	-8.1428e+00 + 1.5934e+01i
-7.7329e+00 + 2.1394e+01i	-6.2154e+00 + 1.8888e+01i	-7.7327e+00 + 2.1394e+01i
-7.3854e+00 + 2.6791e+01i	-6.5407e+00 + 2.4459e+01i	-7.3851e+00 + 2.6791e+01i
-7.1024e+00 + 3.2173e+01i	-6.6212e+00 + 2.9883e+01i	-7.1022e+00 + 3.2172e+01i
-6.8703e+00 + 3.7543e+01i	-6.6505e+00 + 3.5216e+01i	-6.8703e+00 + 3.7539e+01i
-6.6754e+00 + 4.2896e+01i	-6.6631e+00 + 4.0492e+01i	-6.6753e+00 + 4.2892e+01i
-6.5076e+00 + 4.8240e+01i	-6.6690e+00 + 4.5725e+01i	-6.5077e+00 + 4.8233e+01i
4.7642e+00 - 8.2929e-01i	4.7641e+00 - 8.2943e-01i	4.7642e+00 - 8.2930e-01i
-1.5181e-01 - 1.0405e+00i	-2.3073e-01 - 9.9629e-01i	-1.5184e-01 - 1.0405e+00i
-4.8007e+00 - 6.9099e+00i	-6.1815e+00 - 7.7744e+00i	-4.8007e+00 - 6.9100e+00i
-5.5576e+00 - 1.1195e+01i	-6.6262e+00 - 1.4079e+01i	-5.5577e+00 - 1.1195e+01i
-6.7146e+00 - 1.6888e+01i	-6.6816e+00 - 1.9549e+01i	-6.7145e+00 - 1.6888e+01i
-7.2160e+00 - 2.2547e+01i	-6.6787e+00 - 2.4893e+01i	-7.2159e+00 - 2.2546e+01i
-7.5752e+00 - 2.8022e+01i	-6.6736e+00 - 3.0191e+01i	-7.5749e+00 - 2.8022e+01i
-7.8874e+00 - 3.3386e+01i	-6.6721e+00 - 3.5455e+01i	-7.8871e+00 - 3.3385e+01i
-8.1817e+00 - 3.8675e+01i	-6.6736e+00 - 4.0689e+01i	-8.1811e+00 - 3.8673e+01i
-8.4702e+00 - 4.3906e+01i	-6.6777e+00 - 4.5897e+01i	-8.4688e+00 - 4.3900e+01i

5.1.2 Code Verification: sheared Axial Flow

In this section the finite difference code is validated for sheared flow propagation in lined and hard-walled ducts. The velocity profile used consists of a uniform flow in an annular duct with shear layers proposed by by McAlpine [39]. This profile is described as:

$$M = \begin{cases} M_0, r_{in} \leq r \leq r_{out} - \delta \\ M_0 \left(\frac{r}{\delta}\right)^{1/5}, r_{out} - \delta \leq r \leq r_{out} \end{cases}, \tag{5.1}$$

where the boundary layer thickness is assumed to be 4%of the outer radius and $M_0 = 0.5$. Eleven gridpoints are used to describe the boundary layer. The Mach number profile is used as an input of the code.

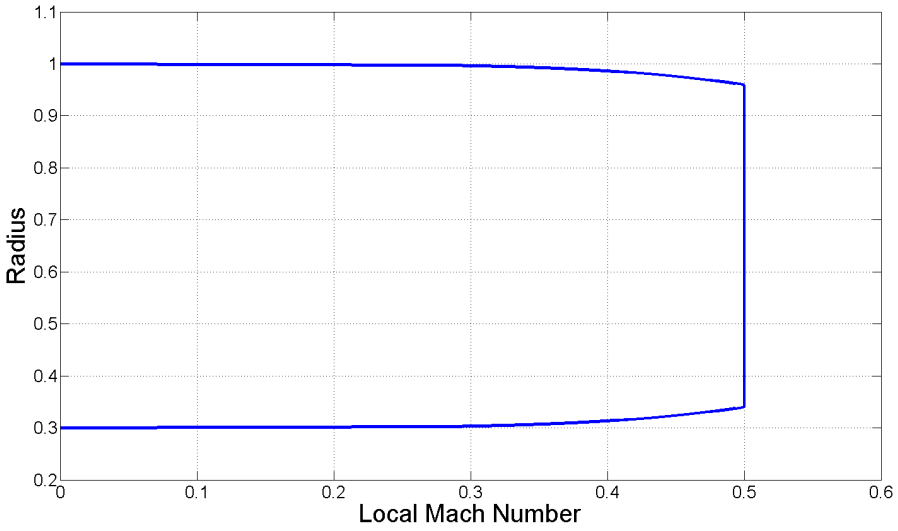

Fig. 5.12 – Power law velocity Profile

Results will now be presented for the cases of sound propagation in hard-walled and lined ducts. The comparison between the two finite difference codes and the shooting method code is presented in the following figures, where the first 20 axial wavenumbers are presented for each case. If the imaginary part of the axial wavenumber is positive, the mode decays and propagates in the negative x-direction. If the imaginary part of the axial wavenumber is negative, the mode decays in the positive x-direction. Real axial wavenumbers higher than $1/M_{min}$ and lower than $1/M_{max}$ are convected modes. Those modes form a continuous spectrum, as opposed to what happens in the uniform flow case where they coincide to a single value. When the Mach number is zero, $1/M$ tends to infinity. In the current code written in MATLAB, the compiler is able to identify $1/0$ as the variable infinity (inf) and no bugs are caused because of that.

Although the maximum and minimum value of the continuum spectrum are checked for validation purposes, the modes from the continuum spectrum do not carry any pressure content and as a consequence do not contribute for the acoustic power and as such are not of interest for this work. Because of that, the continuum spectrum will not be presented in the following figures. Figures 5.13

and 5.14 show the axial wavenumber spectrum for modes m=0 and $m = +5$ and hard-wall boundary condition. There is an excellent agreement between the three sets of results.

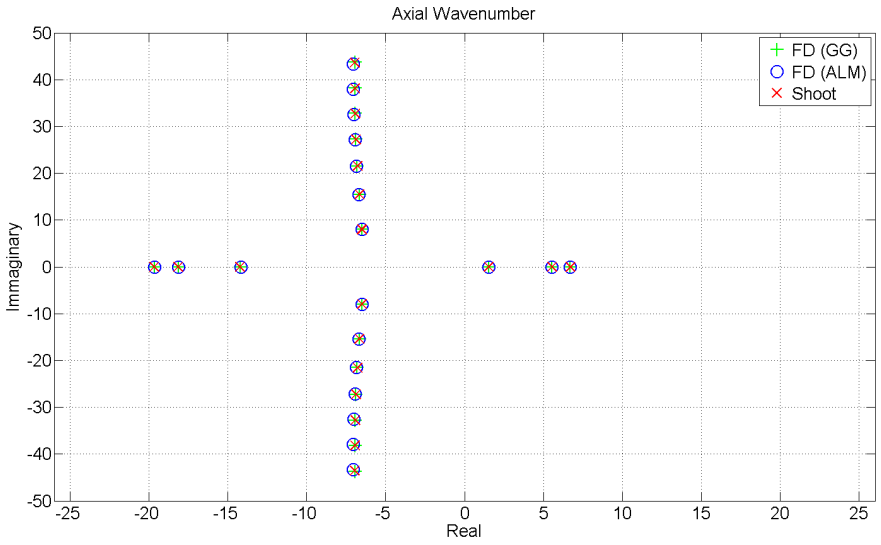

Fig. 5.13 – Axial wavenumber for the sheared flow case with hard walls. Blue circles refer to results obtained with the code developed in this work - FD (ALM), green crosses refer to results provided by Dr. Gabbard - FD (GG) and red crosses refer to results of the shooting method code. Mach=0.5, m=0, He=10

Comparison between axial wavenumbers for .		
Shoot	ALM	GG
6.703300	6.704900	6.703500
5.547900	5.549800	5.548200
1.536300	1.536800	1.536500
-14.173000	-14.225000	-14.2000
-18.162000	-18.093000	-18.146000
-19.658000	-19.628000	-19.651000
-6.4907e+00 + 7.9959e+00i	-6.4807e+00 + 7.9716e+00i	-6.4901e+00 + 7.9914e+00i
-6.6457e+00 + 1.5457e+01i	-6.6701e+00 + 1.5403e+01i	-6.6540e+00 + 1.5450e+01i
-6.7700e+00 + 2.1540e+01i	-6.8324e+00 + 2.1461e+01i	-6.7891e+00 + 2.1533e+01i
-6.8477e+00 + 2.7218e+01i	-6.9459e+00 + 2.7113e+01i	-6.8788e+00 + 2.7214e+01i
-6.8832e+00 + 3.2733e+01i	-7.0117e+00 + 3.2596e+01i	-6.9275e+00 + 3.2732e+01i
-6.8892e+00 + 3.8174e+01i	-7.0421e+00 + 3.8001e+01i	-6.9480e+00 + 3.8176e+01i
-6.8786e+00 + 4.3577e+01i	-7.0508e+00 + 4.3365e+01i	-6.9536e+00 + 4.3582e+01i
-6.4907e+00 - 7.9959e+00i	-6.4807e+00 - 7.9716e+00i	-6.4901e+00 - 7.9914e+00i
-6.6457e+00 - 1.5457e+01i	-6.6701e+00 - 1.5403e+01i	-6.6540e+00 - 1.5450e+01i
-6.7700e+00 - 2.1540e+01i	-6.8324e+00 - 2.1461e+01i	-6.7891e+00 - 2.1533e+01i
-6.8477e+00 - 2.7218e+01i	-6.9459e+00 - 2.7113e+01i	-6.8788e+00 - 2.7214e+01i
-6.8892e+00 - 3.8174e+01i	-7.0117e+00 - 3.2596e+01i	-6.9275e+00 - 3.2732e+01i
-6.8786e+00 - 4.3577e+01i	-7.0421e+00 - 3.8001e+01i	-6.9480e+00 - 3.8176e+01i
-6.8419e+00 - 5.4309e+01i	-7.0508e+00 - 4.3365e+01i	-6.9536e+00 - 4.3582e+01i

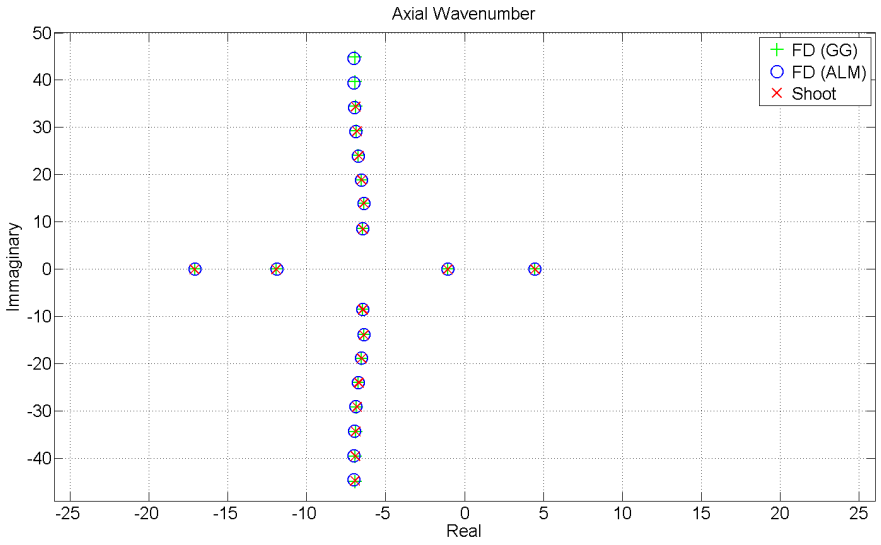

Fig. 5.14 – Axial wavenumber for the sheared flow case with hard walls. Blue circles refer to results obtained with the code developed in this work - FD (ALM), green crosses refer to results provided by Dr. Gabbard - FD (GG) and red crosses refer to results of the shooting method code. Mach=0.5, $m = +5$, He=10

Comparison between axial wavenumbers for .		
GG	ALM	Shoot
4.467600	4.473900	4.467900
-1.065400	-1.066300	-1.065300
-11.931000	-11.857000	-11.925000
-17.122000	-17.007000	-17.109000
-6.4490e+00 + 8.5326e+00i	-6.4092e+00 + 8.5269e+00i	-6.4463e+00 + 8.5311e+00i
-6.3749e+00 + 1.3921e+01i	-6.3255e+00 + 1.3863e+01i	-6.3740e+00 + 1.3915e+01i
-6.5130e+00 + 1.8906e+01i	-6.5217e+00 + 1.8773e+01i	-6.5216e+00 + 1.8897e+01i
-6.6806e+00 + 2.4015e+01i	-6.7622e+00 + 2.3826e+01i	-6.7009e+00 + 2.4007e+01i
-6.7895e+00 + 2.9174e+01i	-6.9262e+00 + 2.8930e+01i	-6.8220e+00 + 2.9169e+01i
-6.8629e+00 + 3.9572e+01i	-7.0172e+00 + 3.4056e+01i	-6.8901e+00 + 3.4359e+01i
-6.4490e+00 - 8.5326e+00i	-6.4092e+00 - 8.5269e+00i	-6.4463e+00 - 8.5311e+00i
-6.3749e+00 - 1.3921e+01i	-6.3255e+00 - 1.3863e+01i	-6.3740e+00 - 1.3915e+01i
-6.5130e+00 - 1.8906e+01i	-6.5217e+00 - 1.8773e+01i	-6.5216e+00 - 1.8897e+01i
-6.6806e+00 - 2.4015e+01i	-6.7622e+00 - 2.3826e+01i	-6.7009e+00 - 2.4007e+01i
-6.7895e+00 - 2.9174e+01i	-6.9262e+00 - 2.8930e+01i	-6.8220e+00 - 2.9169e+01i
-6.8629e+00 - 3.9572e+01i	-7.0172e+00 - 3.4056e+01i	-6.8901e+00 - 3.4359e+01i
-6.8603e+00 - 4.4804e+01i	-7.0563e+00 - 3.9203e+01i	-6.9228e+00 - 3.9574e+01i
-6.8320e+00 - 5.5299e+01i	-7.0636e+00 - 4.4367e+01i	-6.9363e+00 - 4.4809e+01i

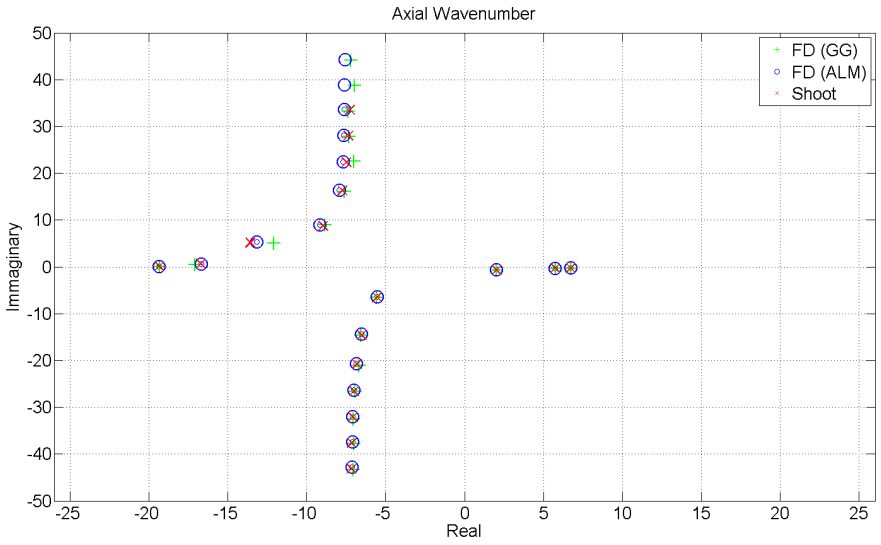

Fig. 5.15 – Axial wavenumber for the sheared flow case with lined outer wall. Comparison between results of two different Finite Difference codes and a shooting method code. Blue circles refer to results obtained with the code developed in this work - FD (ALM), green crosses refer to results provided by Dr. Gabbard - FD (GG) and red crosses refer to results of the shooting method code. Mach=0.5, m=0, He=10

Comparison between axial wavenumbers for .		
Shoot	ALM	GG
-1.9345e+01 + 9.3810e-02i	-1.9331e+01 + 9.2432e-02i	-1.9322e+01 + 8.3624e-02i
-1.6706e+01 + 6.8775e-01i	-1.6683e+01 + 6.5338e-01i	-1.7087e+01 + 4.2123e-01i
-1.3569e+01 + 5.1617e+00i	-1.3140e+01 + 5.3182e+00i	-1.2100e+01 + 5.0118e+00i
-8.9504e+00 + 8.7020e+00i	-9.1852e+00 + 8.9012e+00i	-8.8355e+00 + 8.8967e+00i
-7.7413e+00 + 1.6249e+01i	-7.9130e+00 + 1.6360e+01i	-7.6276e+00 + 1.6108e+01i
-7.4862e+00 + 2.2367e+01i	-7.7079e+00 + 2.2466e+01i	-7.0198e+00 + 2.2514e+01i
-7.3597e+00 + 2.8044e+01i	-7.6506e+00 + 2.8124e+01i	-7.3129e+00 + 2.7888e+01i
-7.2628e+00 + 3.3537e+01i	-7.6247e+00 + 3.3583e+01i	-7.3814e+00 + 3.3183e+01i
6.7278e+00 - 2.8749e-01i	6.7394e+00 - 2.4755e-01i	6.7293e+00 - 2.9597e-01i
5.7508e+00 - 3.0729e-01i	5.7292e+00 - 2.7893e-01i	5.7550e+00 - 3.1336e-01i
2.0179e+00 - 6.8015e-01i	2.0091e+00 - 6.6131e-01i	2.0173e+00 - 6.8522e-01i
-5.5350e+00 - 6.5424e+00i	-5.5149e+00 - 6.4365e+00i	-5.5658e+00 - 6.5993e+00i
-6.5150e+00 - 1.4516e+01i	-6.5232e+00 - 1.4399e+01i	-6.5813e+00 - 1.4570e+01i
-6.8250e+00 - 2.0788e+01i	-6.8362e+00 - 2.0642e+01i	-6.6815e+00 - 2.1048e+01i
-6.9905e+00 - 2.6574e+01i	-6.9966e+00 - 2.6395e+01i	-6.9332e+00 - 2.6655e+01i
-7.0817e+00 - 3.2160e+01i	-7.0754e+00 - 3.1948e+01i	-7.0411e+00 - 3.2489e+01i
-7.1322e+00 - 3.7652e+01i	-7.1069e+00 - 3.7405e+01i	-7.0077e+00 - 3.7766e+01i
-7.1639e+00 - 4.3091e+01i	-7.1138e+00 - 4.2807e+01i	-7.0570e+00 - 4.3289e+01i

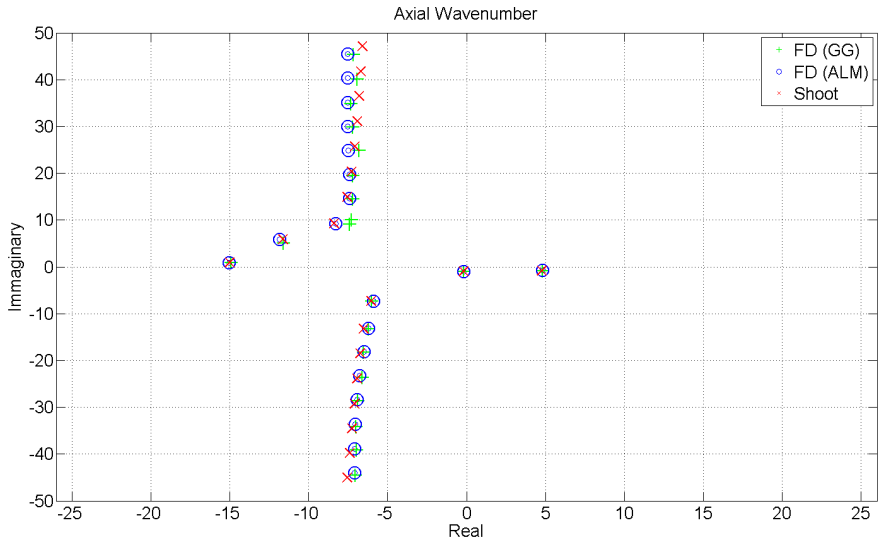

Fig. 5.16 – Axial wavenumber for the sheared flow case with lined outer wall. Comparison between results of two different Finite Difference codes and a shooting method code. Blue circles refer to results obtained with the code developed in this work - FD (ALM), green crosses refer to results provided by Dr. Gabbard - FD (GG) and red crosses refer to results of the shooting method code. Mach=0.5, m=5, He=10

Comparison between axial wavenumbers for .		
GG	ALM	Shoot
-15.000397+0.906801i	-1.5049e+01 + 9.3905e-01i	-1.4917e+01 + 8.6595e-01i
-11.635553+5.844955i	-1.1838e+01 + 5.8575e+00i	-1.1594e+01 + 5.0508e+00i
-8.390088+9.287643i	-8.2888e+00 + 9.2949e+00i	-7.4153e+00 + 9.0898e+00i
-7.2750e+00+1.0062e+01i		
-7.567302+14.892673i	-7.4129e+00 + 1.4592e+01i	-7.2004e+00 + 1.4507e+01i
-7.276234+20.307056i	-7.4121e+00 + 1.9686e+01i	-7.2155e+00 + 1.9458e+01i
-7.070563+25.723634i	-7.4761e+00 + 2.4864e+01i	-6.8091e+00 + 2.4889e+01i
-6.915558+31.106603i	-7.5218e+00 + 3.0026e+01i	-7.1897e+00 + 2.9792e+01i
-6.792423+36.456269i	-7.5446e+00 + 3.5170e+01i	-7.3144e+00 + 3.4797e+01i
-6.690332+41.780802i	-7.5473e+00 + 4.0314e+01i	-6.9276e+00 + 4.0083e+01i
-6.603270+47.087290i	-7.5364e+00 + 4.5466e+01i	-7.1699e+00 + 4.5371e+01i
4.764080-0.829316i	4.8071e+00 - 7.9453e-01i	4.8062e+00 - 8.9903e-01i
-0.193284-1.001822i	-1.8501e-01 - 9.9818e-01i	-1.9599e-01 - 1.0080e+00i
-6.040543-7.343042i	-5.9034e+00 - 7.3490e+00i	-6.0306e+00 - 7.3886e+00i
-6.526668-13.209814i	-6.2256e+00 - 1.3088e+01i	-6.2255e+00 - 1.3217e+01i
-6.746100-18.520573i	-6.4834e+00 - 1.8092e+01i	-6.5425e+00 - 1.8267e+01i
-6.934405-23.878895i	-6.7580e+00 - 2.3220e+01i	-6.6079e+00 - 2.3606e+01i
-7.100358-29.218916i	-6.9343e+00 - 2.8407e+01i	-6.8785e+00 - 2.8669e+01i
-7.253798-34.521111i	-7.0296e+00 - 3.3611e+01i	-6.9926e+00 - 3.4144e+01i
-7.401863-39.787669i	-7.0735e+00 - 3.8827e+01i	-6.9777e+00 - 3.9182e+01i
-7.549009-45.022560i	-7.0888e+00 - 4.4052e+01i	-7.0352e+00 - 4.4533e+01i

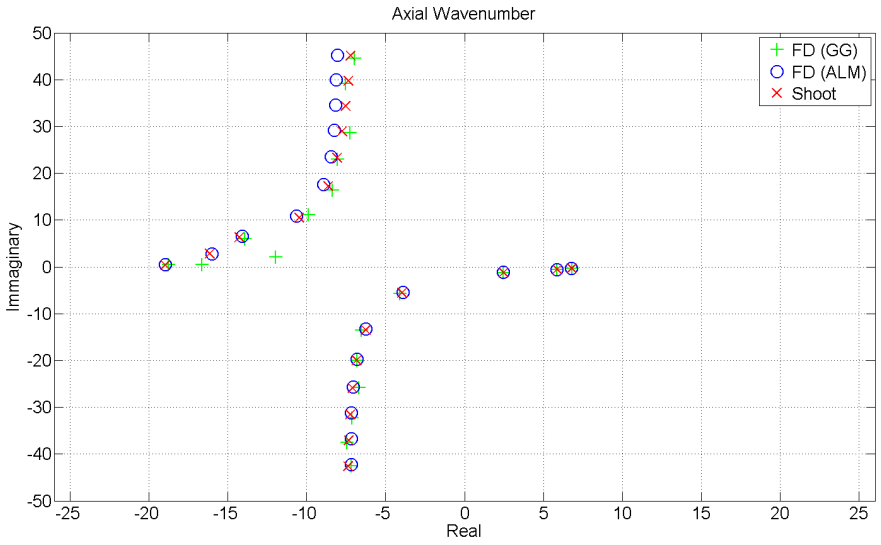

Fig. 5.17 – Axial wavenumber for the sheared flow case with lined walls. Comparison between results of two different Finite Difference codes and a shooting method code. Blue circles refer to results obtained with the code developed in this work - FD (ALM), green crosses refer to results provided by Dr. Gabbard - FD (GG) and red crosses refer to results of the shooting method code. Mach=0.5, m=0, He=10

Comparison between axial wavenumbers for .		
Shoot	ALM	GG
6.7872e+00 - 3.2385e-01i	6.7877e+00 - 2.8162e-01i	6.8063e+00 - 3.2658e-01i
5.8539e+00 - 6.2259e-01i	5.8334e+00 - 5.5959e-01i	5.8460e+00 - 6.4457e-01i
2.4653e+00 - 1.2515e+00i	2.4515e+00 - 1.2038e+00i	2.4699e+00 - 1.2564e+00i
-3.9737e+00 - 5.5847e+00i	-3.8961e+00 - 5.4280e+00i	-4.1007e+00 - 5.7674e+00i
-6.2521e+00 - 1.3477e+01i	-6.2495e+00 - 1.3273e+01i	-6.5236e+00 - 1.3581e+01i
-6.8399e+00 - 1.9961e+01i	-6.8229e+00 - 1.9730e+01i	-6.8165e+00 - 1.9954e+01i
-7.1070e+00 - 2.5876e+01i	-7.0559e+00 - 2.5611e+01i	-6.6938e+00 - 2.5840e+01i
-7.2477e+00 - 3.1547e+01i	-7.1528e+00 - 3.1249e+01i	-7.1368e+00 - 3.2345e+01i
-7.3296e+00 - 3.7098e+01i	-7.1851e+00 - 3.6768e+01i	-7.4415e+00 - 3.7553e+01i
-7.3868e+00 - 4.2577e+01i	-7.1885e+00 - 4.2216e+01i	-7.1847e+00 - 4.2556e+01i
-1.8968e+01 + 4.2922e-01i	2.7414e+01 + 4.9740e-03i	-1.8760e+01 + 5.2547e-01i
-1.6154e+01 + 2.8536e+00i	2.7365e+01 + 5.3394e-03i	-1.6633e+01 + 5.2103e-01i
-1.4260e+01 + 6.3324e+00i	2.8889e+01 + 9.4735e-02i	-1.1953e+01 + 2.1198e+00i
-1.0476e+01 + 1.0456e+01i	2.8933e+01 + 1.0157e-01i	-1.3902e+01 + 6.0339e+00i
-8.6419e+00 + 1.7232e+01i	-1.8962e+01 + 4.1054e-01i	-9.8938e+00 + 1.1110e+01i
-8.0731e+00 + 2.3266e+01i	-1.6000e+01 + 2.8102e+00i	-8.3819e+00 + 1.6410e+01i
-7.7648e+00 + 2.8899e+01i	-1.4063e+01 + 6.5997e+00i	-8.0630e+00 + 2.2939e+01i
-7.5443e+00 + 3.4353e+01i	4.6154e+01 + 9.3353e+00i	-7.2676e+00 + 2.8604e+01i
-7.3663e+00 + 3.9728e+01i	4.5636e+01 + 9.5194e+00i	-7.5091e+00 + 3.9188e+01i
-7.2179e+00 + 4.5073e+01i	-1.0661e+01 + 1.0860e+01i	-6.9600e+00 + 4.4508e+01i

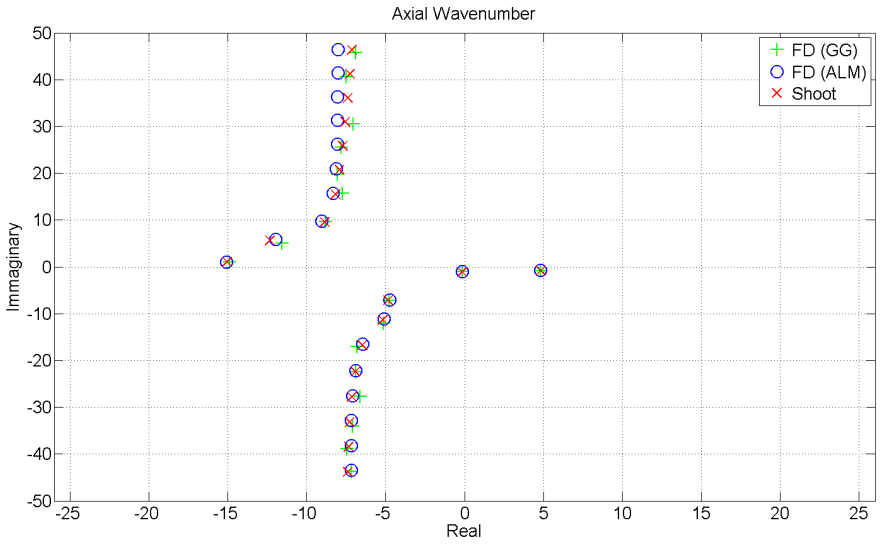

Fig. 5.18 – Axial wavenumber for the sheared flow case with lined walls. Comparison between results of two different Finite Difference codes and a shooting method code. Blue circles refer to results obtained with the code developed in this work - FD (ALM), green crosses refer to results provided by Dr. Gabbard - FD (GG) and red crosses refer to results of the shooting method code. Mach=0.5, m=5, He=10

Comparison between axial wavenumbers for .		
Shoot	ALM	GG
-15.055610+1.026358i	-1.5064e+01 + 9.6478e-01i	-1.4894e+01 + 9.8992e-01i
-12.335078+5.604739i	-1.1981e+01 + 5.8105e+00i	-1.1576e+01 + 4.9995e+00i
-8.862264+9.566783i	-9.0307e+00 + 9.7943e+00i	-8.7968e+00 + 9.6480e+00i
-8.175378+15.481737i	-8.3221e+00 + 1.5700e+01i	-7.7377e+00 + 1.5695e+01i
-7.921835+20.750057i	-8.1456e+00 + 2.1024e+01i	-8.0297e+00 + 1.9810e+01i
-7.721323+25.883161i	-8.0674e+00 + 2.6193e+01i	-7.8086e+00 + 2.5511e+01i
-7.551838+30.979694i	-8.0396e+00 + 3.1293e+01i	-7.0478e+00 + 3.0574e+01i
-7.401104+36.077282i	-8.0306e+00 + 3.6358e+01i	-7.4700e+00 + 4.0630e+01i
-7.264398+41.199023i	-8.0205e+00 + 4.1415e+01i	-6.8891e+00 + 4.5736e+01i
-7.142328+46.354567i	-8.0029e+00 + 4.6484e+01i	-7.3321e+00 + 5.6127e+01i
4.814114-0.866544i	4.8073e+00 - 7.9452e-01i	-4.7694e+00 - 7.1746e+00i
-0.154128-1.046292i	-1.4457e-01 - 1.0367e+00i	-5.1483e+00 - 1.2060e+01i
-4.835060-7.182844i	-4.7318e+00 - 7.1240e+00i	-6.7942e+00 - 1.7097e+01i
-5.188455-11.364455i	-5.1022e+00 - 1.1059e+01i	-6.8841e+00 - 2.2405e+01i
-6.471218-16.794186i	-6.4632e+00 - 1.6549e+01i	-6.6020e+00 - 2.7707e+01i
-6.926139-22.368234i	-6.8879e+00 - 2.2115e+01i	-7.0957e+00 - 3.4000e+01i
-7.148273-27.792817i	-7.0716e+00 - 2.7516e+01i	-7.4640e+00 - 3.8946e+01i
-7.270395-33.149741i	-7.1498e+00 - 3.2847e+01i	-7.1846e+00 - 4.3741e+01i
-7.343849-38.477950i	-7.1755e+00 - 3.8149e+01i	-7.1106e+00 - 5.5092e+01i
-7.396822-43.790632i]	-7.1769e+00 - 4.3434e+01i];	
	-7.3165e+00 - 5.9936e+01i	

Figures 5.15 and 5.16 show the comparison for mode $m = 0$ and mode $m = +5$ for a lined outer wall and figures 5.18 and 5.17 show the comparison for mode $m = 0$ and mode $m = +5$ for both walls lined. Generally the current Finite Difference Scheme was in a generally closer agreement with the shooting method for the propagating modes

For the cases with sheared mean flow and liners, the agreement is not as good for modes propagating against the flow. The fact that the power-law profile has an infinite gradient at the wall and each of the methods compared uses a different scheme to deal with this problem could be a cause for the discrepancy between the three methods. To avoid such a problem in the current Finite Difference code, a forward derivative scheme was used in the inner wall and a backward derivative scheme was used in the outer wall in a way that the gradient at the wall would be always finite.

5.2 Validation of the Swirling Flow Code

The Finite Difference eigenmode formulation based on the Linearized Euler Equation was validated in two stages. First, this formulation was validated for the case without swirl by comparing results from the current code with the analytic solution and with solutions from the previous formulation based on the Pridmore-Brown equation presented in section 5.1. Secondly, the current formulation in validated for the swirling flow case by comparing with solutions from Nijboer [1] and Posson and Peake [2]. A validation against an in-house code from Rolls-Royce is also presented for a more realistic case.

Figure 5.19 shows the natural logarithm of the error against the natural logarithm of the number of the radial points for the case of uniform axial flow ($M = 0.5$) and mode order $m = 5$.The error is calculated based on the difference between the calculated axial wavenumber and the analytical solution. The first axial wavenumber is used. Based on this convergence study, it is considered that 100 elements are sufficient to give accurate results.

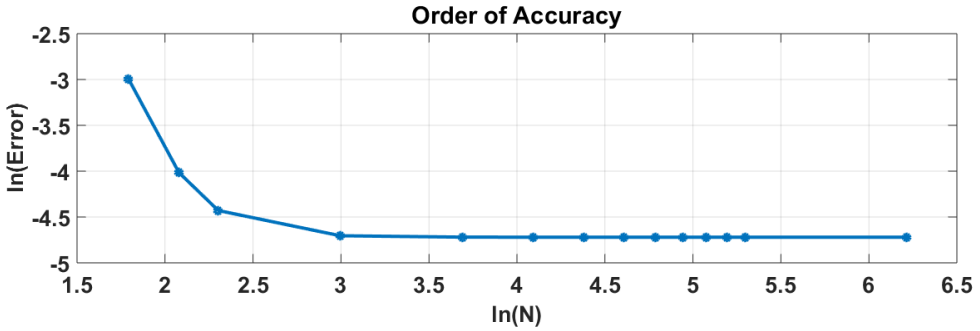

Fig. 5.19 – Order of accuracy for M=0.5 and mode m=5.

5.2.1 Code Verification: Uniform Axial Flow

In this results for an annular duct with flow in the absence of swirl are presented. The current finite difference code was verified against results available in the literature and analytical solutions

(when possible) by comparing the axial wavenumbers. A fourth-order scheme was used instead of a second order scheme as it was the case of the code based on the Pridmore-Brown Equation.

Results from the Finite Difference code were first validated against the analytical theory for sound propagation in a hard-walled uniform mean flow for mode m=+2, mean flow axial mach number $M_{x0} = 0.3$, Helmholtz number $He = 10$ and hub to tip ratio $\sigma = 0.25$. Figure 5.20 shows a comparison between the axial wavenumbers given by the Finite Difference code and analytic solution. Blue crosses refer to results obtained with the FD swirling code and magenta diamonds refer to the analytical solution.

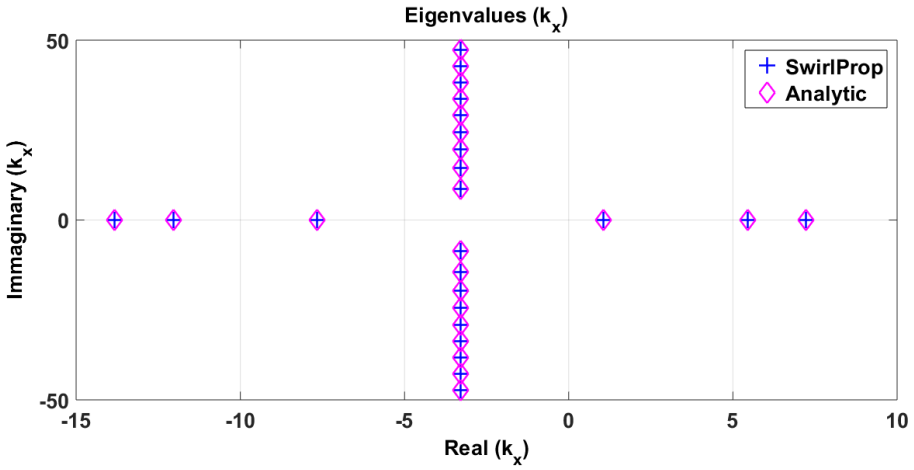

Fig. 5.20 – Validation of Swirling Flow code for uniform flow and Hard-walls. Mach=0.3, m=2, He=10

Modes with purely real axial wavenumbers are propagating, cut on, modes. Modes for which the axial wavenumber has an immaginary part are decaying, cut-off modes. If the imaginary part of the axial wavenumber is positive, the mode decays in the negative direction and propagates in the left direction. If the immaginary part of the axial wavenumber is negative, the mode decays in the positive direction and propagates to the right. For the acoustic modes, the cut-off line is given by:

$$\mathsf{Real}(k_x) = \frac{kM_{x0}}{M_{x0}^2 - 1}, \tag{5.2}$$

that in this case is $Real(k_x) = -3.2967$.

Although only wavenumbers for the acoustic modes are presented in figure 5.20, there is also a group of hydrodynamic modes that are purely convected by the mean flow and are given by:

$$(k_x)_{\mathsf{convective}} = \frac{k}{M_{x0}}, \tag{5.3}$$

that in this case are given by $(k_x)_{\mathsf{convective}} = 33.3$. These are off the scale and will not be shown.

5.2.2 Code Verification: sheared Axial Flow

Results from the Pridmore-Brown code were used to validate the code based on the Linearized Euler Equations. Two sets of results are presented: (i) sheared flow with hard walls and (ii) uniform axial flow with lined walls.

The comparison for the case of the sound propagation in a sheared flow in a hard-walled duct is presented in Figure 5.21. The sheared flow profile used is the same one presented in figure 5.15. Other parameters are azimuthal mode number m=+5, mean flow axial, Helmholtz number $He = 10$, hub to tip ratio $\sigma = 0.3$. This demonstrates that both formulations give the same results. A good agreement is again obtained between this code and the Pridmore-Brown Predictions.

Figure 5.22 shows the comparison for the case of sound propagation in a uniform axial flow inside a lined annular duct. In this case both walls are lined. Other parameters are azimuthal mode m=+5, mean flow axial mach number (M_{x0}) 0.3, Helmholtz number $He = 10$, hub to tip ratio $\sigma = 0.3$ and impedance $0.4 + 0.2i$.

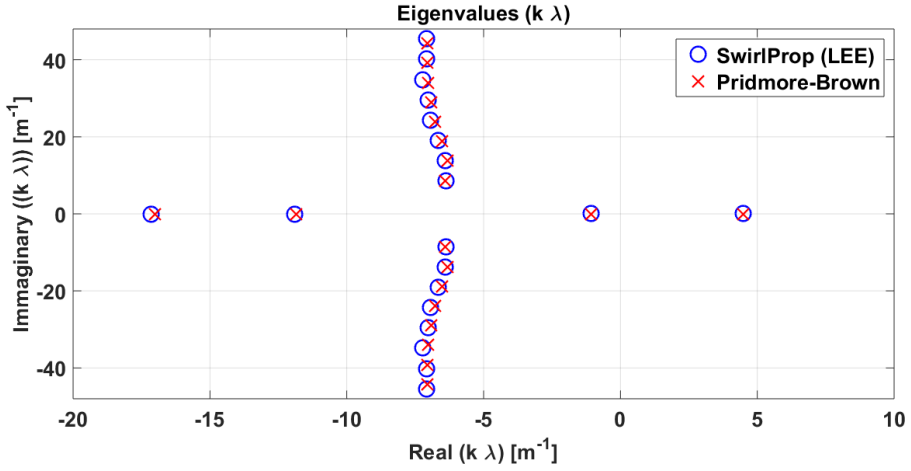

Fig. 5.21 – Validation of the LEE code for sheared flow and Hard-walls. Comparison with results from the Pridmore-Brown code. Uniform axial flow with Power-law boundary layer profile, m=5, He=10

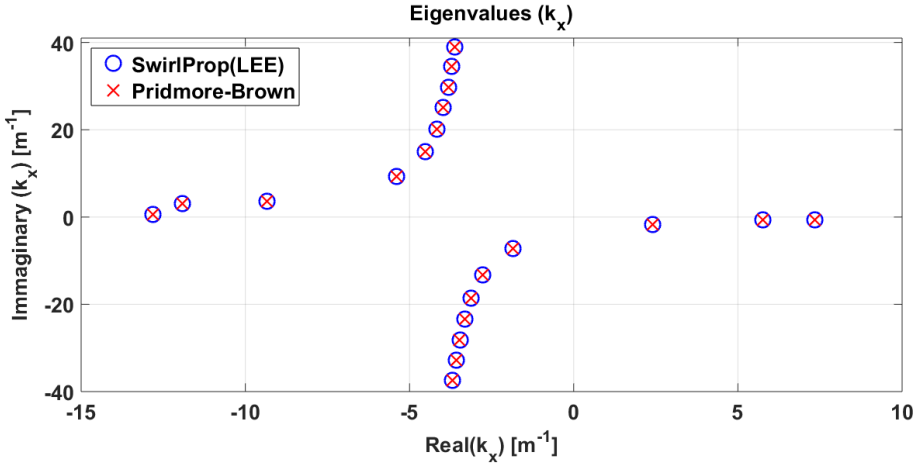

Fig. 5.22 – Validation of the LEE code for uniform axial flow flow and Lined-walls. Comparison with results from the Pridmore-Brown code. Uniform axial flow with Power-law boundary layer profile, Mach=0.3, m=2, He=10, z=$0.4 + 0.2i$

5.2.3 Code verification: Swirling Flow

Swirling Flow: Vortex Swirl

The first swirling flow profile to be evaluated is a vortex swirl with a uniform axial mean flow, as studied by Kousen [65] and Nijboer [1]. The parameters used here are mode order $m = +2$, axial Mach number $M_x = 0.3$, Helmholtz number $He = 10$, hub to tip ratio $\sigma = 0.4$ and magnitude of free vortex swirl $\Gamma^* = 0.2$. The duct is hard-walled and the reduced frequency is calculated using the sound speed on the outer radius. The mean flow Mach number profile is shown in figure 5.23

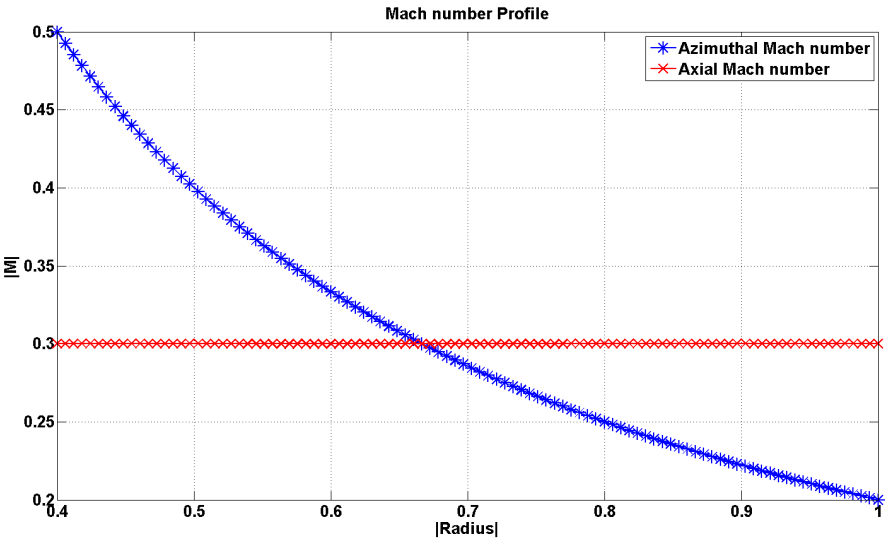

Fig. 5.23 – Mean Mach number profile for the vortex swirl case

Figure 5.24 shows the comparison between axial wavenumbers obtained with the current method and results from Nijboer [1]. The acoustic wavenumbers have real parts between -15 and 10 and are distributed symmetricaly around the cut-off line of $Re(k_x) = -3$ based on the axial Mach number. In addition to those acoustic modes, a continuum of modes correspondent to wavenumbers with real part between 25 and 32 is also found and again are not shown in the pictures. Correspondence between the two sets of results are clearly close.

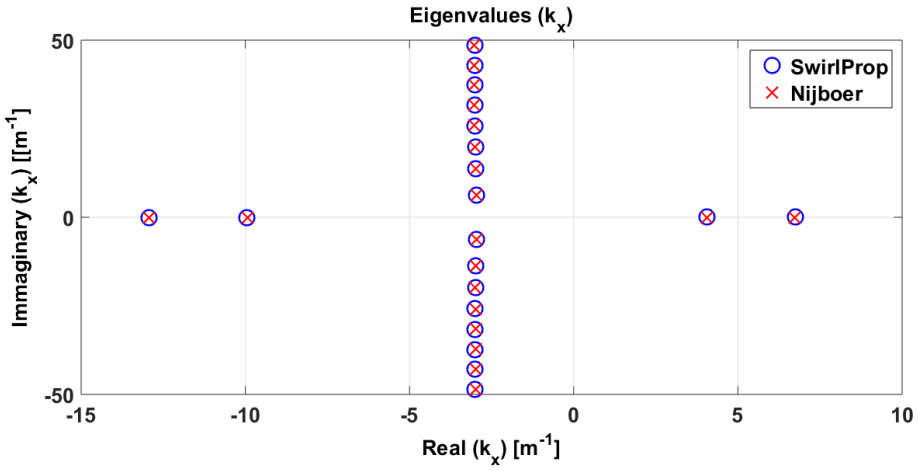

Fig. 5.24 – Comparison between results from the finite difference code and results from Nijboer [1] for a vortex swirl mean flow profile and hard-walled duct. Mode order $m = +2$, axial Mach number $M_x = 0.3$, reduced frequency $k = 10$, hub to tip ratio $\sigma = 0.4$ magnitude of free vortex swirl $\Gamma^* = 0.2$

Comparison between axial wavenumbers	
Finite Difference	Nijboer
-12.94	-12.94
-9.94	-9.94
+4.06	4.06
+6.74	6.73
-2.97+ 6.16i	-2.97+ 6.18i
-2.99+13.68i	-2.99+13.65i
-3.00+19.94i	-3.03+19.90i
-3.00+25.86i	-3.03+25.88i
-3.00+31.63i	-3.03+31.60i
-3.00+37.31i	-3.03+37.32i
-3.00+42.95i	-3.03+42.98i
-3.00+48.55i	-3.02+48.57i
-2.97- 6.16i	-2.97- 6.18i
-2.99-13.68i	-2.99-13.65i
-3.00-19.90i	-3.00-19.90i
-3.00-25.86i	-3.00-25.88i
-3.00-31.63i	-3.00-31.55i
-3.00-37.31i	-3.00-37.25i
-3.00-42.95i	-3.00-42.98i
-3.00-48.55i	-3.02-48.57i

Swirling Flow: Rigid Body rotation

The second swirling flow profile to be evaluated is a combination of uniform axial flow and rigid body rotation. The parameters used are the same ones proposed by Kousen [65] and reported by Nijboer [1] and Guan et al [52] : mode order $m = +2$, axial Mach number $M_x = 0.3$, reduced frequency $k = 10$, hub to tip ratio $\sigma = 0.4$ and magnitude of free vortex swirl $\Omega^* = 0.5$. The duct is hard-walled and the reduced frequency is calculated using the reference sound speed on the outer radius. The mean flow Mach number profile is shown in figure 5.25

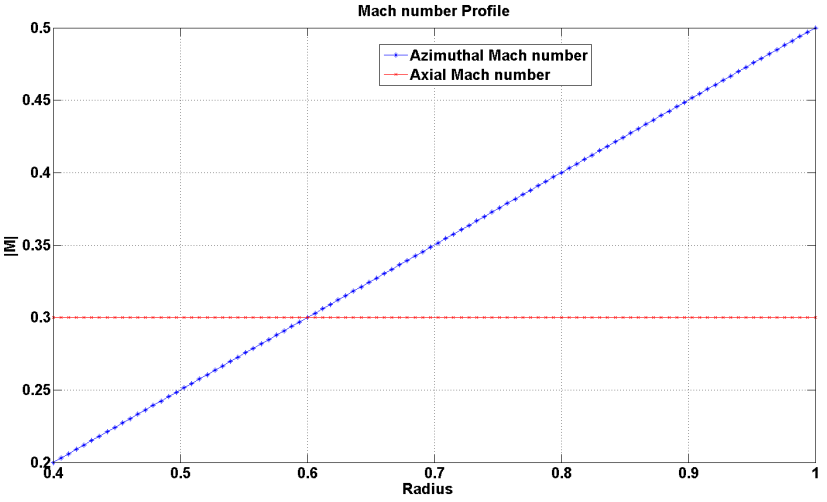

Fig. 5.25 – Mean flow Mach number Profile

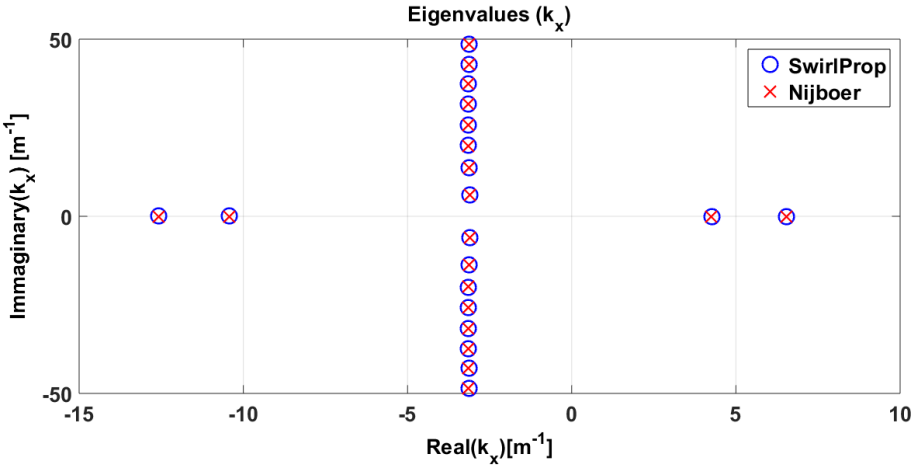

Fig. 5.26 – Comparison between results from the finite difference code and results from Nijboer [1] for rigid body swirl and hard-walled duct. Mode order $m = +2$, axial Mach number $M_x = 0.3$, reduced frequency $k = 10$, hub to tip ratio $\sigma = 0.4$ magnitude of solid body $\Omega^* = 0.5$

In figure 5.26 a comparison is shown between results from the current Finite difference code and results from Nijboer [1]. The acoustic wavenumbers have real parts between -15 and 10 and are distributed symmetricaly around the cut-off line at approximately $Re(k_x) = -3$ based on the axial Mach number. Once again there is a good agreement between the two sets of results.

Comparison between axial wavenumbers	
SwirlProp	Nijboer
-12.59	-12.59
-10.44	-10.44
+4.26	+4.25
+6.55	+6.55
-3.11+ 6.03i	-3.11+ 6.04i
-3.13+13.69i	-3.13+13.70i
-3.14+19.96i	-3.15+19.94i
-3.15+25.87i	-3.15+25.85i
-3.15+31.63i	-3.15+31.62i
-3.15+37.31i	-3.15+37.34i
-3.14+42.93i	-3.14+42.93i
-3.13+48.53i	-3.13+48.51i
-3.11-6.03i	-3.11-6.04i
-3.13-13.69i	-3.13-13.70i
-3.14-19.96i	-3.15-19.94i
-3.14-25.87i	-3.15-25.84i
-3.15-31.63i	-3.15-31.63i
-3.15-37.31i	-3.15-37.34i
-3.14-42.93i	-3.15-42.93i
-3.13-48.53i	-3.13-48.51i

Swirling Flow: Combined rigid Body rotation and Vortex Swirl in a hard-walled duct

The following results were obtained for a swirling mean flow profile which is a combination of rigid body rotation and vortex swirl. The axial velocity profile is the one proposed by Posson & Peake[2] and defined in equation 3.132. The mean flow Mach number profile is presented in figure 5.27

The parameters used here are: mode order $m = 16$, reduced frequency $k = 30$, hub to tip ratio $\sigma = 0.5$ magnitude of solid body swirl $\Omega^* = 0.28$, magnitude of vortex swirl $\Gamma^* = 0.1$, and axial Mach number at the tip 0.4.. The duct is hard-walled and the reduced frequency is calculated using the sound speed of the outer radius.

Figure 5.28 shows a comparison between results from the current Finite difference code and results from Posson & Peake[2]. The acoustic wavenumbers have real parts between -35 and 9. A continuum of modes with axial wavenumbers with real parts between 32 and 59.73 is observed. Results correspond closely.

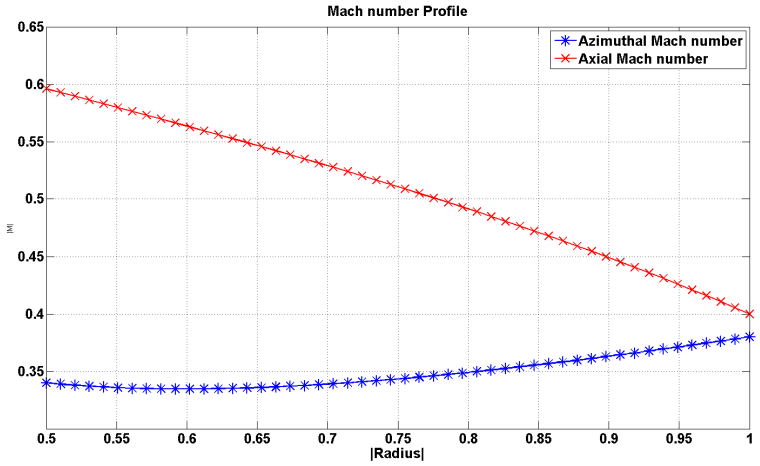

Fig. 5.27 – Mean flow Mach number profile: combination of rigid body rotation, vortex swirl and radial equilibrium. Magnitude of solid body swirl $\Omega^* = 0.28$, magnitude of vortex swirl $\Gamma^* = 0.1$ and axial Mach number at the tip 0.4.

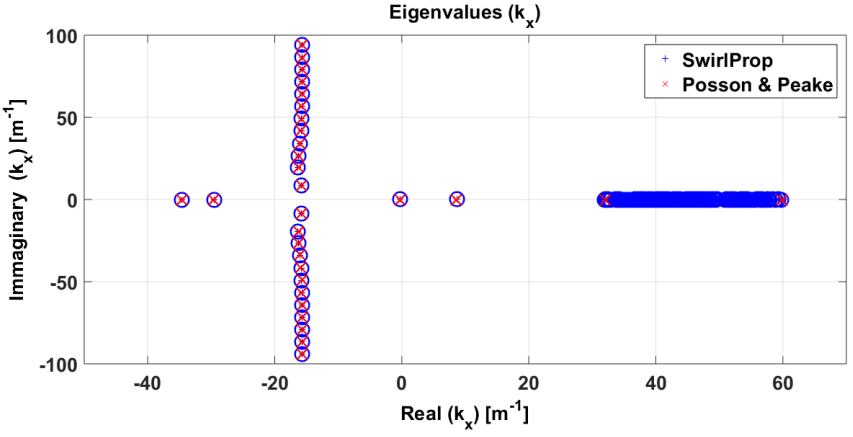

Fig. 5.28 – Comparison between results from the current finite difference code and results from Posson & Peake [2]. Mode order $m = 16$, reduced frequency $k = 30$, hub to tip ratio $\sigma = 0.5$ magnitude of solid body $\Omega^* = 0.28$, magnitude of vortex swirl $\Gamma^* = 0.1$ and axial Mach number at the tip 0.4.

Comparison between axial wavenumbers	
SwirlProp	Posson & Peake
-34.66	-34.61
-29.61	-29.58
-8.612	+8.656
-0.2847	-0.2823
-15.8-8.58i	-15.77+8.447i
-16.3+19.4i	-16.3+19.38i
-16.3+29.49i	-16.28+26.69i
-16+34.1i	-16.01+33.96i
-15.87+41.79i	-15.84+41.69i
-15.8+48.88i	-15.77+49.28i
-15.8+56.72i	-15.73+56.83i
-15.73+64.18i	-15.71+64.34i
-15.73+71.64i	-15.69+71.83i
-15.73+79.1i	-15.68+79.27i
-15.73+86.19i	-15.67+86.68i
-15.73+94.03i	-15.66+94.08i
-16.33-19.4i	-16.33-19.38i
-16.23-26.49i	-16.28-26.69i
-16.01-33.58i	-15.99-34.09i
-15.87-41.42i	-15.85-41.69i
-15.77-49.28i	-15.77-49.28i
-15.8-56.72i	-15.73-56.83i
-15.73-64.18i	-15.71-64.35i
-15.73-71.64i	-15.68-71.83i
-15.73-79.1i	-15.68-79.29i
-15.73-86.57i	-15.66-86.73i
-15.73-94.03i	-15.65-94.08i

Swirling Flow: Combined rigid Body rotation and Vortex Swirl in a lined duct

The following results include the effect of a liner with impedance $z = 1 + 2i$. The mean flow profile is presented in Figure 5.29.

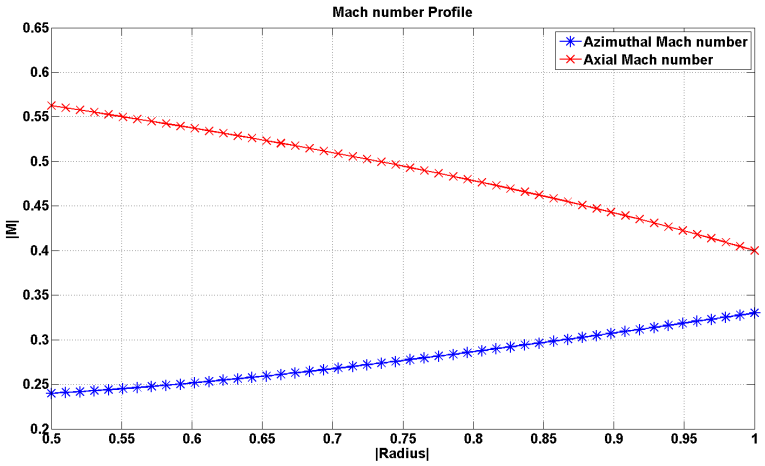

Fig. 5.29 – Mean flow Mach number profile for the lined case. $\Omega^* = 0.28$, $\Gamma^* = 0.05$ and axial Mach number at the tip 0.4.

As in the previous results, the swirling mean flow profile is a combination of rigid body rotation ($\Omega^* = 0.28$) and vortex swirl ($\Gamma^* = 0.1$). The axial profile is the one proposed by Posson & Peake[2] and defined in equation 3.132. The axial Mach number at the tip is 0.4. The remaining parameters used are: mode order $m = 16$, reduced frequency $k = 30$, hub to tip ratio $\sigma = 0.5$ and $\gamma = 1.4$. The reduced frequency is calculated using the sound speed of the outer radius. Figure 5.30 shows a comparison between results from the current Finite difference code and those from Posson & Peake[2]. The acoustic wavenumbers have real parts between -35 and 9. A continuum of modes with axial wavenumbers with real parts between -39.52 and 61.76 is observed.

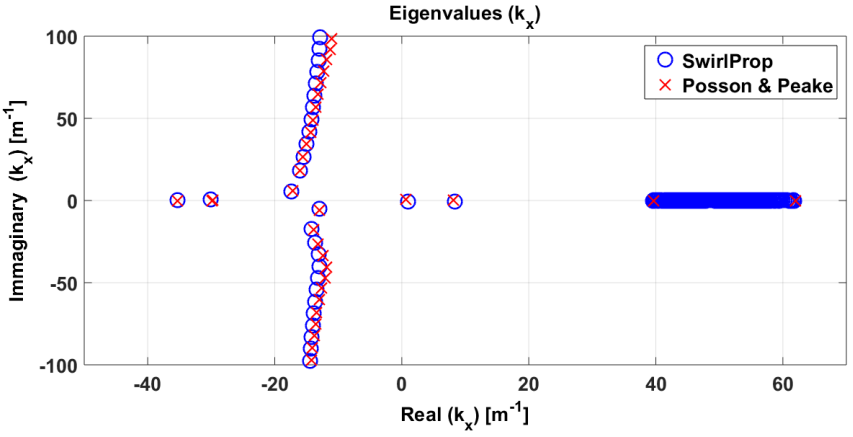

Fig. 5.30 – Comparison between results from the current finite difference code and those from Posson & Peake [2]. Mode order $m = 16$, reduced frequency $k = 30$, hub to tip ratio $\sigma = 0.5$ magnitude of solid body $\Omega^* = 0.28$, magnitude of vortex swirl $\Gamma^* = 0.05$, liner impedance $z = 1 + 2i$ and axial Mach number at the tip 0.4.

Comparison between axial wavenumbers	
SwirlProp	Posson and Peake
-35.37+0.1158i	-35.34+0.00i
-30.09+0.55i	-29.78+0.351i
-17.34+5.283i	-17.12+5.965i
-16.06+18.14i	-16.01+18.25i
-15.5+26.48i	-15.59+26.32i
-14.98+32.35i	-14.97+34.39i
-14.57+41.82i	-14.34+41.4i
-14.24+49.27i	-13.39+49.12i
-13.96+56.63i	-13.57+56.84i
-13.49+71.14i	-13.23+64.56i
-13.29+78.31i	-12.74+71.58i
-13.12+84.43i	-12.32+78.6i
-12.95+92.5i	-11.84+85.61i
-12.82+99.55i	-11.28+91.93i
8.351-0.5099i	+8.122+0.357i
0.9514-0.5358i	0.6815+0.70i
-12.95-4.91i	-13.02-5.96i
-14.19-17.43i	-13.85-17.89i
-13.59-25.53i	-13.16-26.32i
-13.09-32.88i	-12.39-33.68i
-12.98-39.93	-11.84-40.35
-13.17-47.00i	-12.04-47.37i
-13.42-54.18i	-12.6-53.33i
-13.65-61.42i	-12.95-60.35i
-13.86-68.66i	-13.37-68.07i
-14.03-75.91i	-13.57-75.09i
-14.21-83.12	-13.78-82.46i
-14.31-90.34	-14.06-89.47i
-14.43-97.55i	-14.20-97.19i

5.2.4 Swirling Flow: Realistic Case. Comparison with an in-house Rolls-Royce code

Eigenmode solutions obtained with the code developed in this work were compared with solutions from the JM66 in-house code from Rolls-Royce [80].

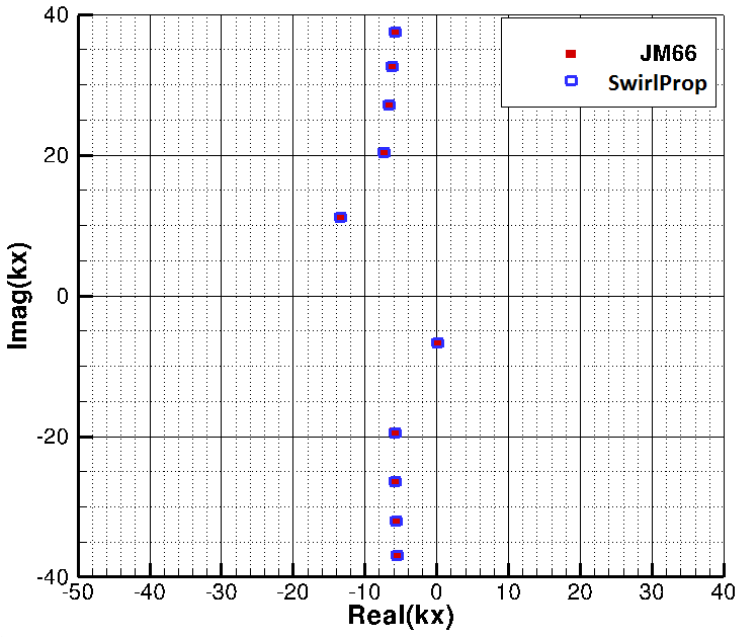

Fig. 5.31 – Comparison between eigenvalue results from the code developed in this work and results from JM66. Mode order $m = +20$, reduced frequency $k = 20$, hub to tip ratio $\sigma = 0.4$, magnitude of vortex swirl $\Gamma^* = 0.15$ and liner impedance $z = 2 - 1.5i$.

Results are presented for a mean flow profile corresponding to a vortex swirl with magnitude $\Gamma^* = 0.15$. The axial velocity profile is an uniform axial flow profile with $M_x = 0.3$. The parameters used here are: reduced frequency $k = 23.28$ and hub to tip ratio $\sigma = 0.4$. The duct is lined in both walls and the impedance value is z$= 2 - 1.5i$. The reduced frequency is calculated using the sound speed of the outer radius.

The axial wavenumbers are organized in order of attenuation from the less attenuated to the most attenuated. The axial wavenumbers for mode $m = 20$ are compared in figure 5.31 and the values of axial wavenumbers are given in the following table. Clearly the agreement is close.

Comparison between axial wavenumbers for m=20		
Current code	JM66 code	Propagation
-33.95+0.276i	-33.98+0.248i	1st Upstream
-31.73+0.965i	-31.81+0.88i	2nd Upstream
-26.70+2.595i	-27.06+2.49i	3rd Upstream
-15.84+6.549i	-16.50+6.51i	4th Upstream
-30.92+7.637i	-30.91+7.64i	5th Upstream
+18.23-0.763i	+18.17-0.74i	1st Downstream
+16.69-0.839i	+16.75-0.86i	2nd Downstream
+13.45-1.014i	+13.51-1.05i	3rd Downstream
+18.35-1.063i	+18.34-1.23i	4th Downstream
+8.071-1.532i	+8.18-1.58i	5th Downstream

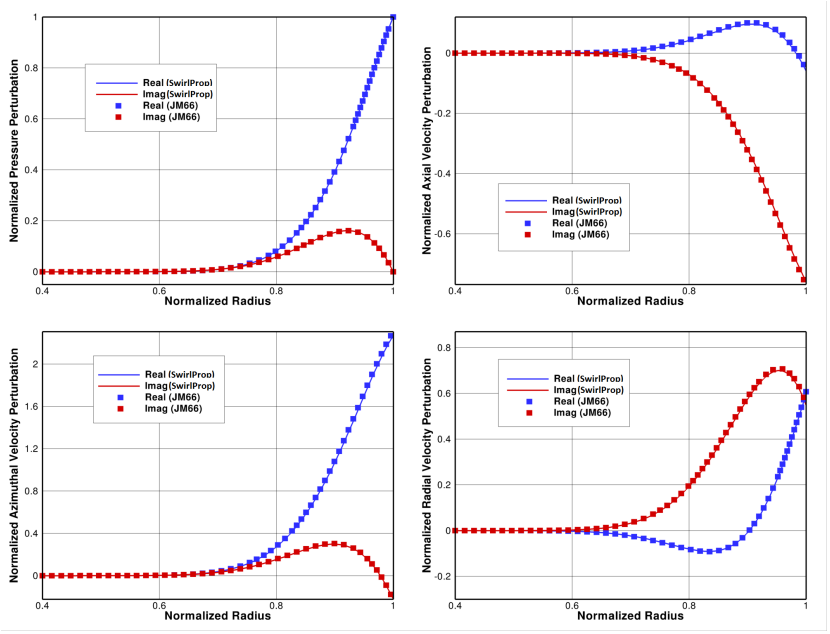

Fig. 5.32 – Comparison between eigenvectors obtained with the code developed in this work and results from JM66 for the first radial mode downstream. Mode order $m = +20$, reduced frequency $k = 20$, hub to tip ratio $\sigma = 0.4$, magnitude of vortex swirl $\Gamma^* = 0.15$ and liner impedance $z = 2 - 1.5i$.

The radial eigenmodes for pressure, axial velocity, azimuthal velocity and radial velocity from the current code are compared with predictions from JM66. The outputs from the JM66 code were provided in a dimensional form and the predictions from the current Finite Difference code were carried out in a non-dimensional form. Non-dimensional velocity eigenvectors from the JM66 code were obtained by dividing the velocity eigenvectors by $u_{ref} = 287.45m/s$ and multiplying them by $c_{ref} = 337.37m/s$. Non-dimensional pressure eigenvectors from the JM66 code were obtained by dividing the pressure eigenvectors by $p_{ref} = 287.45Pa$ and multiplying them by $c_{ref} = 337.37m/s$. All the eigenvectors (pressure and velocities) are normalized by the pressure value in the outer radius. This is an operation involving complex numbers. The comparison for the downstream radial modes for mode $m = +20$ are presented in figures 5.32 to 5.34. A good agreement is obtained.

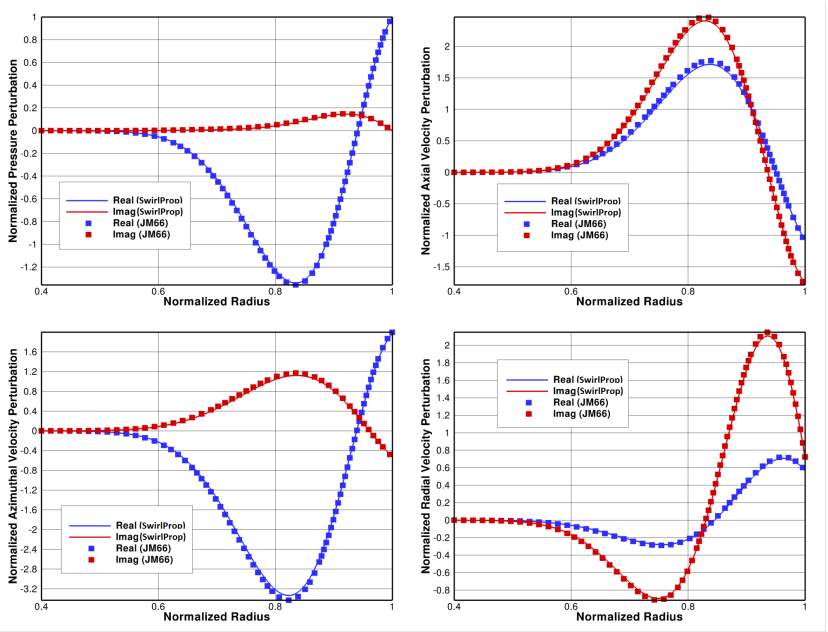

Fig. 5.33 – Comparison between eigenvectors obtained with the code developed in this work and results from JM66 for the second radial mode downstream. Mode order $m = +20$, reduced frequency $k = 20$, hub to tip ratio $\sigma = 0.4$, magnitude of vortex swirl $\Gamma^* = 0.15$ and liner impedance $z = 2 - 1.5i$.

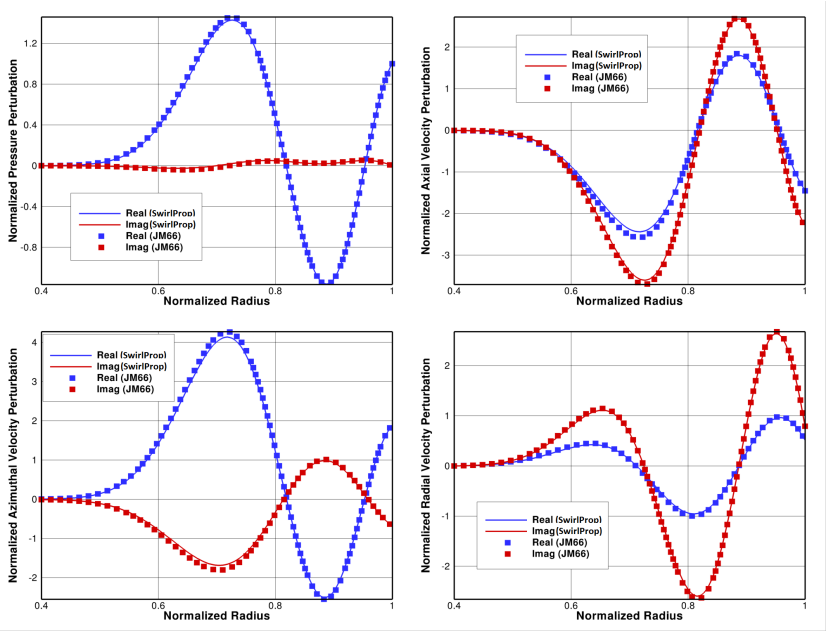

Fig. 5.34 – Comparison between eigenvectors obtained with the code developed in this work and results from JM66 for the third radial mode downstream. Mode order $m = +20$, reduced frequency $k = 20$, hub to tip ratio $\sigma = 0.4$, magnitude of vortex swirl $\Gamma^* = 0.15$ and liner impedance $z = 2 - 1.5i$.

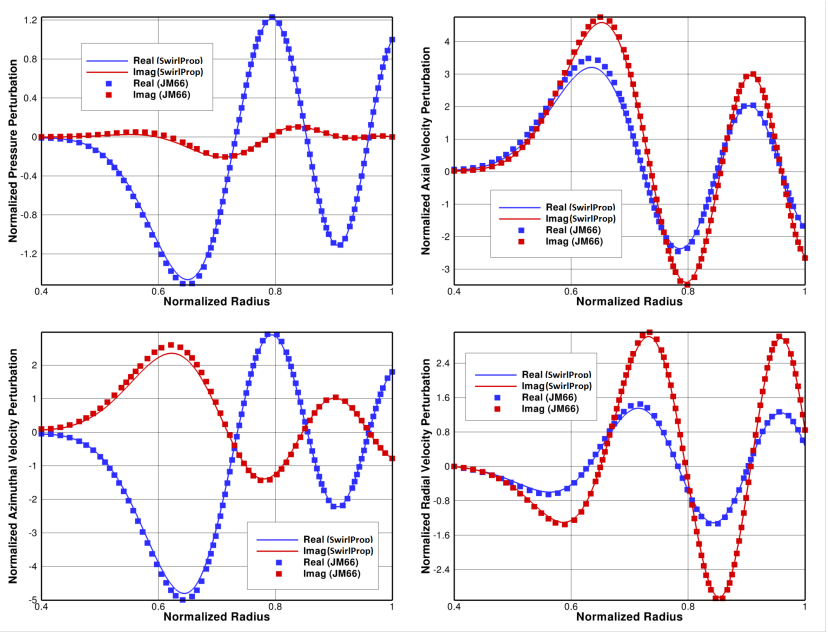

Fig. 5.35 – Comparison between eigenvectors obtained with the code developed in this work and results from JM66 for the fourth radial mode downstream. Mode order $m = +20$, reduced frequency $k = 20$, hub to tip ratio $\sigma = 0.4$, magnitude of vortex swirl $\Gamma^* = 0.15$ and liner impedance $z = 2 - 1.5i$.

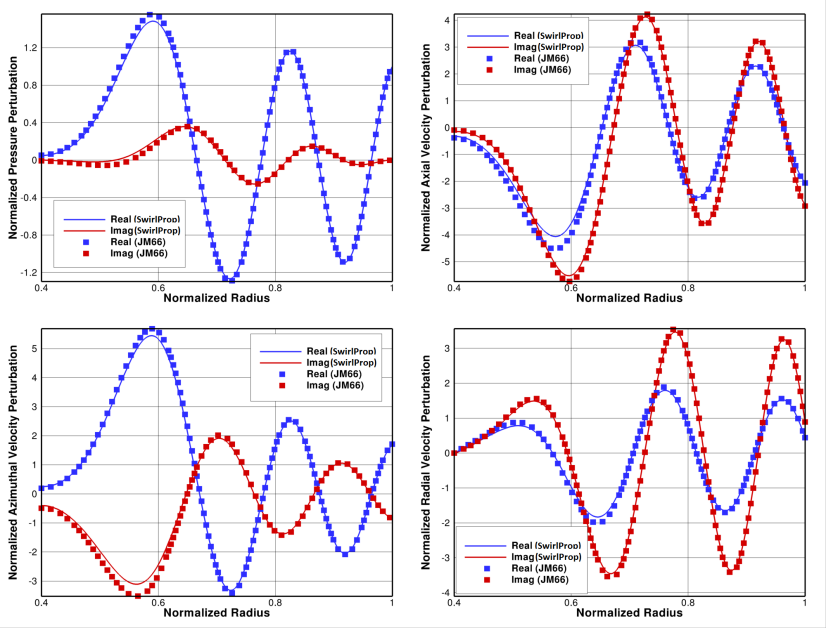

Fig. 5.36 – Comparison between eigenvectors obtained with the code developed in this work and results from JM66 for the fifth radial mode downstream. Mode order $m = +20$, reduced frequency $k = 20$, hub to tip ratio $\sigma = 0.4$, magnitude of vortex swirl $\Gamma^* = 0.15$ and liner impedance $z = 2 - 1.5i$.

A similar comparison of radial eigenmodes for pressure, axial velocity, azimuthal velocity and radial velocity from the code developed in this work and results from JM66 for the first to fifth radial modes upstream and mode $m = +20$ are presented in figures 5.37 to 5.43. A good agreement is obtained.

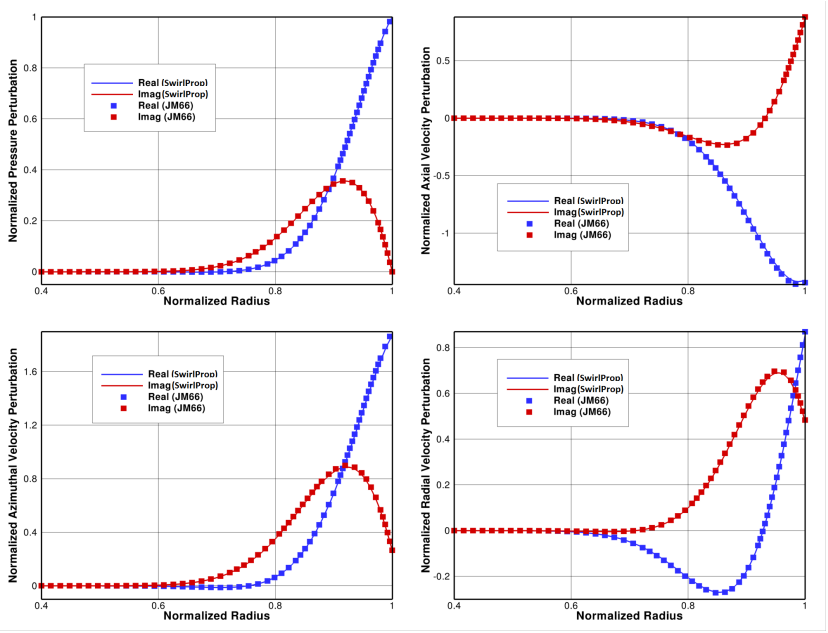

Fig. 5.37 – Comparison between eigenvectors obtained with the code developed in this work and results from JM66 for the first radial mode upstream. Mode order $m = +20$, reduced frequency $k = 20$, hub to tip ratio $\sigma = 0.4$, magnitude of vortex swirl $\Gamma^* = 0.15$ and liner impedance $z = 2 - 1.5i$.

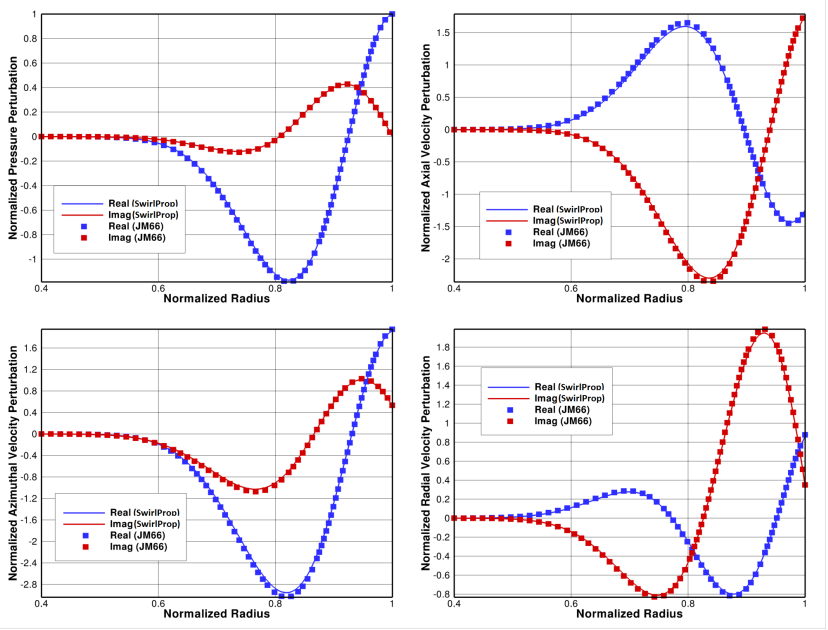

Fig. 5.38 – Comparison between eigenvectors obtained with the code developed in this work and results from JM66 for the second radial mode upstream. Mode order $m = +20$, reduced frequency $k = 20$, hub to tip ratio $\sigma = 0.4$, magnitude of vortex swirl $\Gamma^* = 0.15$ and liner impedance $z = 2 - 1.5i$.

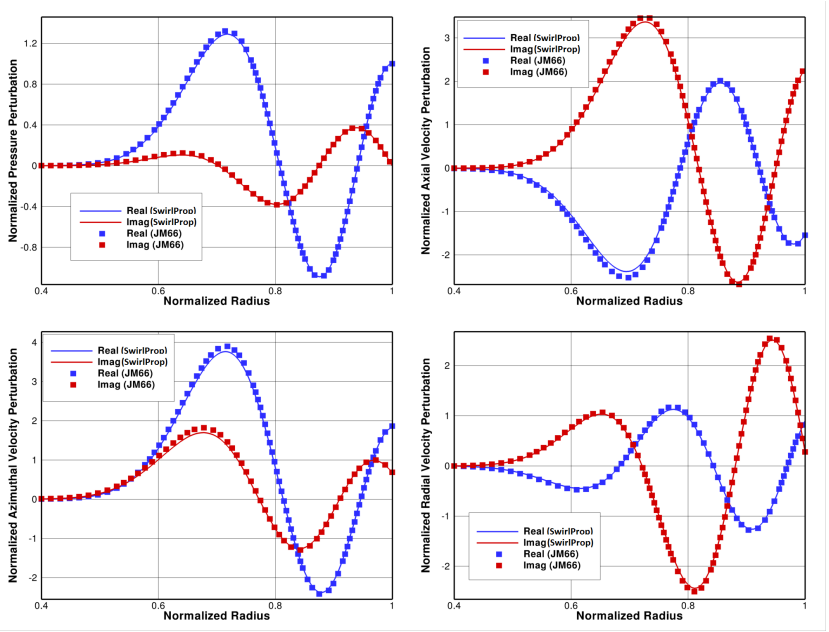

Fig. 5.39 – Comparison between eigenvectors obtained with the code developed in this work and results from JM66 for the third radial mode upstream. Mode order $m = +20$, reduced frequency $k = 20$, hub to tip ratio $\sigma = 0.4$, magnitude of vortex swirl $\Gamma^* = 0.15$ and liner impedance $z = 2 - 1.5i$.

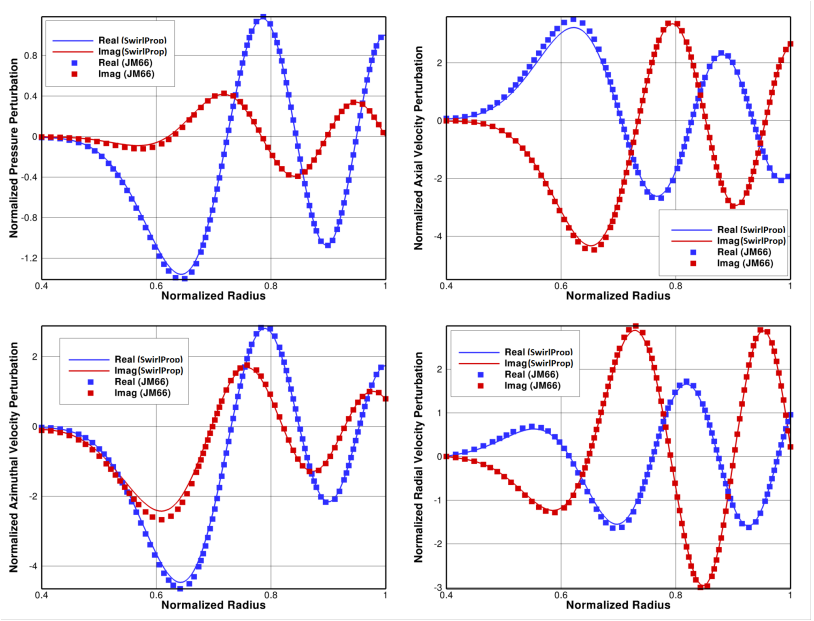

Fig. 5.40 – Comparison between eigenvectors obtained with the code developed in this work and results from JM66 for the fourth radial mode upstream. Mode order $m = +20$, reduced frequency $k = 20$, hub to tip ratio $\sigma = 0.4$, magnitude of vortex swirl $\Gamma^* = 0.15$ and liner impedance $z = 2 - 1.5i$.

Eigenmode solutions obtained with the current FD were also compared to solutions from the JM66 code for mode $m = -4$ for the same set of parameters. The axial wavenumbers are compared in figure 5.42 and the values of axial wavenumbers are given in the table bellow.

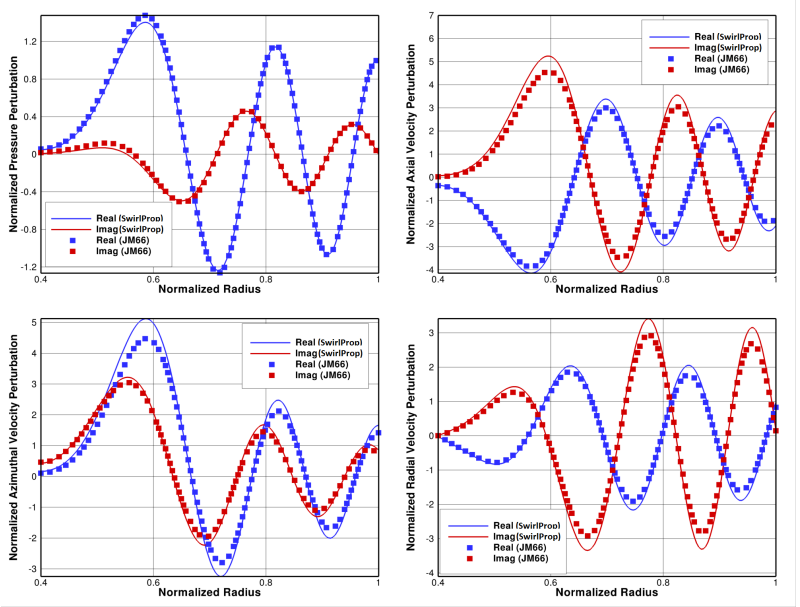

Fig. 5.41 – Comparison between eigenvectors obtained with the code developed in this work and results from JM66 for the fifth radial mode upstream. Mode order $m = +20$, reduced frequency $k = 20$, hub to tip ratio $\sigma = 0.4$, magnitude of vortex swirl $\Gamma^* = 0.15$ and liner impedance $z = 2 - 1.5i$.

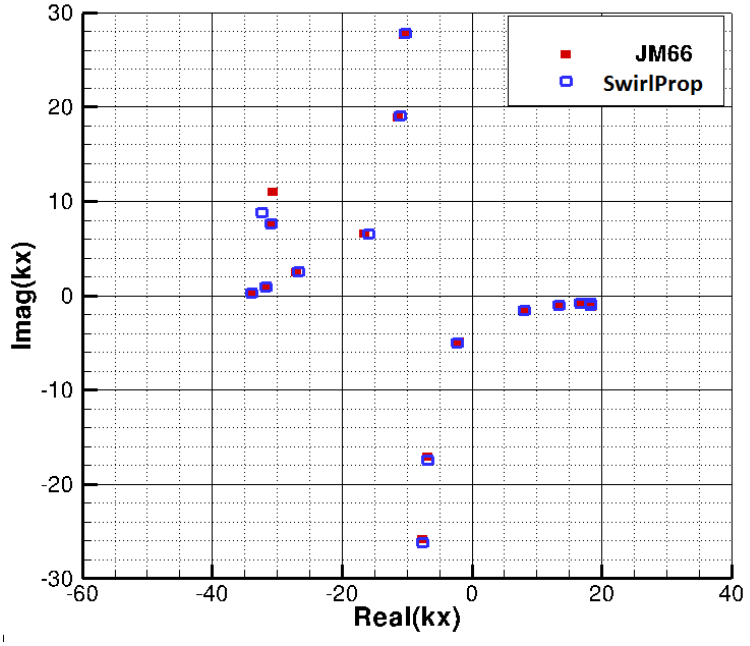

Fig. 5.42 – Comparison between eigenvalue results from the code developed in this work and results from JM66. Mode order $m = -4$, reduced frequency $k = 20$, hub to tip ratio $\sigma = 0.4$, magnitude of vortex swirl $\Gamma^* = 0.15$ and liner impedance $z = 2 - 1.5i$.

Comparison between axial wavenumbers for m=-4		
Current code	JM66 code	Propagation
-33.95+0.276i	-33.98+0.248i	1st Upstream
-31.73+0.965i	-31.81+0.88i	2nd Upstream
-26.70+2.595i	-27.06+2.49i	3rd Upstream
-15.84+6.549i	-16.50+6.51i	4th Upstream
-30.92+7.637i	-30.91+7.64i	5th Upstream
-32.41+8.773i	-30.68+10.97i	6th Upstream
-11.06+19.029i	-11.34+18.88i	7th Upstream
-10.26+27.779i	-10.45+27.64i	8th Upstream
-9.88+35.215i	-10.02+35.02i	9th Upstream
+18.23-0.763i	+18.17-0.74i	1st Downstream
+16.69-0.839i	+16.75-0.86i	2nd Downstream
+13.45-1.014i	+13.51-1.05i	3rd Downstream
+18.35-1.063i	+18.34-1.23i	4th Downstream
+8.071-1.532i	+8.18-1.58i	5th Downstream
-2.35-5.013i	-1.96-4.90i	6th Downstream
-6.89-17.404i	-6.81-17.12i	7th Downstream
-7.58-26.125i	-7.54-25.84i	8th Downstream
-7.89-33.550i	-7.86-33.21i	9th Downstream

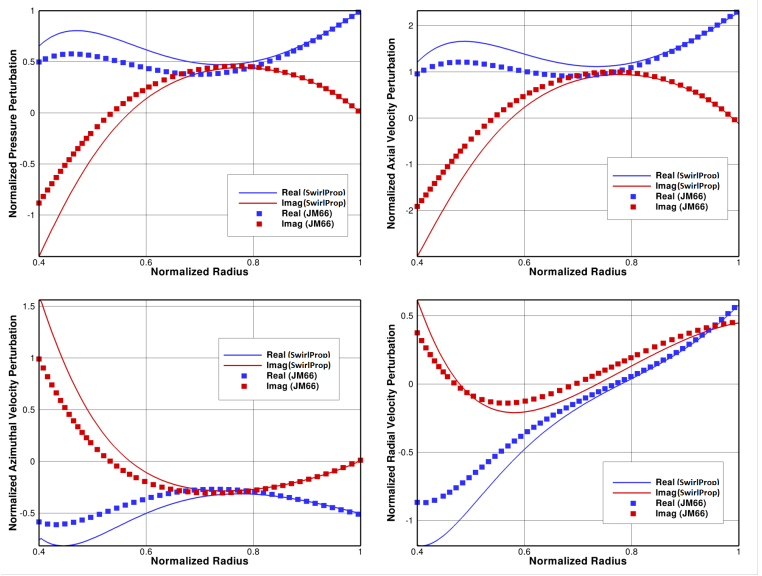

Fig. 5.43 – Comparison between eigenvectors obtained with the code developed in this work and results from JM66 for the first radial mode downstream. Mode order $m = -4$, reduced frequency $k = 20$, hub to tip ratio $\sigma = 0.4$, magnitude of vortex swirl $\Gamma^* = 0.15$ and liner impedance $z = 2 - 1.5i$.

The radial eigenmodes for pressure, axial velocity, azimuthal velocity and radial velocity from de code developed in this work are compared with corresponded results from JM66. The eigenvectors are non-dimensionalized by the value of the correspondent value at the outter radius and normalized by the pressure value at the outter radius. The comparison for the first to fifth radial modes downstream and mode $m = -4$ are presented in figures 5.41 to 5.45. A good agreement is obtained.

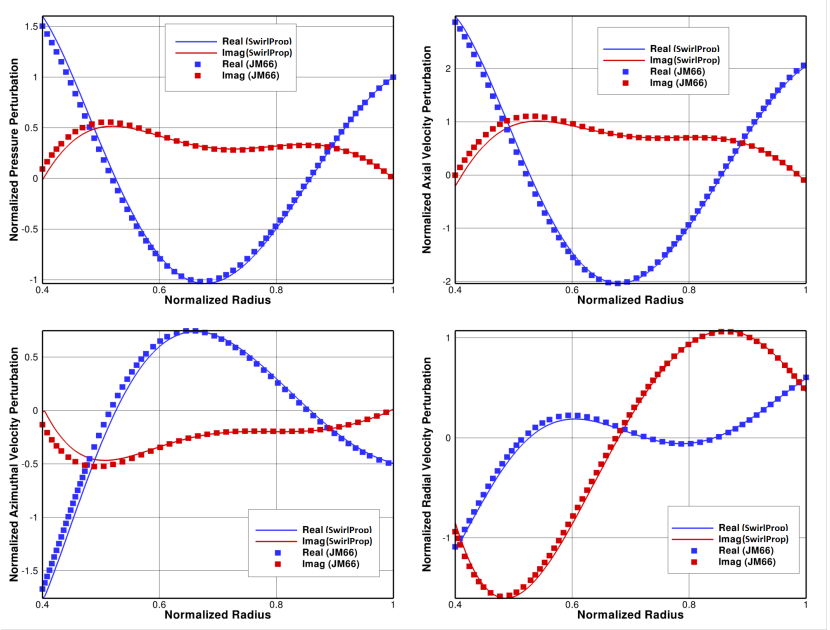

Fig. 5.44 – Comparison between eigenvectors obtained with the code developed in this work and results from JM66 for the second radial mode downstream. Mode order $m = -4$, reduced frequency $k = 20$, hub to tip ratio $\sigma = 0.4$, magnitude of vortex swirl $\Gamma^* = 0.15$ and liner impedance $z = 2 - 1.5i$.

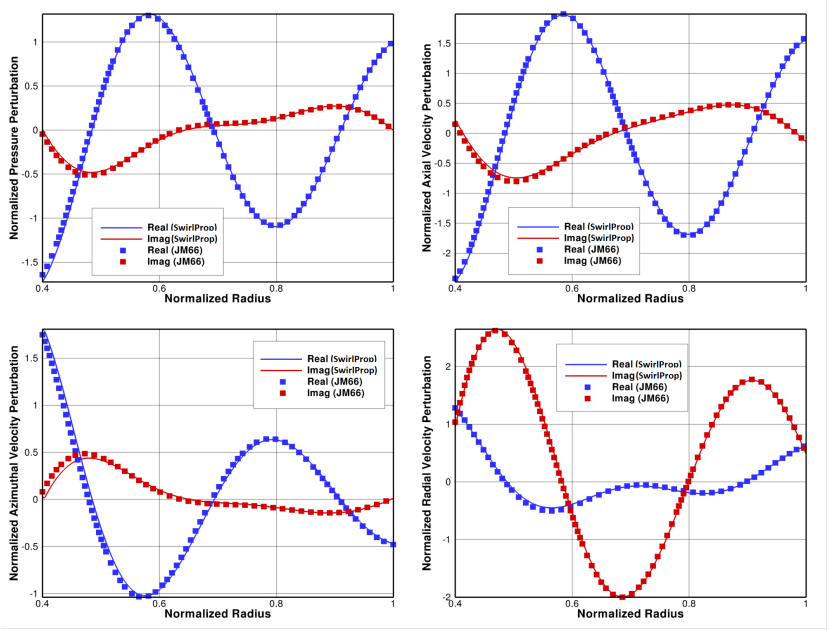

Fig. 5.45 – Comparison between eigenvectors obtained with the code developed in this work and results from JM66 for the third radial mode downstream. Mode order $m = -4$, reduced frequency $k = 20$, hub to tip ratio $\sigma = 0.4$, magnitude of vortex swirl $\Gamma^* = 0.15$ and liner impedance $z = 2 - 1.5i$.

A similar comparison of radial eigenmodes for pressure, axial velocity, azimuthal velocity and radial velocity from de code developed in this work and results from JM66 for the first to fifth radial modes upstream and mode $m = -4$ are presented in figures 5.46 to 5.50.

Results agree for most cases. The results do not agree well for the first and fourth modes downstream and fifth mode upstream.

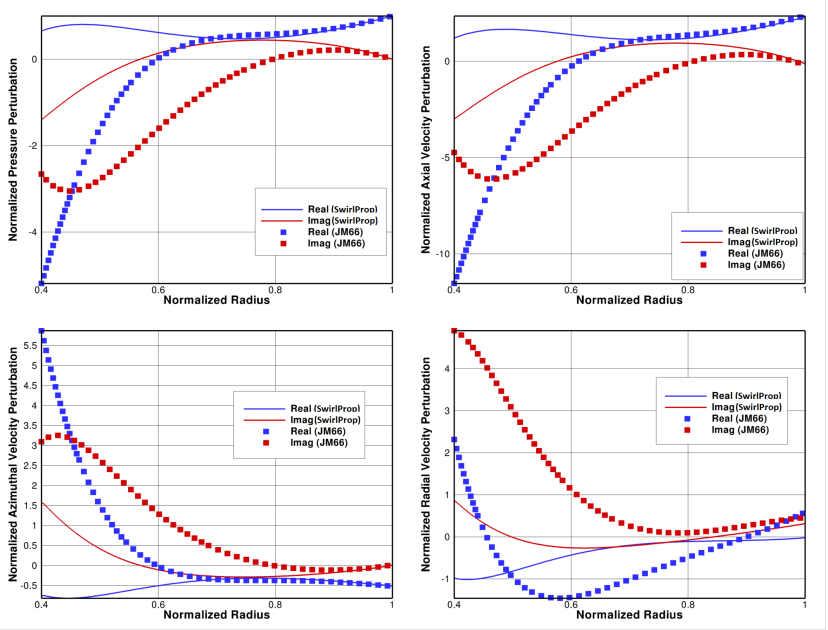

Fig. 5.46 – Comparison between eigenvectors obtained with the code developed in this work and results from JM66 for the fourth radial mode downstream. Mode order $m = -4$, reduced frequency $k = 20$, hub to tip ratio $\sigma = 0.4$, magnitude of vortex swirl $\Gamma^* = 0.15$ and liner impedance $z = 2 - 1.5i$.

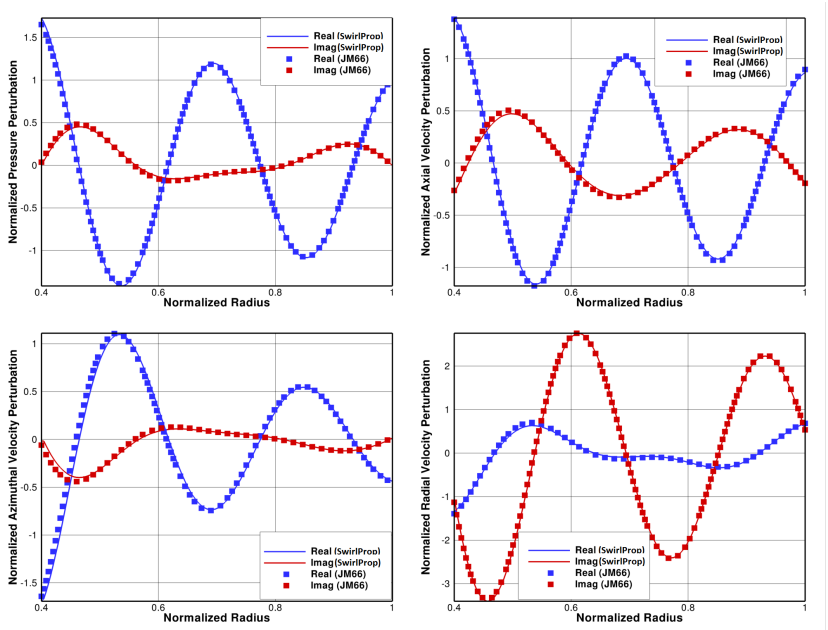

Fig. 5.47 – Comparison between eigenvectors obtained with the code developed in this work and results from JM66 for the fifth radial mode downstream. Mode order $m = -4$, reduced frequency $k = 20$, hub to tip ratio $\sigma = 0.4$, magnitude of vortex swirl $\Gamma^* = 0.15$ and liner impedance $z = 2 - 1.5i$.

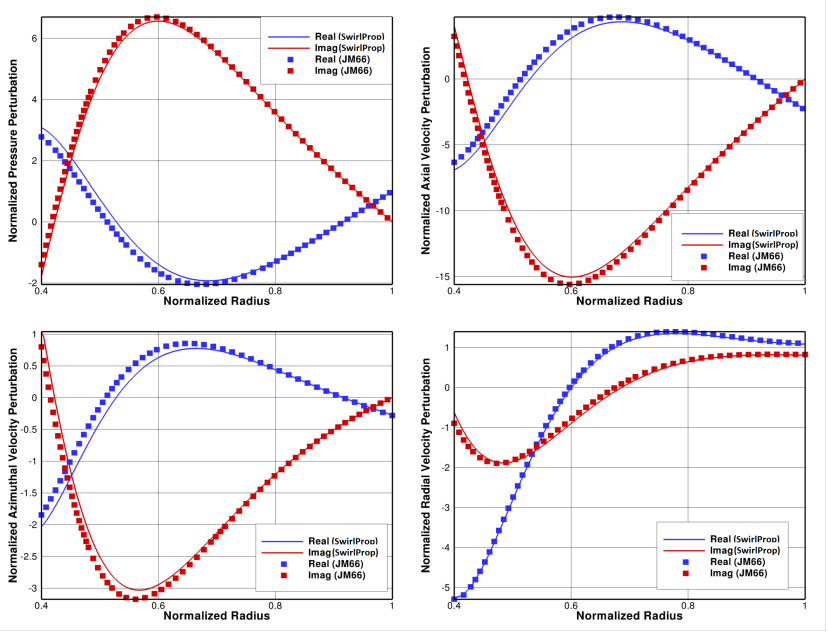

Fig. 5.48 – Comparison between eigenvectors obtained with the code developed in this work and results from JM66 for the first radial mode upstream. Mode order $m = -4$, reduced frequency $k = 20$, hub to tip ratio $\sigma = 0.4$, magnitude of vortex swirl $\Gamma^* = 0.15$ and liner impedance $z = 2 - 1.5i$.

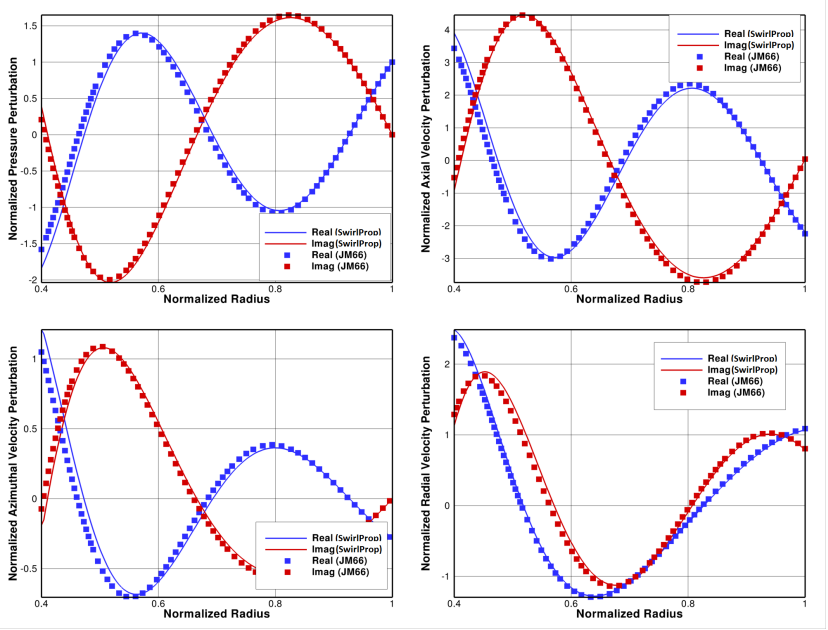

Fig. 5.49 – Comparison between eigenvectors obtained with the code developed in this work and results from JM66 for the second radial mode upstream. Mode order $m = -4$, reduced frequency $k = 20$, hub to tip ratio $\sigma = 0.4$, magnitude of vortex swirl $\Gamma^* = 0.15$ and liner impedance $z = 2 - 1.5i$.

Although only the first five modes upstream and downstream were to be presented, the sixth mode upstream will also be presented to seek further clarification. The results from the current code and the JM66 code does not agree for this case. This mode has a characteristic of a surface mode [49] and most of its power content is located in the inner wall.

If the results are normalised by the inner radius, results look slightly better, as shown in Figure 5.54. However, real and immaginary results obtained from both codes are inverted.

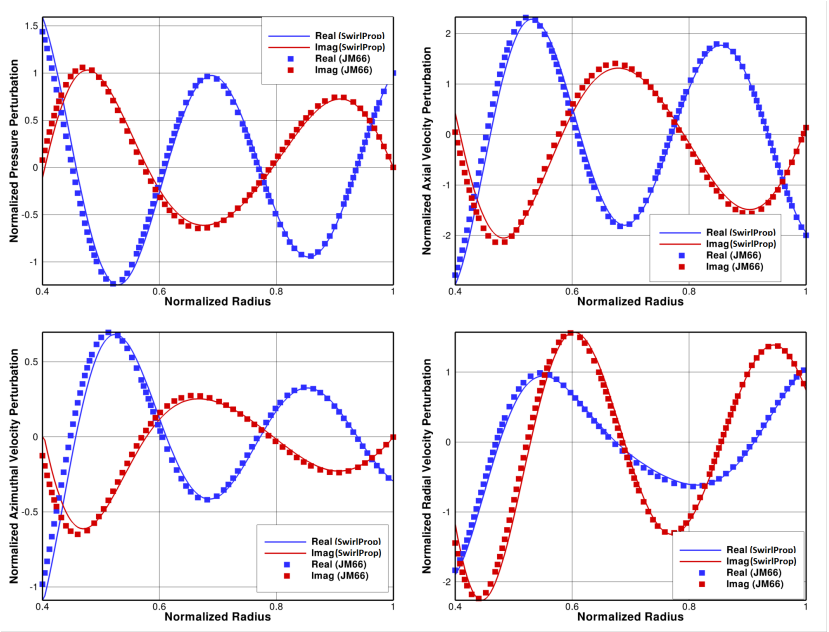

Fig. 5.50 – Comparison between eigenvectors obtained with the code developed in this work and results from JM66 for the third radial mode upstream. Mode order $m = -4$, reduced frequency $k = 20$, hub to tip ratio $\sigma = 0.4$, magnitude of vortex swirl $\Gamma^* = 0.15$ and liner impedance $z = 2 - 1.5i$.

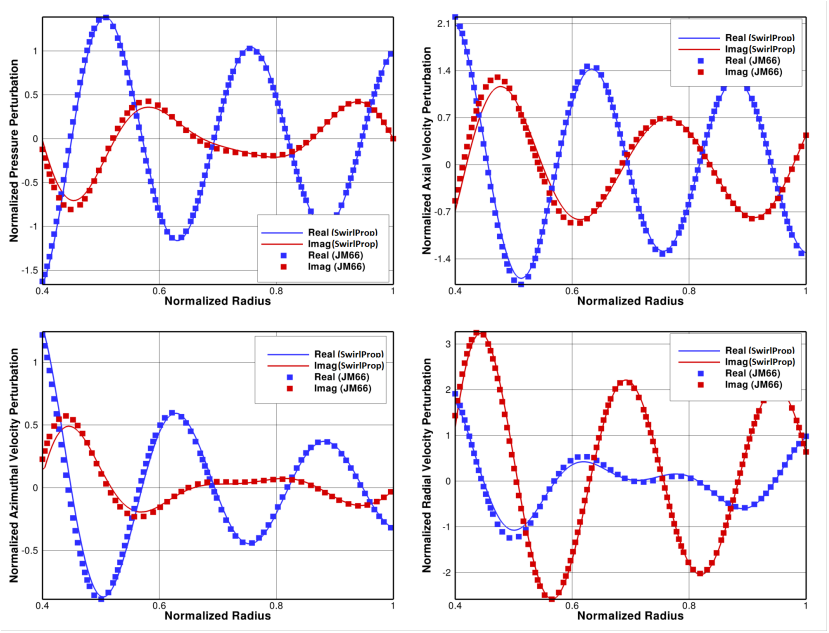

Fig. 5.51 – Comparison between eigenvectors obtained with the code developed in this work and results from JM66 for the fourth radial mode upstream. Mode order $m = -4$, reduced frequency $k = 20$, hub to tip ratio $\sigma = 0.4$, magnitude of vortex swirl $\Gamma^* = 0.15$ and liner impedance $z = 2 - 1.5i$.

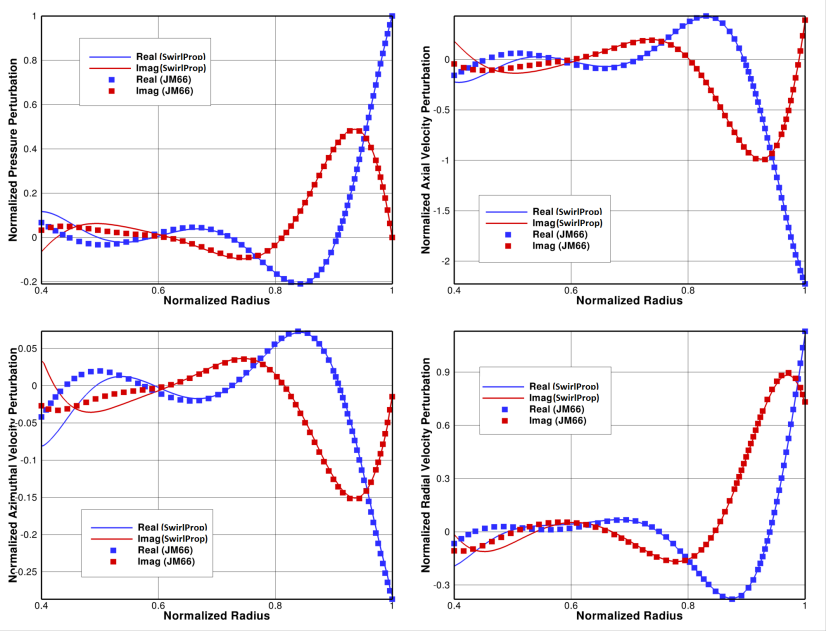

Fig. 5.52 – Comparison between eigenvectors obtained with the code developed in this work and results from JM66 for the fifth radial mode upstream. Mode order $m = -4$, reduced frequency $k = 20$, hub to tip ratio $\sigma = 0.4$, magnitude of vortex swirl $\Gamma^* = 0.15$ and liner impedance $z = 2 - 1.5i$.

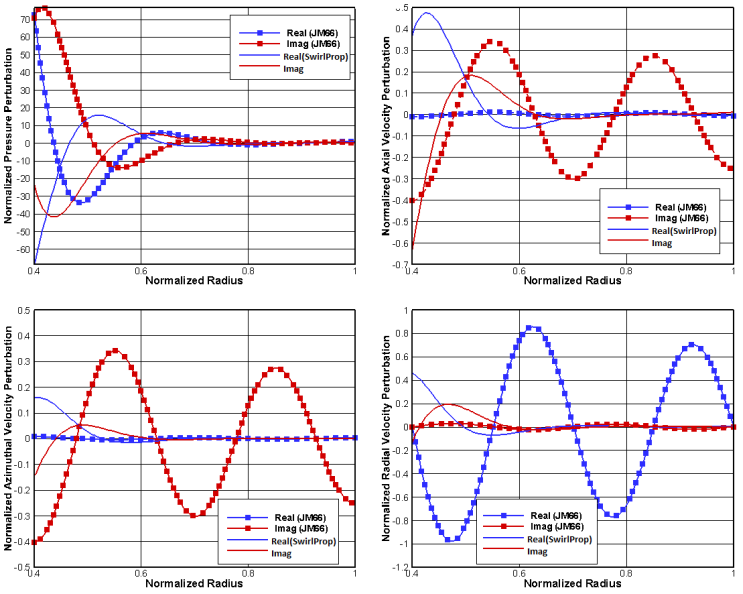

Fig. 5.53 – Comparison between eigenvalue results from the code developed in this work and results from JM66 fot the sixth radial mode upstream. Mode order $m = -4$, reduced frequency $k = 20$, hub to tip ratio $\sigma = 0.4$, magnitude of vortex swirl $\Gamma^* = 0.15$ and liner impedance $z = 2 - 1.5i$.

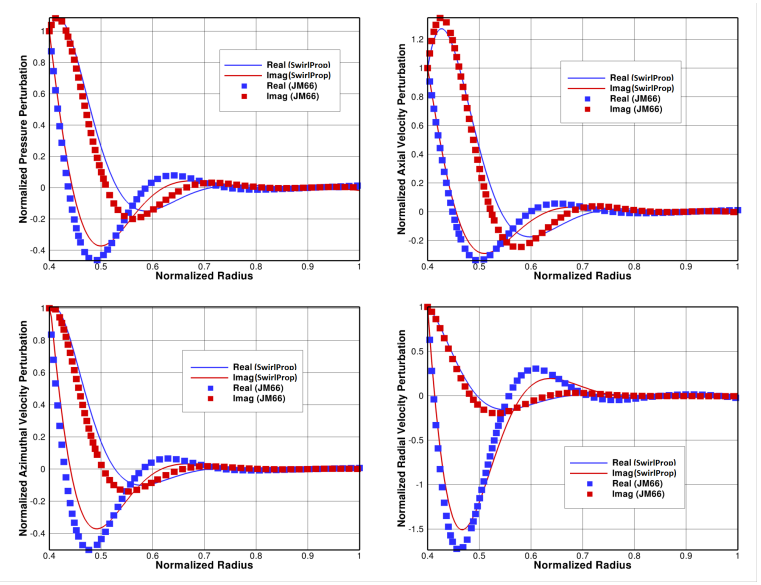

Fig. 5.54 – Comparison between eigenvalue results from the code developed in this work and results from JM66 fot the sixth radial mode upstream. Mode order $m = -4$, reduced frequency $k = 20$, hub to tip ratio $\sigma = 0.4$, magnitude of vortex swirl $\Gamma^* = 0.15$ and liner impedance $z = 2 - 1.5i$.

5.3 The particular case of the Hard-Walled Boundary Condition- Further Details

The implementation of the Ingard Myers boundary condition in the swirling flow code was introduced in section 4.2. As a particular case, the different ways to impose the hard-wall boundary condition are detailed in section 4.2.3 as well as the specific case of the hard-walled boundary condition implemented in the SwirlProp code.

So far, it was observed in the bibliographic review that the hard-walled boundary condition has been implemented by other authors in the velocity field. In the current code a different way to impose the boundary condition is proposed. The boundary-condition is implemented in the pressure field, satisfying at the same time the condition that the pressure gradient at the wall is zero and the radial velocity at the wall is also zero.

The comparison between the two ways to impose the hard-walled boundary condition as a special case of the Ingard-Myers boundary condition is presented in this section for the case of the plane wave, with uniform axial flow ($Mx = 0$), mode $m = 0$, He=10, hub-to tip ratio 0.3. To provide evidence that this is not an artifact of the filter used, results are presented before and after applying the filter. The comparison between axial wavenumbers obtained by imposing the boundary condition in the pressure and in the velocity field and the analytic solution are presented in the table 5.3.1. Those are non-filtered results. Filtered results are presented in table 5.3.2.

It is observed that when the boundary condition is imposed in the velocity field, instead of obtaining a single axial wavenumber $k_x = -10$, a pair of acoustic wavenumbers are obtained ($k_x = -10 - 6.29x10^{-15}i$ and $k_x = -10$). The same happens for $k_x = 10$ in which the a pair of acoustic wavenumbers $k_x = +10 - 1.92x10^{-14}i$ and $k_x = +10 + 3.23x10^{-14}i$ are obtained. One of the reasons why the occurence of those "twin axial wavenumbers" might not have been noticed in the past by other authors is because Finite difference schemes regard filters to eliminate spurious modes that often mask these axial wavenumbers. Also, in this case for example the immaginary part is very small and can be easily disregarded.

Non-filtered results		
Analytic	Pressure	Velocity
-4.13680	-4.13679 + 3.18015e-14 i	-4.13679 + 3.89439e-14 i
+4.13680	+4.13679 - 9.74101e-15 i	+4.13679 - 1.24449e-14 i
-8.82360	-8.82359 + 5.45442e-14 i	-8.82359 + 4.28579e-14 i
+8.82360	+8.82359 - 2.45369e-14 i	+8.82359 - 3.47594e-15 i
-10.0000	**-10.0000 - 7.96251e-16 i**	**-10.0000 + 0.0000 i**
		-10.0000 - 6.29254e-15 i
+10.0000	**+10.0000 - 1.92093e-14 i**	**+10.0000 + 3.23466e-14 i**
		+10.0000 - 2.39876e-14 i
	-6.21665 - 2.06092e-13 i	-6.56398 + 9.32620e-15 i
	+6.21665 + 2.15959e-13 i	+6.56398 - 1.033650e-14 i
-5.6016e-16 - 9.1481 i	+6.36015e-14 - 9.14807 i	+1.02697e-14 - 9.14808 i
+5.6016e-16 + 9.1481 i	-6.14497e-14 + 9.14808 i	-1.37797e-14 + 9.14808 i
	-2.68153e-14 + 11.6961 i	-1.43116e-14 + 11.4773 i
	+1.94165e-14 - 11.6961 i	7.54389e-15 - 11.4773 i
-9.1791e-16 - 14.991 i	-5.33687e-14 + 14.9905 i	-6.65472e-15 - 14.9905 i
+9.1791e-16 + 14.991 i	4.97698e-14 - 14.9905 i	-4.01644e-15 + 14.9905 i
-1.2338e-15 - 20.150 i	-2.92991e-13 - 20.1498 i	-3.22287e-14 - 20.1494 i
+1.2338e-15 + 20.150 i	+1.28683e-13 + 20.1498 i	1.48475e-14 + 20.1494 i
	+2.40681e-13 - 20.6718 i	3.82068e-14 - 20.5450 i
	-9.12201e-14 + 20.6718 i	-2.32323e-14 + 20.5450 i
-1.5340e-15 - 25.052 i	-4.13619e-14 + 25.0508 i	-1.47065e-14 + 25.0505 i
1.5340e-15 + 25.052 i	-2.05551e-14 - 25.0508 i	-8.64222e-16 - 25.0505 i
	-1.53161e-13 + 28.8318 i	-3.91809e-15 - 28.7399 i
	+8.40726e-14 - 28.8318 i	5.59146e-14 + 28.7399 i
-1.8262e-15 - 29.824 i	-1.16390e-13 - 29.8216 i	0.00000 - 29.8212 i
1.8262e-15 + 29.824 i	+1.39952e-13 + 29.8216 i	1.90168e-14 +29.82112 i
-2.1137e-15 - 34.519 i	-1.40567e-15 - 34.5144 i	9.36499e-14 -34.51413 i
2.1137e-15 + 34.519 i	-2.40544e-14 + 34.5144 i	2.88638e-15 +34.51413 i
	7.78260e-14 - 36.6899 i	-6.02979e-14 -36.61584 i
	-8.60882e-14 + 36.6899 i	-7.36884e-14 +36.61584 i
-2.3982e-15 - 39.166 i	-1.52266e-15 - 39.1567 i	-6.52192e-14 -39.15734 i
2.3982e-15 + 39.166 i	+5.72943e-14 + 39.1567 i	5.65678e-14 +39.15734 i
-2.6808e-15 - 43.780 i	1.22622e-13 - 43.7792 i	1.45899e-14 -43.76573 i
2.6808e-15 + 43.780 i	-1.47721e-13 + 43.7792 i	-1.70983e-13 +43.76573 i
	+7.25103e-14 + 44.3523 i	-4.26919e-14 -44.30355 i
	-5.83813e-14 - 44.3523 i	7.91482e-14 +44.30355 i
-2.9618e-15 - 48.370 i	-3.27216e-14 + 48.3521 i	-2.73155e-14 -48.34714 i
2.9618e-15 + 48.370 i	-3.14148e-14 - 48.3521 i	-1.07511e-13 +48.34714 i

Filtered results		
Analytic	Pressure	Velocity
-4.13680	-4.13679 + 3.18015e-14 i	-4.13679 + 3.89439e-14 i
+4.13680	+4.13679 - 9.74101e-15 i	+4.13679 - 1.24449e-14 i
-8.82360	-8.82359 + 5.45442e-14 i	-8.82359 + 4.28579e-14 i
+8.82360	+8.82359 - 2.45369e-14 i	+8.82359 - 3.47594e-15 i
-10.0000	-10.0000 - 7.96251e-16 i	-10.0000 + 0.0000 i
		-10.0000 - 6.29254e-15 i
+10.0000	+10.0000 - 1.92093e-14 i	+10.0000 + 3.23466e-14 i
		+10.0000 - 2.39876e-14 i
-5.6016e-16 - 9.1481 i	+6.36015e-14 - 9.14807 i	+1.02697e-14 - 9.14808 i
+5.6016e-16 + 9.1481 i	-6.14497e-14 + 9.14808 i	-1.37797e-14 + 9.14808 i
-9.1791e-16 - 14.991 i	-5.33687e-14 + 14.9905 i	-6.65472e-15 - 14.9905 i
+9.1791e-16 + 14.991 i	4.97698e-14 - 14.9905 i	-4.01644e-15 + 14.9905 i
-1.2338e-15 - 20.150 i	-2.92991e-13 - 20.1498 i	-3.22287e-14 - 20.1494 i
+1.2338e-15 + 20.150 i	+1.28683e-13 + 20.1498 i	1.48475e-14 + 20.1494 i
-1.5340e-15 - 25.052 i	-4.13619e-14 + 25.0508 i	-1.47065e-14 + 25.0505 i
1.5340e-15 + 25.052 i	-2.05551e-14 - 25.0508 i	-8.64222e-16 - 25.0505 i
-1.8262e-15 - 29.824 i	-1.16390e-13 - 29.8216 i	0.00000 - 29.8212 i
1.8262e-15 + 29.824 i	+1.39952e-13 + 29.8216 i	1.90168e-14 +29.82112 i
-2.1137e-15 - 34.519 i	-1.40567e-15 - 34.5144 i	9.36499e-14 -34.51413 i
2.1137e-15 + 34.519 i	-2.40544e-14 + 34.5144 i	2.88638e-15 +34.51413 i
-2.3982e-15 - 39.166 i	-1.52266e-15 - 39.1567 i	-6.52192e-14 -39.15734 i
2.3982e-15 + 39.166 i	+5.72943e-14 + 39.1567 i	5.65678e-14 +39.15734 i
-2.6808e-15 - 43.780 i	1.22622e-13 - 43.7792 i	1.45899e-14 -43.76573 i
2.6808e-15 + 43.780 i	-1.47721e-13 + 43.7792 i	-1.70983e-13 +43.76573 i
-2.9618e-15 - 48.370 i	-3.27216e-14 + 48.3521 i	-2.73155e-14 -48.34714 i
2.9618e-15 + 48.370 i	-3.14148e-14 - 48.3521 i	-1.07511e-13 +48.34714 i

The correspondent eigenvectors corresponding to axial wavenumbers $k_x = 10$ and $k_x = -10$ are presented in Figures 5.55 to 5.60. Axial wavenumbers obtained from the boundary condition imposed in the velocity field are presented in Figures 5.55 to 5.58 and boundary condition imposed in the pressure field are presented in Figures 5.59 to 5.60. The eigenvectors are well behaved and do not correspond to numerical errors. The difference between them is connected to the boundary condition used. The use of the boundary condition in the velocity field do not fully represent the physics of the problem. It imposes a restriction in the velocity field, but doesn't add the boundary condition $dp/dr = 0$. If the boundary condition is imposed in the pressure field, both $dp/dr = 0$ and $u_r = 0$ are satisfied.

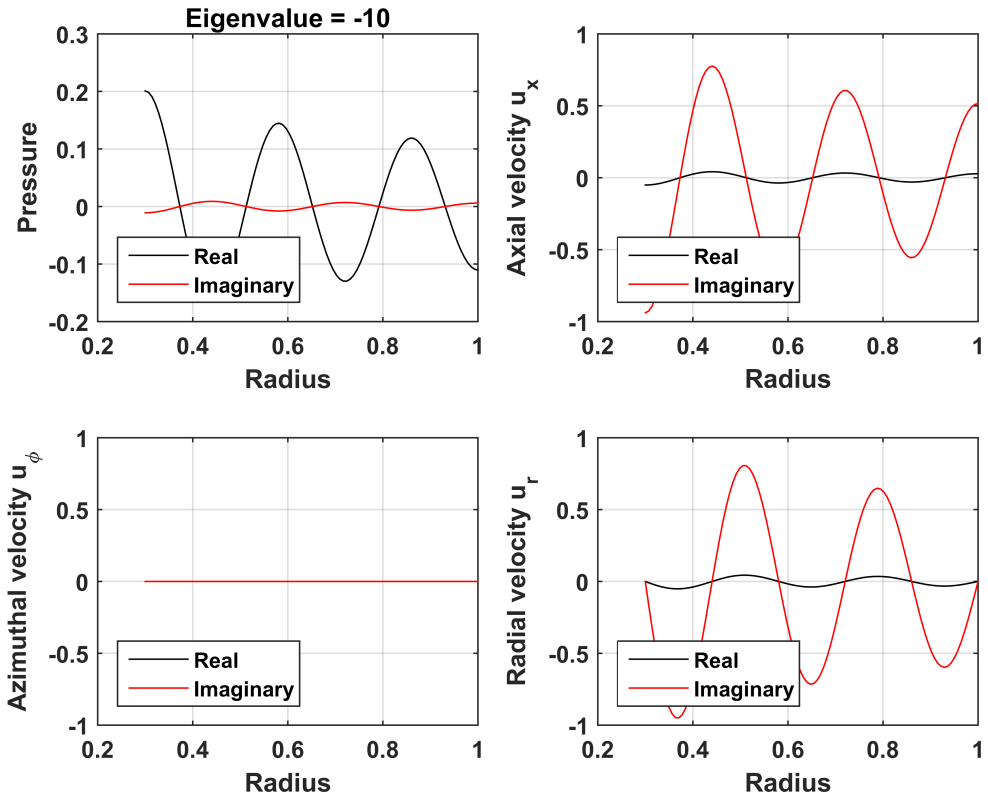

Fig. 5.55 – Velocity

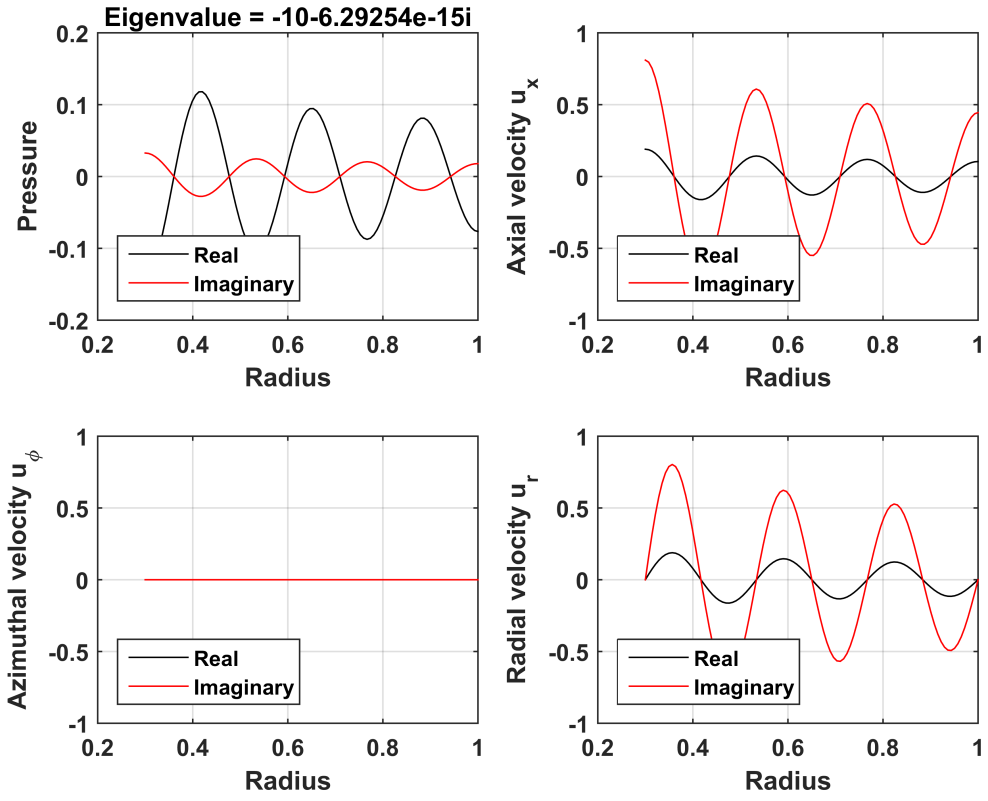

Fig. 5.56 – Velocity

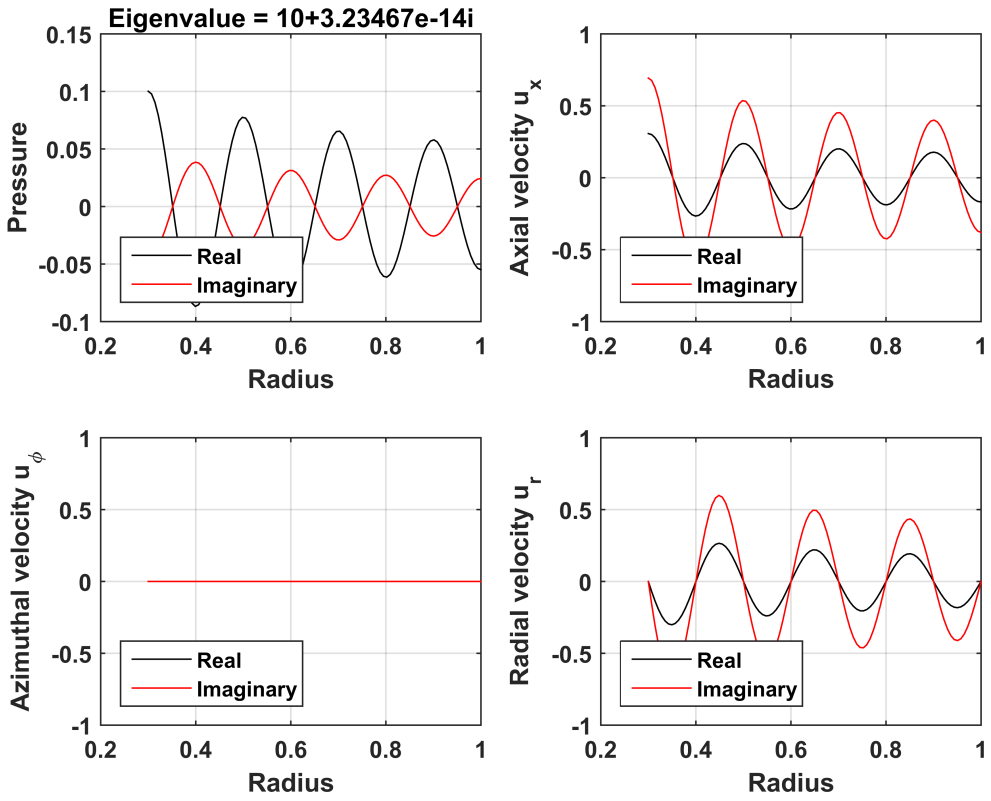

Fig. 5.57 – Velocity

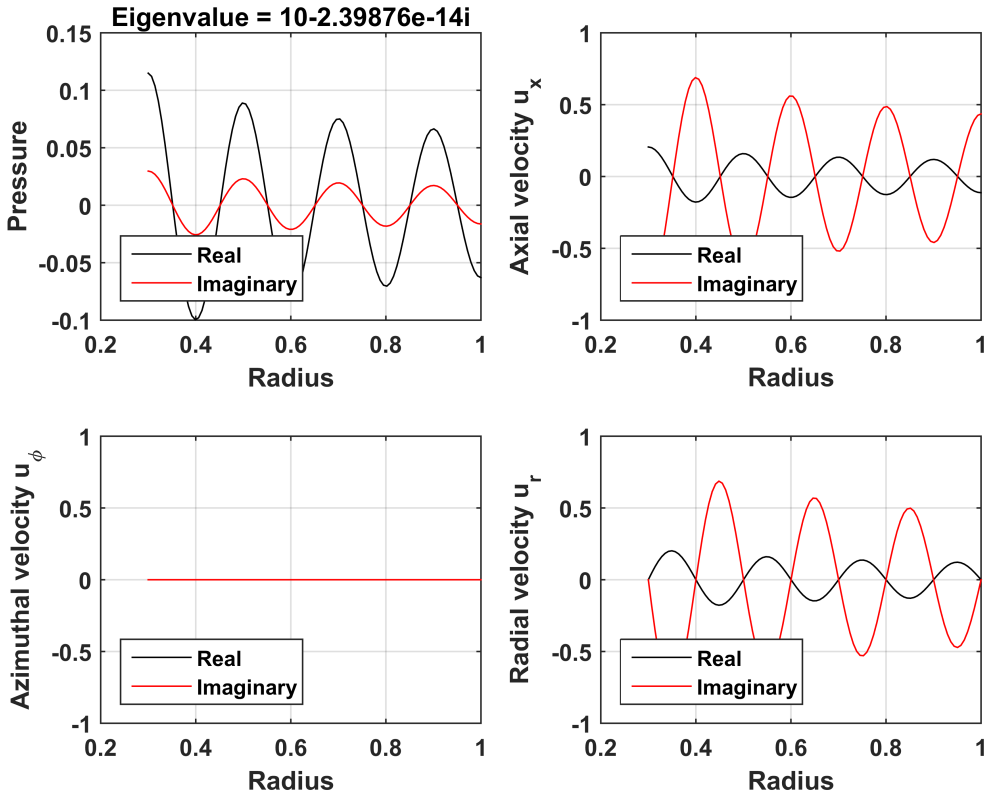

Fig. 5.58 – Velocity

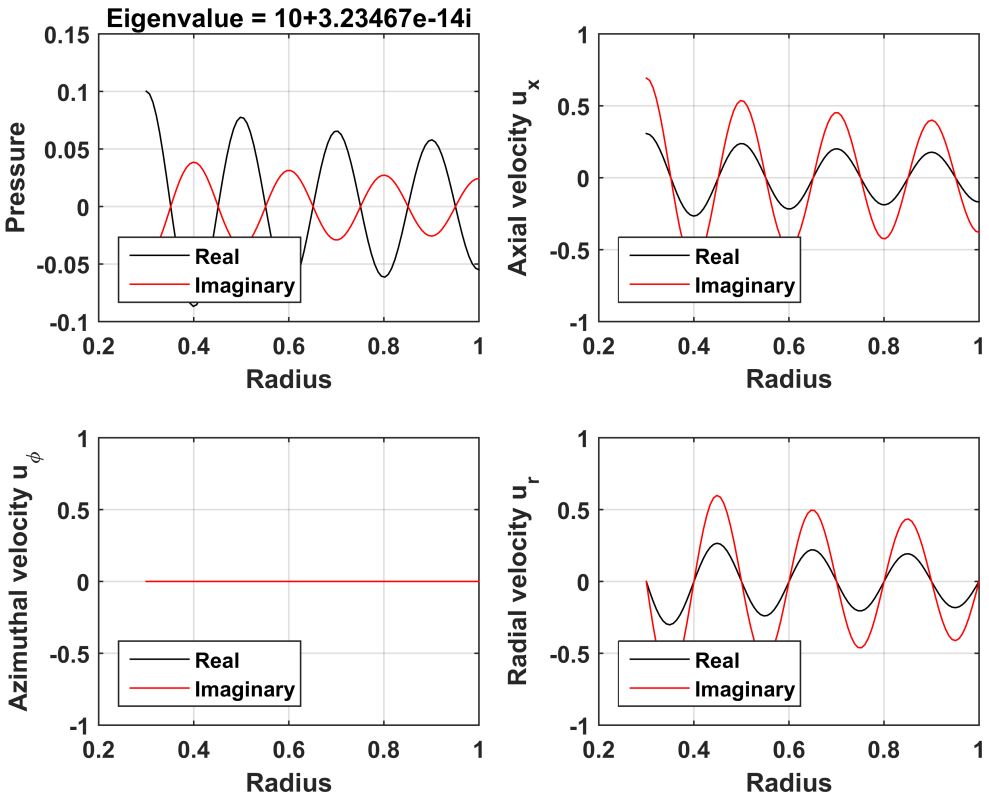

Fig. 5.59 – Pressure

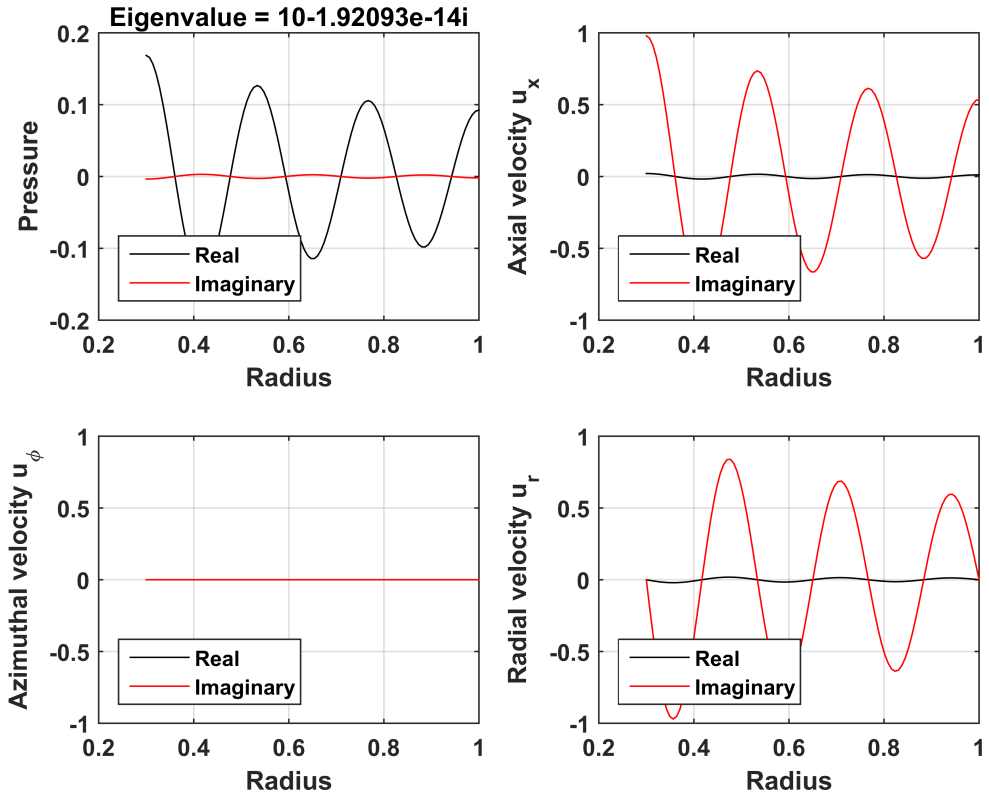

Fig. 5.60 – pressure

5.4 Summary

The two codes introduced in the previous chapter were validated. The first code is based on the Pridmore-Brown Equation. Results from this code were compared to numerical results from another finite difference code and a shooting method code. Results from the current code were also compared with analytical results. The comparison was established for uniform and sheared axial mean flows and different boundary conditions (hard walls, inner wall lined and outer wall rigid and inner wall rigid and outer wall lined).

This code named SwirlProp is based on the Linearized Euler Equations. This fourth order Finite Difference code is unique in the sense it can deal with any mean flow profile (as it is not restricted to the combination of rigid body and vortex swirl), there are no damping artefacts (as it is the case of the Rolls-Royce in-house code) and the boundary condition is imposed in the velocity field instead of in the pressure field, as detailed in sections 4.2.2, 4.2.3 and 5.3. Also, it uses a regular cartesian mesh that guarantees a better resolution.

This code was validated in two stages. First, this formulation was validated for the case without swirl by comparing results from the current code with the analytic solution and with solutions from the previous formulation based on the Pridmore-Brown equation. Secondly, the current formulation in validated for the swirling flow case by comparing with solutions from Nijboer [1] and Posson and Peake [2]. A validation against an in-house code from Rolls-Royce is also presented for a more realistic case.

Chapter 6

Comparison with Experimental Data

Results from the current Finite Difference Code were compared to experimental results from the Advanced Noise Control Fan at the Nasa Glen Research Center [3]. In this chapter the Experimental Setup is described and comparison between experiments and predictions are presented.

6.1 Experimental Setup: The Advanced Noise Control Fan

The Advanced Noise Control Fan (ANCF) was designed in the early 90's in the context of the Advanced Subsonic Technology program as a partnership between NASA, the U.S. aviation industry and the Federal Aviation Administration to support fundamental fan acoustic research. The purpose of the Advanced Noise Control Fan testbed was twofold: to develop a verified code for fan noise prediction and to use fan noise physics understanding to design new experimental tests. The Advanced Noise Control Fan (ANCF) is shown in Figure 6.1

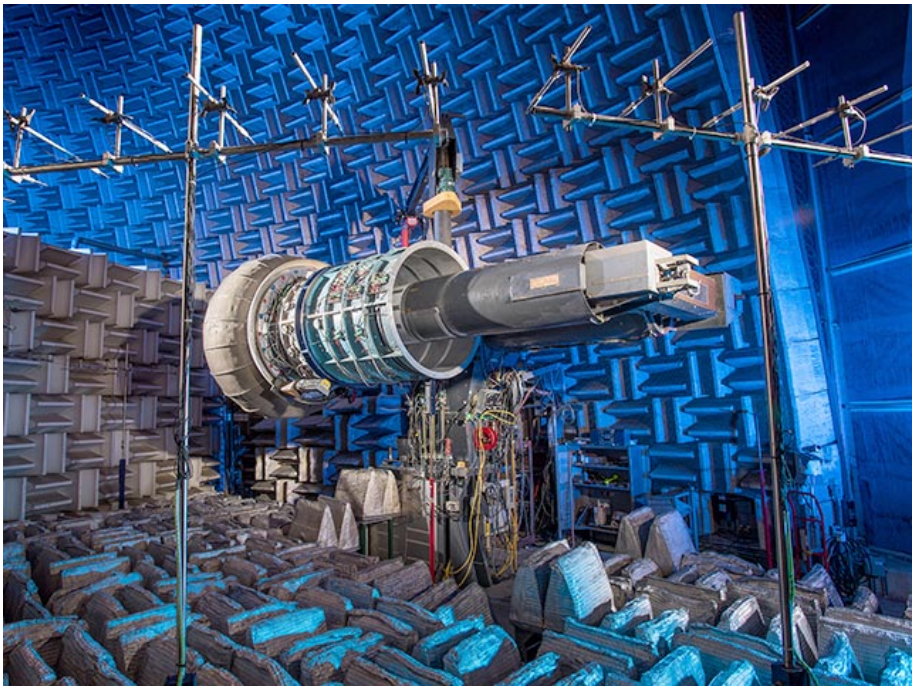

Fig. 6.1 – The Advanced Noise Control Fan (NASA C2014-5654)

The ANCF is a unique highly and flexible testbed. The tests can be undertaken using various configurations that include fan blade angle setting, stator number and spacing, variable centerbody, measurements in the absence of stators with a rotor-only configuration. It also has the ability take farfield and in-duct measurements at the same time, [3].

The ANCF is located at the Aero-Acoustic Propulsion Laboratory (AAPL) at the NASA Glenn Research Center. The AAPL is a hemispherical anechoic (above 125 Hz.) test facility used for aero-acoustic research. An exterior view of the 65-foot high dome is shown on the left of figure 6.2 and an internal view of the anechoic chamber is presented on the right.

Fig. 6.2 – Aero-Acoustic Propulsion Laboratory: External view (left) and internal view (right) [3]

The nominal shaft speed of the Advanced noise control fan is is 1800 RPM corresponding to a tip speed of 375ft/sec. The fan speed ranges from 100 to 2400rpm The Mach number is 0.15 in the inlet and the fundamental blade passing frequency (BPF) is 500Hz. Although this is a low speed fan, this is a first effort to define an experimental protocol to measure the impact of the swirl on liner insertion loss. In addition, this is a testbed that was created with the purpose of verifying numerical codes that is one of the objectives of this thesis.

6.1.1 ANCF Mechanical Description

Figure 6.3 shows a schematic of the Advanced Noise Control Fan. The duct flow consists of an inlet control device (ICD), two 12-inches-long duct sections to the rotor support, stators, and three 13-inches-long exhaust duct sections. The rig is highly interchangeable and can be easily modified according to the purpose of the test. The overall duct length and the number of duct sections can be changed and other sections such as liners are easily incorporated. The inlet control device (ICD) reduces large scale turbulence and ground vortices. It is made up of 2-inches-thick honeycomb mesh panels attached to 20 thin metal ribs along the outer contour of the surface. Both ribs and mesh are bonded to a fiberglass lip that bolts to the first inlet duct section.

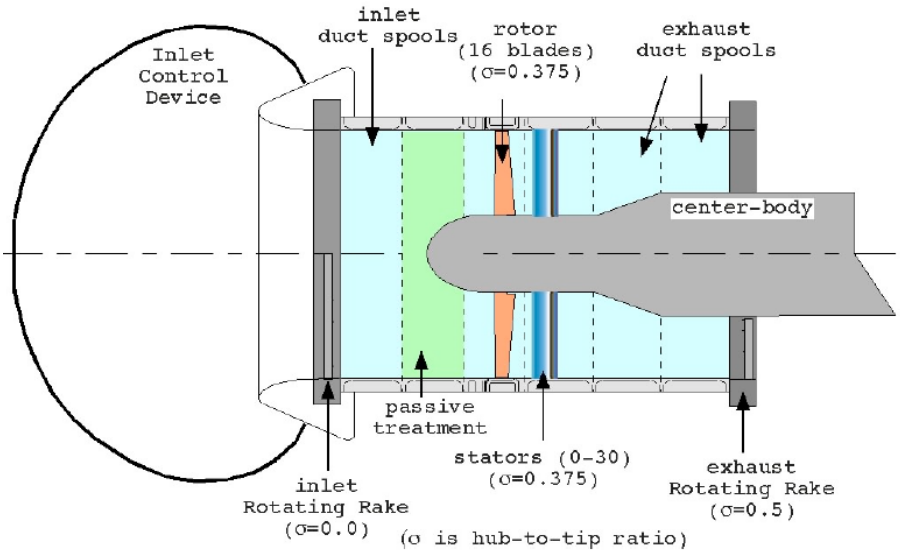

Fig. 6.3 – Schematic of the Advanced Noise Control Fan showing the position of rotor, stator, inlet control device and two rotating rakes. [3]

The ANCF rotor has 16 blades and the blade chord length is 5.25 in. A variety of stators can be used or it is possible to run the rig without the stators mounted. Some of the available stator vane counts are 13, 14, 15, 26, 28, and 30 and nominal spacings of 0.5, 1.0, and 2.0 times the rotor chord length (i.e., 2.625, 5.25, and 10.5 in.), measured at the hub from the fan blade trailing edge to the stator blade leading edge. The stators are made of machined aluminum and are identical. The fan's center-body, the rotor support ring and duct sections are rigidly supported and cantilevered from a center column mounted over this base at a 10 ft centerline height, as shown in figure 6.4

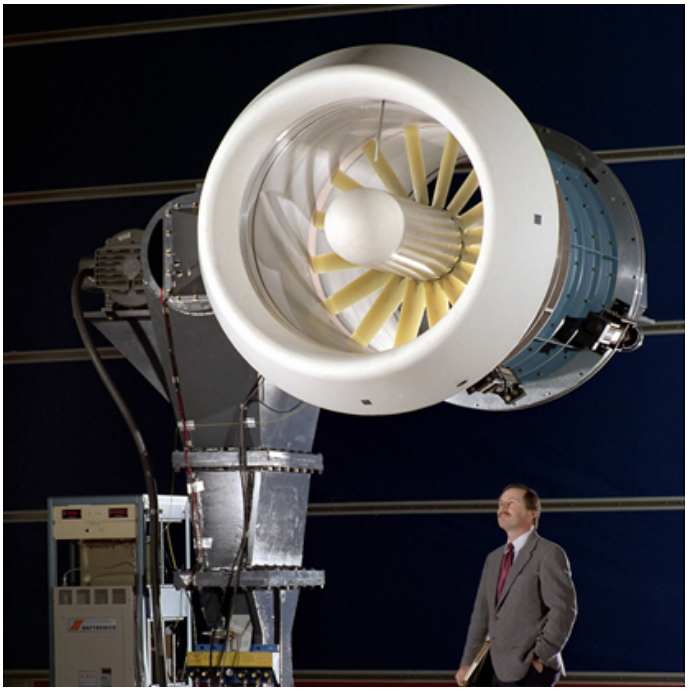

Fig. 6.4 – The Advanced Noise Control Fan. The fan's center-body, the rotor support ring and duct sections are rigidly supported and cantilevered from a center column mounted over this base at a 10 ft centerline height. [3]

6.1.2 Noise source generation and the Configurable Fan Artificial Noise Source

One possible way of generating different modes in the Advanced Noise Control Fan is to change the combination of rotor blades and stator vanes. Another possibility is to use an artificial noise source, which is the choice made for the current tests. It allows the generation of a prescribed mode field in the inlet or in the exhaust, working with one mode at a time even when both rotor and stators are mounted.

The Configurable Fan Artificial Source (CFANS) [81] is utilized to generate and control circumferential modes (m) in the audible regime. The system consists of 4 axially distributed rows, each with 16 circumferentially distributed sets of loudspeakers flush mounted on the inner wall. There are two spool pieces, each having 2 driver rows. A Labview^{TM} program is used to generate the waveforms sent to each driver independently, in the proper phase relationship to generate the desired circumferential mode. The signals to each row can be adjusted relative to one another to effect the radial distribution, if desired. The practical limits of the system are $-7 < m < 7$, and frequency $< 1500Hz$. A schematic is presented in figure 6.5. A photograph of the installation for this test program is presented as figure 6.10.

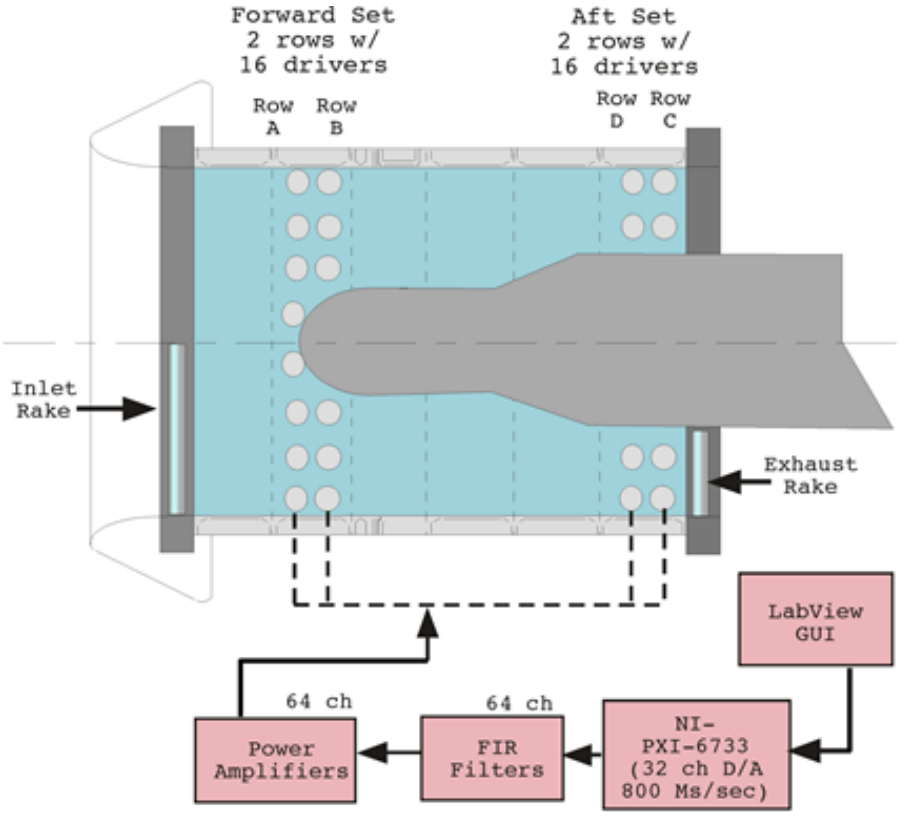

Fig. 6.5 – Schematic of the Configurable Fan Artificial Noise System (CFANS) showing the CFANS in the inlet (A+B) and the CFANS in the exhaust (C+D) and the two rotating rakes (inlet and exhaust) that are described in the next section. [4]

6.1.3 The Rotating Rake Turbofan Duct Mode Measurement System

The modal content is measured using a rotating radial microphone rake. The rotating rake design was based in two principles: (1) Each circumferential mode spins with a unique discrete speed and (2) By slowly rotating an array of microphones in phase with the shaft rotation and with a speed that is an exact fraction of the shaft speed, there is a relative movement between the microphones and the source that causes a doppler shift. Based on those two principles, the frequency is separated as a function of the mode order and the rotation speed. Figure 6.6 shows the sound pressure level spectrum of a single microphone when the rake is stationary on the left and when the rake is rotating on the right. Modes are separated about the fundamental shaft order 16 and the rotor-stator interaction mode is clearly seen.

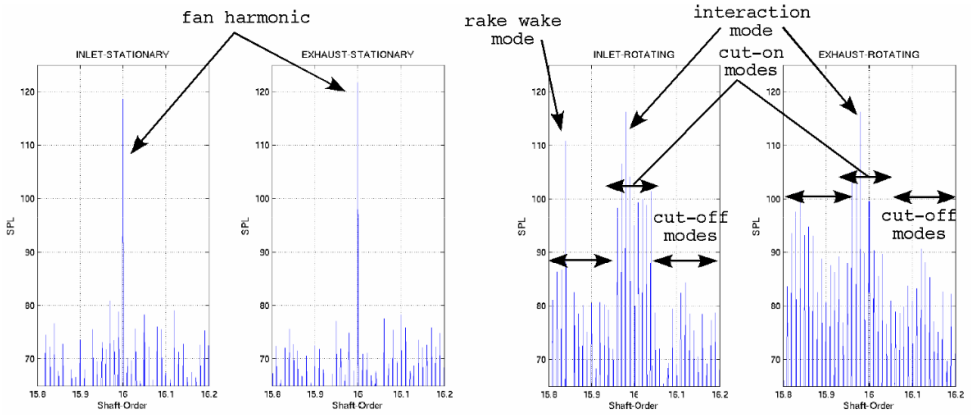

Fig. 6.6 – spectrum of a single microphone when the rake is stationary (left) and when the rake is rotating (right) [4]

The pressure time signals of each microphone is acquired and stored. The rotating rake is able to record and store long continuous time signals (around 5 min). The time-history is time domain averaged and the FFT is computed, reducing the data to the complex magnitude of each Doppler-shifted circunferential mode at each radial location. The modal pressure are computed from the least-squares-fit of radial Bessel functions to the real pressure profile [4] .

The modal power amplitude is calculated by

$$P = \pm \frac{\pi R^2 (1-\sigma^2)}{\rho_0 c_0} |\sqrt{1-M^2}|^4 \mathrm{Re}\left\{ \frac{\sqrt{1-\frac{1}{\zeta^2}}}{1 \pm \sqrt{M\frac{1}{\zeta^2}}} \right\} |p|^2, \tag{6.1}$$

where ζ is the cut-off ratio and p is the modal pressure amplitude . The derivation for Eq. and further details regarding post-processing can be found in reference [4]. While this analysis is based on zero swirl eigenmodes, it is applied for the case with swirl as well.

Typical data output showing among other information the mode power for circunferential mode $m = 2$ and radial modes $n = 0$ and $n = 1$ calculated at the inlet rake is given by Figure 6.7.

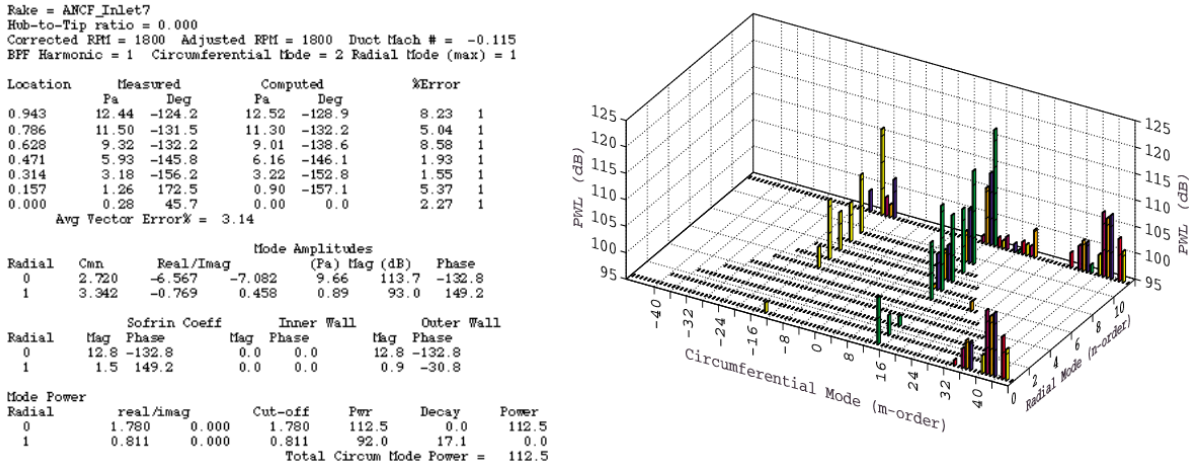

```
Rake = ANCF_Inlet7
Hub-to-Tip ratio = 0.000
Corrected RPM = 1800  Adjusted RPM = 1800  Duct Mach # =  -0.115
BPF Harmonic = 1   Circumferential Mode = 2 Radial Mode (max) = 1

Location      Measured          Computed          %Error
              Pa     Deg        Pa     Deg
0.943       12.44  -124.2     12.52  -128.9       8.23    1
0.786       11.50  -131.5     11.30  -132.2       5.04    1
0.628        9.32  -132.2      9.01  -138.6       8.58    1
0.471        5.93  -145.8      6.16  -146.1       1.93    1
0.314        3.18  -156.2      3.22  -152.8       1.55    1
0.157        1.26   172.5      0.90  -157.1       5.37    1
0.000        0.28    45.7      0.00     0.0       2.27    1
      Avg Vector Error% =  3.14

                          Mode Amplitudes
Radial   Cmn       Real/Imag          (Pa) Mag (dB)    Phase
  0      2.720    -6.567    -7.082     9.66   113.7   -132.8
  1      3.342    -0.769     0.458     0.89    93.0    149.2

                Sofrin Coeff       Inner Wall        Outer Wall
Radial     Mag  Phase          Mag  Phase          Mag  Phase
  0       12.8 -132.8          0.0    0.0         12.8 -132.8
  1        1.5  149.2          0.0    0.0          0.9  -30.8

Mode Power
Radial        real/imag          Cut-off     Pwr      Decay     Power
  0          1.780     0.000      1.780     112.5        0.0     112.5
  1          0.811     0.000      0.811      92.0       17.1       0.0
                                    Total Circum Mode Power =     112.5
```


Fig. 6.7 – Typical data output showing among other information the mode power for circunferential mode $m = 2$ and radial modes $n = 0$ and $n = 1$ calculated at the inlet rake [4]

6.1.4 Assembly of Liner for the Advanced Noise Control Fan

The honeycomb liner core was manufactured separately and incorporated into an existing duct section. Starting from the outer radius working inward, the liner assembly was as follows: First, 2 layers of carpet padding were laid in the spool in order to provide a compression mechanism for the entire assembly. This mitigated the geometric imperfections of the spool wall, ultimately allowing for a tight fit.

Next, a hard rubber sheet was laid down. This provided a seal at the base of the honeycomb core to prevent acoustic leakage between the cells. On top of this was placed the honeycomb core. A fine wire resistance mesh (nominal flow resistance of 60 cgs Rayls) was placed on top of the core, followed by a coarse screen covering approximately 37 percent of the open area. The screen was fastened in such a manner to compress the entire lay-up securely and provide a flush flow surface in the duct. The liner depth is 0.0508m (2.0 in) and the liner length is 0.381 m (16 in). Figure 6.8 shows the liner schematic.

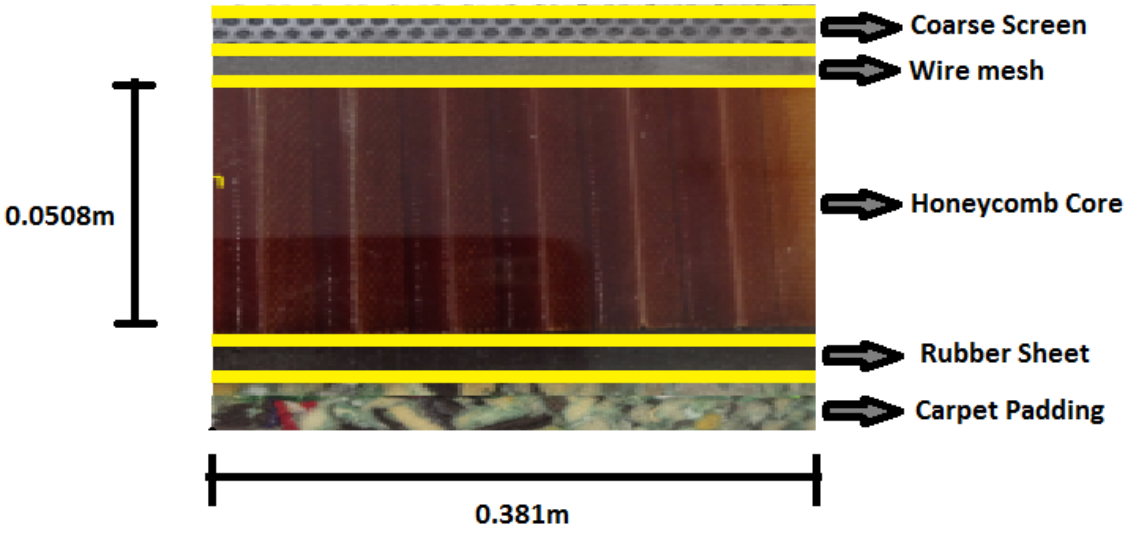

Fig. 6.8 – Schematic of Liner build up

The normalized impedance of a 2*inx*2*in* flat sample of the liner assembly as measured in the NASA Langley Normal Impedance Tube (NIT)[**?**] is shown in figure 6.9.

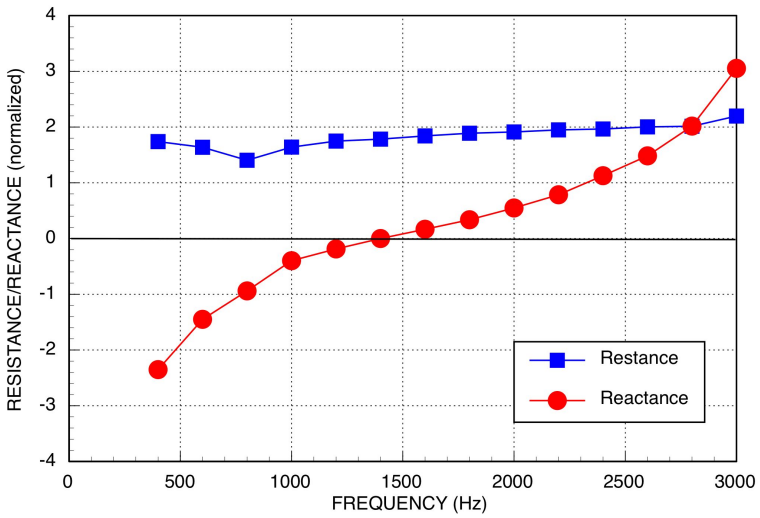

Fig. 6.9 – Liner Assembly Impedance Measured in LaRC NIT

6.1.5 Configurations Tested

The experimental portion of this project test goal was to measure the liner insertion loss in swirl and no-swirl flow conditions, in the flow direction and against the flow. Figure 6.10 shows the experimental setup and represents the rotating rake and the artificial noise source systems presented in Figures 6.3 and 6.5 superposed.

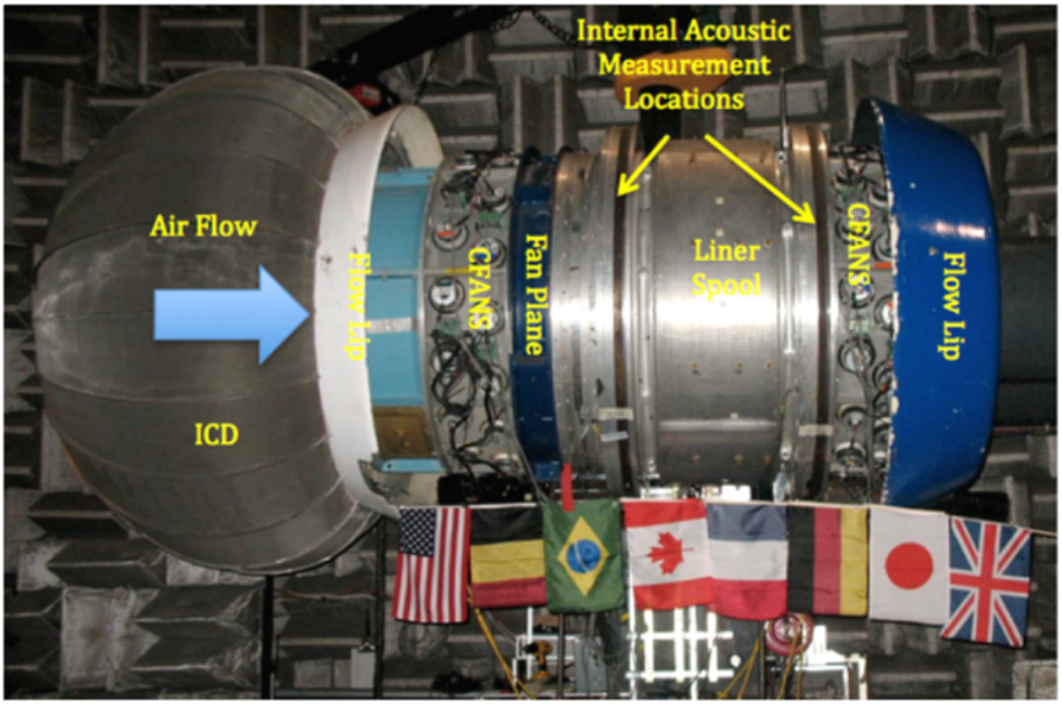

Fig. 6.10 – External view of ANCF Showing Relevant Locations

Figure 6.10 shows the flow path that is assembled in the following order: Inlet Control Device, the CFANS placed in the inlet, the rotor (and the stator when it is not absent), the first rotating rake, a hard-walled or lined duct, the second rotating rake and the second CFANS in the exhaust. First, the CFANS at the inlet generate a prescribed noise field that propagates through the duct with the flow and is measured in the inlet rotating rake and in the exhaust rotating rake. Then, the CFANS at the exhaust generate a prescribed noise field that propagates through the duct against the flow and is measured in the exhaust rotating rake and in the inlet rotating rake.

Figures 6.11 show schematic of the experimental setups for the case where both rotor and stator are mounted and figure 6.12 for the rotor-only configuration. Swirl is removed by the presence of the stator vanes, and is present when the fan is run without the stator vanes installed (rotor alone)[82]. This may not be absolutely correct, but it is a reasonable assumption. Modes propagating with the flow are generated by the inlet CFANS (actuator rows $A+B$) and measured by rotating rakes placed immediately upstream of the liner (forward rotating rake) and immediately downstream of the liner (aft rotating rake). Modes propagating against the flow are generated by the exhaust CFANS (actuator row C) ; modes are also measured at the two rake locations. A single circumferential mode is generated at a time. Each of these cases was tested with the liner installed, and with the liner taped over to represent the hard-wall case. Also, the cases were repeated with the fan rotating very slowly to represent the no-flow case to avoid that the rotor and the stator generate an interference because of blockage. The tests were performed for 500 Hz and 1.0 KHz, which correspond to Helmholtz numbers of 5.6 and 11.2 respectively. The Helmholtz number is calculated here based on the outer radius as $He = kR_{out}$ and the outter radius is 0.6096 m.

The transmission loss is measured by the difference in the power measured by those two rakes (in the direction of acoustic propagation) for the lined test minus the transmission loss measured by the difference in the power measured by those two rakes for the hard-walled test, that is:

$$\mathrm{TL} = \mid [(\mathrm{PWL}_{\mathrm{FWD,Lined}}) - (\mathrm{PWL}_{\mathrm{AFT,Lined}})] - [(\mathrm{PWL}_{\mathrm{FWD,Hard}}) - (\mathrm{PWL}_{\mathrm{AFT,Hard}})] \mid \tag{6.2}$$

In Eq. 6.2 the theoretical value for the transmission loss in a hard-walled duct is zero. However, this is not always the case for experimental results. The transmission loss for a hard-walled duct is incorporated in this equation as an attempt to compensate for any non-zero values in the hard-walled case.

Three aspects should be emphasized. First, this thesis shows comparisons for 500 Hz tests only, the reason being that experimental results for those tests show a lower transmission loss for the hard-walled case.

Secondly, the hub-to-tip ratio is assumed to be constant in the formulation of the current finite difference code, but this is not absolutely true for the Advanced noise control fan. The hub-to-tip ratio is 0.375 at the forward rake and 0.5 in the aft rake.

Finally, the change in the geometry can cause the second radial mode (n=1) at lower m-orders to cut-off as it propagates down the duct. This can have significant effect on the modes measured between the two rake stations due to reflections resulting from a mode cutting off. The modes

generated their respective cut-off ratios at relevant duct locations are presented in Table 6.1.

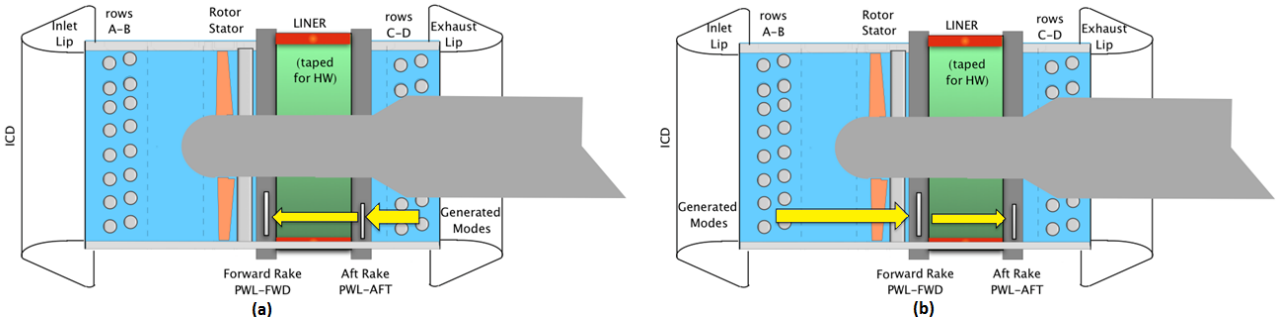

Fig. 6.11 – Rotor-Stator Installed for No-Swirl Condition. (a) Propagation against the flow (b) Propagation with the flow

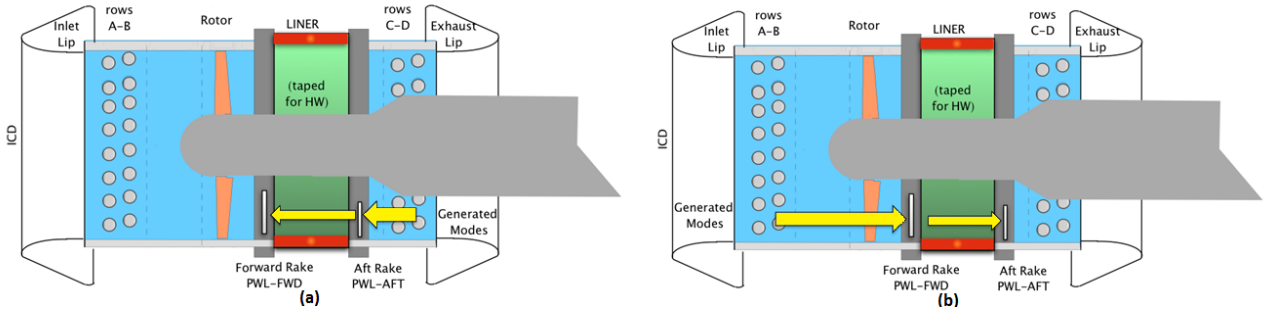

Fig. 6.12 – Rotor-Alone Installed for Swirl Condition. (a) Propagation against the flow (b) Propagation with the flow

Table 6.1 – Typical Modes Generated for Parametric Analysis using CFANS. Values for hard-wall, nominal plug flow (Daniel Sutliff, private communication)

Frequency	Modes (m,n)		Cut-off ratios	
.	m	n	FWD (rotor-stator) $\sigma_{mn} = 0.375$, M=0.13	AFT (exhaust) $\sigma_{mn} = 0.5$, M=0.15
500 Hz	0	0	∞	∞
500 Hz	0	1	1.09	0.87
500 Hz	$\pm$1	0	3.81	4.20
500 Hz	$\pm$1	1	1.03	0.89
500 Hz	$\pm$2	0	1.97	2.12
500 Hz	$\pm$3	0	1.37	1.44
500 Hz	$\pm$4	0	1.08	1.10

6.2 Comparison Between Measurements and Predictions

Results from the Finite Difference code were compared to data from the Advanced Noise Control Fan for the case of modes propagating upstream (generated by actuator C, see Figures 6.11a and 6.12a) and at the lower frequency of $500Hz$. The $500Hz$ subset of results had a smaller transmission loss for the hard-walled case and the subset of results from the actuator C was less influenced by the near acoustic field of the rotor. .

Hot-wire measurements were used to measure the axial and azimuthal mean flow profile. A fit to the hot-wire measurements for the azimuthal velocity data showed that the azimuthal velocity profile is very similar to a combination of rigid body and vortex swirl swirling flows given by eq 6.3. The rigid body swirling flow is dominant. This is the opposite of what is expected from a realistic aeronautical fan. The axial profile is close to a uniform axial flow. The actual mean flow mach profile and the fit used in the calculations that follow are shown in figure 6.13. The liner impedance is $z = 1.5 - 1.975i$

$$u_{\phi_0} = 44.05r + \frac{0.05234}{r} \tag{6.3}$$

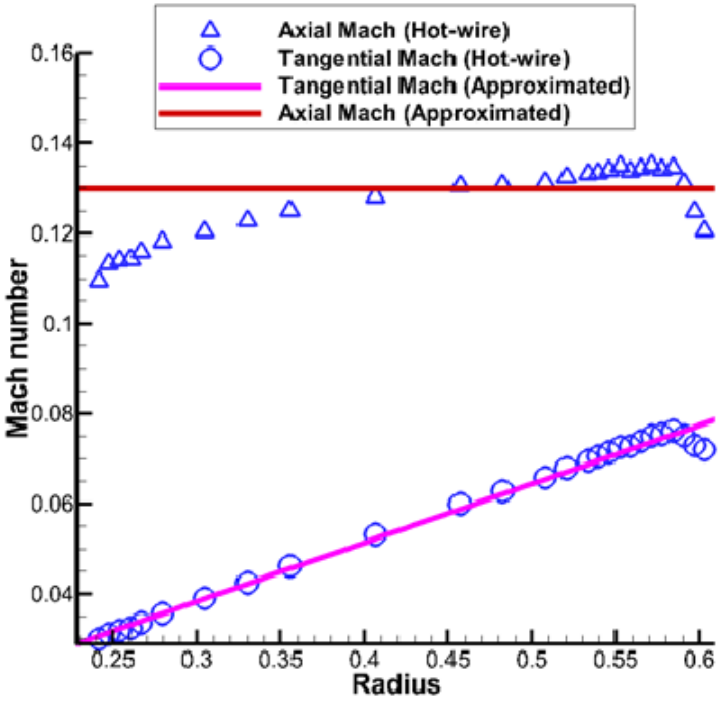

Fig. 6.13 – Mean flow

The power levels at each rake (inlet or aft), for each case (with or without acoustic liners, when swirl is present or absent) are given by the post-processed output data (see Figure 6.7). The experimental transmission loss is then calculated using eq 6.2. For the numerical results, the sound power transmission loss for a single mode is calculated as [52]

$$\mathrm{TL} = 10 \times \log_{10} \frac{\mathrm{W}_{in}}{\mathrm{W}_{out}} = 20 \times \mathrm{Imag}(\mathrm{k_x}) \times \mathrm{L} \times \log_{10} e \tag{6.4}$$

where L is the liner length and k_x is the calculated axial wavenumber for the hub-to-tip ratio 0.375 It is assumed that all the power is contained in the first radial mode. Also, scattering between hard and lined walls are not taken into account.

The transmission loss for the first radial mode for azimuthal mode orders from -4 to 4 are presented in Figure 6.14. Comparison between predicted results from the current FD code and ANCF data for (a) no flow, (b) axial flow and (c) swirling flow conditions are presented in this figure.

Figure 6.14 (A) shows the comparison for the no flow case. Symmetry in the transmission loss for $\pm$ modes is noted in the FD results and in general for the experimental results. There is also evidence of some discrepancy between measured and predicted data for mode -4. Earlier data from the ANCF show modes $m = \pm 4$ has significant reflection (Daniel Sutliff, private communication). This is also true for the uniform axial flow and swirling flow cases that will be presented later in this section. In this case, the $m = +4$ data point was not recorded and is not presented here. The correspondence between experiments and predictions is not very close for modes $m = 0$ and $m = \pm 1$. One possible reason is that the cut-off ratio of the second radial mode for mode $m = 0$, ie $(m,n) = (0,1)$, changes with the geometry (see table 6.1). This mode is cut-on in the forward rake. As it travels upstream, it becomes cut-off and creates some reflection inside the duct. This could be true, to a lesser extent for $m = \pm 1$.

The comparison for axial flows is shown in the Figure 6.14 (b) Modes $m = 0$ again show some discrepancy between measured and predicted data. The FD results are still symmetrical in axial flow, but the experimental data TL shows an increase in attenuation for the positive modes. This may indicate that the stator vanes do not remove all the swirl.

The comparison for swirling flow is shown in Figure 6.14 (c). Both the FD and the ANCF experimental data show an increase in the TL as an effect of the swirl. The agreement between the FD prediction and the ANCF data is better for the negative values of m.

The same data presented so far will be shown in a different format. A comparison between results for the three flow conditions are presented for measured and predicted data in figures 6.15 (a) and (b)

Figure 6.15 (a) shows the Transmission loss versus circumferential mode number as determined by the FD predictions. As expected for the no flow, and axial flow cases the transmission loss is symmetric with $\pm$m-order, although the transmission loss increases as a result of the axial flow. The inclusion of swirl biases the transmission loss toward negative m-orders. Since the magnitude of the swirling flow is small in this experimental setup, this variation is quite subtle. It happens because the swirling flow changes the relative phase speed of the modes. Modes that rotate against the flow (represented by negative values of m) will have a higher phase speed and become more cut-on when swirl is included. Those modes will be more attenuated when the duct is lined with acoustic treatment.

Figure 6.15 (b) presents the experimental transmission loss as measured in the ANCF. For no flow, modes $\pm$2,3 demonstrate the symmetry. The addition of flow and swirl effect the transmission loss. The experimental accuracy of the mode measurements in ANCF is known to be about 1 dB (Daniel Sutliff, private communication) , and the effects of non-uniform geometry, and the relatively low

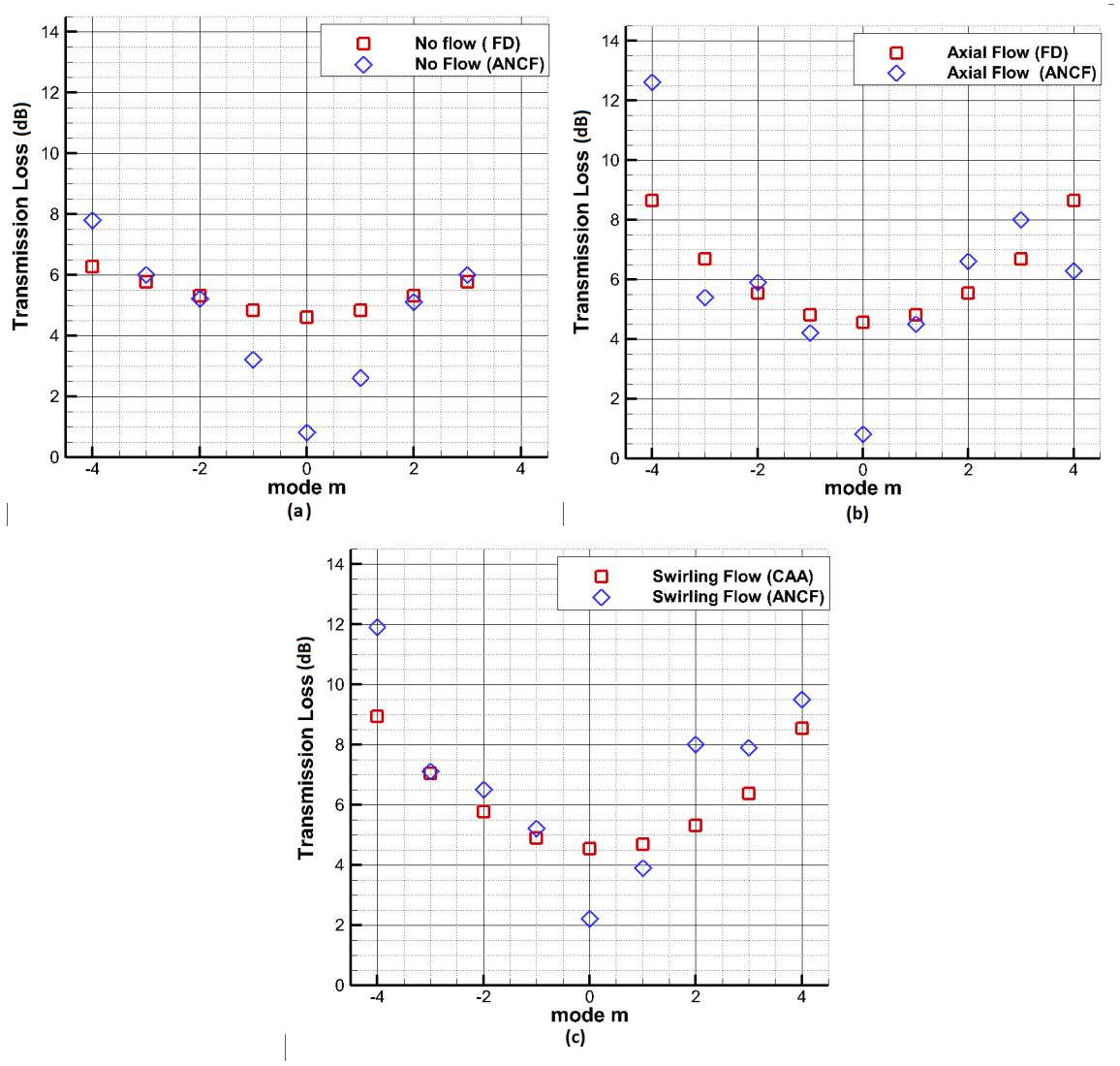

Fig. 6.14 – Comparison between predicted results from the current FD code and ANCF data for (a) no flow, (b) axial flow and (c) swirling flow conditions at $500Hz$ and impedance $z = 1.5 - 1.975i$

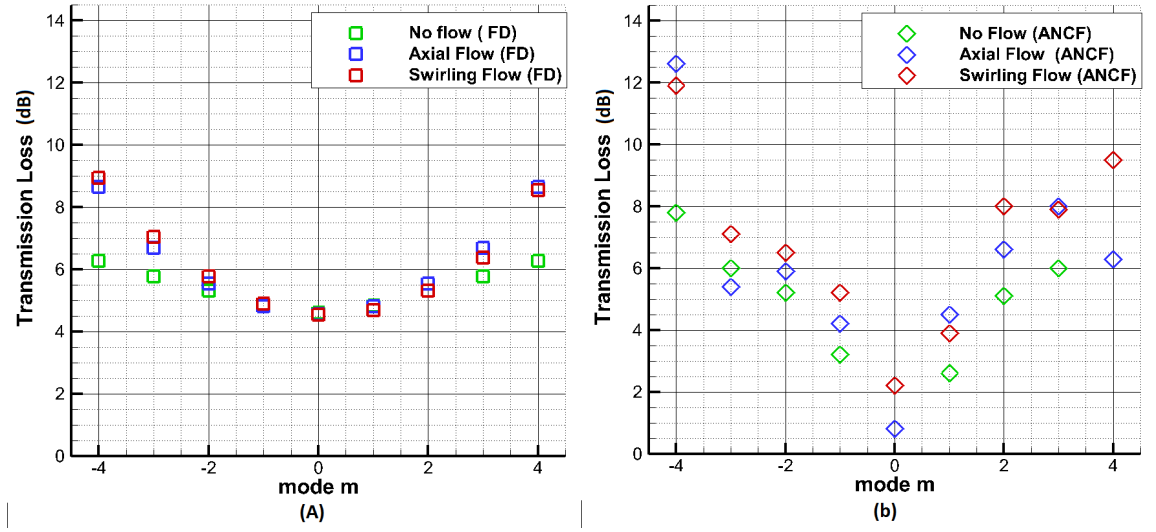

Fig. 6.15 – Comparison between results for the three flow cases (a) Computed Data (b) Experimental Data. f=500 Hz, z=1.5-1.975i

swirl magnitude results in a less clear distinction. The results are slightly more spread through the plot because those are experimental results.

6.2.1 Summary

In summary, predictions from the current FD code were compared with measurements from the Advanced Noise Control fan for axial and swirling mean flows in a hard-walled and a lined duct (z=1.5-1.975i) at the frequency of 500 Hz. The modes propagating upstream and downstream were generated one at a time using a configurable artificial noise sourse (CFANS). Predictions were compared with experimental results for no flow, axial flow and swirling flow for circunferential modes m between -4 and 4. Qualitative agreement is obtained with the measured Power Transmission loss (TL) that increases as an effect of the swirl for a prescribed impedance, but low Mach numbers and modest Transmission loss levels have made it difficult to validate the FD code thus far. To the author's knowledge, it is the first time that an experimental protocol has been designed to tackle the effect of swirling flow on interstage liners and one of the suggestions for future studies would be to repeat this protocol in a rig with higher speed. A parametric analysis for lined ducts with swirling flows for more realistic mean swirling flows is presented in the next chapter.

Chapter 7

Parametric Studies

The intent of this chapter is to analyse the effect of swirl and liners on sound propagation in the insterstage region of turbofan engines. Geometric and mean flow parameters and frequency range were carefully chosen to correspond to realistic values. In section 7.1 the effect of swirling flow *per se* is evaluated. As a first step, the effect of swirling flows on cut-on ratio of modes, axial wavenumbers and phase speeds are discussed in the absence of acoustic treatment. Section 7.2 focuses on the effect of swirling flow on optimal liner attenuation in the interstage region. A source consisting of all propagating modes with equal power in each mode is used. This simulates a broadband source downstream at the OGV propagating upstream, against the flow. Optimum impedance plots are generated for approach and take-off mean flow conditions. The effect of swirl on liner optimum impedance and reactance and optimum insertion loss is observed for a frequency range characteristic of real turbofan engines.

7.1 The Effect of Swirl in the Absence of Acoustic Treatment

The purpose of this section is twofold. Firstly, the effect of swirling flows on sound propagation in an annular duct in the absence of acoustic treatment is analysed to create a baseline for the study presented in the next section where both swirling flow and acoustic treatments are included. Secondly, a suitable multi-modal source is defined for the optimum impedance calculations in section 7.2. The modal content for this broadband source for both cases (with and without acoustic treatment), is defined based on uncorrelated cut-on acoustic modes for the hard walled case, as presented in section 7.1.3

7.1.1 Flow Parameters and Geometry

Results are presented in section 7.1 for two types of mean swirling flows: rigid body ($u_{0\phi} = \Omega^* \times r^*$) and vortex swirl ($u_{0\phi} = \frac{\Gamma^*}{r^*}$). The former is characteristic of low speed rigs such as the Advanced Noise Control Fan and the latter is characteristic of more realistic turbofan engines. The non-dimensional magnitude of vortex swirl Γ^* and rigid body swirl Ω^* vary from zero to 0.30 and frequencies correspond to Helmholtz numbers He=kR where R is the outer radius in the range 0 to 30 in the following calculations. The duct geometry is annular with an outer radius of 1m and a

hub-to-tip ratio 0.25 or 0.4. The hub-to-tip ratio 0.25 has been used by other authors in the past [60] and is used in section 7.1.2 to illustrate the effect of swirl on the axial wavenumbers. The hub-to-tip ratio 0.4 is used in the remaining calculations as a more realistic value for a large modern engine.

7.1.2 Typical Eigensolutions for the Hard-Walled Case

The effect of swirl is greater for radial modes near cut-off and tends to vanish for higher radial mode orders. The concepts of cut-off line and cut-off ratio will be used to impact of swirling flow in axial wavenumbers. The cut-off ratio for the sound propagation in uniform flows inside annular ducts was defined in equation 3.86. If the cut-off ratio is higher than one, the mode propagates. If it is lower than 1, it decays. The limiting case occurs when the cut-off ratio is equal to one. If the cut-off ratio is made equal to one in Equation 3.86 and substituted in Equation 3.85, an expression for the cut-off line is obtained and is given by

$$k_x^{cutoffline} = \frac{kM_0}{1-M_0^2} \tag{7.1}$$

The lower order circumferential modes $m = \pm 2$ were chosen to illustrate the effect of swirling flow on the axial wavenumbers. Figure 7.1 shows axial wavenumbers computed using the current FD code for a uniform axial flow (non-swirling) and for a free vortex swirl mean flow profile superposed for the co-rotating mode $m = +2$ and the contra-rotating mode $m = -2$. The other parameters used are axial Mach number $M_x = 0.3$, Helmholtz number He= 10 and hub to tip ratio $\sigma = 0.25$.
Figure 7.1 (a) shows that if the circumferential mode rotates with the flow, the radial modes become more cut-off when swirl is present. Notice that for the uniform axial flow case there are three cut-on modes in each direction, while for the swirling flow case there are two cut-on modes in each direction. Otherwise, if the circumferential mode rotates against the flow, the radial modes become more cut-on as the swirl increases, as shown in figure 7.1 (b). Notice that for the swirling flow case the cut-on axial wavenumbers are farther from the cut-off line.

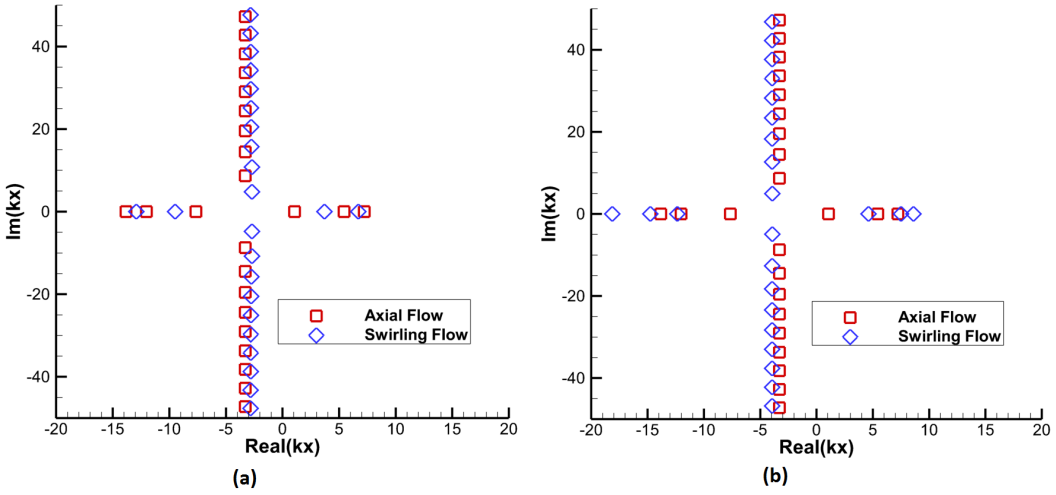

Fig. 7.1 – Comparison of axial wavenumbers with and without swirl for a (a) co-rotating mode $m = 2$ and (b) contra-rotating mode $m = -2$. Results for a vortex swirl mean flow profile $\Gamma = 0.2$ and $He = 10$.

Figure 7.2 shows similar results for a rigid-body swirling flow profile with magnitude $\Omega^* = 0.2$. Figure 7.2 (a) shows the comparison between axial wavenumbers from non-swirling and swirling flows for a co-rotating mode while Figure 7.2 (b) shows similar results for a contra-rotating mode. The trend is the same as the one presented in figure 7.1. Co-rotating modes become more cut-off and contra-rotating modes become more cut-on. When compared to results for the vortex swirl mean flow profile, the rigid body mean flow profile seems to have less influence on the axial wavenumbers. Notice that although the magnitude of the rigid body and the vortex swirl mean flows might be the same, the corresponding azimuthal mach number is higher for the vortex swirl mean flow case

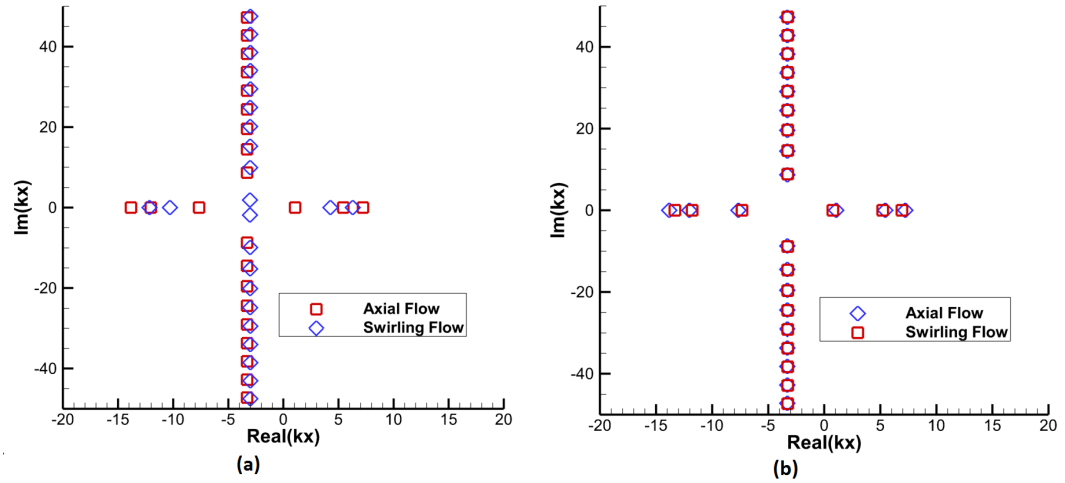

Fig. 7.2 – Comparison of axial wavenumbers with and without swirl for a (a) co-rotating mode $m = 2$ and (b) contra-rotating mode $m = -2$. Results for a rigid body swirl mean flow profile $\Omega = 0.2$ and $He = 10$.

Since the axial wavenumbers at the lower radial mode orders are more influenced by the mean swirling flow than higher order modes, the impact of swirl in the first radial mode upstream and downstream was evaluated. The frequency of excitation and the magnitude of the swirling flow were varied and the phase velocity corresponding to the first axial wavenumber upstream and downstream was calculated. Figure 7.4 (a) shows the phase velocity corresponding to the first upstream radial mode and Figure 7.4 (b) shows the phase velocity corresponding to the first downstream radial mode as a function of frequency and swirling flow magnitude for a free vortex swirl and circumferential mode $m = -2$.

It is observed that the phase speed decreases for an upstream propagating radial mode and increases for a downstream propagating radial mode as the swirling flow magnitude increases. It shows that the modes represented by those axial wavenumbers become more cut-on with the increase of the swirling flow magnitude. Notice that mode $m = -2$ spins in the opposite direction of the flow and the conclusion would be the opposite for a mode spinning with the flow. The variation of the vortex swirl magnitude is the same in both plots. However, the variation of phase speed for downstream propagating modes (Fig 7.3 right) is higher than for upstream propagating modes (Fig 7.3 left). This shows that modes propagating downstream are more influenced by the swirling flow than modes propagating upstream.

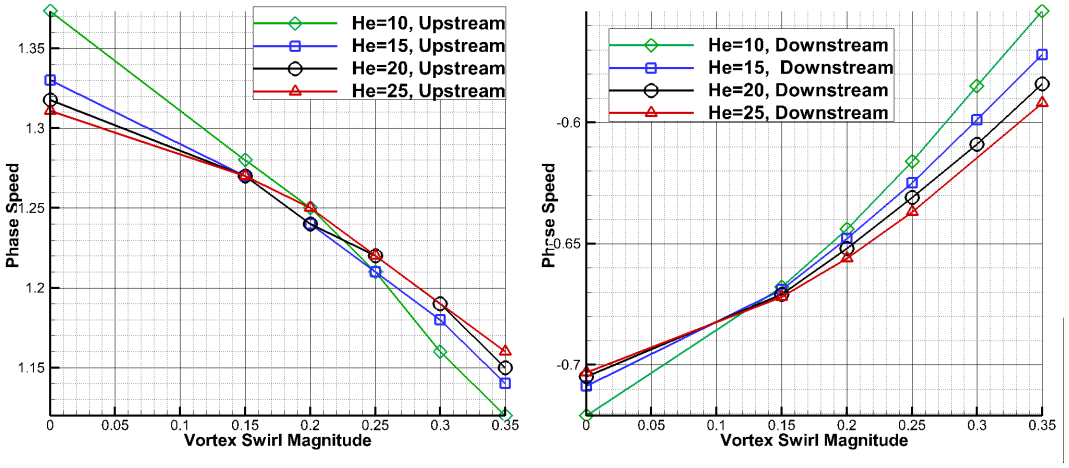

Fig. 7.3 – Phase speed as a function of Helmholtz number and swirling flow magnitude for the contra-rotating mode$m = -2$ and free vortex swirl mean flow.

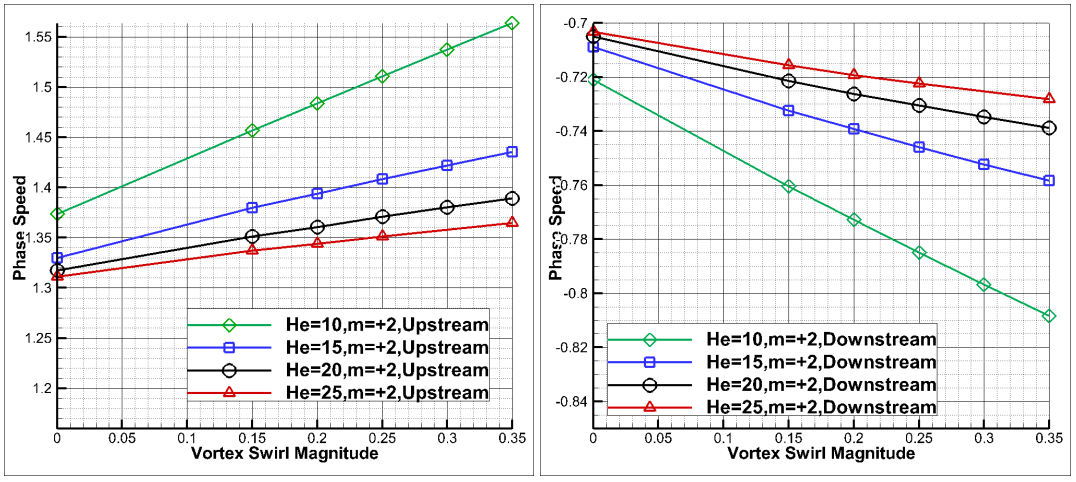

Fig. 7.4 – Phase speed as a function of Helmholtz number and swirling flow magnitude for the co-rotating mode$m = +2$ and free vortex swirl mean flow.

7.1.3 The Effect of Swirl on Mode cut-on ratio

The purpose of this section is to indicate how the swirling flow modifies the cut-on modal content for various levels of swirl and for a range of frequencies. This is particularly important because to define a suitable multi-modal source for the optimum impedance calculations in section 7.2 one has to decide how many circumferential and radial modes to consider. In this work the modal content for the broadband source is defined by the cut-on acoustic modes for the hard-walled duct case. Axial wavenumbers are calculated for a specific frequency and mean flow for a range of circumferential mode numbers m. For each circumferential mode number, the number of cut-on radial modes n propagating upstream is calculated. The existance of a cut-on (m,n) mode is indicated on a two dimensional grid at m versus n to form a modal triangle. Examples of modal triangles are presented in figures 7.5 to 7.8 for a varying set of flow parameters and frequencies.

In all the cases presented in this section the geometry is an annular duct with a hub to tip ratio 0.4 which is a reasonable value for the interstage region of a modern turbofan engine. In terms of mean flows, two cases are presented. The first case in which the axial mean flow Mach number is

$M_{x0} = 0.3$ and the swirling flow Mach number $M_{\phi_0} = 0.15/r$. This corresponds approximately to the approach condition. The second case in which the axial mean flow Mach number is $M_{x0} = 0.5$ and the swirling flow Mach number $M_{\phi_0} = 0.25/r$ corresponds to the take-off condition. Both of these cases will be studied in section 7.2. In the current section results are presented only for the first case for which the axial Mach number will be kept as $M_{x0} = 0.3$. Similar modal triangles were calculated for $M_{x0} = 0.5$ and similar trends were observed, but are not presented here.

Variation of the modal triangle at the cut-on modes for varying levels of vortex swirl at a single frequency ($He = 10$) are presented in Figure 7.5. It is observed that the location of the cut-on the acoustic modes are highly influenced by the mean swirling flow. The modal distribution for a no-swirling flow is symmetrical. When swirl is included, this symmetry is broken. The higher the swirling flow magnitude is, the more the modal content is shifted to negative mode orders. Similar results for a rigid body swirl profile are presented in figure 7.6.

When comparing figures 7.5 and 7.6, it is observed that modal triangles for the vortex swirl is more affected by the increase of the swirling flow magnitude than the ones for rigid body. Notice that although the magnitude of the rigid body mean flow profile Ω^* and the magnitude of the vortex swirl mean flow profile Γ^* might be the same, those two different profiles have different maximum swirling flow Mach numbers. While a solid body mean flow profile has a maximum swirling flow Mach number at the tip, a vortex swirl mean flow profile maximum swirling flow Mach number at the root. Also, if a case in which both swirling flow magnitudes are the same ($\Gamma^* = \Omega^*$), the maximum swirling flow Mach number will be higher for the vortex swirl case and the cut-off ratio will be smaller when compared to the rigid body case. As a consequence, there will be more cut-on modes for the vortex swirl mean flow profile than for the rigid body mean flow profile. Engines with low Mach numbers will have a swirling flow profile more similar to a rigid body, while real engines will have a mean flow profile more similar to a vortex swirl.

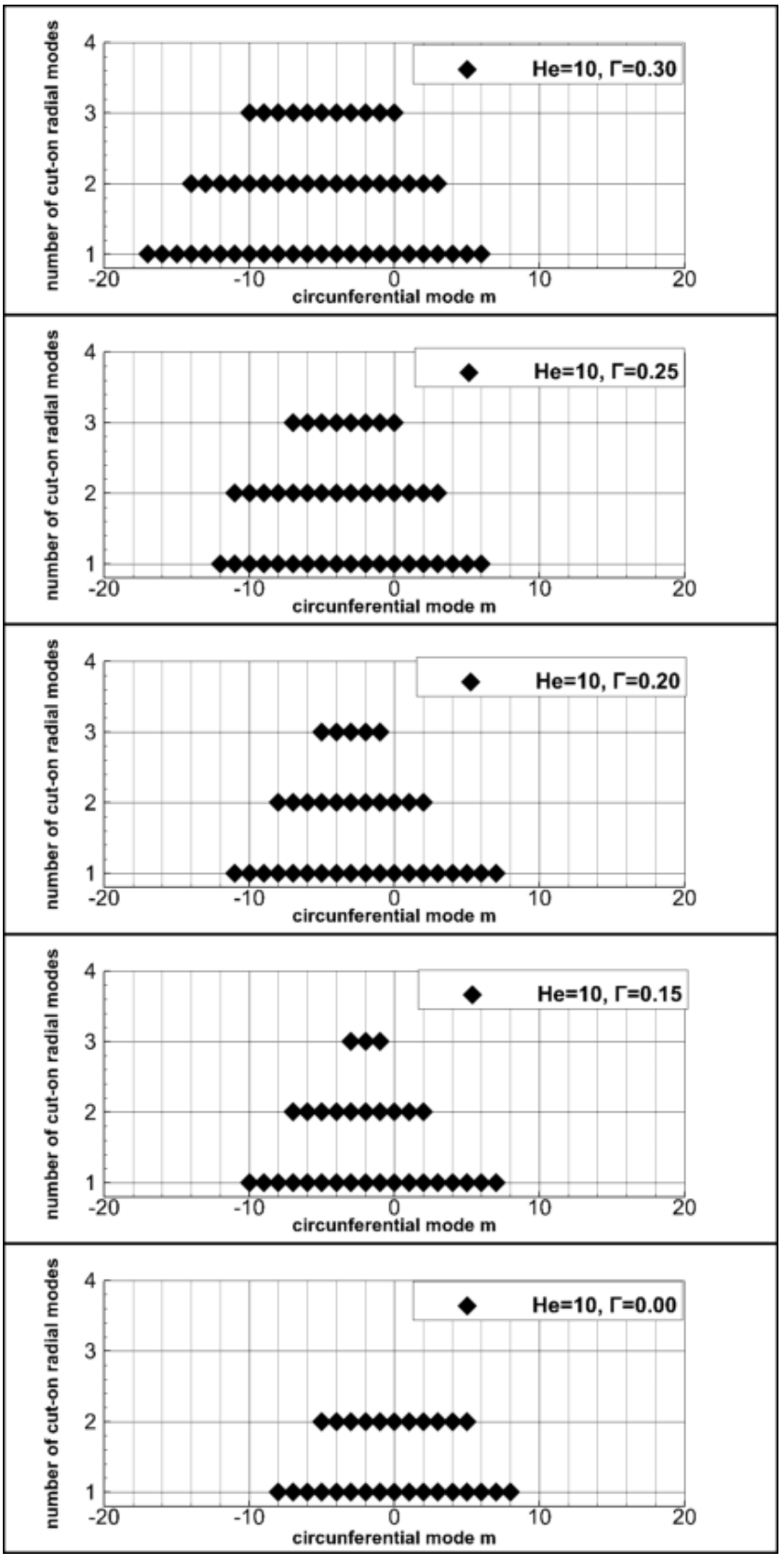

Fig. 7.5 – Variation of the modal triangle at cut-on modes for varying levels of vortex swirl and $He = 10$.

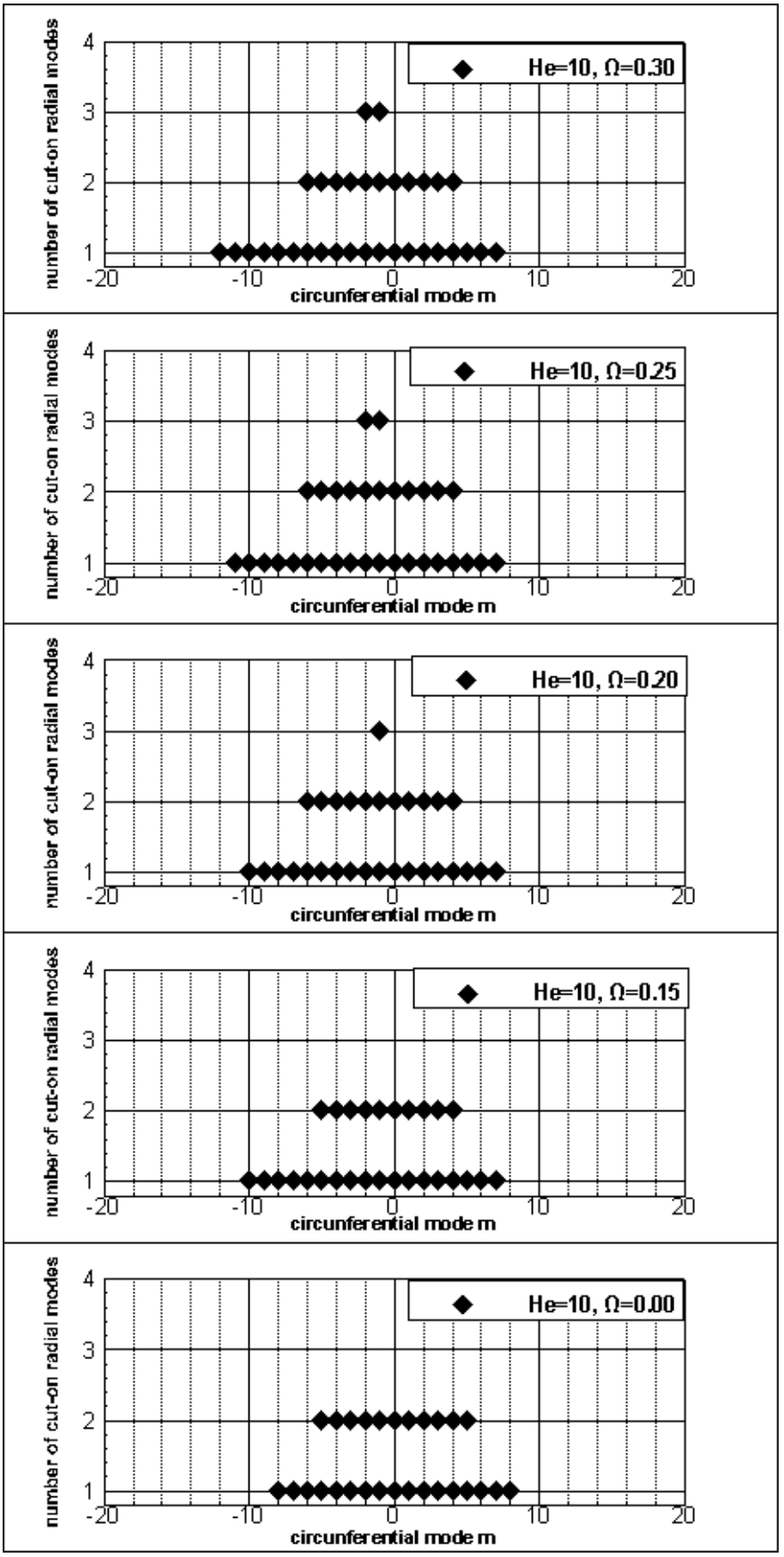

Fig. 7.6 – Variation of the modal triangle at cut-on modes for varying levels of solid body and $He = 10$.

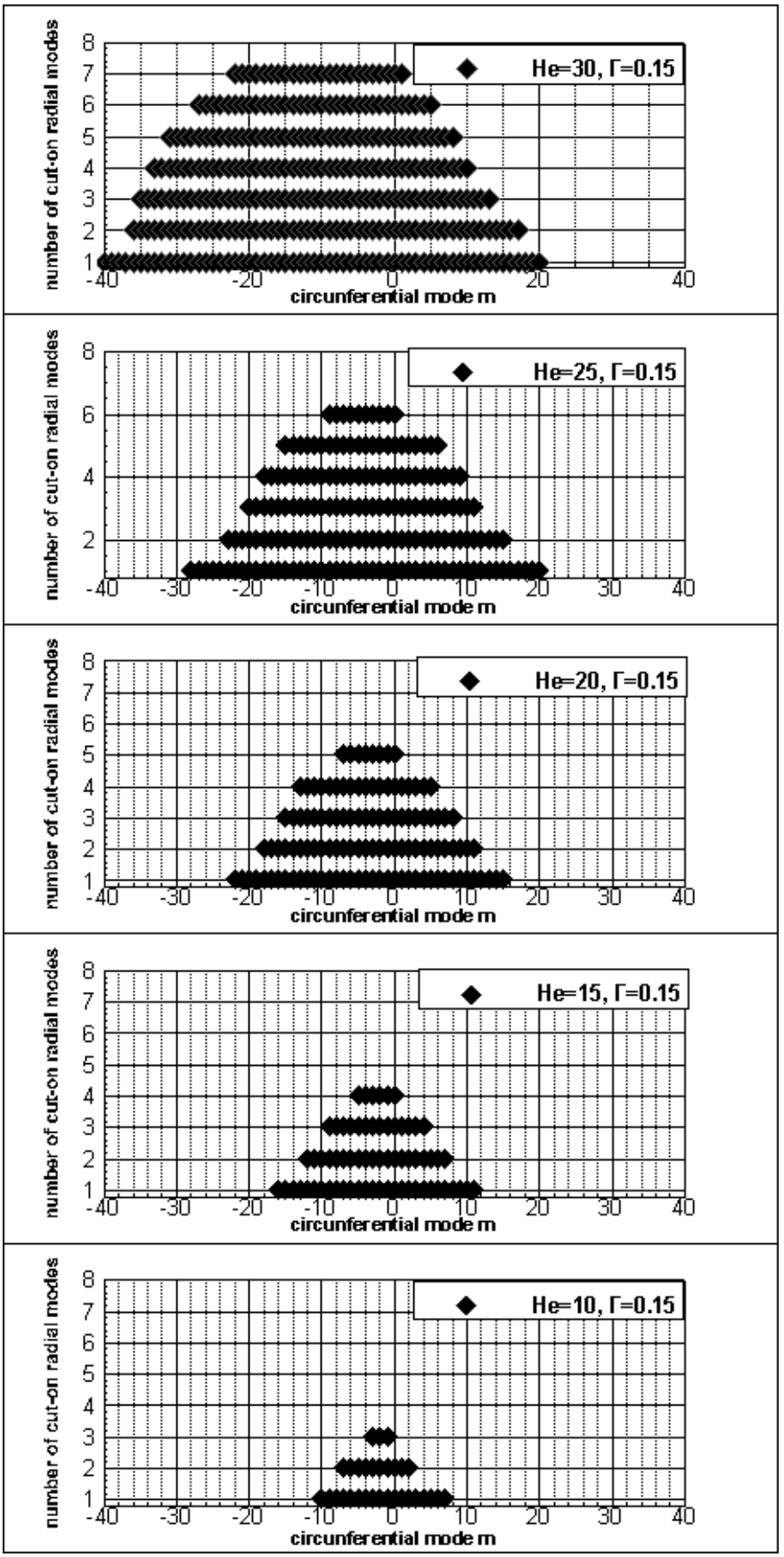

Fig. 7.7 – Increasing the frequency, the number of cut-on modes increase Results for a vortex swirl mean flow profile and $\Gamma = 0.15$.

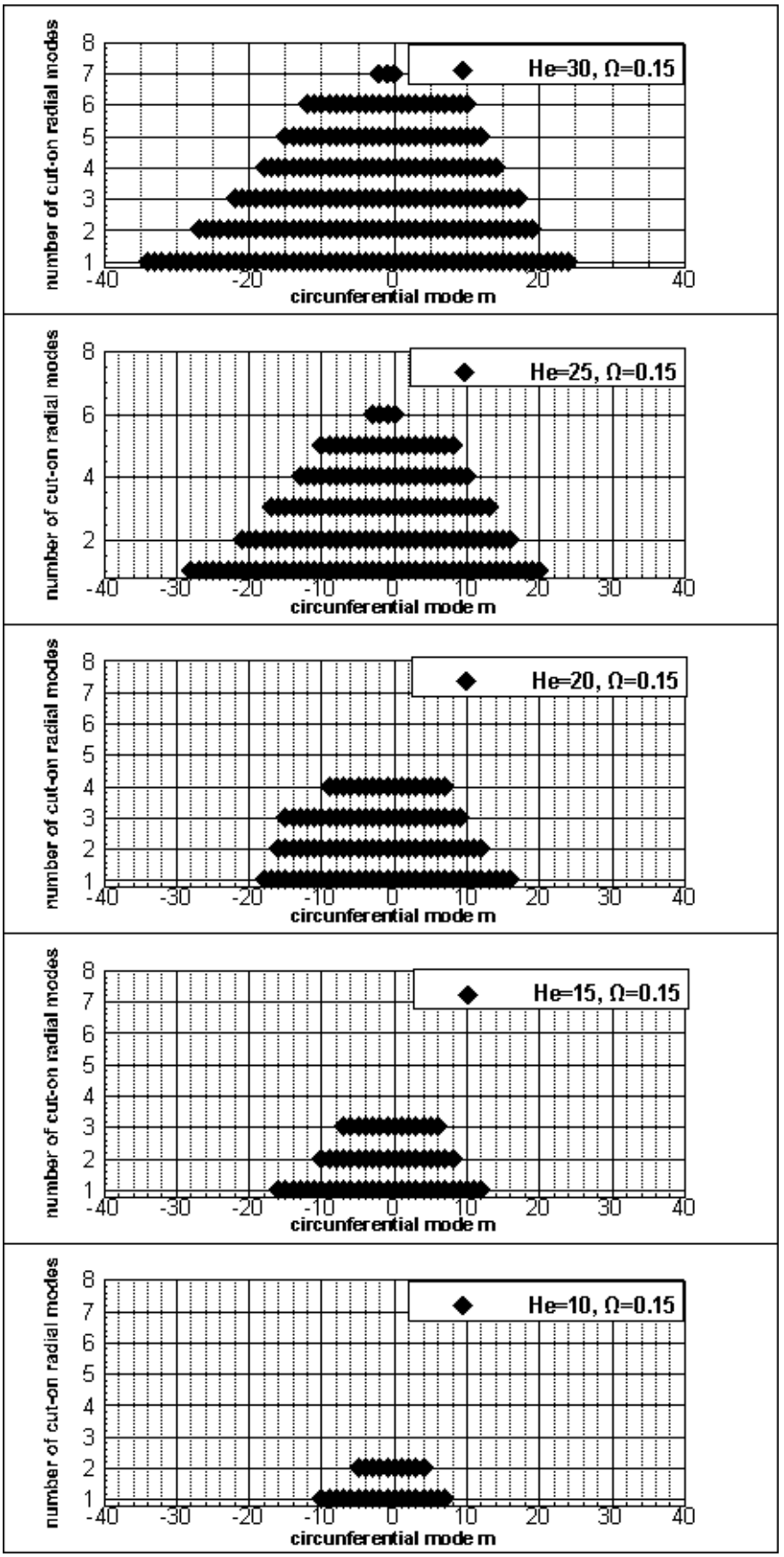

Fig. 7.8 – Increasing the frequency, the number of cut-on modes increase Results for a solid body mean flow profile and $\Omega = 0.15$.

The effect of frequency on the number and location of cut-on modes for a fixed mean swirling flow is ilustrated in Figures 7.7 and 7.8. If the frequency is increased, more acoustic modes cut on, as expected [83] and the bias towards negative azimuthal moode orders is preserved.

7.2 The Effect of Swirl on Liner Attenuation

The purpose of this section is to analyse the effect of swirling flow and liners on the optimum impedance and optimum insertion loss of a liner in a region where the flow is highly swirling. Currently the swirling mean flow is not generally taken into account when designing liners for the interstage region of a turbofan engine and this parametric study aims to evaluate whether the insertion loss is significantly affected by the swirling flow. Section 7.2.1 describes the test case. Section 7.2.2 illustrates a characteristic modal attenuation for a Lined case. Section 7.2.3 defines the broadband source. Section 7.2.4 presents the optimization of the insertion loss. Section 7.2.5 shows the variation of optimised liner resistance, liner reactance and insertion loss with swirl magnitude and frequency. Section 7.2.6 summarizes the parametric study.

7.2.1 The Test Case

The geometry is exactly the same as the described in section 7.1.3, ie an annular duct with a hub-to-tip ratio of $\sigma = 0.4$ and an outer radius of 1m. The liner impedances are selected to cover those of practical liners. The liner resistance ranges from 0 to $5\rho_0 c_0$ and the liner reactance from $-5\rho_0 c_0$ to $5\rho_0 c_0$ (with a step of 0.5). The frequency varies from 500 Hz to 1250 Hz focusing on BPF at approach and take-off and correspond to Helmholtz numbers between 9 and 24. The frequency range was divided into $1/3$ octave bands and the solutions are calculated at 1/3 octave centre frequencies to generate the optimum impedance plots in section 7.2.4.
The flow conditions are described in the table below. This study intends to assess the liner performance using a baseline case case which is the case without swirl for a given liner resistance resistance and reactance frequency and mean flow. There are two baseline cases because the take-off and approach regimes have different axial Mach numbers. Only vortex swirl mean flow profiles are used here. Indications suggest that this type of flow corresponds more closely to realistic mean flow profiles in an interstage than a rigid body swirl.

Table 7.1 – Mean Flow Conditions used in the Testcase

Case	Swirling Flow		Axial Flow	
.	Γ	$M_{\phi 0_{max}}$	M_{x0}	
1	0.00	0.00	0.30	Baseline (Approach)
2	0.00	0.00	0.50	Baseline (Take-off)
3	0.15	0.375	0.30	Swirl (Approach)
4	0.25	0.625	0.50	Swirl (Take-off)

7.2.2 Characteristic Modal Attenuation for a Lined Case

The computation of each case described in the previous section will generate a set of axial wavenumbers for a given resistance and reactance frequency and mean flow parameters. Each axial wavenumber is associated with a radial and circumferential mode number. The attenuation (or insertion loss) for a single mode can be obtained from Equation 3.162 and is given by

$$IL = -10\log_{10} e^{-2|\mathrm{Im}(k_x)\mathrm{L}|}. \tag{7.2}$$

The intent of this subsection is to illustrate the modal distribution of the calculated liner attenuation for a single frequency and a given impedance. Figure 7.9 shows the liner attenuation as a function of the azimuthal and radial mode orders for the take-off case, for a frequency of 1250 Hz and non-dimensional impedance of $1-0.5i$. Figure 7.9 (a) includes the swirling flow, while Figure Figure 7.9 (b) considers only the axial flow. The red plot in the xy plane is the modal triangle previously presented in section 7.1.3 and the value of the insertion loss for each pair of radial and azimuthal modes is plotted on the z-axis. It is observed that in both cases the attenuation is lower for low-order modes and increases for higher-order modes at the edges of the mode triangle. The swirling flow generally reduces the level of the attenuation and shifts the modal content to lower azimuthal mode-orders.

7.2.3 Defining a Broadband Source

The current study aims to investigate how the swirling flow affects optimum impedance by carrying out multimode calculations for a simulated broadband noise source propagating upstream from the stators towards the fan in the interstage region. The insertion loss for a broadband source is calculated from Equation 3.162. The modal content to be considered is defined based on modal triangles from section 7.1.3. All cut-on modes from the hard-walled case were considered in the lined case.

For a given frequency and azimuthal mode order m, the axial wavenumbers corresponding to each radial mode order n are calculated and stored in order of attenuation (from lower to higher). A script reads the modal triangle for the same case, checks how many radial modes should be considered for a certain azimuthal mode order and calculates the transmission loss for a each radial and circunferential mode order, for a single frequency and single impedance using the first n_{HW} radial modes. The transmission loss for the multimode case is then obtained by assuming equal power in each mode and applying Equation 3.162.

By changing the impedance value and repeating the same calculations, one can obtain attenuation plots presented in Figures 7.10 to 7.25 in the next section. Those plots were made by using the software package Tecplot and the optimum impedance was obtained by using the same software package.

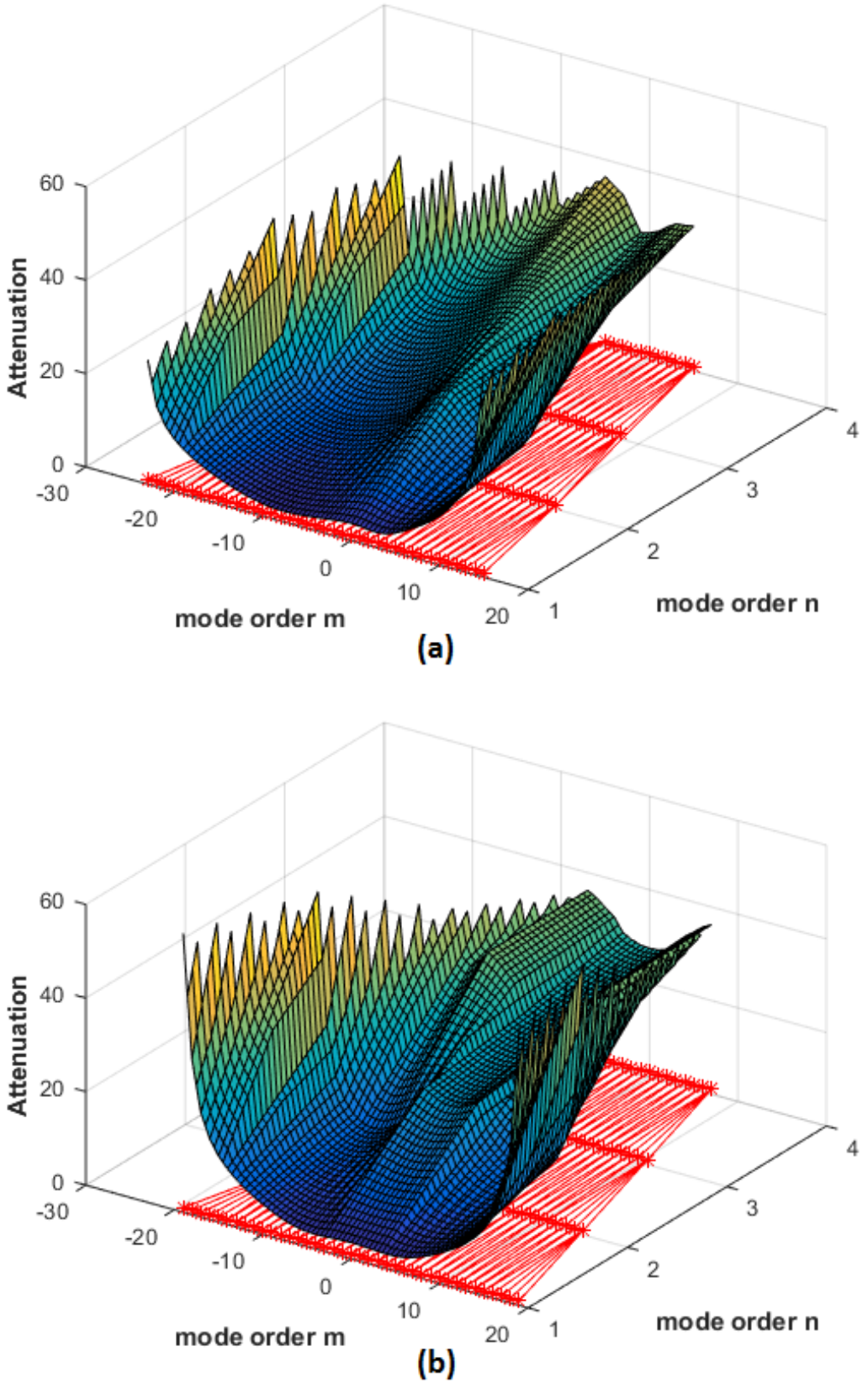

Fig. 7.9 – Liner attenuation as a function of the azimuthal and radial mode orders for the take-off case, frequency 1250 Hz and impedance $1 - 0.5i$. (a) swirling flow (b) axial flow.

7.2.4 Optimizing the Insertion Loss

The computed insertion loss was plotted against liner resistance and reactance for each azimuthal mode m, Helmoltz number He and flow condition described in section 7.2.1. In all the cases that follow, the broadband source is placed downstream so that the sound propagates upstream against the flow. Figures 7.10 and 7.11 show the results for the approach condition and frequency of 500 Hz ($He = 9.24$) for the cases whithout swirling flow and when the swirling flow is present, respectively. For the case without swirl, the optimum attenuation is 18.30 dB/m and the optimum impedance is $z = 0.66 - 0.53i$. When swirl present, the optimum attenuation is 15.27 dB/m and the optimum impedance is $z = 0.98 - 0.54i$. In this case the optimum attenuation is reduced with the swirl.

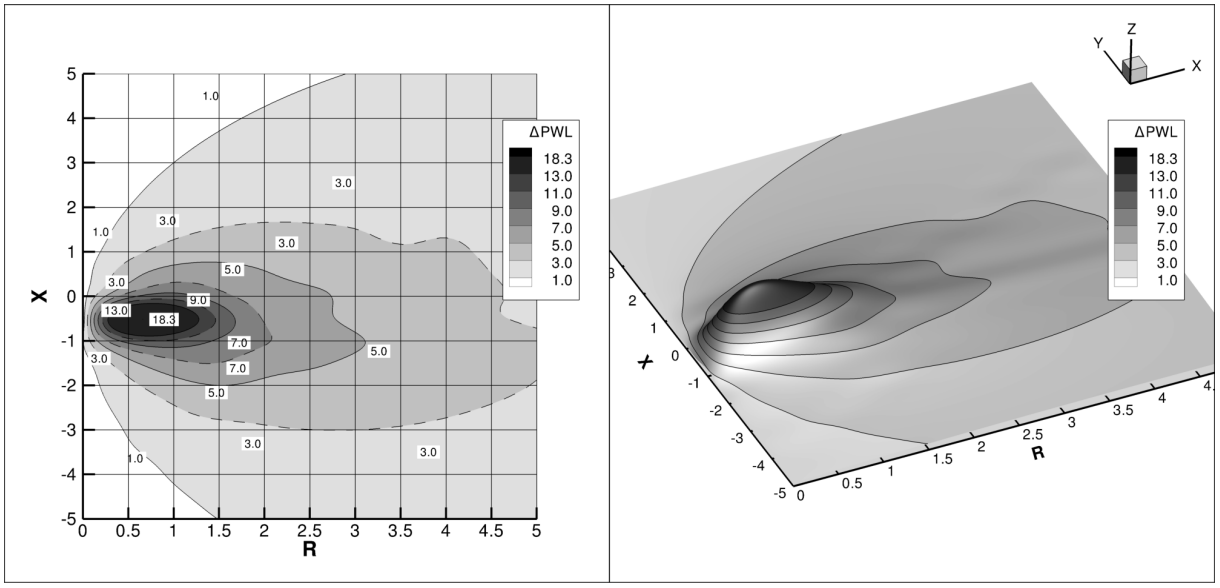

Fig. 7.10 – Optimum impedance for the case 500 Hz, $M_x = 0.3$, without swirl. Maximum attenuation of 18.30 dB and optimum impedance of z=0.66-0.53i

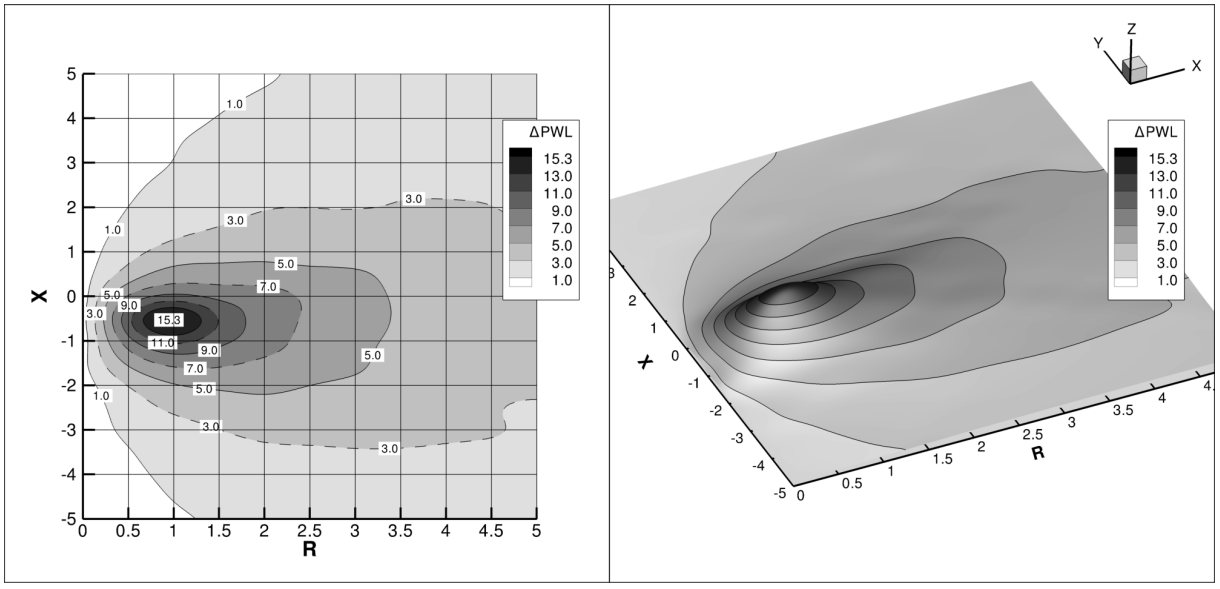

Fig. 7.11 – Optimum impedance: 500 Hz, $M_x = 0.3$, $M_\phi = 0.15$. Maximum attenuation of 15.27 dB and optimum impedance of z=0.98-0.54i

Figures 7.12 and 7.13 show results in the same format for the Take-off condition at the same frequency of 500 Hz ($He = 9.24$). For the axial flow case, the optimum attenuation is 15.22 dB/m and the optimum impedance is $z = 0.60 - 0.46i$. When swirl is present, the optimum attenuation is 12.23 dB/m and the optimum impedance is $z = 1.195 - 0.44i$. Similarly to the approach condition, the optimum attenuation is reduced with the swirl. The difference in attenuation is even higher when compared to the previous case.

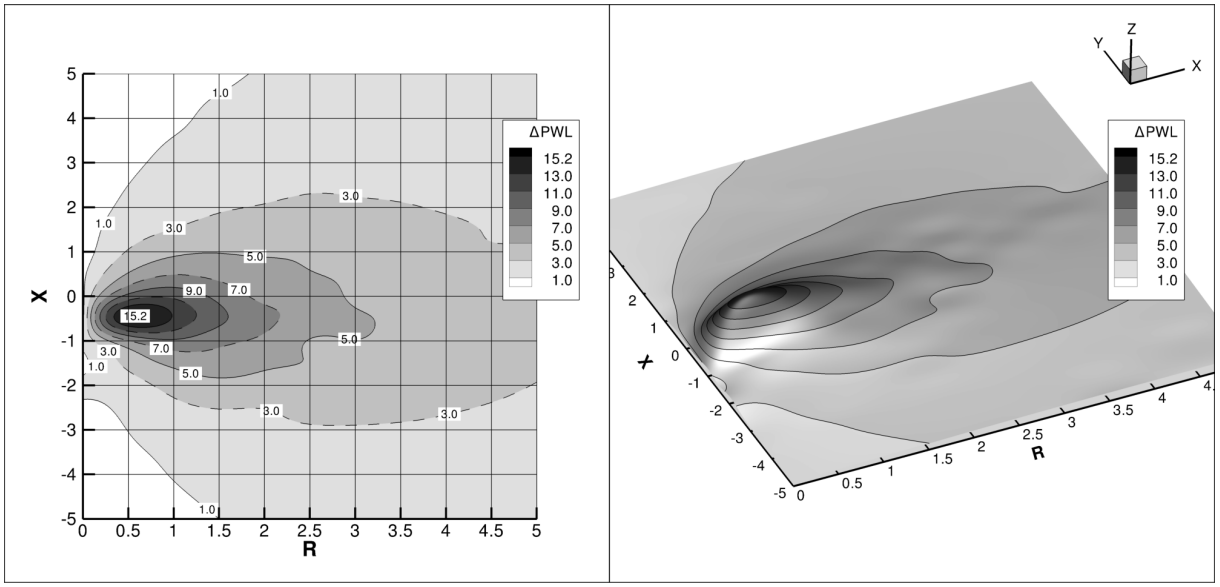

Fig. 7.12 – Optimum impedance for the case 500 Hz, $M_x = 0.5$, without swirl. Maximum attenuation of 15.22 dB and optimum impedance of z=0.60-0.46i

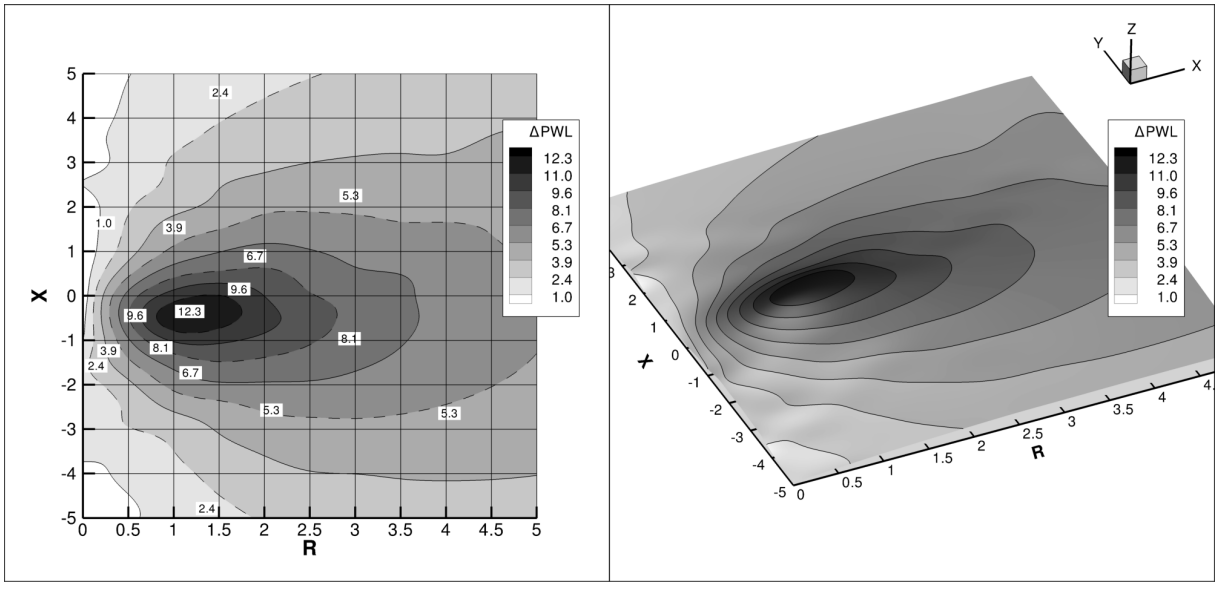

Fig. 7.13 – Optimum impedance: 500 Hz, $M_x = 0.5$, $M_\phi = 0.25$. Maximum attenuation of 12.23 dB and optimum impedance of z=1.195-0.44i

To observe the effect of the increasement in frequency, similar results were plotted for the frequency of 630 Hz. Figures 7.14 and 7.15 show results in the same format for the approach condition at a frequency of 630 Hz ($He = 11.64$). For the case without swirl, the optimum attenuation is 14.26 dB/m and the optimum impedance is $z = 0.87 - 0.54i$. When swirl is present, the optimum attenuation is 12.81 dB/m and the optimum impedance is $z = 1.085 - 0.565i$. In this case the optimum attenuation is reduced with the swirl. When compared to the previous results for 500Hz, it is important to keep in mind that more circunferential modes are considered, as more modes cut-on for higher frequencies.

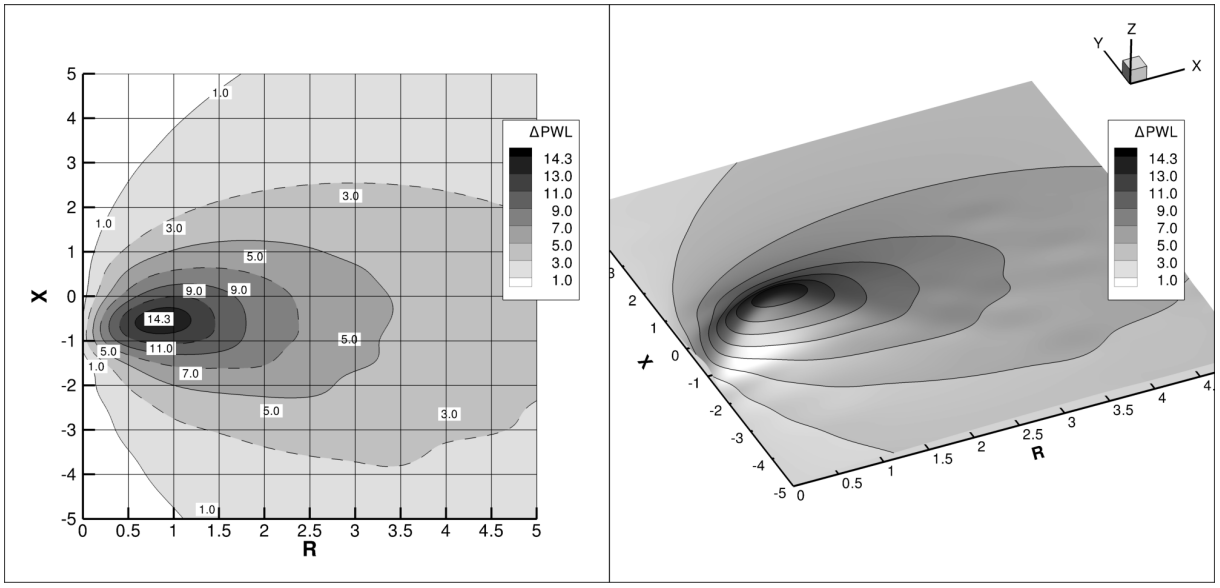

Fig. 7.14 – Optimum impedance for the case 630 Hz, $M_x = 0.3$, without swirl. Maximum attenuation of 14.26 dB and optimum impedance of z=0.87-0.54i

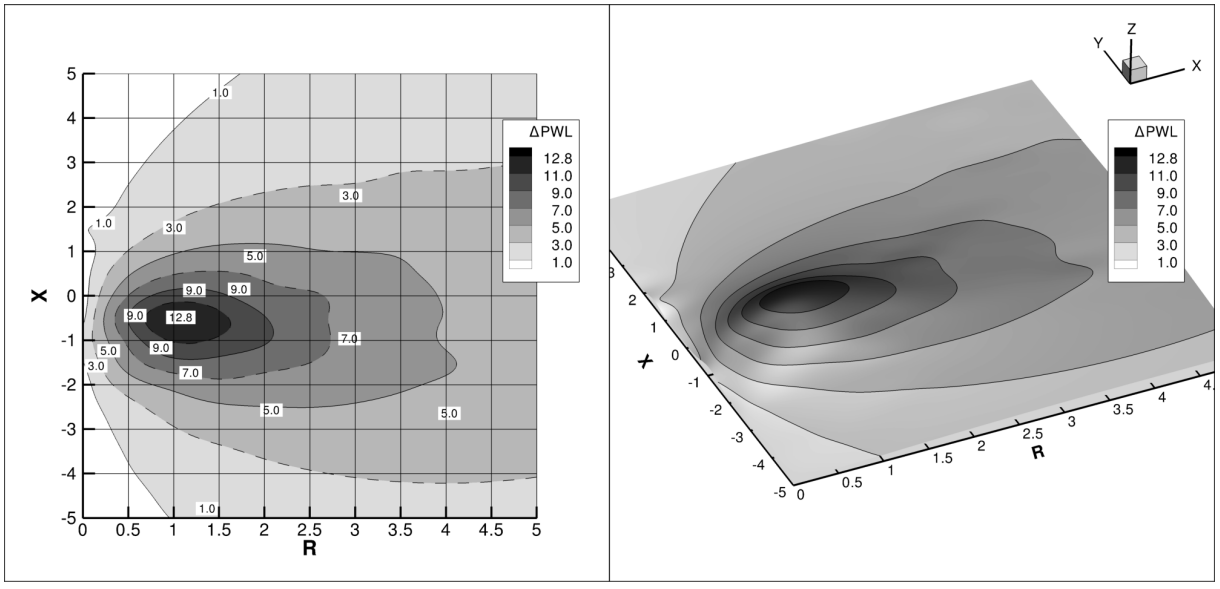

Fig. 7.15 – Optimum impedance: 630 Hz, $M_x = 0.3$, $M_\phi = 0.15$. Maximum attenuation of 12.8 dB and optimum impedance of z=1.08-0.56i

Figures 7.16 and 7.17 show results in the same format for the take-off condition and frequency of 630 Hz ($He = 11.64$). For the case without swirl, the optimum attenuation is 14.26 dB/m and the optimum impedance is $z = 0.87 - 0.54i$. When swirl is present , the optimum attenuation is 10.025dB/m and the optimum impedance is $z = 1.27 - 0.455i$. It is observed that the optimum attenuation is also reduced with the swirl. Although the frequency is the same as the previous case, both axial and swirling flow Mach numbers are higher for the take-off condition. This causes the difference in insertion loss between the swirling and the axial flow case even higher.

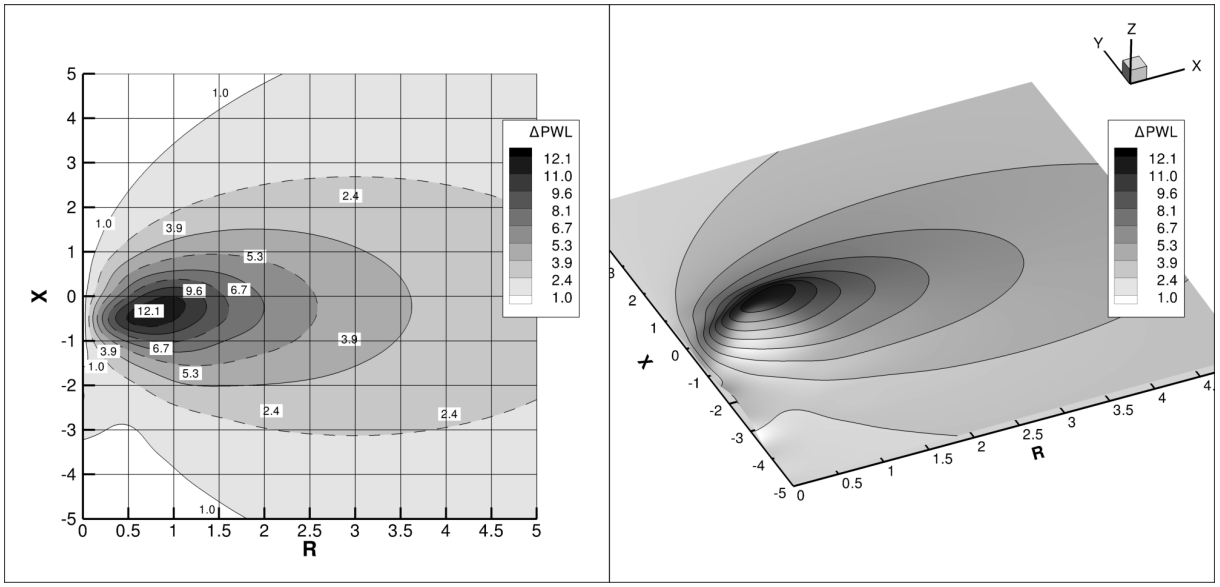

Fig. 7.16 – Optimum impedance for the case 630 Hz, $M_x = 0.5$, without swirl. Maximum attenuation of 14.26 dB and optimum impedance of z=0.87-0.54i

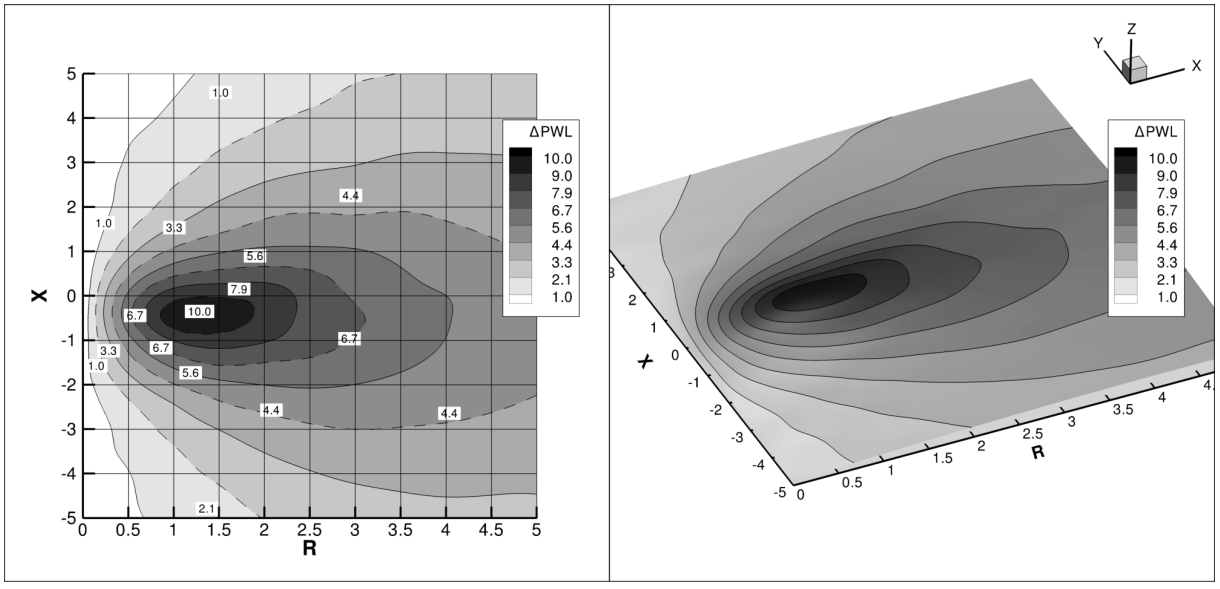

Fig. 7.17 – Optimum impedance: 630 Hz, $M_x = 0.5$, $M_\phi = 0.25$. Maximum attenuation of 10.02 dB and optimum impedance of z=1.27-0.46i

Figures 7.18 and 7.19 show results in the same format for the approach condition for frequency of 800 Hz ($He = 14.67$) for the cases without swirl and when the swirling flow is present, respectively. For the case without swirl, the optimum attenuation is 12.18 dB/m and the optimum impedance is $z = 1.19 - 0.54i$. When swirl is present, the optimum attenuation the optimum attenuation is 12.24 dB/m and the optimum impedance is $z = 1.41 - 0.47i$. In this case the optimum attenuation is almost the same for both cases.

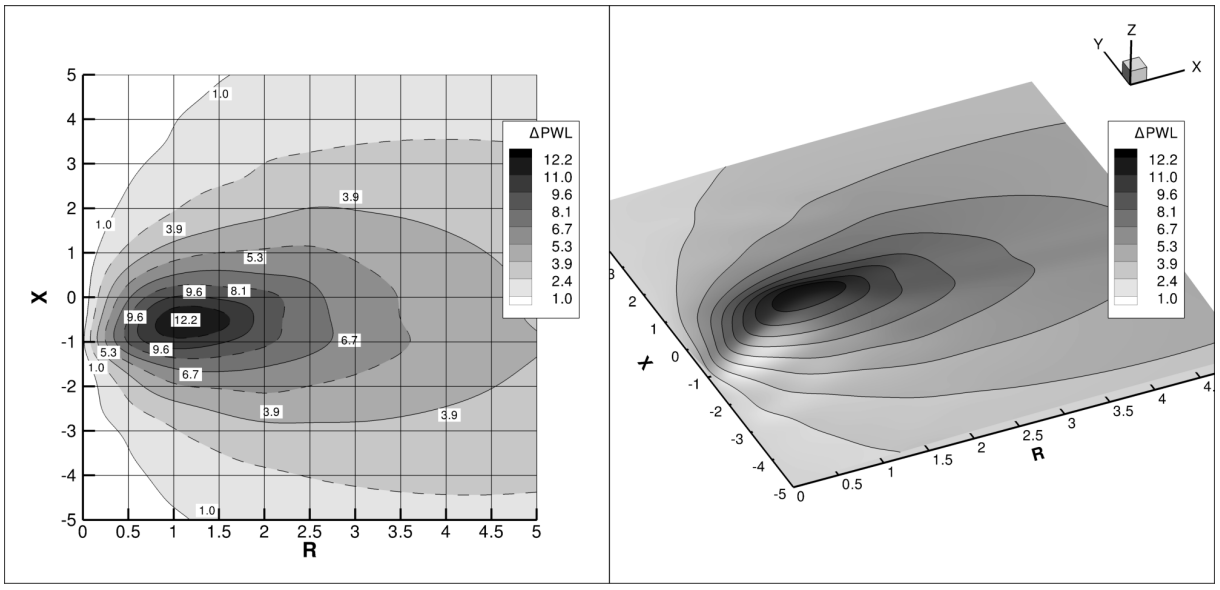

Fig. 7.18 – Optimum impedance for the case 800 Hz, $M_x = 0.3$, without swirl. Maximum attenuation of 12.18 dB and optimum impedance of z=1.19-0.54i

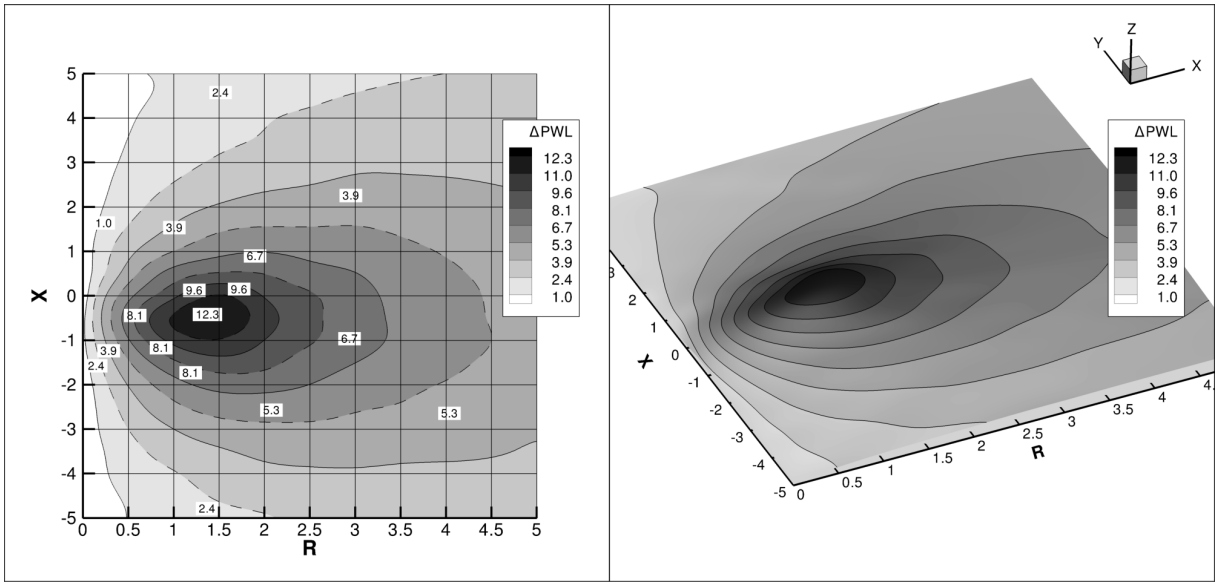

Fig. 7.19 – Optimum impedance: 800 Hz, $M_x = 0.3$, $M_\phi = 0.15$. Maximum attenuation of 12.24 dB and optimum impedance of z=1.41-0.47i

Figures 7.20 and 7.21 show results in the same format for the take-off condition and frequency of 800 Hz ($He = 14.67$) for the cases without swirl and when the swirling flow is present, respectively. For the case without swirl, the optimum attenuation is 12.34 dB/m and optimum impedance is $z = 0.98 - 0.30i$. When swirl is present, the optimum attenuation is 9.85 dB/m and optimum impedance is $z = 1.48 - 0.42i$

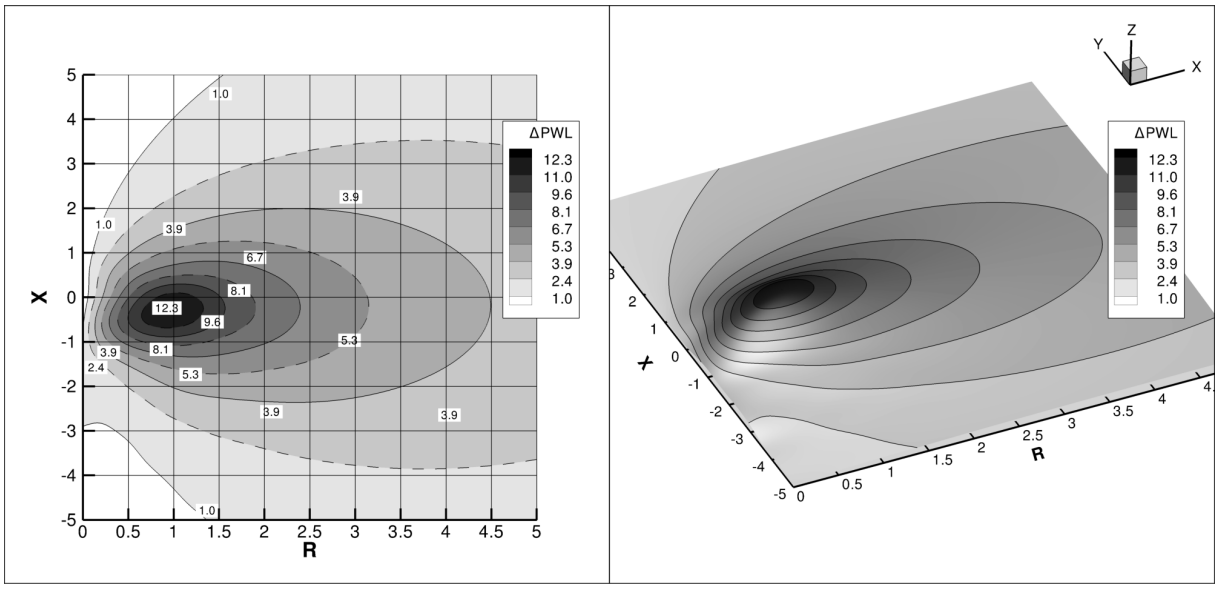

Fig. 7.20 – Optimum impedance for the case 800 Hz, $M_x = 0.5$, without swirl. Maximum attenuation of 12.34 dB and optimum impedance of z=0.98-0.30i

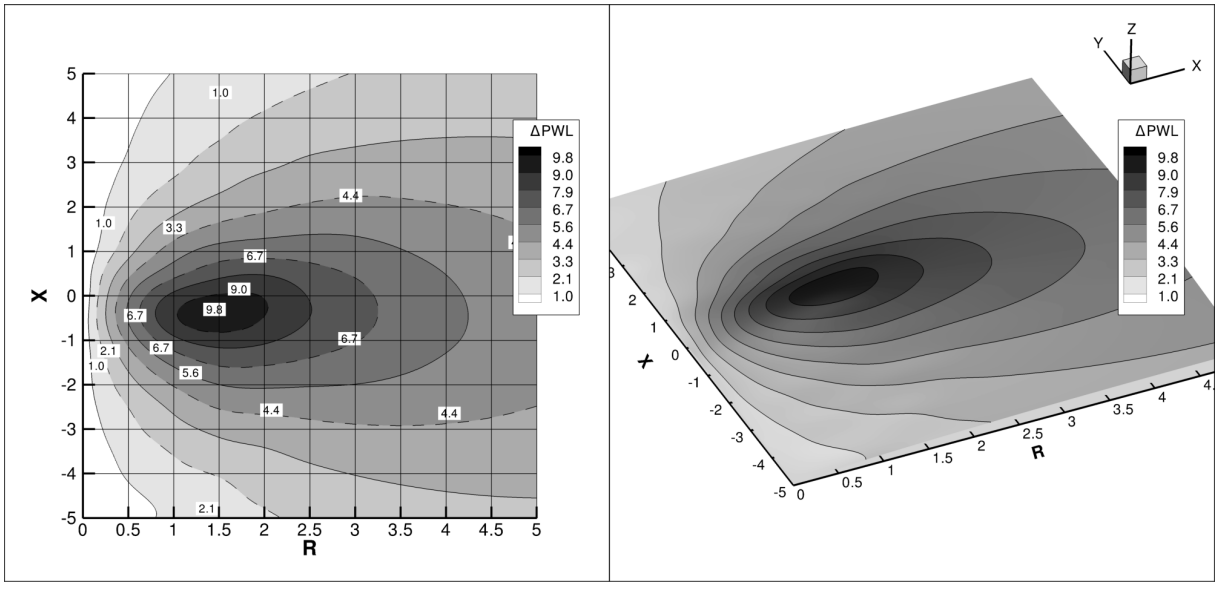

Fig. 7.21 – Optimum impedance: 800 Hz, $M_x = 0.5$, $M_\phi = 0.25$. Maximum attenuation of 9.85 dB and optimum impedance of z=1.48-0.42i

Figures 7.20 and 7.21 show results in the same format for the approach condition and frequency of 1000 Hz ($He = 18.47$) for the cases without swirling flow and when the swirling flow is present, respectively. For the axial flow case, the optimum attenuation the optimum attenuation is 11.39 dB/m and optimum impedance is z=1.28-0.51i . When swirl is taken into account, the optimum attenuation the optimum attenuation is 10.76 dB/m and optimum impedance of z=1.52-0.48i.

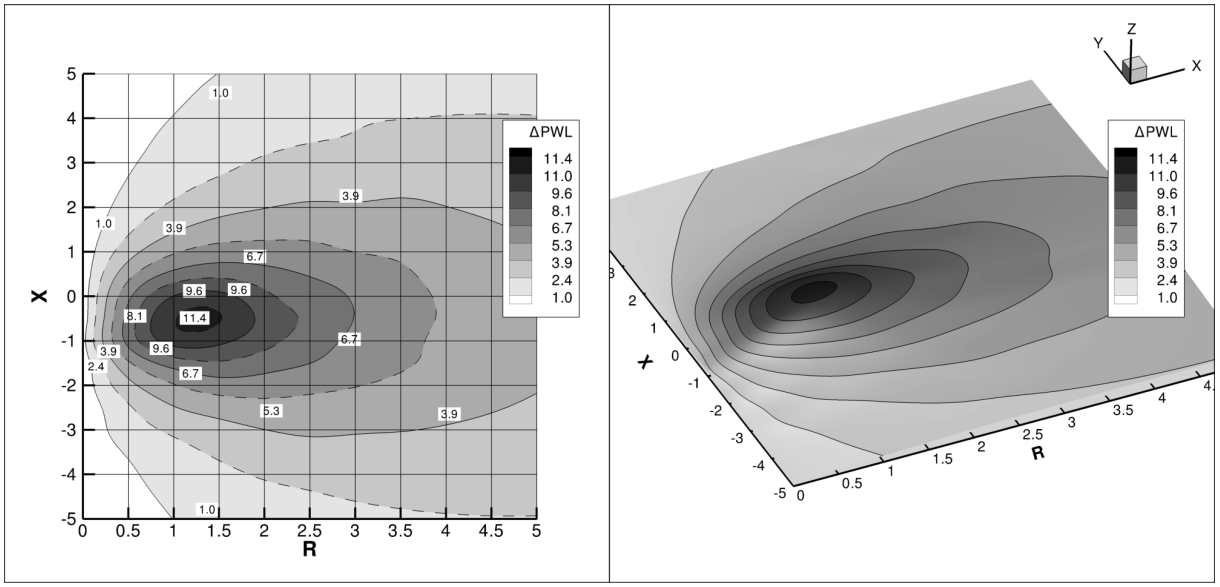

Fig. 7.22 – Optimum impedance for the case 1000 Hz, $M_x = 0.3$, without swirl. Maximum attenuation of 11.39 dB and optimum impedance of z=1.28-0.51i

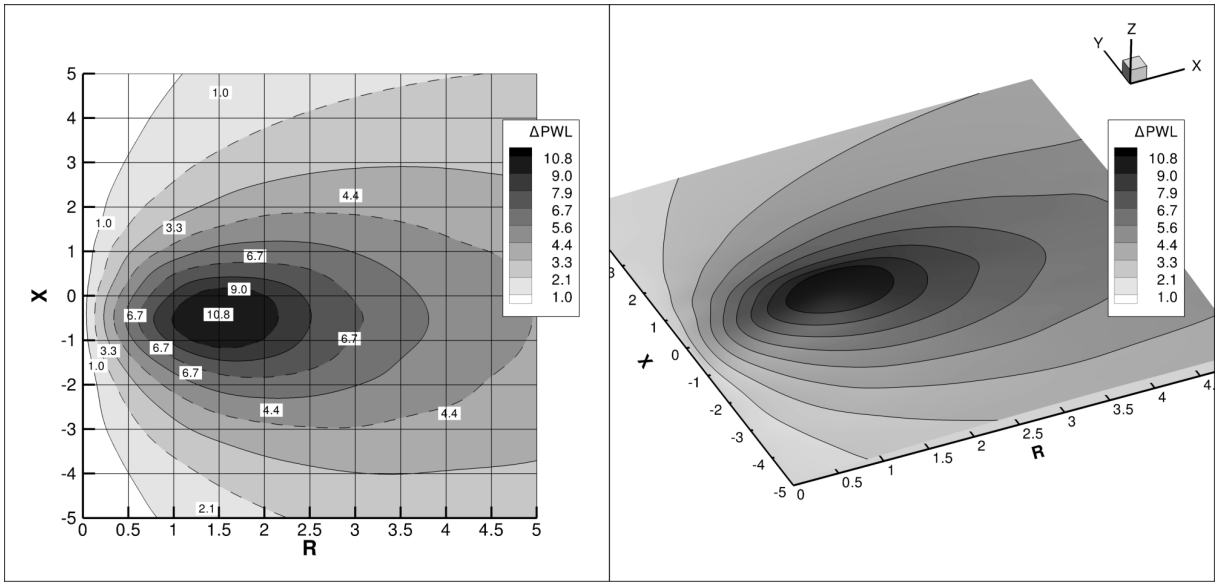

Fig. 7.23 – Optimum impedance: 1000 Hz, $M_x = 0.3$, $M_\phi = 0.15$. Maximum attenuation of 10.76 dB and optimum impedance of z=1.52-0.48i

Figures 7.24 and 7.25 show results in the same format for the take-off condition and frequency of 1000 Hz ($He = 18.47$) for the cases without swirl and when the swirling flow is present, respectively. For the case without swirl, the optimum attenuation is 12.12 dB/m and optimum impedance is z=1.12-0.30i . When swirl is present, the optimum attenuation is 11.00 dB/m and optimum impedance is z=1.65-0.24i.

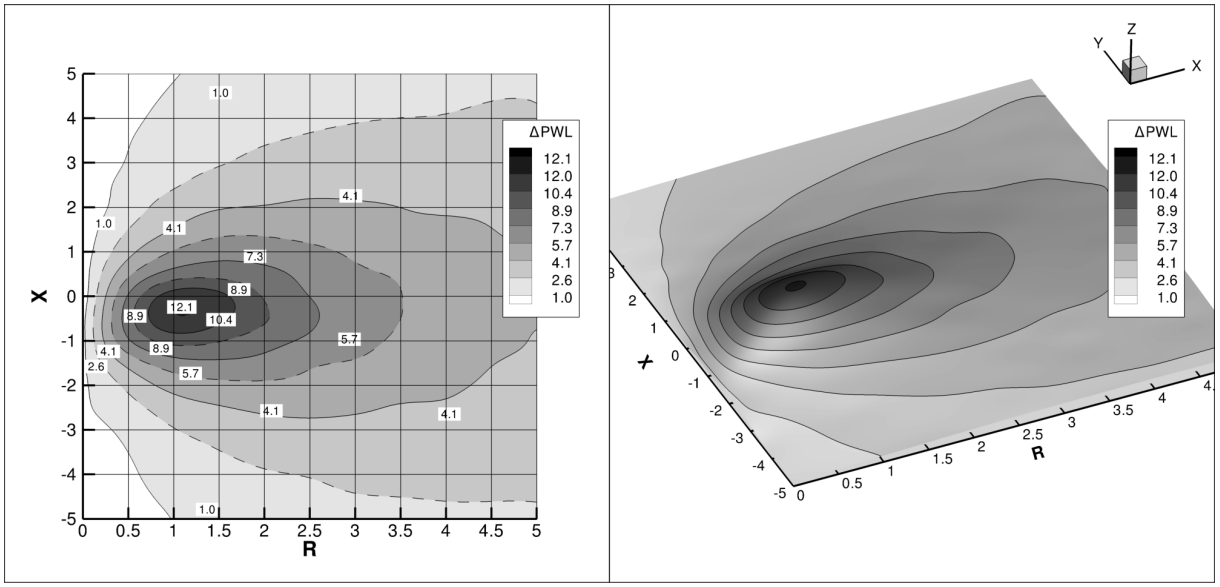

Fig. 7.24 – Optimum impedance for the case 1000 Hz, $M_x = 0.5$, without swirl. Maximum attenuation of 12.12 dB and optimum impedance of z=1.12-0.30i

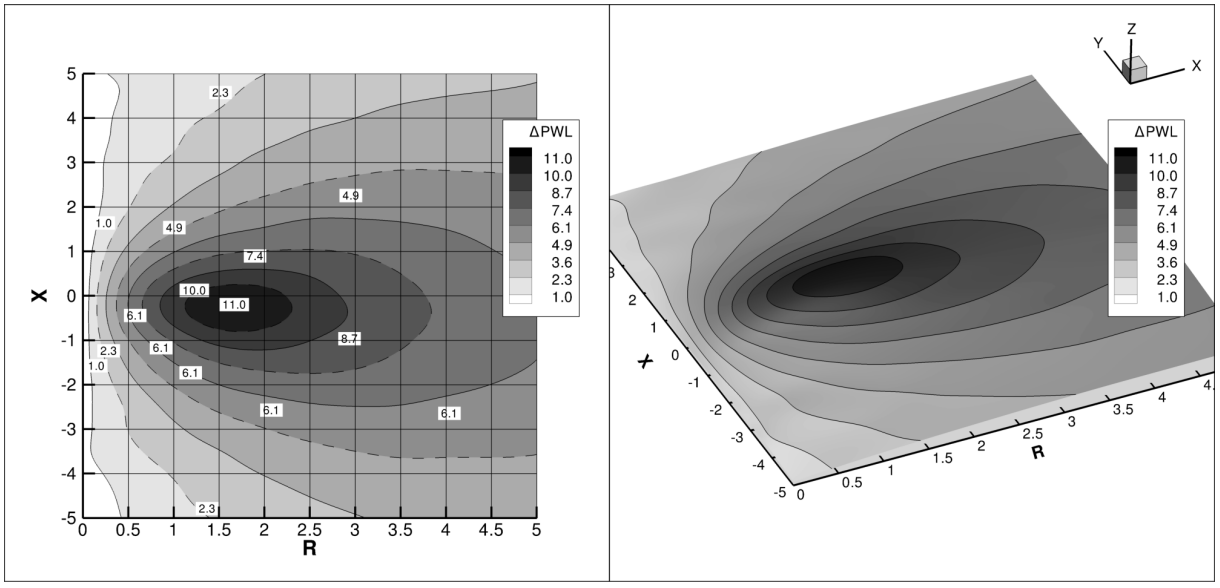

Fig. 7.25 – Optimum impedance: 1000 Hz, $M_x = 0.5$, $M_\phi = 0.25$. Maximum attenuation of 11.00 dB and optimum impedance of z=1.65-0.24i

Figures 7.26 and 7.25 show results in the same format for the take-off condition and frequency of 1250 Hz ($He = 23.28$) for the cases where the swirling flow is absent and the swirling flow is present, respectively. For the case without swirl, the optimum attenuation the 11.032 dB/m and optimum impedance is $z = 1.42 - 0.42$. When swirl is present, the optimum attenuation is 10.53/m dB and optimum impedance is z=1.54-0.44i.

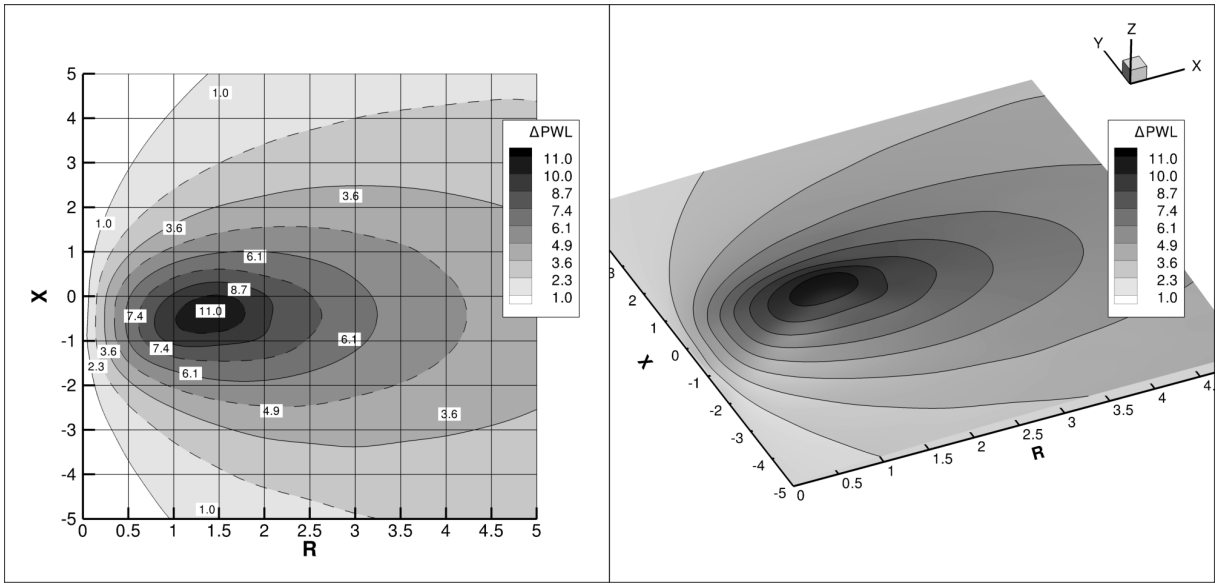

Fig. 7.26 – Optimum impedance for the case 1250 Hz, $M_x = 0.3$, without swirl. Maximum attenuation of 11.032 dB and optimum impedance of $z = 1.42 - 0.42$

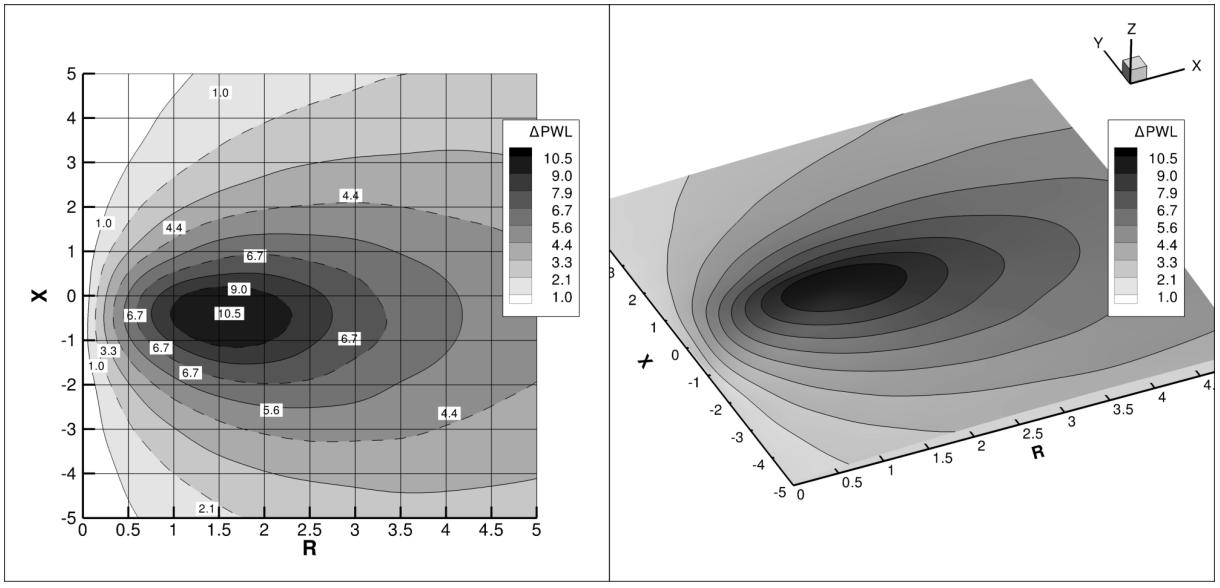

Fig. 7.27 – Optimum impedance: 1250 Hz, $M_x = 0.3$, $M_\phi = 0.15$. Maximum attenuation of 10.53 dB and optimum impedance of z=1.54-0.44i

Figures 7.28 and 7.25 show results in the same format for the take-off condition and frequency of 1250 Hz ($He = 23.28$) for the cases without swirl and when swirl is present, respectively. For the case without swirl, the optimum attenuation is 11.48 dB/m and optimum impedance is $z = 1.145 - 0.24$. When swirl is taken into account, the optimum attenuation is 10.096 dB/m and optimum impedance is z=1.695-0.17i.

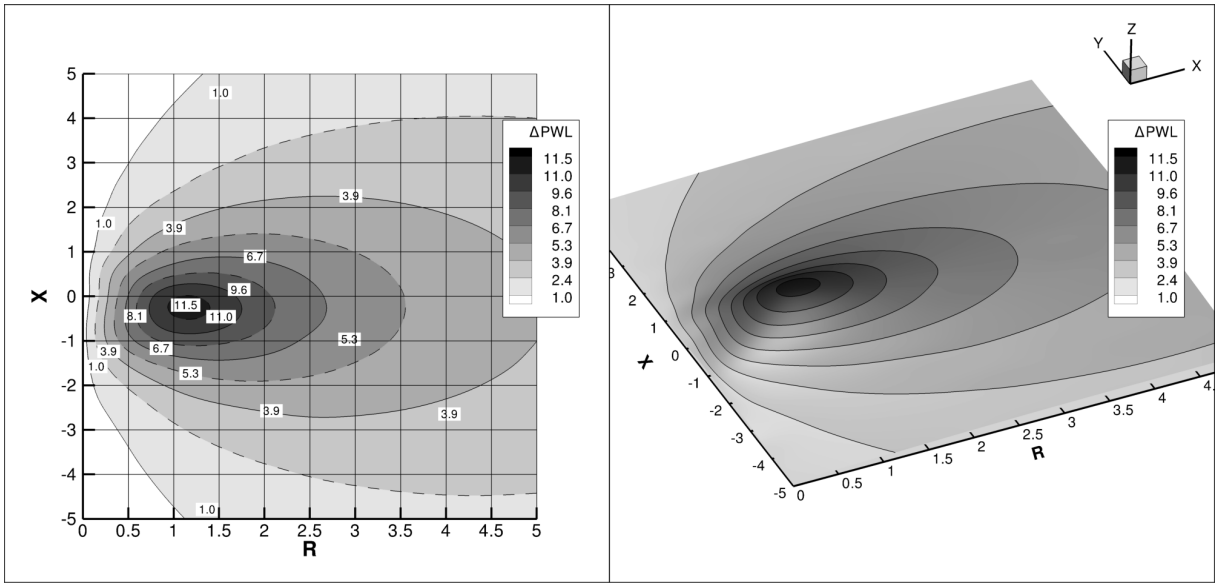

Fig. 7.28 – Optimum impedance for the case 1250 Hz, $M_x = 0.5$, without swirl. Maximum attenuation of 12.34 dB and optimum impedance of z=0.98-0.30i

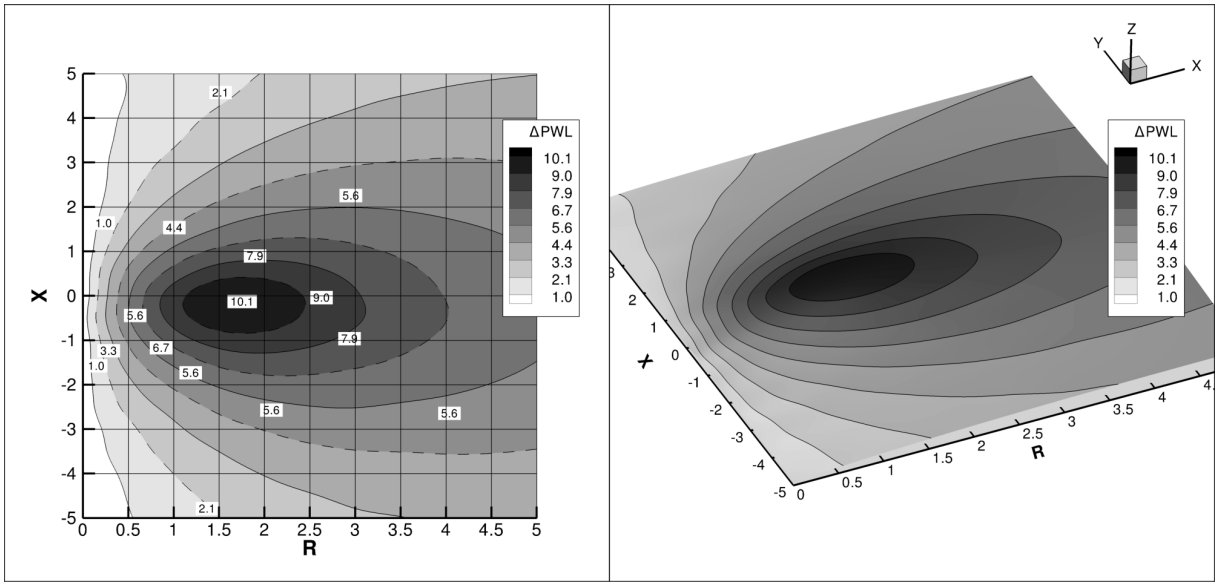

Fig. 7.29 – Optimum impedance: 1250 Hz, $M_x = 0.5$, $M_\phi = 0.25$. Maximum attenuation of 11.48 dB and optimum impedance of $z = 1.145 - 0.24$

7.2.5 Variation of Optimal Impedance with Swirl Magnitude and Frequency

Results obtained for optimum impedance and transmission loss presented in the previous section are now analysed. Optimum resistance and reactance values as well as optimum insertion loss are plotted against frequency for the four mean flow cases to look for trends. Figure 7.30 show the variation of optimum resistance with frequency for the cases with and without swirl for the approach and case. Figure 7.31 show the variation of optimum resistance with frequency for the case without swirl for the approach and take-off cases.

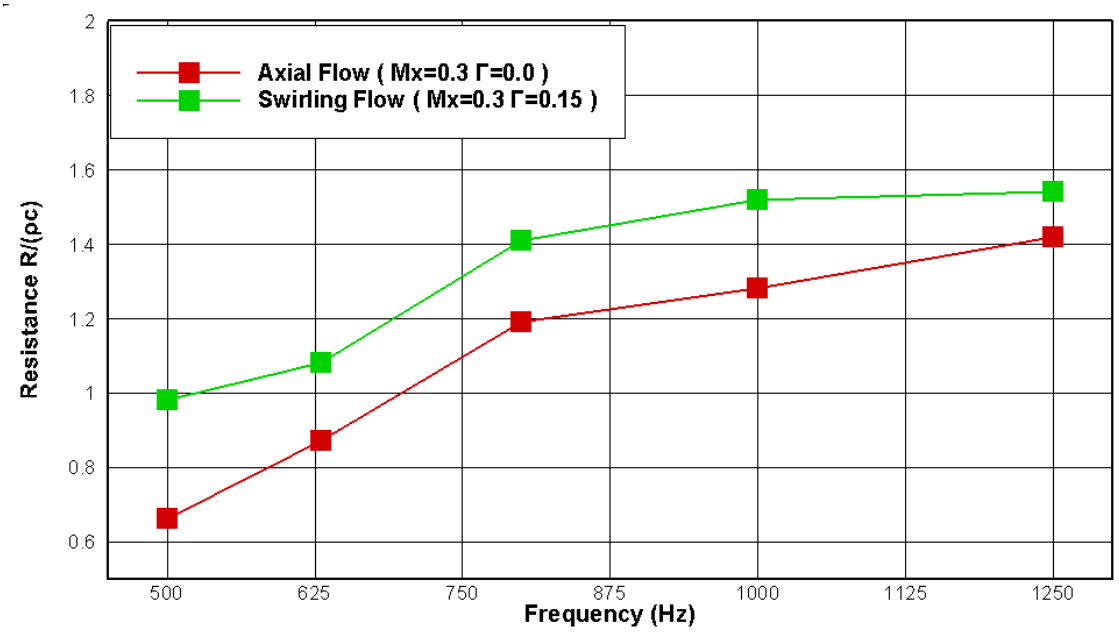

Fig. 7.30 – Variation of Optimum resistance with frequency for the cases with and without swirl for the approach case

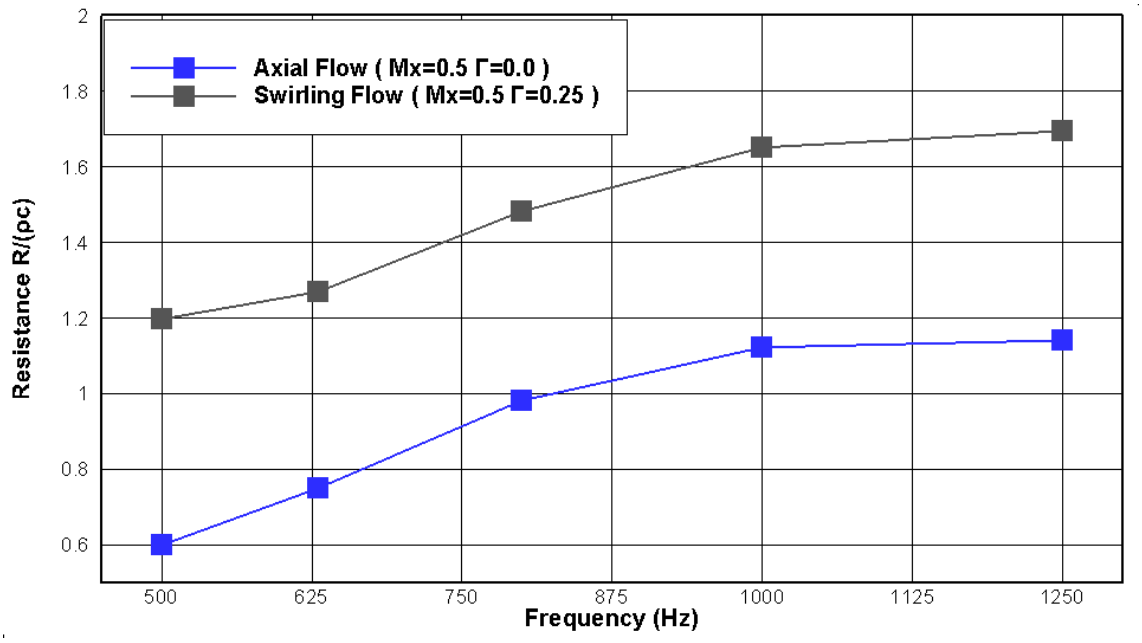

Fig. 7.31 – Variation of Optimum resistance with frequency for the cases with and without swirl for the take-off case

When swirl is present, the optimum resistance increases for all frequencies in the cases presented. The difference is greater for the take-off case in which both axial and swirl Mach numbers are larger. Figures 7.32 and 7.33 show the variation of optimum reactance with frequency for the cases with and without swirl for the approach and take-off cases. For both swirling and no-swirling flow cases, the optimum reactance increases with frequency. When swirl is considered, the optimum reactance changes, but whether it increases or decreases depends on the frequency range and Mach number.

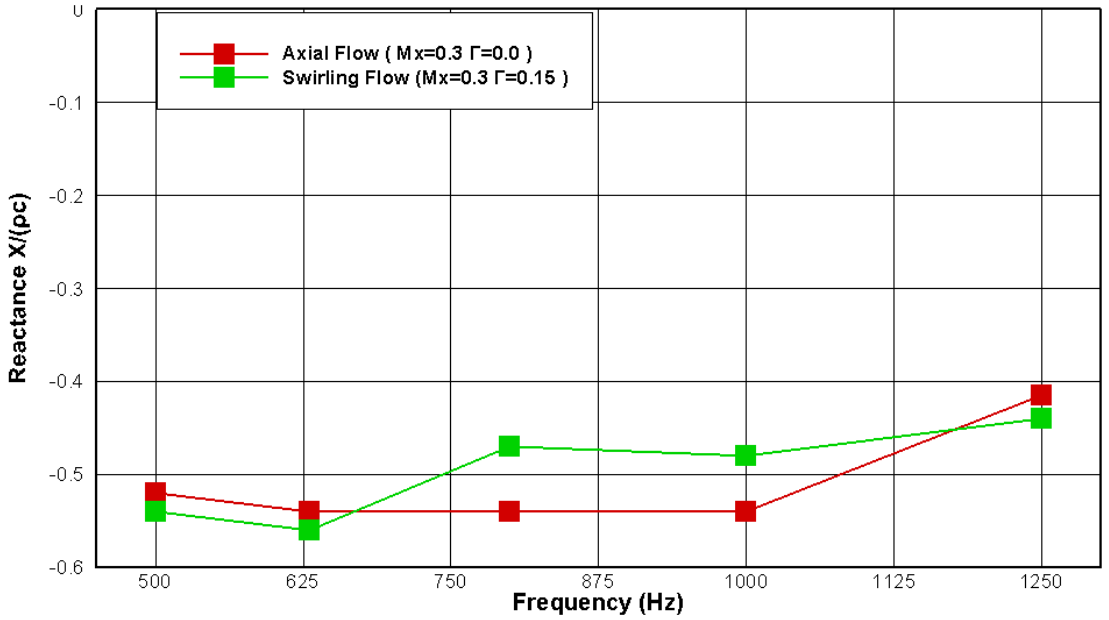

Fig. 7.32 – Variation of Optimum reactance with frequency for the cases with and without swirl for the approach case

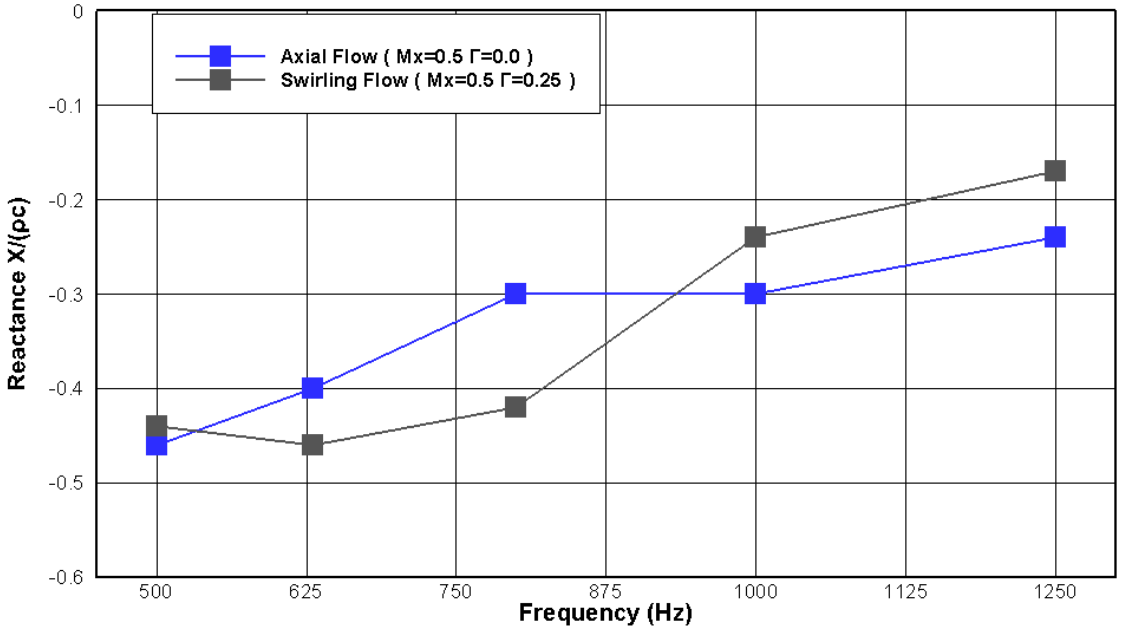

Fig. 7.33 – Variation of Optimum reactance with frequency for the cases with and without swirl for the take-off case

Figures 7.34 and 7.35 show the variation of optimum insetion loss with frequency for the cases with and without swirl at approach and take-off. The swirl causes the insertion loss to decrease for most cases, except for the approach case and 800 Hz, where the insertion loss is almost the same for both cases. For take-off the trends are more straightforward. In this case the insertion loss decreases when swirl is present. For the case, the Mach number is higher and the amount of circunferential modes considered is larger, as more modes cut on.

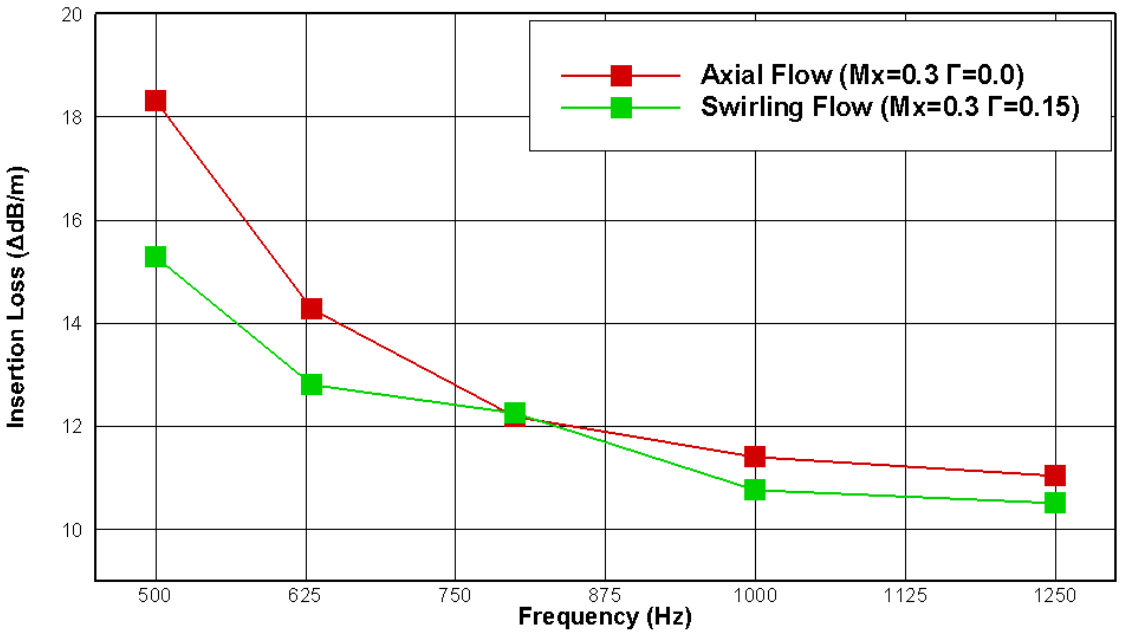

Fig. 7.34 – Variation of Optimum insertion loss with frequency for the cases with and without swirl for the approach case

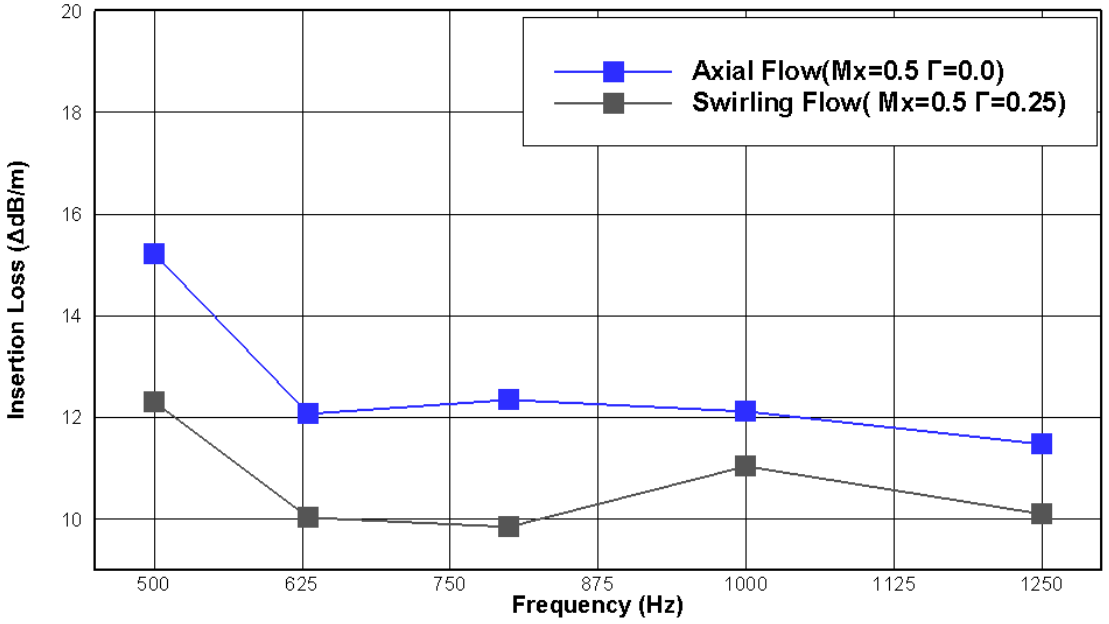

Fig. 7.35 – Variation of Optimum insertion loss with frequency for the cases with and without swirl for the take-off case

7.2.6 Variation of Optimal Impedance and Insertion Loss with the direction of propagation

So far, the parametric study that investigated how the swirling flow affects optimum impedance was undertaken by carrying out multimode calculations for a simulated broadband noise source propagating upstream from the stators towards the fan in the interstage region. The results are not exactly the same when a simulated broadband noise source propagating downstream of the rotor towards the stator in the interstage region is considered.

To exemplify the case in which a simulated broadband noise source propagating downstream of the rotor towards the stator in the interstage region is considered, further calculations were carried out for the approach condition and frequency of 500 Hz $(He = 9.24)$.

The insertion loss for the broadband source was calculated in the same way as previous cases (from Equation 3.162). The modal content considered was also defined based on modal triangles from section 7.1.3. The nearly convected modes are not considered in this calculations because they carry a very small pressure component that is not of significance for the calculation of acoustic power.

As shown in Figure 7.36, the optimum impedance for this case is $z = 0.98 - 0.54i$ and the transmission loss is $15.5 dB/m$. Results are also compared in the table below for the case in which swirling flow is neglected, for the swirling flow case with an upstream source and for the swirling flow case with a downstream source.

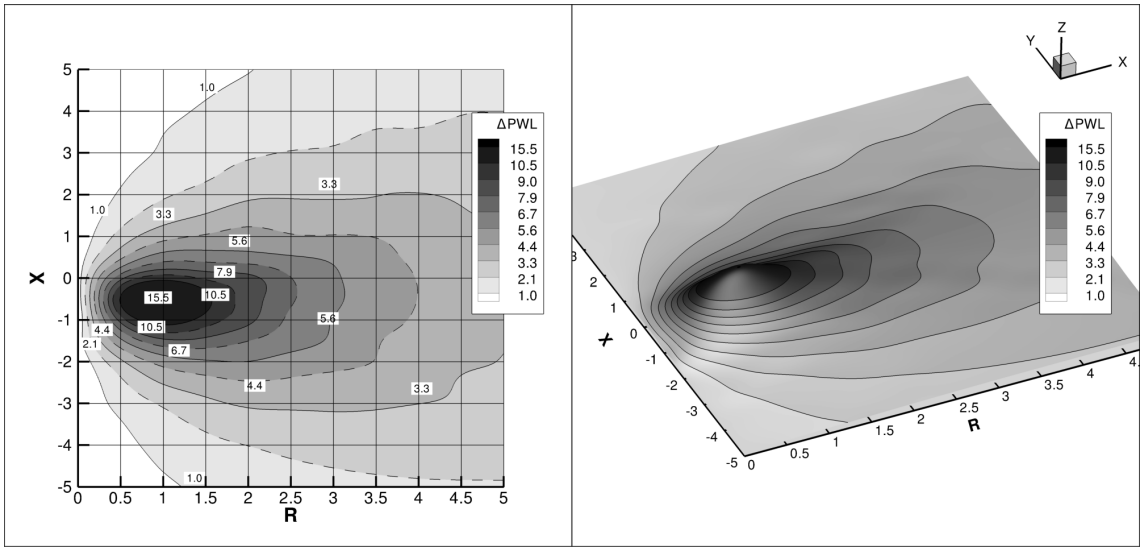

Fig. 7.36 – Results for a simulated broadband noise source propagating downstream of the rotor towards the stator in the interstage region.Approach condition and frequency of 500 Hz $(He = 9.24)$.

Comparison between optimum impedance and insertion loss		
No Swirl	Source upstream	Source Downstream
18.3 dB/m z=0.66-0.53i	15.5 dB/m z=0.98-0.54i	15.3 dB/m z=0.98-0.54i

It is observed that when the source is placed upstream the trends remain the same when the swirling flow case is compared to the case in which the swirling flow is neglected in terms of optimum insertion loss and optimum impedance. When swirl is considered, the optimum insertion loss decreases, the optimum resistance increases and the change in optimum reactance is not of significance. When the two swirling flows are compared, it is observed that the optimum insertion loss is lower for the case in which the source is placed downstream, although the optimum impedance remains the same.

7.2.7 Summary and Comments

In this chapter a parametric study has been presented to evaluate the effect of swirl and liners on sound propagation in the insterstage region of a turbofan engine. The study focuses on a broadband noise source generated by the OGVs propagating upstream in a swirling flow. Geometric and mean flow parameters and frequency were chosen to correspond to realistic values in a turbofan engine at approach and take-off conditions. The first part of the study was carried out for hard-walled ducts. It was observed that the swirl changes the modal content. The higher the swirling flow magnitude, the more modal content is shifted to negative circumferential mode orders. Co-rotating modes become more cut-on and contra-rotating modes become more cut-off.

Results are presented for two types of mean swirling flows: rigid body and vortex swirl The former occurs in low speed rigs such as the Advanced Noise Control Fan while the latter is more characteristic of more realistic turbofan engines.

The second part of this chapter focused on the effect of swirling flow on optimal liner attenuation in the interstage region. It is considered that the broadband noise source is placed downstream and that the sound propagates upstream, against the flow. The modal content for the broadband source was defined based on equal energy power distributed among the cut-on acoustic modes for the hard walled case. Contour plots of attenuation versus impedance were generated for approach and take-off mean flow conditions. When swirl is present, the optimum resistance and the optimal resistance increase and the change in optimal liner reactance is not as pronounced. The swirling flow also reduces overall attenuation when the optimum impedance is chosen. The insertion loss is lower when swirl is present. As a conclusion, the effect of swirl is significant and should be considered when designing liners for the interstage region .

To exemplify the case in which a simulated broadband noise source propagating downstream of the rotor towards the stator in the interstage region is considered, further calculations were carried out for the approach condition and frequency of 500 Hz ($He = 9.24$). It is observed that when the source is placed upstream the trends remain the same when the swirling flow case is compared to the case in which the swirling flow is neglected in terms of optimum insertion loss and optimum

impedance. When swirl is considered, the optimum insertion loss decreases, the optimum resistance increases and the change in optimum reactance is not of significance. When the two swirling flows are compared, it is observed that the optimum insertion loss is lower for the case in which the source is placed downstream, although the optimum impedance remains the same.

Chapter 8

Conclusion and Future Research

The current trends for next generation turbofan engines are towards shorter nacelles and increased distances between the fan and the outer guide vanes. This leads to an overall reduction in lined surface areas as well as an increase in the relative importance of the interstage liner. To date most research on liners in terms of physical insight, prediction methods and experimental data have been for intakes and bypass ducts. The interstage is different in that the liner is subject to a mean flow with a strong swirl component. This region is of high significance when it comes to turbomachinery noise since much of the aircraft noise is generated in this region. This project contributes to understanding and predicting the effect of the swirl on liner attenuation.

The novel contributions of this PhD thesis include the development and validation of a unique computational tool (SwirlProp code), a cross-validation with a Rolls-Royce in-house code, the comparison between predictions from this tool and experimental results from the Advanced Noise Control Fan at NASA Glen Research Center and a parametric study that analyses the effect of swirling flows on sound propagation in annular lined and hard-walled ducts. Also, this is the first time that a parametric study is carried out for lined ducts in terms of optimum impedance. The key achievements are presented in the following paragraphs.

First, an introduction on Aircraft Noise Theory and Interstage Liners was presented. A comprehensive literature review has been undertaken, first focusing on sound propagation in Axisymmetric parallel shear flows only and then including the effect of swirling flow. From the review of the state of the art it has become evident that the studies on sound propagation in swirling flows are very limited and that to develop a model that includes the effect of swirling flows is more challenging than to develop a model that includes only the effect of parallel sheared flow. To model the effect of swirl, one has to take into account the full set of Linearized Euler Equations or one single equation with a sixth order operator.

Two models were developed in this thesis following the cronological approach presented in the bibliographic review. Firstly, a model based on a ducted (non-swirling) sheared mean flow using a single equation model based on the the Pridmore-Brown equation. Secondly, a more complex model based on the Linearized Euler equations. The Ingard-Myers boundary condition is used in

both cases. The boundary condition was implemented in the velocity field instead of in the pressure field, giving good results specially for the plane wave case. A normal mode analysis was applied to obtain the eigenvalue problem and the equations were discretized using a Finite Difference method. For the case of the Pridmore-Brown equation, the Finite Difference method is of second order, while for the swirling flow case the Finite Difference method is of fourth order.

Both codes were exhaustively validated. The first Finite Difference code based on the Pridmore-Brown equation was validated against a shooting method code and a Finite Difference code for the uniform flow case and for the sheared flow case with and without liners. For the sheared flow case, a power-law profile was used in the validation. This profile has a singularity at the wall and each of the numerical methods deal with this singularity in a different way, causing some discrepancy in the results obtained.

The second code was a fourth-order Finite Difference code that was proposed to evaluate sound propagation in lined annular ducts with swirling flows. This code was verified for axial flows by comparing results with analytical results for the uniform axial flow and hard walls and with predictions from the code based on the Pridmore-Brown equations for sheared flows and lined walls. The fourth-order Finite Difference code was also verified for the swirling flow case against predictions from different methodologies for two different types of swirling flow: the vortex swirl and rigid body. A combination of both types and an axial profile in radial equilibrium were also used in the validation. Good results were obtained.

A cross-validation between the Finite difference code based on the Linearized Euler Equation and the JM66 code from Rolls-Royce was carried out for a more realistic case. Axial wavenumbers and pressure and velocity eigenvectors obtained with the JM66 code were compared with the current Finite Difference code. Results were presented for a mean flow profile corresponding to a vortex swirl with magnitude $\Gamma^* = 0.15$. The axial velocity profile is an uniform axial flow profile with $M_x = 0.3$. Other parameters were reduced frequency $k = 23.28$ and hub to tip ratio $\sigma = 0.4$. The duct is lined in both walls and the impedance value is z$= 2 - 1.5i$. Results were presented for mode orders $m = 20$ and $m = -4$. Results for $m = 20$ are in excelent agreement. Most of the results for $m = -4$ also agree, except for a surface mode. agreement.

A preliminary comparison has been conducted of predictions from the FD code with experimental results from the low speed Advanced Noise Control fan for axial and swirling mean flows in a hard-walled and a lined duct (z=1.5-1.975i) at the frequency of 500 Hz. The modes propagating upstream and downstream were generated one at a time using a configurable artificial noise sourse (CFANS). Predictions were compared with experimental results for no flow, axial flow and swirling flow for circunferential modes m between -4 and 4. Qualitative agreement is obtained with the measured Power Transmission loss (TL) that increases as an effect of the swirl for a prescribed impedance, but low Mach numbers and modest Transmission loss levels have made it difficult to validate the FD code thus far. To the author's knowledge, it is the first time that an experimental protocol is

designed to tackle the effect of swirling flow on interstage liners and one of the suggestions for future studies would be to repeat this protocol in a rig with higher speed.

A parametric study was undertaken for hard-walled and lined ducts to evaluate the effect sound propagation in swirling flows. The swirl changes the modal content. The higher the swirling flow magnitude, the more modal content is shifted to negative circumferential mode orders. Co-rotating modes become more cut-on and contra-rotating modes become more cut-off. When acoustic absorptive liners are considered, the swirl changes the liner optimum resistance and reactance and affects the optimum insertion loss. The optimum resistance becomes considerably higher and the change in optimal liner reactance is not as pronounced. The swirling flow also reduces attenuation; the insertion loss is lower when swirl is considered. As a conclusion, swirling flow should be considered when designing liners. To exemplify the case in which a simulated broadband noise source propagating downstream of the rotor towards the stator in the interstage region is considered, further calculations were carried out for the approach condition and frequency of 500 Hz ($He = 9.24$). It is observed that when the source is placed upstream the trends remain the same when the swirling flow case is compared to the case in which the swirling flow is neglected in terms of optimum insertion loss and optimum impedance. When swirl is considered, the optimum insertion loss decreases, the optimum resistance increases and the change in optimum reactance is not of significance. When the two swirling flows are compared, it is observed that the optimum insertion loss is lower for the case in which the source is placed downstream, although the optimum impedance remains the same.

The original contributions of this thesis are:

- An engineering model named SwirliProp that is able to deal with the effect of the swirl behind the rotor and in front of the stator and that considers the effect of liners on the inner and outer walls was developed. In the current study the duct is considered approximately uniform. The tool is based on an axisymetric Finite Difference formulation for modes in swirling flow and is implemented in Matlab. In this code, the Ingard-Myers boundary condition is implemented in the velocity field instead of in the pressure field, giving good results specially for the plane wave case and making the code more stable. A validation of the engineering model was presented against predictions from different methodologies including the shooting method methodology and an alternative modal model from Poisson & Peake [2]

- The SwirlProp code was cross-validated with from a Rolls-Royce in-house code, giving good results.

- Comparison with real data from the Advanced Noise Control Fan at NASA Glenn Research Center. It was possible to take part in all stages of this comparison. From the tests design to, through the data acquisition and finally in the comparison between measurements and predictions. To the author's knowledge, it is the first time that an experimental protocol is designed to tackle the effect of swirling flow on interstage liners.

- Parametric Study: A parametric study has been carried out with the objective of understanding

the effect of swirling flows on broadband noise propagation in the interstage region in the presence of liners. Also, this is the first time that a parametric study is carried out for lined ducts in terms of optimum impedance.

While all the projects objectives have been accomplished, a list of recommendations for future work are listed below:

- Engineering Model: In the current study the duct is considered approximately uniform. The next step to improve this engineering model would be to include the effect of the change in the duct radius in the formulation. Also, the model used in this thesis to calculate the acoustic power has its limitations. This has been used by previous authors, but this is certainly an open topic.
- Numerical implementation of the engineering model: It would be useful to implement and test different filters. The filter implemented in section 4.2.4 gives accurate results and it is stable, but maybe it could be improved.
- Comparison with real data: It would be useful to compare predictions from the current code with experimental results from a rig that has a higher swirling flow Mach number. Also, the rotating rake mode measurement system from the Advanced Noise Control Fan does not take into consideration the swirling flow to calculate the modal power amplitude (see Equation 6.1). The formulation presented in this thesis could contribute to improve the rotating rake turbofan duct mode measurement system or systems from other rigs that do not include the effect of the swirl.
- Parametric Study: The parametric study has been carried out to account for a broadband source generated at the OGVs propagating upstream. Although an example was presented for a broadband noise source generated at the rotor, propagating downstream, further studies are needed. Also, if the contour plots from the parametric study for a source downstream and a similar study for a source placed upstream are overlapped, an optimum impedance that accounts for the sound propagating on both directions could be estimated.

References

[1] R. Nijboer, "Eigenvalues and eigenfunctions of ducted swirling flows," *7th AIAA/CEAS Aeroacoustics Conference, AIAA 2001-2178*, 2001.

[2] Posson, H. and Peake, N., "Swirling Mean Flow Effect on Fan-trailing Edge Broadband Noise in a Lined Annular Duct," *19th AIAA/CEAS Aeroacoustics Conference, AIAA 2013-2150*, 2013.

[3] R.Loew, J.Lauer, J.McAllister and D.Sutliff, "The Advanced Noise Control Fan," *25th AIAA Aerodynamic Measurement Technology and Ground Testing Conference, Fluid Dynamics and Co-located Conferences*, AIAA-2006-3150, 2013.

[4] D. Sutliff, "Rotating rake turbofan duct mode measurement system," *Nasa Technical Memorandum*, NASA TM-2005-213828, 2005.

[5] N. Peake and A. B. Parry., "Modern challenges facing turbomachinery aeroacoustics," *Annu. Rev. Fluid Mechanics*, vol. 44, pp. 227–248, 2012.

[6] Boeing Commercial Airplanes, "Boeing Market Outlook 2013-2032," Available at http://www.boeing.com/assets/pdf/commercial/cmo/pdf/Boeing_Current_Market_Outlook_2013.pdf month = July, year = 2013,.

[7] G. L. Dillingham., "Aviation and the Environment: Airport Operations and Future Growth. Present Environmental Challenges," United States General Accounting Office (GAO), Report RCED-00153, 2000.

[8] R. Astley, *Propulsion System Noise :Turbomachinery, Encyclopedia of Aerospace Engineering*, R. Blockley and W. Shyy, Eds. New York: John Wiley & Sons, 2010.

[9] A. E.Envia and D.L.Huff., "Fan noise: A challenge to caa," *International Journal of Computational Fluid Dynamics*, vol. 18, pp. 471–480, 2004.

[10] E. J.Groeneweg, T.Sofrin and P.Gliebe, *Turbomachinery Noise , Aeroacoustics of Flight Vehicles: Theory and Practice, NASA Ref. Pub. 1258, Vol . 1.*, H. Hubbard, Ed. New York: Acoustic Society of America, 1991.

[11] A.L.P.Maldonado, R. Miserda, and B.Gutierrez., "Computational tonal noise prediction for the advanced noise control fan," *18th AIAA/CEAS Aeroacoustics Conference (33rd AIAA Aeroacoustics Conference)*, vol. AIAA 2012-2128, 2012.

[12] M. J. T. Smith., *Aircraft Noise*. Cambridge: Cambridge University Press, ISBN 9780521331869, 1989.

[13] U. Michel and H. Siller, "Aircraft noise course," 2010, dLR Lecture series 2010, DLR IB 92517-09/B2.

[14] J. M. Tyler and T. G. Sofrin, "Axial flow compressor noise studies," *SAE Transactions* , vol. 309, p. 32, 1965.

[15] Rolls-Royce Website, "http://www.rolls-royce.com/products-and-services/civil-aerospace/products/future-products/ultrafan.aspx , Accessed on the 15th of June of 2016."

[16] R. Astley, "Predicting and treating fan and turbomachinery noise current technology, research & facilities," *UK-Japan Bilateral Workshop, Aircraft Emissions and Noise*, 2006.

[17] R. Motsinger and R. Kraft, *Design and Performance of Duct Acoustic Treatment , Aeroacoustics of Flight Vehicles: Theory and Practice, NASA Ref. Pub. 1258, Vol . 2.*, H. H. Hubbard, Ed. New York: Acoustic Society of America, 1991.

[18] D. C. Pridmore-Brown, "Sound propagation in a fluid flowing through an attenuation duct," *Journal of Fluid Mechanics*, vol. 4 (4), pp. 393–406, 1958.

[19] S. D. Savkar, "Propagation of sound in ducts with shear flow," *Journal of Sound and Vibration*, vol. 19 (3), pp. 355–372, 1971.

[20] J. E. Nayfeh, A. H. Kaiser and D. P. Telionis, "acoustics of aircraft engine-duct systems," *AIAA Journal* , vol. 13 (2), pp. 60–65, 1975.

[21] D. H. Tack and R. F. Lambert., "Influence of shear flow on sound attenuation in a lined duct," *Journal of Acoustic Society of America*, vol. 38, p. 655, 1965.

[22] P. Mungur and G. L. Gladwell., "Acoustic wave propagation in a sheared fluid contained in a duct," *Journal of Sound and Vibration*, vol. 9 (1), pp. 28–48, 1969.

[23] P. Mungur and H. E. Plumbee., "Propagation and attenuation of sound in as soft-walled annular duct containing a sheared flowt," *NASA*, vol. SP-207, p. 305327, 1969.

[24] W.Eversman, "Effect of boundary layer on the transmission and attenuation of sound in an acoustically treated circular duct," *Journal of Acoustical Society of America*, vol. 49, pp. 1372–1380, 1971.

[25] W. Eversman, "Representation of a 1/n power law boundary layer in the sheared flow acoustic transmission problem," *Journal of Sound and Vibration*, vol. 24 (4), pp. 459–469, 1972.

[26] P. N. Shankar, "Sound propagation ducts shear layers," *Journal of Sound and Vibration*, vol. 22 (2), pp. 221–232, 1972.

[27] W. Mohring, "On the resolution into modes of sound field in ducts, with shear flow," *presented at the symposium of Acoustics of Flow in Ducts, University of Southampton*, 1972.

[28] B.Tester, "The propagation and attenuation of sound in lined ducts containing uniform or plug flow," *Journal of Sound and Vibration*, vol. 28, pp. 151–203, 1973.

[29] B. Tester, "Some Aspects of Sound Attenuation in Lined Ducts ContainingInviscid Mean Flows with Boundary Layers," *Journal of Sound and Vibration*, vol. 28, pp. 217–245, 1973.

[30] K. J. E. Nayfeh, A. H. and D. P. Telionis, "Transmission of sound trough annular ducts of varying cross sections," *AIAA Journal* , vol. 13 (1), pp. 60–65, 1975.

[31] S.-H. Ko, "Sound attenuation in lined rectangular ducts with flow and its aplication to the reduction of aircraft engine noise," *Journal of the Acoustical Society of America*, vol. 50, pp. 1418–1432, 1971.

[32] U. J.Kurze and C. H. Allen., "Influence of flow and high sound level on the attenuation in a lined duct," *Bolt, Beranck and Newman, Inc. Progress Report N4*, 1969.

[33] A. S. Hersh and I. Catton, "Effect of shear on sound propagation in rectangular ducts," *Journal of the Acoustical Society of America*, vol. 50, pp. 992–1003, 1971.

[34] S.Mariano, "Effects of sound shear layers on the sound attenuation in acoustically lined rectangular ducts," *Journal of Sound and Vibration*, vol. 19, pp. 261–275, 1971.

[35] S.-H. Ko, "Sound attenuation in acoustically lined circular ducts in the presence of uniform and shear flow," *Journal of Sound and Vibration*, vol. 22 (2), pp. 193–210, 1972.

[36] E. Dokumaci, "A plane wave approximation to sound transmission in parallel sheared mean flow." *Journal of Sound and Vibration*, vol. 284, pp. 551–565, 2005.

[37] P. N. Shankar, "On acoustic refraction of duct shear layers," *Journal of Fluid Mechanics*, vol. 47 (01), pp. 81–91, 1971.

[38] G. Vilenski and S. W. Rienstra, "Acoustic modes in a ducted shear flow." *11th AIAA/CEAS Aeroacoustics Conference* , vol. AIAA 2005-3024, 2005.

[39] A.McAlpine, M. J. Fischer, and B. J. Tester, "Buzz-saw noise: A comparison of modal measurements with an improved prediction method." *Journal of Sound and Vibration*, vol. 306, pp. 419–443, 2007.

[40] J. Unruh and W. Eversman, "The transmission of sound in an acoustically treated rectangular duct with boundary layer," *Journal of Sound and Vibration*, vol. 25 (3), pp. 371–382, 1972.

[41] G. A. Wynne and H. E. Plumbee., "Calculation of eigenvalues of the finite difference equations describing sound propagation in a duct carrying sheared flow," *Presented at the 79th Spring Meeting of the Acoustical Society of America*, 1970.

[42] K. A. Kousen., "Eigenmodes of ducted flows with radially-dependant axial and swirl components," *NASA CR-1999-208881*, 1999.

[43] C. Hirsch, *Numerical Computation of Internal and External Flows*, K. S. Peat, Ed. Butterworth-Heinemann, John Wiley and Sons, Oxford. ISBN: 9780750665940, 2007.

[44] R. Astley and W. Eversman, "a finite element formulation of the eigenvalue problem in lined ducts with flow." *Journal of Sound and Vibratio*, vol. 65(1), pp. 61–74, 1979.

[45] R. Astley and W. Eversman, "Finite element duct eigenvalue problem: An improved formulation with hermitian elements and no-flow condensation." *Journal of Sound and Vibratio*, vol. 69(1), pp. 13–25, 1980.

[46] R. G. Gabard, "A computational mode-matching approach for sound propagation in three-dimensional ducts with flow." *Journal of Sound and Vibration*, vol. 315, pp. 1103–1124, 2008.

[47] G. G.Vileski and S. W. Rienstra, "On hydrodynamic and acoustic modes in a ducted shear flow with wall lining," *Journal of Fluid Mechanics*, vol. 583, pp. 45–70, 2007.

[48] C. K. Tam and L. Ariault., "The wave modes in ducted swirling flows," *Journal of Fluid Mechanics*, vol. 371, pp. 1–20, 1998.

[49] S. W. Rienstra, "A classification of duct modes based on surface waves," *Wave motion* , vol. 37, pp. 119–135, 2003.

[50] G. G. Vileski and S. W. Rienstra, "Numerical study of acoustic modes in ducted shear flows," *Journal of Sound and Vibration*, vol. 307 (3-5), pp. 610–625, 2007.

[51] Y. Guan and T. Q.Wang., "Effect of mean entropy on eigenmodes in annular duct with swirling flow ." *13th AIAA/CEAS aeroacoustics conference, AIAA 2007-35361* , 2007.

[52] Y. Guan, K. Luo, and T. Q.Wang., "Sound transmission in lined annular duct with mean swirling flow." *NoiseCon 2008/ASME NCAD, Dearborn, Michigan, USA, NCAD2008-73081* , 2008.

[53] C. J. Brooks and A. McAlpine, "Sound transmission in ducts with sheared mean flow," *13th AIAA/CEAS aeroacoustics conference, AIAA-2007-3545*, 2007.

[54] M.Oppeneer, S. W. Rienstra and P. Sijtsma, "Efficient Mode-Matching Based on closed Form Integrals of Pridmore-Brown Modes," *19th AIAA/CEAS Aeroacoustics Conference*, vol. AIAA-2013-2172, 2013.

[55] G.Gabbard, "Private Communication."

[56] V. V. Golubev and H. M. Atassi., "Sound propagation in an annular duct with mean potential swirling flow," *Journal of Sound and Vibration*, vol. 198, pp. 601–616, 1996.

[57] A. J. Cooper and N. Peake, "Upstream-radiated rotor-stator interaction noise in mean swirling flow," *Journal of Fluid Mechanics*, vol. 523, pp. 219–250, 2005.

[58] A. Cooper and N. Peake, "Propagation of unsteady disturbances in slowly varying duct with mean swirling flow," *Journal of Fluid Mechanics*, vol. 445, pp. 207–234, 2001.

[59] H. Posson and N. Peake., "The acoustic analogy in an annular duct with swirling mean flow." *Journal of Fluid Mechanics*, vol. 726, pp. 439–475, 2013.

[60] K. A. Kousen, " Eigenmode analysis of ducted flows with radially dependent axial and swirl components ," Proceedings of the first joint CEAS/AIAA Aeroacoustics Conference, Munich, Germany, pages 1085-1094, 1995.

[61] J. R. Mathews and N. Peake, "Asymptotic and numerical Green's functions in a lined duct with realistic shear and swirl," *22nd AIAA/CEAS Aeroacoustics Conference, AIAA 2016-2922*, 2016.

[62] J. Kerrebrock, "Small disturbances in turbomachine annuli with swirl," *AIAA Journal*, vol. 445, pp. 207–234, 1977.

[63] J.L. Kerrebrock, "Waves and wakes in turbomachine annuli with swirll," *12th Aerospace Sciences Meeting* , AIAA Paper 1974-87.

[64] V. V. Golubev and H. M. Atassi., "Acoustic-vorticity waves in swirling flows," *Journal of Sound and Vibration*, vol. 209, pp. 203–222, 1998.

[65] K. A. Kousen, " Pressure Modes in Ducted Flows with Swirl. ," AIAA paper 96-1679,, 1996.

[66] A.J.Cooper., "Effect of mean entropy on unsteady disturbance propagation in a slowly varying duct with mean swirling flow," *Journal of Sound and Vibration*, vol. 291, pp. 779–801, 2006.

[67] C. J. Heaton and N. Peake, "Algebraic and exponential instability of inviscid swirling flow," *Journal of Fluid Mechanics*, vol. 565, pp. 279–318, 2006.

[68] V. V. Golubev and H. M. Atassi., "Aerodynamic and acoustic response of a blade row in unsteady swirling flow," *Proceedings of the first joint CEAS/AIAA Aeroacoustics Conference, Munich, Germany*, pp. 167–176, 1995.

[69] M. Myers, "An exact energy corollary for homentropic flow," *Journal of Sound and Vibration*, vol. 109, pp. 277–284, May 1986.

[70] Myers, M.K., "Transport of energy by disturbances in arbitrary steady flows," *Journal of Fluid Mechanics*, vol. 226, pp. 383–400, May 1991.

[71] O. Atassi, "Computing the sound power in nonuniform flow," *7th AIAA/CEAS Aeroacoustics Conference*, vol. AIAA 2001-2120, 2001.

[72] U. Ingard, "Influence of fluid motion past a plane boundary on sound reflection, absorption and transmission," *Journal of Acoustical Society of America*, vol. 31(7), pp. 1035–1036, 1959.

[73] D. L. Huff, "Source noise modeling efforts for fan noise in nasa research programs," *Presentation at Honeywell Acoustics Symposium; Phoenix, AZ*, 2006.

[74] G. Gabard, "A comparison of impedance boundary conditions for flow acoustics," *Journal of Sound and Vibration*, vol. 332, pp. 714–724, 2013.

[75] M. Myers, "On the acoustic boundary condition in the presence of Flow," *Journal of Sound and Vibration*, vol. 71(3), pp. 429–434, May 1980.

[76] S. W. Rienstra and A. Hirschberg, *An Introduction to Acoustics*, 2006.

[77] M. E. Goldstein, *Aeroacoustics*. McGrawn-Hill, New York, 1976.

[78] C. B. Moler and G. W. Stewart, "An algorithm for generalized matrix eigenvalue problems," *SIAM Journal on Numerical Analysis*, vol. 10 (2), pp. 241–256, 1973.

[79] C. K. W. Tam, *Computational Aeroacoustics. A wave Number Approach*, W. Shyy and V. Yang, Eds. Cambridge Aerospace Series. ISBN 978-0-521-80678-7, 2012.

[80] D.Giacche, L. Xu, and A. Wilson, "Comparison between postprocessing methods applied to rotor-stator-interaction tone-noise problems." *AIAA Journal*, vol. 49, pp. 1214–1229, 2011.

[81] Sutliff, D. L. and Walker, B. E., "Artificial Noise Systems for Parametric Studies of Turbomachinery Aero-acoustics," *International Journal of Aeroacoustics*, vol. 15, pp. 103–130, 2016.

[82] J. McAllister and D. Sutliff, "The advanced noise control fan baseline measurements," *Nasa Technical Memorandum*, vol. TM2009-215595, 2009.

[83] V. V. Golubev and H. M. Atassi., "Sound propagation in an annular duct with mean potential swirling flow," *Journal of Sound and Vibration*, vol. 198 (5), pp. 601–616, 1996.